THE UNIVERSITY *of* EDINBURGH

Superconducting Wireless Power Transfer for Electric Vehicles

Philip Emanuel Machura

A thesis submitted for the degree of Doctor of Philosophy

The University of Edinburgh

2020

Declaration of originality

1. I declare that this thesis has been composed solely by myself and that it has not been submitted, in whole or in part, in any previous application for a degree. Except where states otherwise by reference or acknowledgment, the work presented is entirely my own.
2. I confirm that this thesis presented for the degree of Doctor of Philosophy, has
   i) been composed entirely by myself
   ii) been solely the result of my own work
   iii) not been submitted for any other degree or professional qualification
3. I declare that this thesis was composed by myself, that the work contained herein is my own except where explicitly stated otherwise in the text, and that this work has not been submitted for any other degree or processional qualification except as specified.

Edinburgh, July 2020

Philip Machura

Acknowledgements

First and foremost, I would like to thank my supervisor Dr Quan Li for the opportunity to pursue this research, for his guidance and advice throughout the years.

A special thanks to my second supervisor Dr Sasa Djokic for his critical thinking, tough questions and valuable feedback.

I am truly grateful to the technical staff at the School of Engineering, particularly Steven Gourlay, Douglas Carmichael and Jamie Graham as well as Mike from Fountain Design Ltd who have offered me significant help with their practical expertise.

I wish to thank the Applied Superconductivity group members for their insight into their projects, many talks, their time and critical questions. Similarly, I would like to recognise the help of Joseph Burchell, Ignacio Barajas-Solano and Ben McGilton throughout my time in Edinburgh.

Furthermore, I would like to thank the Wireless power transfer group of Tianjin Polytechnic University for their hospitality and practical expertise during my time in Tianjin.

On a more personal note, I would also like to thank Kevin, Manuel, Encarni, Anna, Thomas and Yvonne for making my time in Edinburgh more enjoyable.

I must express my deepest gratitude to my family for their continuous support and understanding.

Finally, I would like to express great appreciation to Valérie for believing in me when I did not and supporting me through all ups and downs.

Abstract

Electric vehicles (EVs) are an important pillar for the transition towards a cleaner and more sustainable future as renewable energy can penetrate into the transportation section and act as energy storage to cope with the intermittent supply of such energy sources. EVs have recently been significantly developed in terms of both performance and drive range. Various models are already commercially available, and the number of EVs on roads increases rapidly. Rather than being limited by physical cable connections, the wireless (inductive) link creates the opportunity of dynamic charging – charging while driving. Once realised, EVs will no longer be limited by their achievable range and the requirement for battery capacity will be greatly reduced. However, wireless charging systems are limited in their transfer distance and power density. Such drawbacks can be alleviated through high-temperature superconductors (HTS) and their increased current carrying capacity, which can substitute conventionally used copper coils in the charging pads.

This thesis investigates the effectiveness of wireless power transfer (WPT) systems as a whole and when HTS coils are used as well as HTS performance at operating frequencies commonly used in WPT-systems. Initially, the fundamentals of superconductivity are outlined to give some background on how such conductors can help tackle problems occurring in WPT-systems and how their behaviour can be simulated. Subsequently, key technical components of wireless charging are summarised and compared, such as compensation topologies, coil design and communication. In addition, health and safety concerns regarding wireless charging are addressed, as well as their relevant standards. Economically, the costs of a wide range of wireless charging systems has also been summarised and compared.

To explore the benefits of WPT-system for EVs, a force-based vehicle model is coupled with an extended battery model to simulate the impact of wireless charging on the state of charge of the accumulator sub-system. In total, three different scenarios, i.e. urban, highway and combined driving are presented. The trade-off between having a standalone charging option versus combined dynamic (or on-road charging) and quasi-dynamic (stationary charging in a dynamic environment) wireless charging is outlined and minimum system requirements, such as charging power levels and road coverage, for unlimited range are established. Furthermore, the effects of external factors such as ambient temperature, battery age and wireless transfer efficiency are investigated. It is shown that employing combined charging at medium power levels is sufficient to achieve unlimited range compared to high power requirements for standalone charging.

HTS coils show great potential to enhance the WPT-system performance with high current-carrying capability and extremely low losses under certain conditions. However, HTS coils exhibit highly nonlinear loss characteristics, especially at high frequencies (above 1 kHz), which negatively influence the overall system performance. To investigate the improvements, copper, HTS and hybrid wireless charging systems in the frequency range of 11-85 kHz are experimentally tested. Results are compared with finite element analysis (FEA) simulations, which have been combined with electrical circuit models for performance analysis. The measurements and modelling results show good agreement for the WPT-system and HTS charging systems have a much higher transfer efficiency than copper at frequencies below 50 kHz. As the operating frequency increases towards 100 kHz, the performance of HTS systems deteriorates and becomes comparable to copper systems. Similar results are obtained from hybrid systems with a mixture of HTS and copper coils, either as transmitting or receiving coils. Nevertheless, it has been demonstrated that HTS significantly improves the transfer efficiency of wireless charging within a certain range of frequencies.

The AC losses occurring in HTS coils, particularly transport current loss, magnetisation loss and combined loss, at high frequencies are studied further. A multilayer 2D axisymmetric coil model based on ***H***-formulation is proposed and validated by experimental results as the HTS film layer is inapplicable at such frequencies. Three of the most commonly employed coil configurations, namely: double pancake, solenoid and circular spiral are examined. While spiral coils experience the highest transport current loss, solenoid coils are subject to the highest magnetisation loss due to the overall distribution of the turns. Furthermore, a transition frequency is defined for each coil when losses in the copper layer exceed the HTS losses. It is much lower for coils due to the interactions between the different turns compared to single HTS tapes. At higher frequencies, the range of magnetic field densities, causing a shift where the highest losses occur, decreases until losses in the copper stabilisers always dominate. In addition, case studies investigating the suitability of HTS-WPT are proposed.

Lastly, methods to reduce AC losses of HTS coils are investigated with particular focus on flux diverters, which have been used for low frequency superconducting applications but their effectiveness at high frequencies is unexplored. Therefore, the impact of flux diverters on HTS double pancake coils operating at high frequencies up to 85 kHz is researched. Various geometric characteristics of the flux diverter are investigated such as air gap between diverter and coil, width and thickness. An FEA-model was used to examine the coil and diverter losses at such frequencies

and different load factors between 0.1 and 0.8. It is demonstrated that flux diverters are a viable option to reduce the coil losses even at high frequencies and the width of the coil has the biggest impact on the loss reduction. In general, flux diverters are more suitable for applications using high load factors. Lastly, the impact of the diverter in terms of magnetic field distribution above the coil and overall loss distribution in the HTS coil was examined.

"[…] we think that when we suffer a defeat that all is ended. […] that the light had left […] forever. Not true. It is only a beginning, always. The young must know it; the old must know it. It must always sustain us, because the greatness comes not when things go always good for you, but the greatness comes and you are really tested, when you take some knocks, some disappointments, when sadness comes, because only if you have been in the deepest valley can you ever know how magnificent it is to be on the highest mountain." – Richard Nixon

Table of contents

List of Figures

List of Tables

Acronyms and abbreviations

A4WP	Alliance for Wireless Power Transfer
AIMD	active implantable medical
BCS	Bardeen-Cooper-Schrieffer theory
BMS	battery management system
BSCCO	Bismuth strontium calcium copper oxide
CC	coated conductors
CPT	capacitive power transfer
CSM	critical state model
DSRC	designated short-range communication
DWPT	dynamic wireless power transfer
EVs	electric vehicles
EMF	electromagnetic field
FEA	finite element analysis
FOD	foreign object detection
FRP	fibre reinforced plastics
G2V	grid to vehicle
GA	ground assembly
GRP	glass-fibre reinforced plastic
H&S	health and safety
HTS	high temperature superconductors
HVAC	heating, ventilation and air conditioning
HWFET	Highway Fuel Economy Test

ICE	internal combustion engine
ICNIRP	International Commission on Non-Ionizing Radiation Protection
IGBT	insulated gate bipolar transistors
IPT	inductive power transfer
ISO	International Organization for Standardization
LN_2	liquid nitrogen
LOD	living object detection
LTS	low temperature superconductors
MgB_2	Magnesium diboride
MOSFETs	metal-oxide-semiconductor field effect transistors
OLEV	on-line electric vehicle
PAS	Publicly Available Specification
PFC	power factor correction
Ps	phase shift
QDWPT	quasi-dynamic wireless power transfer
REBCO	rare-earth barium copper oxide
RFID	radio-frequency identification
RSU	roadside unit
Rx	receiving coil
SAE	Society of Automotive Engineers
SoC	state of charge
SWPT	stationary wireless power transfer
TRL	Technology Readiness Level

Tx	transmitting coil
UDDS	Urban Dynamometer Driving Schedule
V2G	vehicle to grid
VA	vehicle assembly
WHO	World Health Organization
WiMAX	Worldwide Interoperability for Microwave Access
WPC	Wireless Power Consortium
WPT	wireless power transfer
YBCO	Yttrium-barium-copper-oxid
ZCS	zero current switching
ZVS	zero voltage switching

Publications

[1] **P. Machura** and Q. Li, "A critical review on wireless charging for electric vehicles," *Renewable and Sustainable Energy Reviews,* vol. 104, pp. 209-234, 2019.

[2] **P. Machura**, K. Kails and Q. Li, "Loss analysis of superconducting wireless charging of electric vehicles," *Journal of Physics: Conference Series*, vol. 1559, pp. 012095, 2020.

[3] **P. Machura**, V. De Santis and Q. Li, "Driving Range of Electric Vehicles Charged by Wireless Power Transfer," *IEEE Transactions on Vehicular Technology,* vol. 69, no.6, pp. 5968-5982, 2020.

[4] **P. Machura**, H. Zhang, K. Kails and Q. Li, "Loss characteristics of superconducting pancake, solenoid and spiral coils for wireless power transfer," *Superconductor Science and Technology,* vol. 33, no. 7, p. 074008, 2020.

[5] **P. Machura** and Q. Li, "AC Loss Reduction through Flux Diverters for Superconducting Wireless Charging Coils at High Frequency," *IEEE Transactions on Applied Superconductivity*, vol. 31, no. 3, p. 5900510, 2021.

[6] K. Kails, M. Yao, H. Zhang, **P. Machura**, M. Mueller and Q. Li, "T-formulation based numerical modelling of dynamic loss with a DC background field," *Journal of Physics: Conference Series*, vol. 1559, pp. 012145, 2020.

[7] K. Kails, H. Zhang, **P. Machura**, M. Mueller and Q. Li, "Dynamic loss of HTS field windings in rotating electric machines," *Superconductor Science and Technology,* vol. 33, no. 4, 2020.

[8] H. Zhang, M. Yao, K. Kails, **P. Machura**, M. Mueller, Z. Jiang, Y. Xin and Q. Li, "Modelling of electromagnetic loss in HTS coated conductors over a wide frequency band," *Superconductor Science and Technology,* vol. 33, no. 2, 2020.

[9] H. Zhang, **P. Machura**, K. Kails, H. Chen and M. Mueller, "Dynamic loss and magnetization loss of HTS coated conductors, stacks, and coils for high-speed synchronous machines," *Superconductor Science and Technology*, vol. 33, no. 8, 2020.

[10] H. Zhang, K. Kails, **P. Machura** and M. Mueller, “Conceptual Design of Electrodynamic Wheels Based on HTS Halbach Array Magnets,” *IEEE Transactions on Applied Supercondutivity*, vol. 31, no. 5, p.3601306, 2021.

1 Introduction

1.1 Motivation

The transportation sector is one of the main contributors towards global climate change and CO_2 emissions [11]. With about 60% of the global oil consumption in transportation in 2017, the need for a clean alternative is urgent [12]. Electric vehicles (EVs) are a vital technology to achieve the transition towards a clean energy society. Yet with a share of only 0.5% in global light duty vehicles and 2 million newly sold EVs in 2018, the widespread deployment on a global scale is still hampered [13] [14]. EVs have recently been significantly improved in terms of both performance and drive range. On the current vehicle market, various models are commercially available. Along with the increasing number of EVs on road, how to charge them effectively and efficiently is still challenging, which has a significant impact on power networks [15], [16]. Electric cables charge almost all existing EVs. No matter if at home or on a highway, cables need to be physically connected to the EVs for charging. A more flexible and convenient charging method attracted broad attention, which is wireless charging. Several companies, such as Tesla, BMW and Nissan, have already started to develop wirelessly charged EVs that do not require a physical connection of the two charging sub-systems. Rather than physical cable connections, the wireless (inductive) link enables dynamic charging – charging while driving. Therefore, it tackles one of the weaknesses of current EV technology, the battery system by reducing the required battery capacity by up to 20% [17]. Hence, lowering the initial investment into new EVs but also improving the carbon footprint of such vehicles as fewer resources are required. WPT is therefore highly compelling for EVs and can help increasing the EV uptake.

The idea of wireless power transfer (WPT) can be traced back to the late 19th century, when Nicola Tesla designed the first wireless device, a wireless lightning bulb [18]. Tesla powered the bulb through high-frequency AC potentials between two closely located, but separated, metal plates. This application initiated new opportunities in wireless charging. However, unsolved technical challenges, such as very limited power density and low transfer efficiencies as the distances increase, made this WPT technology develop very slowly. After two centuries, recent advances in WPT technology enable wireless charging over distances longer than two meters by using ‘strongly coupled’ coils [19]. There are two major WPT technologies, inductive power transfer (IPT) and capacitive power transfer (CPT). In the strongly coupled regime, magnetic resonance couples transmitting and receiving coils and realises IPT, while CPT is realised through electric

field interaction between coupled capacitors [20]. The coupling capacitance of such capacitors is determined by the available area of the devices [21]. CPT is limited to short air gaps by the low capacitive current resulting in low power output [22]. On the contrary, IPT can be used for large air gaps around several metres, and its output power is much higher than CPT.

WPT, including both CPT and IPT enable power transfer without solid connections. This advantage ensures inherent safety and convenience due to a clear separation between the subsystems, especially for daily applications such as TVs [23], phone chargers [24], and induction heating [25], [26] [27]. Also in medicine, WPT is used to charge active implantable medical devices (AIMD) [28], [29] i.e. pacemakers [30] [31] and other medical equipment [32]. Additional applications include radio-frequency identification (RFID) [33], [34], Sensors [35], [36], and robotics [37] [38].

WPT–systems for EV are categorized into stationary (SWPT), semi/quasi-dynamic (QDWPT), or dynamic charging systems (DWPT). SWPT systems are similar to current plug-in chargers but provide the advantages of WPT systems. An on-board receiving pad and an external charging pad in the pavement substitute the conductive charging system. QDWPT systems can be installed at bus and taxi stops, as well as traffic lights to provide short term charging while accelerating and decelerating in a dynamic environment. DWPT systems work while vehicles are on the move, hence providing energy to the battery, increasing the driving range and overcoming 'range anxiety' depending on the transmission power level [39].

With the work conducted by Sedwick in 2010 [40], new coil materials such as high temperature superconductors (HTS) were introduced to further improve the performance of wireless charging systems. Superconductors are popular due to their unique properties of virtually zero resistance under certain conditions as well as their very high current density, which allows for high power density systems. These characteristics make HTS an interesting material for WPT systems which require low losses and high power densities. However, since then, HTS charging systems kept being a niche field.

1.2 Research objectives and contributions

This thesis aims at investigating the impact of wireless charging on the electric vehicle, more specifically the battery system. Furthermore, the impact of using high temperature superconductors and their performance at frequencies relevant to wireless charging of electric vehicles has been researched.

Each chapter of this thesis represents one step towards understanding the impact of superconductors and their applicability for wireless charging systems. To understand the charging system and its components a thorough literature review is conducted. Based on this, a force-based model of an EV is coupled with a battery model to quantify the impact of stationary and on-road wireless charging on the battery. For the first time, a direct practical comparison between copper. HTS and hybrid systems was conducted in the frequency range relevant to wireless charging of EVs. Experiments were combined with finite element analysis (FEA) models to propose a way of simulating HTS WPT-system performance. The most commonly used coil configurations for wireless charging were further investigated in terms of high frequency HTS AC losses using a novel multilayer model. Furthermore, loss mechanisms and distributions amongst the different coil turns and tape layers were explored. Finally, a commonly used method to reduce AC losses, namely flux diverters, was investigated at this frequency range. Results of the different stages of this research project are published in several high-impact scientific journal articles as well as presented at international conferences. A list of relevant publications of this project can be found below and an extended list is available in the 'Publications' sections.

1. A critical review on wireless charging for electric vehicles [1]
2. Driving Range of Electric Vehicles Charged by Wireless Power Transfer [3]
3. Loss characteristics of superconducting pancake, solenoid and spiral coils for wireless power transfer [2], [4]
4. Analysis of AC Loss Reduction through Flux Diverters for Superconducting Coils at high frequency [5]

1.3 Thesis outline

Chapter 2 presents the fundamentals of superconductivity and its underlying principles as well as mechanisms that lead to the phenomena of superconductivity. Different classifications of superconductors are introduced with their corresponding year of discovery. In addition, existing modelling techniques such as the critical state model (CSM) and the ***H***-formulation are outlined followed by analytical solutions for certain geometries. The chapter concludes with the AC loss mechanisms present in superconductors.

Chapter 3 introduces key components of wireless power transfer systems, particularly used for charging electric vehicles. These include the power supply, compensation topologies and coil designs that use copper as well as superconductors. Furthermore, system functions such as control

strategies, foreign object detection and communications between the different sub-systems are described. The impact of wireless charging stations on the electricity grid is illustrated. Finally, costs, health & safety and related standards are evaluated.

Chapter 4 investigates the effectiveness of wireless charging under different external and internal conditions for a variety of scenarios, including quasi-stationary charging, dynamic charging and combined charging. External and internal factors comprise ambient temperature, charging efficiency, time spent on the charging pad, battery life and regenerative braking. Standardised driving cycles, a force-based vehicle model and an electrical battery model are implemented in MATLAB and the impact on the battery state of charge (SoC) is exposed. Minimum charging requirements and system specifications are outlined to achieve unlimited range with a vehicle.

Chapter 5 describes the copper and HTS wireless power transfer experiments. It includes the experimental setup, transfer efficiency results obtained for four different operating frequencies, namely, 11 kHz, 25 kHz, 55 kHz and 85 kHz. In addition, a large number of different combinations with respect to coil arrangements are presented. Firstly, copper and HTS coil systems are investigated and secondly hybrid systems that employ both, copper and HTS coils in one system. The experimental measurements are compared to a combination of circuit simulations and FEA models.

In chapter 6, the AC loss modelling of superconducting coils, namely, double pancake, spiral and solenoid coils is presented. A 2D axisymmetric multilayer model comprising all layers of an HTS tape such as, copper stabilisers, silver overlayer, substrate and superconducting layer is introduced. It relies on the ***H***-formulation, which is implemented in COMSOL and it is validated with experimental data. The multilayer FEA model is compared with the commonly used HTS film approximation and its suitability is investigated. Furthermore, the simplification of the magnetic field dependency of the critical current density is explored. Results obtained explore the transport current loss, magnetisation loss and a combined loss at high frequencies up to 85 kHz, which is commonly used in wireless charging systems for electric vehicles. In addition, the angular dependency of the magnetisation loss and combined loss has been shown. Finally, a transition frequency is introduced defining the operating frequency at which the losses in the copper stabilisers is equal to the HTS losses.

Chapter 7 summarises methods commonly used to reduce AC losses occurring in HTS coils. These methods comprise of substituting the YBCO superconductor for MgB_2, which is widely used due

to its beneficial AC loss characteristic, using stabiliser-free superconducting tapes and implementing flux diverters. An in-depth analysis of the geometric features of flux diverters and their impact on the AC losses of the HTS coil is presented.

Chapter 8 presents HTS-WPT cases studies for different load factors, ranging from low to high power scenarios and frequencies between 1 kHz – 85 kHz. The overall system efficiency is evaluated, which includes the widely neglected impact on the cooling system. Furthermore, this chapter concludes and summarises the research conducted in this project and outlines future areas that should be explored.

2 Fundamentals of Superconductors

2.1 Introduction

Superconductivity was first discovered by H. Kamerlingh Onnes in 1911 and coined ‘supraconductivity’ [41] [42]. It manifests itself with a sudden decrease in resistance as the temperature is reduced below a critical point as shown in Figure 2-1. This critical temperature is specific to the material and marks the transition to a ‘new state’, called superconducting or critical state. Such a transition was first observed in mercury and later in tin and lead at temperatures of 4.2K, 3.8K and 6K, respectively. To achieve such low temperatures sophisticated cooling techniques were employed to liquify helium.

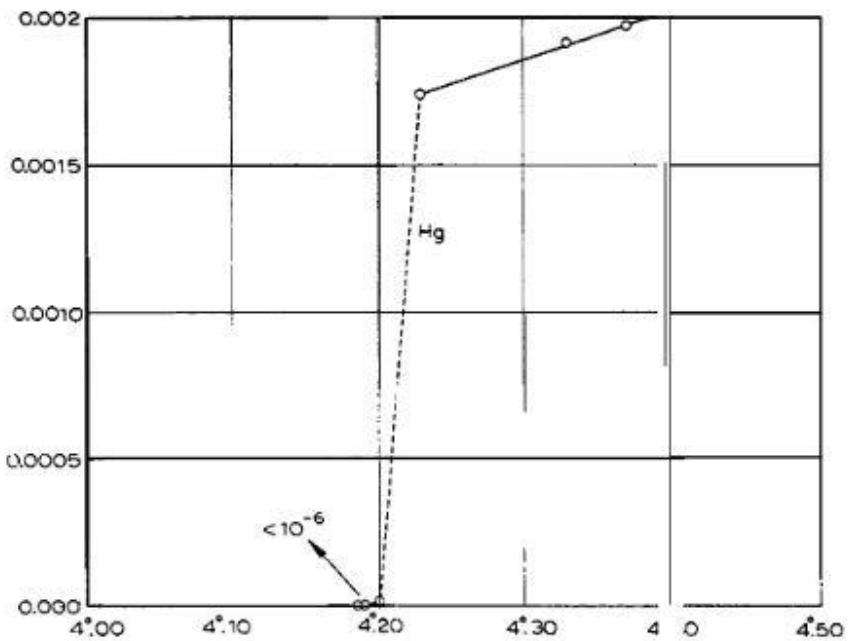

Figure 2-1 Resistance vs temperature for Mercury [41]

The discovery of the perfect conductivity of superconductors raised questions regarding the magnetic field inside the conductor. Meissner and Ochsenfeld, solved the mystery, with the discovery of the second characteristic of superconductors, the so-called Meissner effect in 1933 [43]. It describes the perfect diamagnetism of superconductors, meaning that magnetic fields are expelled from the interior of the conductor when it is cooled below the critical temperature. This phenomenon is theoretically explained by the London equations and it is based on the minimisation of the free energy of the superconducting current [44]. To maintain the

superconducting state, a current flows within a small portion of the outer shell of the conductor, called penetration depth λ.

If the superconducting current exceeds a certain threshold I_c (or current density J_c), it can no longer be contained within the penetration depth and therefore the conductor loses its superconductivity. Similarly, if the external magnetic field exceeds an upper limit H_c, it will penetrate farther into the conductor and the Meissner effect cannot be maintained. Therefore, additionally to the critical temperature T_c, a superconductor is characterised by its critical current density J_c, and a critical magnetic field H_c. All three form the superconducting or critical state in which the material exhibits the previous two properties as shown in Figure 2-2. Outside of those parameters the superconductor converts back into a normal conductor.

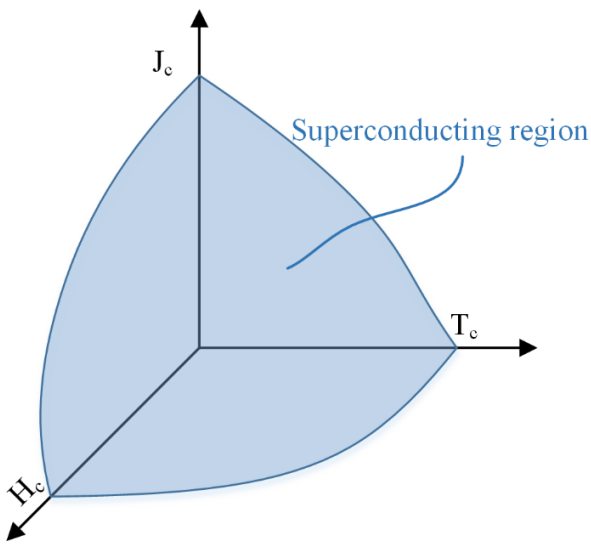

Figure 2-2 Critical parameters of superconductivity

A first mathematical approach towards modelling superconductivity was made by Landau and Ginzburg and was based on the underlying thermodynamic mechanisms without describing the underlying microscopic processes [45]. It was later used to classify different types of superconductors (see chapter 2.2). The gap of a microscopic mechanisms was later filled through the research conducted by John Bardeen, Leon Cooper and John Schrieffer in 1957 [46], [47]. The BCS theory describes superconductivity through the formation of Cooper pairs between electrons. The newly formed pairs move through the material and behave like a boson. Multiple pairs can overlap and ultimately form a Bose-Einstein condensate, which results in an increased minimum energy to excite the system. Due to the higher minimum energy, electrons flow in pairs without

experiencing any resistance when moving through the lattice of a material. The presented theories form the basis of the classic understanding of superconductivity.

2.2 Type-I and Type-II superconductors

Over the years, many occasions of anomalous magnetic behaviour in superconductors were reported and attributed to impurities within the superconductor. However, in 1957, Alexei Abrikosov proposed that this behaviour was an inherent characteristic of a new type of superconductor. This type of superconductor was classified as Type II- superconductor [48].

As described above, the Meissner effect is an important characteristic of superconductors, particularly Type-I. Below the critical magnetic field H_c, the material becomes superconducting and the magnetic field is expelled from the material due to screening currents, whereas above H_c it transitions back into a normal conductor and the external field fully penetrates as shown on the left-hand side in Figure 2-3. Furthermore, according to Ampere's law, the current within a superconductor causes a self-induced magnetic field. This means that even in the absence of an external magnetic field, the current carrying capacity of a superconductor is limited by the self-generated magnetic field. If the self-field exceeds H_c, the superconductor will also convert back into a normal conductor. This behaviour is known as the Silsbee effect and is characteristic for Type-I superconductors [49].

On the contrary, a Type-II superconductor does not revert into a normal conductor once the magnetic field exceeds H_c but rather transitions into a mixed state as depicted on the right-hand side in Figure 2-3. Additionally, H_c and $H_{c1/2}$ depend on the temperature. The transition into a mixed state is more favourable based on the surface energy in Type-II superconductors. This surface energy, as derived in the Ginzburg-Landau theory [45], is also a criterion to classify superconductors. Type-I superconductors have a positive surface energy whereas Type-II superconductors have a negative surface energy

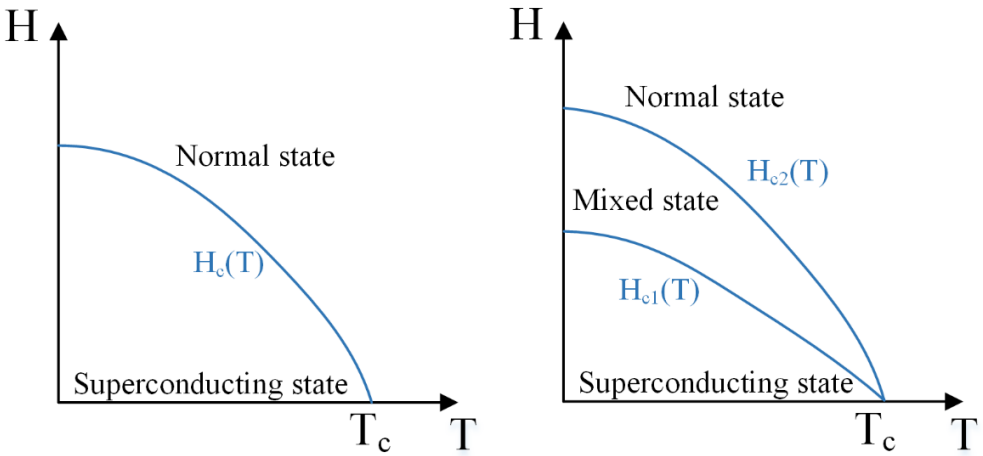

Figure 2-3 Critical magnetic field vs temperature of a Type-I (shown on left hand side) and Type-II (right hand side) superconductor

Within the mixed state, the external magnetic field partially penetrates the superconductor and forms 'normal' regions that are no longer superconducting. The normal regions are of cylindrical nature with a radius of approximately ξ (coherence length) and are called vortices. Each of the vortices is accompanied by a persistent current circulating around the normal region and in constant interaction with surrounding vortices. The interaction results in a repulsion force locking the vortices into an Abrokosov-lattice. As the external magnetic field is further increased, more vortices are formed and start to overlap, eventually resulting in a complete transition into a normal conductor.

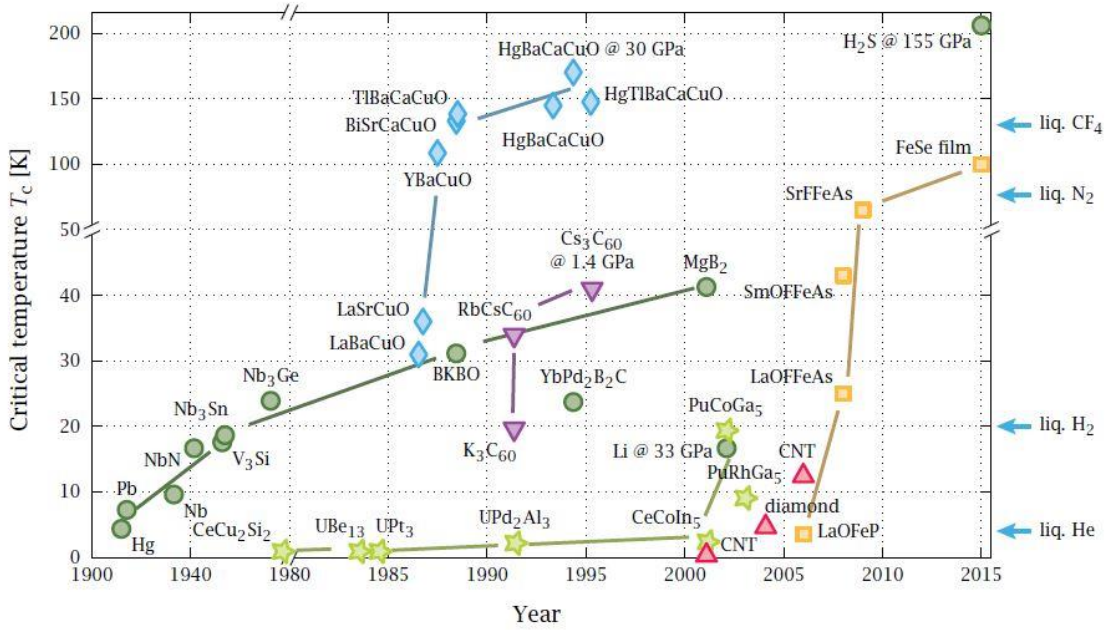

Figure 2-4 Discovery of superconducting compounds and corresponding critical temperature [50]. BCS superconductors (green circles), cuprates (blue diamonds) and iron-based superconductors (yellow squares)

Another classification among Type-II superconductors is high temperature superconductors (HTS). HTS were first discovered in 1986 with the ceramic material $La_{2-x}Ba_xCuO_4$ and are classified by a critical temperature of 30K and above [51] [52]. Since then, as outlined in Figure 2-4, many newly discovered materials and compounds have been found to be superconducting. One of the most commonly used HTS is $YBa_2Cu_3O_7$ with a critical temperature of 93K [53]. Its critical temperature is high enough to use liquid nitrogen as coolant. In addition, MgB_2 was discovered in 2001, which has the highest critical temperature of non-copper oxide superconductors with 39K [54].

2.3 Modelling of HTS

2.3.1 Critical state model

The possibility to model the behaviour of HTS relies on either microscopic or macroscopic features. Microscopic models, such as the London equations, BCS and Ginzburg-Landau theory describe the processes within a superconductor. On the other hand, macroscopic models rely on simplifications of internal processes, however, are powerful tools to predict and design superconducting devices and machines. Here, macroscopic models such as Bean model, Kim's model and *E-J* power law are introduced. Most macroscopic models are based on the critical state

model (CSM) and are derived from experiments. In a CSM, it is assumed that the outer shell of the superconductor fully enters the critical state when subject to low transport current and/or external magnetic field, while the interior is in a normal state [55].

2.3.1.1 Bean model

As initially stated, the Bean model is a CSM and introduces two assumptions [56] [57]:

1) the resistance of the material is zero for current densities below the critical current density J_c and finite for current densities of J_c
2) J_c is independent of the magnetic field strength

A commonly used example is an infinitely long slab of superconducting material with a thickness of 2*a* in *x*-direction within an external magnetic field as depicted in Figure 2-5. Its aspect ratio is very large, hence only the magnetic field B_z in *z*-direction needs to be considered. In general, two distinct regions can be distinguished, a current carrying and a current free region. A shielding current J_y is induced in *y*-direction by the external magnetic field.

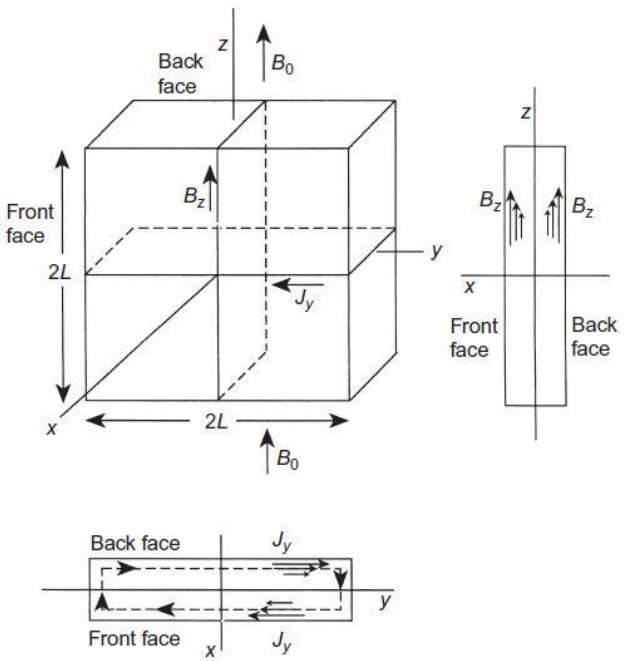

Figure 2-5 Superconducting slab of thickness 2a placed within an external magnetic field B_{app} along the z-axis inducing the shielding current density J_y [58]

Due to the resistance, a current boundary is created and the local current densities can only be $\pm J_c$ or zero. The current density and magnetic field profiles are shown in Figure 2-6.

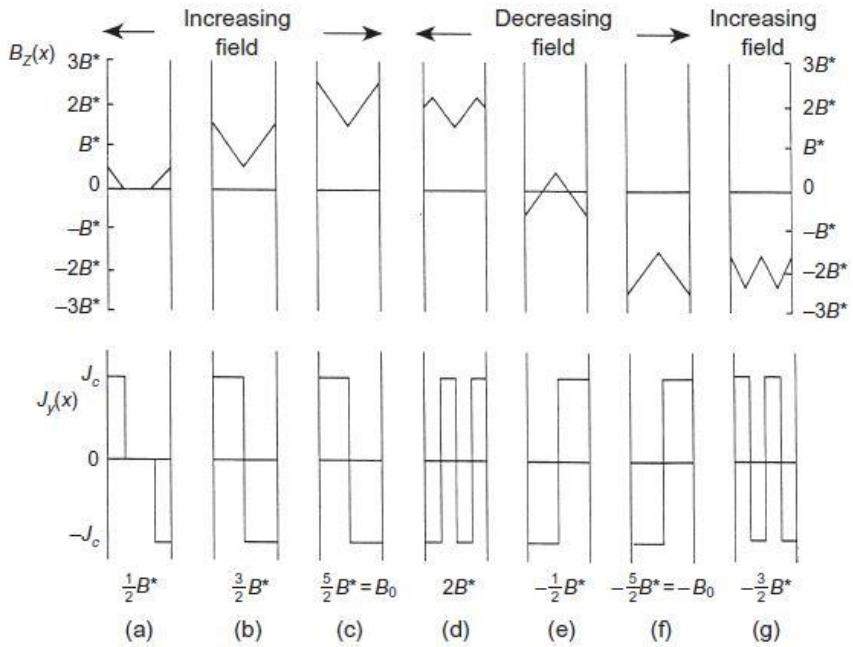

Figure 2-6 Relationship between shielding current density J_y and externally applied magnetic field B_{app} over a cycle according to Bean's model [58]

The boundary will shift farther inside the material as the local current density cannot rise above J_c and current flows into adjacent layers (depicted in Figure 2-6 (a) and (b)). As soon as the current penetrates the centre of the superconductor, the penetration field B^* is reached and the superconductor fully conducts either J_c or - J_c. Further increasing the magnetic field to $2B^*$ causes the internal field to reach the penetration field B^* in the centre of the conductor (Figure 2-6 (c)). Similarly to increasing the external magnetic field, a reduction is propagated from the outer layers inwards as illustrate in Figure 2-6 (e)-(g).

The assumption that J_c is independent of the magnetic field is inaccurate for real scenarios. Therefore, an extension to the Bean model was introduced that links the magnetic field with the critical current density and is outlined in the following chapter.

2.3.1.2 Kim model

Another commonly used CSM incorporates the temperature and magnetic field dependency of the critical current density and was postulated by Kim [59], [60] and Anderson [61] in 1962 and is shown in Eq. 2.1.

$$J_c(B) = \frac{\alpha(T)}{B_0 + B} = \frac{J_{c0}(T)}{1 + \frac{B}{B_0}} \tag{2.1}$$

Where the critical current density $J_{c0} = \frac{\alpha(T)}{B_0}$, B_0 is a material constant and α is a temperature dependent coefficient based on Eq. 2.2 with a constant b dependent on the microstructure of the material.

$$\alpha(T) = \frac{1}{d}(a - bT) \text{ ; with } \frac{a}{b} \leq T_c \tag{2.2}$$

Furthermore, for HTS tapes, it was shown that the main contributor to AC losses is the perpendicular field B_{perp} (to the wide tape surface) and the parallel component can generally be neglected [62]. Therefore, Eq. 2.1. can be rewritten as

$$J_c(B) = \frac{J_{c0}}{1+\frac{|B_{perp}|}{B_0}} \tag{2.3}$$

It is assumed that the generated losses, and therefore heat, is removed instantaneously by the cryocoolers and therefore, J_{c0} is constant for the chosen operating temperature. Eq. 2.3 can be extended further with material constants k and β obtained from experiments [63]. The fully extended field dependency of the critical current is shown in Eq. 2.4, which will also be used throughout this dissertation.

$$J_c(B) = \frac{J_{c0}}{\left(1+\frac{\sqrt{k^2 B_{para}^2 + B_{perp}^2}}{B_0}\right)^{\beta}} \tag{2.4}$$

2.3.2 *E-J* power law

With the introduction of Bean's model, superconductors, particularly low temperature superconductors (LTS) can be adequately described based on the assumption that there is a well-defined critical current density. However, such a condition is generally not applicable for HTS, as the critical current density is an ill-defined quantity [64]. With the aid of experiments, an *E-J* power law was introduced by Rhyner in 1993 to describe the highly non-linear relationship between the electric field and the current density [64].

$$E = E_0 \left(\frac{J}{J_c}\right)^n \tag{2.5}$$

Where, E_0 is the characteristic electric field with a magnitude of 10^{-4} V/m, J_c is the critical current density and n is the material dependent power factor. Two limiting cases exist where n=1

resembles Ohm's law and $n=\infty$ corresponds to Bean's CSM. Typical power factor values for the YBCO tapes used in this dissertation are approximately between 20-26 [65].

2.3.3 ***H***-formulation

There are multiple tools, models and so called 'formulations' to calculate the electromagnetic properties of superconductors. In the centre of those formulations are Maxwell's equations to relate currents, electric fields and magnetic field variables. To accommodate the use for superconductors, additional material equations need to be included. The most commonly used models include ***H***-formulation [66] [67] [68] [69], ***T*-Ω** [70] [71] [72] [73] formulation and ***A*-*φ*** formulation [74] [75] [76].

Here, the ***H***-formulation was used which combines the following equations: Ampere's law Eq. 2.6, Faraday's law combined with constitutive law Eq. 2.7, *E*-*J* power law Eq. 2.8 and Ohm's law Eq. 2.9.

$$\nabla \times \mathbf{H} = \mathbf{J} \tag{2.6}$$

$$\nabla \times \mathbf{E} = -\mu_0 \mu_\mathrm{r} \frac{\partial \mathbf{H}}{\partial t} \tag{2.7}$$

$$E = E_0 \left(\frac{J}{J_\mathrm{c}}\right)^n \tag{2.8}$$

$$\mathbf{E} = \rho \mathbf{J} \tag{2.9}$$

Where **H** is the magnetic field intensity, **J** is the current density, **E** is the electric field, μ_0 is the permeability of free space, μ_r is the relative permeability.

To apply the ***H***-formulation to a 2D geometry, the following simplifications need to be adopted. Initially, the geometry is limited to the *xy*-plane, reducing the ***H*** vector to ***H***=[H_x,H_y]. Applying Eq. 2.6, the current density ***J*** can be calculated as follows:

$$J_z = \frac{\partial \mathrm{H}_y}{\partial x} - \frac{\partial \mathrm{H}_\mathrm{x}}{\partial y} \tag{2.10}$$

As the current density is reduced to its *z*-component, the electric field only occurs in z too, according to Eq. 2.11.

$$E_\mathrm{z} = \rho J_\mathrm{z} \tag{2.11}$$

Combining Eq. 2.10 and 2.11 with Faraday's law and the *E*-*J* power law:

$$\begin{Bmatrix} \frac{\partial\left(E_0\left[\frac{\frac{\partial H_y}{\partial x}-\frac{\partial H_x}{\partial y}}{J_c}\right]^n\right)}{\partial y} \\ -\frac{\partial\left(E_0\left[\frac{\frac{\partial H_y}{\partial x}-\frac{\partial H_x}{\partial y}}{J_c}\right]^n\right)}{\partial x} \end{Bmatrix} = -\mu_0\mu_r \begin{Bmatrix} \frac{\partial H_x}{\partial t} \\ \frac{\partial H_y}{\partial t} \end{Bmatrix} \tag{2.12}$$

Eq. 2.12 can be put into FEA software such as COMSOL and be solved for a 2D geometry. In addition to Eq. 2.12 which applies to superconducting domains, Ohm's law can be applied to other conductive and non-conductive regions.

2.4 AC losses in superconductors

Superconductors are characterised by having virtually no DC resistance and in most cases have very low DC losses. However, when carrying a DC current while located within a time-varying external magnetic field, so called dynamic losses can occur, which are significantly higher than DC losses [7], [9], [77]. Additionally to losses that have a DC component, superconductors also exhibit AC losses caused by time-varying currents and/or magnetic fields. Such losses will cause thermal hotspots through Joule heating which can not only negatively affect the performance of the HTS coated conductor (CC), through quenching, but also lower the overall system efficiency as they increase the burden on the cooling system. The Carnot cycle dictates the theoretical maximum efficiency that can be achieved when heat is removed from a system (see Eq. 2.13).

$$\eta_{carnot} = \frac{T_C}{T_H - T_C} \tag{2.13}$$

Where T_c represents the cold temperature and T_H the hot temperature. In order to achieve superconductivity, the conductor must be operated at a temperature (T_c) below the critical temperature, which is far below the ambient temperature (T_H). In addition, depending on the size of the cryostat used in the HTS application, its efficiency is only a fraction of the Carnot efficiency between 10-30%, with smaller cryostats achieving a lower efficiency than larger ones [78]. A specific power k_c is introduced to quantify the impact of the losses on the cooling system. It is the reciprocal of the combined Carnot and cryostat efficiency. Figure 2-7 shows k_c for different operating temperatures below 130K, a reference temperature of 300K and a variety of cryostat efficiencies. As shown, the operating temperature is crucial, which is one of the advantages of HTS over LTS.

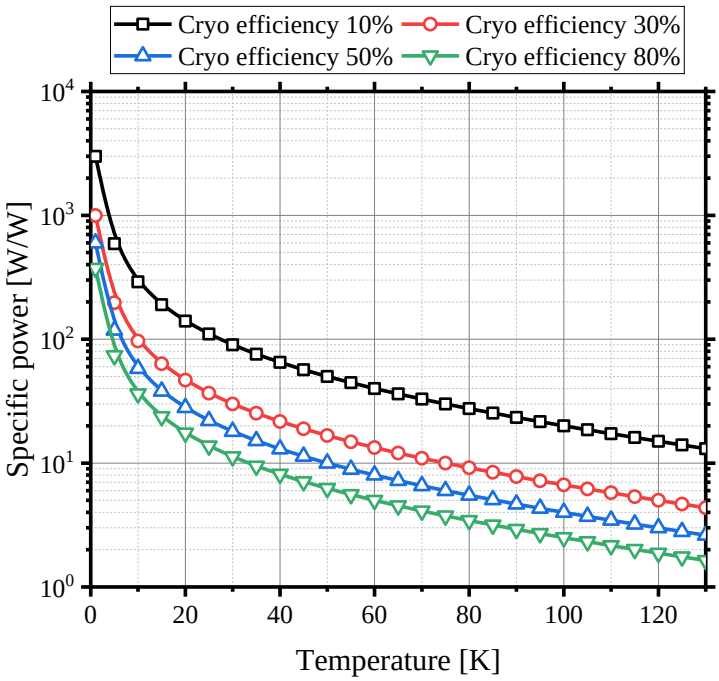

Figure 2-7 Specific power required to remove 1 W of heating at different operating temperatures for various cryostat efficiencies

In order to be viable for power applications, the losses in superconductors must be low enough to justify additional costs for the conductor itself (180-500 $/kAm in 2014 [79]) as well as the required cooling system. Furthermore, the benefit of a higher power density should not be compromised by extra components. Generally, with proper design, superconductors are already used in DC and low frequency applications such as wind turbines [80], [81], [82], fault current limiters [83], [84], [85] and power cables [86], [87],but also in applications with higher operating frequencies such as aircraft propulsion motors [88], [9], [89]. However, as the frequency increases losses scale too and the use of superconductors must be reconsidered.

Furthermore, superconducting tapes and wires are multilayer systems comprised of several different materials and layers. A conventional YBCO tape consists of many metallic layers such as silver and copper stabilisers, magnetic or non-magnetic substrates and buffer layers. Each layer affects the losses in other layers as magnetic and electric fields are shifted between layers through different loss mechanisms. Such mechanisms can be categorised into the following types and will be discussed in the subsequent chapters [55]:

1. Hysteresis loss
2. Coupling loss
3. Eddy current loss
4. Ferromagnetic loss

2.4.1 Hysteresis loss

Hysteresis losses are based on the changes in either a time-varying external magnetic field or transport current [90]. An external magnetic field larger than H_{c1}, can partly penetrate the outer layers of the Type-II superconductors as vortices. Those vortices are pinned into place by a pinning force. However, motion is induced by the Lorentz force. The interplay between Lorentz force and pinning force causes irreversible losses within the superconductor. In addition, as the external field cycles through, some vortices remain and cause losses. A similar mechanism causes losses when there is only an AC transport current. The external magnetic field is replaced by a so-called self-field, which is generated by the time varying transport current according to Ampere's law (Eq. 2.6). Analytical equations for the hysteresis loss in superconductors are available and the most well-known are the Norris equation and Brandt equation introduced in chapter 2.4.4.

2.4.2 Eddy current and coupling loss

In general, eddy current losses can occur in all power applications that operate under AC conditions. Eddy currents are induced through time-varying magnetic fields in normal conductors and cause power dissipation. At low frequencies such as 50/60 Hz, eddy current losses are negligible [91]. However, as the frequency increases higher losses in the normal conducting material are generated [8].

Coupling losses are a special type of eddy current loss that occur in multifilamentary superconductors such as BSCCO and MgB_2, more specifically in the normal conducting matrix which embeds the superconducting filaments. As an external magnetic field traverses the tape, eddy currents are induced in the normal conducting matrix, linking superconducting filaments. Coupled filaments behave as one superconducting system and share currents. Eddy currents flow within the normal conducting matrix and within the superconducting filaments. Around this loop, the superconducting sections conduct the current without any resistance. The lack of resistance along parts of the current loop, causes a much higher magnitude of the eddy current than they would achieve within a normal conductor.

The eddy-current and therefore the coupling losses increase with frequency according to Faraday's law and the length of the superconducting filaments, as the enclosed area increases. However, there are also ways to reduce such losses. One commonly employed option is to introduce a twist to the filaments [92].

2.4.3 Ferromagnetic loss

The final loss mechanism originates in magnetic materials used in HTS CCs. Such materials are commonly used as mechanical stabilisers and can include Ni and W alloys. Ferromagnetic losses are based on hysteresis within those alloys. In addition to being origin of hysteretic losses, ferromagnetic materials also alter the magnetic field distribution, which can negatively affect AC losses in other layers [93], [94].

2.4.4 Analytical approach for AC loss in superconductors

There are a multitude of analytical solutions to estimate AC losses in different superconductors of various shapes. The most well-known approaches are the Norris equations [95] and Brandt equation [96]. Norris equation focusses on the self-field loss or transport current loss. It assumes that there is no external magnetic field other than the self-field generated by the transport current flowing through the superconductor. This self-field penetrates the superconductor and causes hysteretic losses. Depending on the geometry of the superconductor, either with elliptic cross-section or strip, the transport current loss per cycle and unit of length can be calculated using Eq. 2.14-2.15.

$$Q_{\mathrm{Ellipse}} = \frac{I_c^2 \mu_0}{\pi}\left[\left(1-\frac{I_a}{I_c}\right)\ln\left(1-\frac{I_a}{I_c}\right)+\left(2-\frac{I_a}{I_c}\right)\frac{I_a}{2I_c}\right] \tag{2.14}$$

$$Q_{\mathrm{Strip}} = \frac{I_c^2 \mu_0}{\pi}\left[\left(1-\frac{I_a}{I_c}\right)\ln\left(1-\frac{I_a}{I_c}\right)+\left(1+\frac{I_a}{I_c}\right)\ln\left(1+\frac{I_a}{I_c}\right)-\left(\frac{I_a}{I_c}\right)^2\right] \tag{2.15}$$

Where I_a is the applied current and I_c is the critical current. The ratio of both can be substituted for the more commonly used load factor $i=I_a/I_c$. According to [97], [98] the measured transport current loss for Bi-2223 tapes is between the calculated loss using both Eq. 2.14 and Eq. 2.15. The Norris equation is based on the CSM and therefore assumes a discontinuous current profile and does not consider the magnetic field dependency of the critical current.

Brandt's equation (Eq.2.16) is used to calculate the hysteresis loss in [W/m] of a thin superconducting strip subject to a perpendicular external magnetic field to the wide side of the strip.

$$P_{Strip} = 4\pi\mu_0 a^2 H_a H_c f \left[\frac{2H_c}{H_a} \ln\cosh\left(\frac{H_0}{H_c}\right) - \tanh\left(\frac{H_0}{H_c}\right)\right] \quad (2.16)$$

Where a is half the strip width and it is assumed that the thickness of the tape d is much smaller than the tape width $2a$. Furthermore, H_a is the external magnetic field and H_c is the critical field.

2.5 Conclusion

As shown superconductivity was discovered recently and has since come a long way. Multiple theories and models have been established to describe the phenomenon on both micro- and macroscopic level. Superconductors are characterised by three parameters, namely temperature, magnetic field and current density, and are categorised into multiple types with different behaviours. Depending on the structure of the superconductor, various loss mechanisms must be considered. For some special cases, analytical equations can be used to quantify losses present in superconductors. However, these are limited to DC conditions or very low operating frequencies of hundreds of Hz. Other applications of superconductors require FEA-modelling to correctly evaluate losses and properly design necessary cooling systems. These models can be based on a wide range of formulations such as ***T***-formulation, ***H***-formulation or other variations.

3 Fundamentals of wireless power transfer for EV charging

3.1 Introduction

The methodology to review wireless charging for EVs is three-fold: technology, health and safety, and economic impact. All of these aspects will be covered and discussed in this chapter in great detail. Specifically, the status of main areas of a wireless charging system for EVs and aspects of implementing this technology into our daily life's are reviewed. This chapter presents recent technical progress in many key areas of WPT, introduces important research centres, evaluates risks associate with WPT and standards put into place, and explores grid impact and cost competitiveness of dynamic wireless charging. The remainder of the chapter is structured as follows: Chapter 3.2 reviews key components of a WPT-system such as power converter, compensation topology and coils as well as important auxiliary features like foreign object detection and communication. In addition, high temperature superconductors (HTS), as emerging coil material, and changes to the system to accommodate HTS are presented. Chapter 3.3 presents control strategies followed by the communication in WPT-systems in chapter 3.4 and foreign object detection, which is discussed in chapter 3.5. Chapter 3.6 addresses arising concerns regarding safe operation and the impact on the health of operators and bystanders. Evolving standards for WPT-systems are summarised in chapter 3.7. Chapter 3.8 investigates the impact of shifting from oil consumption in transportation to electric vehicles and operating wireless charging systems on the distribution network. Finally, chapter 3.9 reviews preliminary cost analysis, to show the cost incurred by introducing WPT-systems to various stretches of road as well as the potential savings due to battery size reduction. This chapter has been published in [1].

3.2 Current technology of WPT

By adopting a stationary wireless charging system, the recharging process can be simplified and becomes safer. In addition, dynamic charging systems create the unique opportunity to overcome 'range anxiety' while decreasing the upfront costs of an EV. The main components of a WPT-system for EV charging are depicted in Figure 3-1. It consists of two main sub-systems, one is located underneath the road surface (ground assembly, GA) and one is built into the vehicle underbody (vehicle assembly, VA) [99]. The GA comprises of the grid connection, rectifier and high frequency inverter, primary compensation network and the primary/ transmitter coil (Tx). In the VA, the secondary/ receiving coil (Rx) and secondary compensation network are forming the resonance circuit and feed into a high frequency rectifier, a filter network and the battery system.

Both sub-systems are separated by an air gap. The distance between the two systems depends on the type of vehicle and its ground clearance as well as road conditions such as pavement thickness. Conventionally the air gap is smaller than 0.4 m. Additionally, both sub-systems share information via a communication link. A more in-depth discussion of key features of the components is presented below.

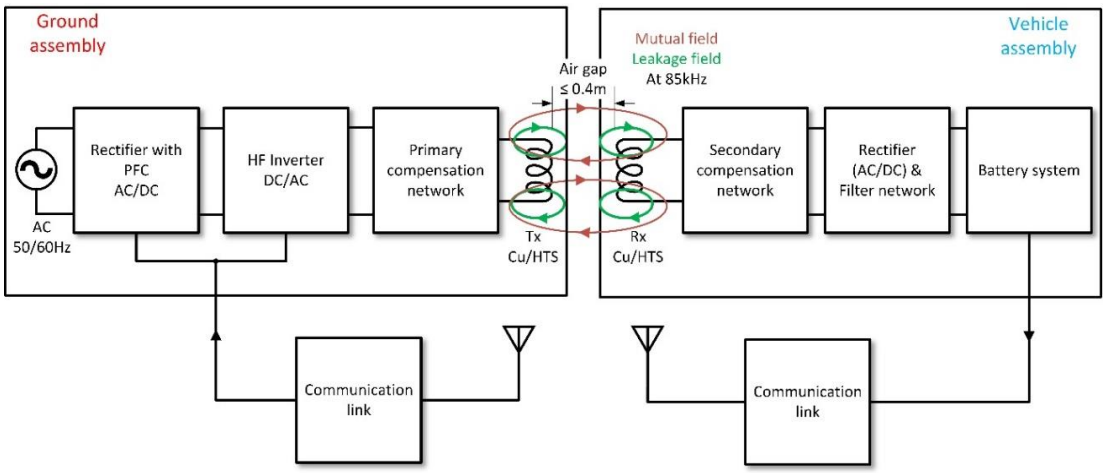

Figure 3-1 Main components of WPT-systems for EVs

3.2.1 Power source and converter

On the transmitting side, the GA is connected to the distribution network of the electricity grid and is fed by low-frequency AC power. The supply frequency is too low to produce a high-frequency magnetic field that links both coils and transfers power. Therefore, the power is converted in either a single step or a two-step process. Even though a direct conversion from low-frequency AC grid power to a high-frequency input into the primary coil is possible, most charging systems employ a two-stage AC/DC/AC conversion [100]. In the first stage, a rectifier converts the AC power to DC, followed by a power factor correction stage (PFC) to ensure a high-power factor and low harmonic content. It is also possible to use a BUCK converter after the PFC stage to modify the DC voltage and ensure 'soft' starting and stopping of the charger [101], [102]. The high-frequency inverter converts the DC power to high frequency AC and powers the primary pad. On the secondary side, the high-frequency output of the receiving pad is rectified to DC power and filtered to produce a ripple free current, which can charge the on-board battery. A diode-bridge rectifier is commonly used [17]. To maximise the power transfer, the load impedance must be matched to the source impedance. The resonance frequency of the compensation topologies and coils determines the required switching frequency of the inverters. Commonly used resonance

frequencies for WPT EV-chargers are in the range of 20 kHz to 100 kHz [103]. At higher frequencies, effects like increased electromagnetic radiation and higher resistances due to skin and proximity effect are present. Converter losses scale with increasing switching frequency [104]. This is particularly true for switching losses. Zero-voltage/zero-current switching (ZVS/ZCS) reduces switching losses. Therefore, the switching between *on* and *off* states should occur at either zero voltage or zero current. An additional benefit is the reduced voltage stress in the components.

As shown, high-frequency power converters are essential for WPT charging systems and can be categorised into single [105], [106] and three-phase topologies [107]. Power converters commonly comprise multiple devices, such as metal-oxide-semiconductor field effect transistors (MOSFETs) or insulated gate bipolar transistors (IGBTs) connected in parallel to form full or half-bridge configurations. A lot of research is going into high-frequency converters and key features of a suitable power converter include circuit simplicity, and uncomplicated control strategies, high efficiency at high switching frequencies and high-power levels, as well as robustness against high voltage and current stress [108]. For unidirectional power transfer from grid to vehicle (G2V) H-bridge converters are commonly used [109]. In [110], a high-power DC/AC converter is proposed in a 22 kW wireless charging system for EVs. The converter comprises four switches each with an IGBT and SiC-MOSFET in parallel, known as hybrid switch [111]. The system can use soft and hard switching modes and achieves 98% efficiency at 5 kW. Experimental results in a DWPT-system with loss analysis are not available. Other converter layouts include multi-level converter [112], [113], [114], cascaded multi-level converter [115] [116], [117], and matrix converter [118], [119]. Multi-level converters are particularly interesting for medium to high voltage applications and reduce the required voltage rating and component stress of single switches by using a modular approach, increasing its scalability [112]. However, such architectures require complex control schemes and deal with high circulating currents between capacitors. The complexity reduces if the circulating currents are minimised [120]. A cascaded multilevel converter uses multiple, in series connected, converters (modules) to increase the power capacity. Therefore, it provides a high degree of scalability and a simpler control scheme [117]. One drawback of such a system is the need of multiple power sources and therefore higher system costs, as each converter requires its own power supply. Furthermore, depending on the number of modules, the conduction loss can be larger than that of a conventional H-bridge converter if the same number of switching devices is used [116]. Matrix converter might be employed to reduce the total number of conversion stages,

as it is possible to convert the AC grid supply directly into high-frequency AC power, but the power capacity is limited and soft switching is difficult to achieve [121].

A unique approach of DWPT for EV is to use a super-capacitor in tandem with the secondary power rectifier, to enable power transfer and energy storage in a single device [122]. Super-capacitors can provide an additional energy buffer before the on-board battery pack in a conventional EV due to their high-power density [123]. Nevertheless, using this topology increases the current stress in the secondary converter and introduces harmonics into the voltage waveform. To allow bidirectional power transfer, G2V and vehicle to grid (V2G), bidirectional converters on transmitting and receiving side are required [124]. With the aid of bidirectional power transfer EVs can act as energy storage for times with high renewable energy penetration. While renewable energy sources feed into the grid, the energy can be used to charge EV batteries, which reduces the load on the grid [125]. In addition, to prevent intermittency issues within the grid network, EV batteries are discharged to balance the demand [126].

3.2.2 Compensation topologies

Magnetically coupled coils act like a transformer, but with higher leakage inductance due to a larger air gap between the coils. Hence, the fraction of magnetic coupling linking both coils is much smaller compared to traditional transformers, making them loosely coupled. To be able to transfer sufficient power over long distances, the system operates at resonance frequency with zero phase angle between input current and voltage. In order to achieve a resonant circuit, multiple reactive elements, like inductors and capacitors are linked together in series and/or parallel. As shown in Figure 3-1, these compensation networks are located between the high-frequency inverter and the primary coil, in the GA and between the secondary coil and the rectifier in the VA. Capacitors resonate with the transmitting and receiving coils to supply reactive power [127]. The main purpose of the primary compensation network is to reduce the reactive power rating (VAr) of the power supply by cancelling out the reactive component of the primary coil [128]. In addition, the compensation network helps to achieve soft switching in the primary power converter. Compensation networks are also used on the secondary side to improve the power transfer capability of the system by nullifying the receiver inductance [129]. Figure 3-2 depicts the most basic compensation topologies currently used in WPT-systems, each consisting of a single capacitor in either series (S) or parallel (P) to the coil inductance i.e. SS stands for a series capacitor on the primary side and a series capacitor on the secondary side.

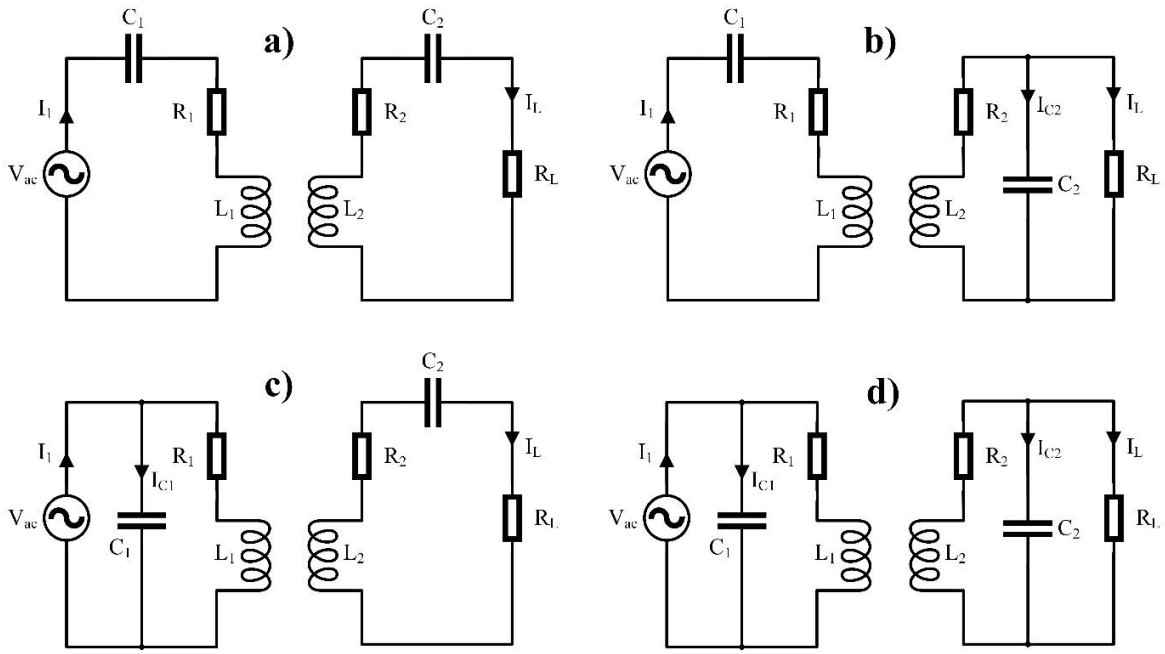

Figure 3-2 Basic compensation topologies for primary and secondary resonant circuits a) SS b) SP c) PS d) PP

The primary I_1 and load current I_L, as well as power transfer efficiency η are derived for an SS-compensation topology. Using Kirchhoff's Law, by defining the loop-currents for the circuit shown in Figure 3-2a) the circuit can be solved using Eq. 3.1.

$$\begin{bmatrix} V_{\mathrm{ac}} \\ 0 \end{bmatrix} = \begin{bmatrix} R_1 + j(L_1 * \omega - \frac{1}{C_1 * \omega}) & -j\omega M \\ -j\omega M & R_2 + R_L + j(L_2 * \omega - \frac{1}{C_2 * \omega}) \end{bmatrix} * \begin{bmatrix} I_1 \\ I_L \end{bmatrix} \tag{3.1}$$

Equivalent total impedance Z_{tot} of the circuit with SS-compensation is the sum of primary circuit impedance Z_1 and secondary reflected impedance Z_{r} shown in Eq. 3.2. The secondary reflected impedance is the ratio of reflected voltage and primary current.

$$Z_{\mathrm{tot}} = Z_1 + Z_r = \left(R_1 + j\left(L_1 * \omega - \frac{1}{C_1 * \omega}\right)\right) + \frac{(\omega * M)^2}{\left(R_2 + R_{\mathrm{L}} + j\left(L_2 * \omega - \frac{1}{C_2 * \omega}\right)\right)} \tag{3.2}$$

The current drawn from the power supply can be evaluated with Eq. 3.3.

$$I_1 = \frac{V_{\mathrm{ac}}}{Z_{\mathrm{tot}}} = \frac{V_{\mathrm{ac}} * \left(R_2 + R_{\mathrm{L}} + j\left(L_2 * \omega - \frac{1}{C_2 * \omega}\right)\right)}{\left(R_1 + j\left(L_1 * \omega - \frac{1}{C_1 * \omega}\right)\right) * \left(R_2 + R_{\mathrm{L}} + j\left(L_2 * \omega - \frac{1}{C_2 * \omega}\right)\right) + (\omega * M)^2} \tag{3.3}$$

According to Eq. 3.1 and Eq. 3.3, the current that supplies the load is:

$$I_{\mathrm{L}} = \frac{-V_{\mathrm{ac}} * j\omega M}{\left(R_1 + j\left(L_1 * \omega - \frac{1}{C_1 * \omega}\right)\right) * \left(R_2 + R_{\mathrm{L}} + j\left(L_2 * \omega - \frac{1}{C_2 * \omega}\right)\right) + (\omega * M)^2}. \tag{3.4}$$

Input power P_{in}, output power P_{out} and efficiency η of the power transfer are calculated using Eq. 3.5-Eq. 3.7. It is assumed that the power is supplied with unity power factor into the primary compensation network.

$$P_{\mathrm{in}} = V_{\mathrm{ac}} * I_1 = \frac{{V_{\mathrm{ac}}}^2 * \left(R_2 + R_{\mathrm{L}} + j\left(L_2 * \omega - \frac{1}{C_2 * \omega}\right)\right)}{\left(R_1 + j\left(L_1 * \omega - \frac{1}{C_1 * \omega}\right)\right) * \left(R_2 + R_{\mathrm{L}} + j\left(L_2 * \omega - \frac{1}{C_2 * \omega}\right)\right) + (\omega * M)^2} \tag{3.5}$$

$$P_{\mathrm{out}} = R_{\mathrm{L}} * |I_{\mathrm{L}}|^2 = R_{\mathrm{L}} * \left| \frac{-V_{\mathrm{ac}} * j\omega M}{\left(R_1 + j\left(L_1 * \omega - \frac{1}{C_1 * \omega}\right)\right) * \left(R_2 + R_{\mathrm{L}} + j\left(L_2 * \omega - \frac{1}{C_2 * \omega}\right)\right) + (\omega * M)^2} \right|^2 \tag{3.6}$$

$$\eta = \frac{P_{\mathrm{out}}}{P_{\mathrm{in}}} = \frac{R_{\mathrm{L}}}{\left(R_2 + R_{\mathrm{L}} + j\left(L_2 * \omega - \frac{1}{C_2 * \omega}\right)\right) + \left(R_1 + j\left(L_1 * \omega - \frac{1}{C_1 * \omega}\right)\right) * \left(\frac{R_2 + R_{\mathrm{L}} + j\left(L_2 * \omega - \frac{1}{C_2 * \omega}\right)}{\omega M}\right)^2} \tag{3.7}$$

At zero-phase-angle frequency, the reactive power flow is zero. To form a resonance circuit with maximum power transfer capability, this frequency must be equal to the resonance frequency ω_0, where the reactive parts in Eq. 3.5-Eq. 3.7 cancel out. Assuming identical coils in the primary and secondary circuit, the resonance frequency can be calculated using Eq. 3.8.

$$\omega_0 = \sqrt{\frac{1}{L_1 C_1}} = \sqrt{\frac{1}{L_2 C_2}} = \sqrt{\frac{1}{LC}} \tag{3.8}$$

The efficiency at resonance frequency is expressed by Eq. 3.9 with the quality factors Q for each coil in Eq. 3.10.

$$\eta(\omega_0) = \frac{R_{\mathrm{L}}}{(R_2 + R_{\mathrm{L}}) + R_1 * \left(\frac{R_2 + R_{\mathrm{L}}}{\omega M}\right)^2} = \frac{R_{\mathrm{L}} k^2 Q_1 Q_2}{R_2 \left[\left(\frac{R_2 + R_{\mathrm{L}}}{R_2}\right)^2 + \left(\frac{R_2 + R_L}{R_2}\right) * k^2 Q_1 Q_2\right]} \tag{3.9}$$

$$Q_{1/2} = \frac{\omega_0 * L_{1/2}}{R_{1/2}} \tag{3.10}$$

The same approach can be used for SP, PS, and PP-compensation networks. Table A-1 in the appendix summarises the total impedance, power transfer efficiency under resonance and the primary capacitance of the basic compensation topologies.

Figure 3-3 shows the power transfer efficiency and output power characteristics under varying mutual inductance for all four compensation topologies. Under perfectly aligned conditions, the mutual inductance is high and depends on the length of the air gap. Mutual inductance reduces with increasing air gap length and misalignment. The SS-compensated system reaches a high and stable transfer efficiency at low mutual inductances. Furthermore, it transmits the highest output power for a fixed input power. A PS-compensated system has the same power transfer efficiency as the SS-compensated system, however, transfers less power to the load. While the SP-topology transfers slightly less power to the load, the input power required is much higher, resulting in an overall lower efficiency. The lowest power is transferred by a PP-compensated system.

Using an SS-compensation network is beneficial for application with variable load conditions i.e. DWPT charging, as the primary compensation capacitance C_1 is independent of the load. The opposite is true for the remaining topologies, where C_1 changes with varying load and coupling, potentially compromising the resonance frequency and transfer efficiency [130]. As shown in Eq. 3.2, the total impedance of the SS-compensated system drops with decreasing mutual inductance. This leads to an increase in primary current and therefore to a higher secondary current that supplies the load [131]. While using an EV, it is not always guaranteed to be in perfect alignment with the primary pad or track particularly during DWPT, which causes a reduction in mutual coupling. If the misalignment is too pronounced, the switching components experience high current peaks and can be damaged. Using a parallel primary can prevent this behaviour, as the primary current reduces under misalignment.

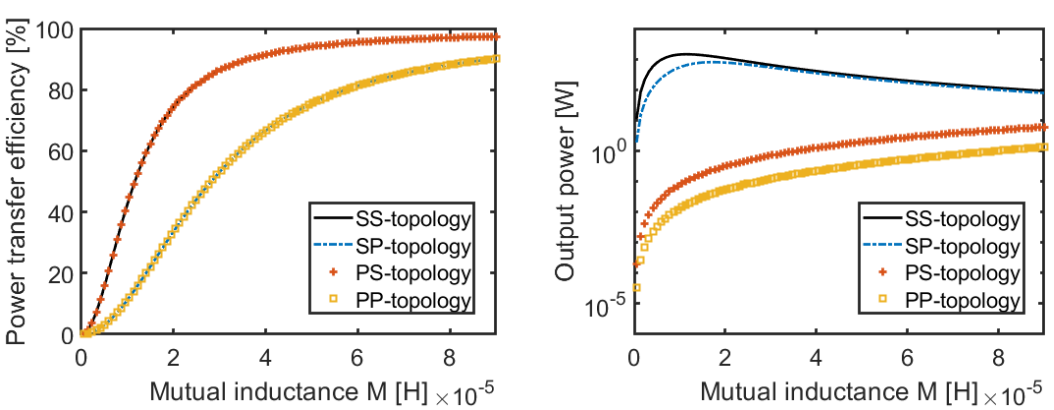

Figure 3-3 Power transfer efficiency and output power vs varying mutual inductance M for the basic compensation topologies SS, SP, PS, and PP

An optimal selection process of the compensation topology based on the economics of the system is suggested in [132]. It concludes that SS and SP-compensation networks are the most suitable topologies for high-power WPT-systems. Additionally, SS-compensation requires less copper than the other basic compensation networks. However, this study does not consider soft switching or bifurcation. Bifurcation or frequency splitting results in multiple frequencies in which a zero-phase angle is possible. It can be avoided by adopting the criteria given in [128]. A specific design guideline for SS-compensated systems is presented in [133].

Each of the basic compensation topologies has disadvantages. Therefore, it is required to investigate other arrangements that alleviate these problems. Proposed extensions to the conventional SS-compensation are the so-called S/SP and SP/S topologies. Systems with S/SP-topology use an additional parallel capacitance on the secondary side compared to the SS-network [134]. It provides a higher tolerance to varying air gap lengths. Using an SP-compensation on the primary side instead and an S-network on the secondary side improves the misalignment tolerance of the system, as the additional parallel capacitor allows for a transition between maximum power and maximum allowable misalignment [131]. However, there is a trade-off between power source rating and achievable misalignment tolerance. To increase the tolerance from 40% to 75%, the power source has to supply five times the rated output. Furthermore, load fluctuations caused by a varying state of charge (SoC) of the battery load have an impact on the resonant state of the system due to the parallel capacitor. This results in non-zero phase angle operation when the load changes [135].

Samanta & Rathore proposed a WPT-system with a CCL-compensated transmitter side and an LC-compensated receiver side [136]. The design uses an additional capacitor connected in series to the conventional parallel-compensated primary and a series compensated secondary side. By using an additional series capacitor, the voltage stress on the inverter switches is reduced, which was a major drawback of conventional current-fed systems. One issue with this topology is the reduced efficiency in comparison to other compensation networks.

An LCL-compensated receiving coil was developed in [137] and [138]. It uses a parallel capacitor and an additional inductor in series to the receiving coil. By adopting this compensation, the switching loss of the rectifier is reduced. One advantage of LCL-compensated coils is that it produces a constant current output, which is required for supplying multiple receiving coils. If LCL-compensation is used on both sides of the WPT-system, it enables bidirectional power

transfer [139]. However, it requires a complex control scheme with an external coil for synchronous switching [140].

One of the most investigated compensation topologies in more recent years is the LCC-compensation shown in Figure 3-4 [135], [141], [142]. It combines a conventional series-parallel compensation on one side with a series inductor. This additional inductor can be integrated with the receiving or transmitting coil, hence no additional space is required [143], [144]. By using a bipolar compensation coil, the coupling between main coil and series inductor can be minimised [145], [146]. The resonance frequency is independent of load and coupling conditions, while the current through the primary coil and the output current are constant [147]. Generally, the power transfer efficiency is lower as more components are connected, but the stress on the capacitors and coils is lower [148]. Zhu *et al*. compared the LCC-compensation with a conventional SS-topology [149]. A critical load resistance $R_{\mathrm{L,crit}}$ is determined to compare the transfer efficiency – mutual inductance characteristics and is shown in Eq. 3.11.

$$R_{\mathrm{L,crit}} = \sqrt{\frac{L_{\mathrm{sc}}}{C_{\mathrm{sc,2}}}} \tag{3.11}$$

Secondary compensation inductor and secondary parallel compensation capacitor are denoted L_{sc} and $C_{\mathrm{sc,2}}$ respectively. If $R_{\mathrm{L,crit}}$ is bigger than $\sqrt{\frac{L_{\mathrm{sc}}}{C_{\mathrm{sc,2}}}}$ then the efficiency of the LCC-compensation is more robust to variations in mutual inductance, but has a lower efficiency under perfect alignment. The opposite is true when $R_{\mathrm{L,crit}}$ is smaller. Under these conditions, the SS-compensation is less susceptible to changes in mutual inductance but offers lower efficiency under no misalignment. SS and LCC-compensation offer the same performance for the condition shown in Eq. 3.11. Due to the parallel capacitance, the total impedance of the LCC-system increases similarly to the parallel primary compensation. Thus, it guarantees safe operation under high misalignment. Furthermore, LCC-compensation offers lower magnetic field radiation [141]. LCL and LCC topologies can also be combined, where LCL is used on the primary side and LCC on the secondary [150].

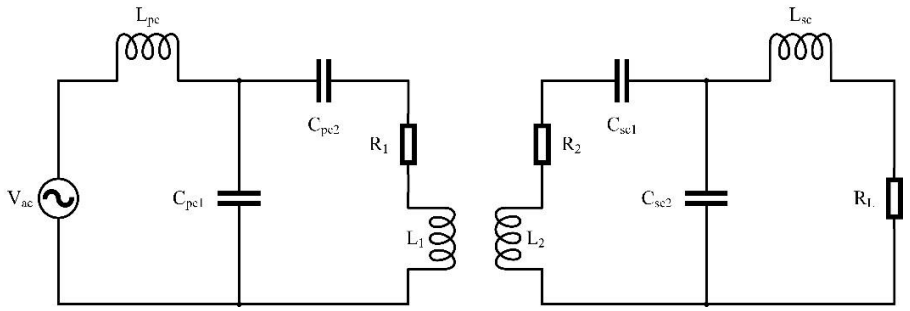

Figure 3-4 LCC-compensation network on primary and secondary side of a WPT-system, not showing primary side inverter and secondary side rectifier and filter

3.2.3 Coil designs

The main component of the WPT-system is the pair of coupled coils that allows power transfer via a magnetic field. A current flows through the primary coil and generates a time-varying magnetic field around it. In the vicinity of the primary coil, the secondary coil intercepts the magnetic field, which induces a voltage. The amount of induced voltage depends on the air gap length between the coils, the number of turns and the rate of change of the magnetic field. Due to this voltage, a current is flowing in the secondary coil that can supply a load. The set of coils forms a loosely coupled transformer linked by the main flux path and produces a leakage field that does not contribute towards the power transfer. By connecting each coil to the compensation network, the current flowing in the coils is maximised due to resonance. Main parameters that should be maximised during the design process of the primary and secondary pads are coil quality factor Q and the coupling coefficient k with a high tolerance for increasing air gap lengths and lateral/longitudinal displacements.

In order to increase the coupling between the coils, ferromagnetic materials, so called cores, can be used to guide the magnetic flux. Prevalent losses within the coil-system arise from the core losses of the ferrite material and ohmic losses of the coils, including proximity and skin effect losses. Skin effect losses are reduced by using Litz wire, whereas core losses depend on the core material. To reduce core losses, the flux density should be below the saturation flux density of the material. However, the available design choices are limited by power and space requirements. After reducing potential losses, the efficiency of the power transfer can be improved by three design parameters, which ultimately affect the product kQ [151], [152]. As shown in Eq. 3.9, these parameters include the mutual inductance M or coupling coefficient k, the self-inductance of the coils L and the frequency ω. An increase in frequency increases the induced voltage in the

secondary coil, but at the same time increases frequency dependent losses like switching losses in the inverter, resistances in the coil, and core losses. Additionally, high frequency inverters are more expensive than 'slower' power electronics [151]. It is therefore important to choose the design frequency carefully. The self-inductance of coils increases with increasing coil dimensions or number of turns. In practice, the maximum size of the coil is limited by the size of the underbody of the vehicle. Increasing the number of turns is possible but constrained by the available volume. In addition, the area enclosed by the windings is important, as it affects the coupling coefficient. A larger area enclosed by the winding results in higher coupling [153]. Another way to increase the coupling is to decrease the air gap length or increase the coil dimension. Again, the air gap length is pre-determined by the application i.e. EV-charging and the size of the coils is limited. The coupling can be maximised by using equally sized coils as shown in Figure 3-5. Having equally sized coils also reduces eddy currents induced in the vehicle chassis and leakage magnetic field surrounding the coils [152]. Reducing the size of the receiving coil is convenient, as it would be easier to incorporate in the vehicle. However, the receiving coil will intercept less magnetic flux, lowering the magnetic coupling and efficiency.

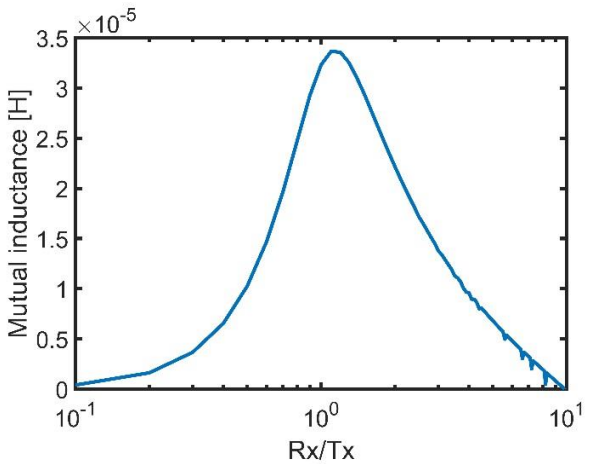

Figure 3-5 Mutual inductance vs ratio of receiving Rx and transmitting Tx coil radius at an air gap length of 0.1 m

Keeping these dependencies in mind, the coils can be designed. In the beginning, circular coil designs were common due to their simplicity. This design originated from pot cores, where the magnetic field is guided within a small volume as the core material encloses the coil [154], [155], [156]. As the secondary circuit must be installed on the underbody of the vehicle, a reduction in size and weight is advantageous. In addition, using less ferrite reduces the price of each pad. Therefore, pot structures were converted to plates, disks or rods that are evenly spaced out above

the coil [157]. A pad structure designed by Budhia *et al.*, shown in Figure 3-6, minimizes the amount of ferrite used, while maintaining a critical coupling between primary and secondary circuit [158].

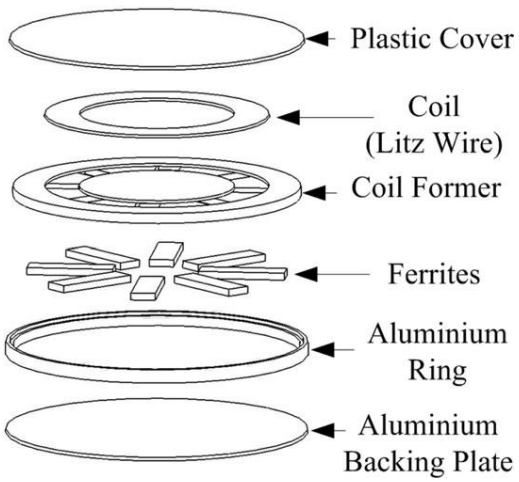

Figure 3-6 Circular primary/secondary pad design using minimal amount of ferrite to achieve critical coupling [158]

The magnetic field produced by circular coils has its maximum in the centre of the coil. It drops off significantly with any offset, resulting in a low non-directional misalignment tolerance. At a lateral offset of circa 40% of the diameter, circular pads have a null in their power distribution, as equal amounts of magnetic flux enter the coil from either side. Consequently, this makes a circular coil unsuitable for DWPT. Another disadvantage of circular coils is the achievable flux height. The coupling height depends on the diameter of the coil and is with one quarter of the diameter limited. Nevertheless, circular coils exhibit the highest magnetic coupling amongst similar sized coil geometries like square and rectangular designs [153]. Therefore, circular coils are still popular for stationary WPT-systems where the coil performance is maximised using multi-objective optimisation algorithms. These algorithms range from parametric sweeps [159] to genetic [160] and evolutionary algorithms [161]. In contrast, rectangular pads are the most common design for DWPT due to their high tolerance against longitudinal misalignment and efficient use of space on the vehicle [162], [163]. According to [164], rectangular pads are the most cost-effective option in comparison to circular and hexagonal design. Rectangular pads transfer the highest power over a specific area with a given material use.

To increase the flux path height and misalignment tolerance of the transmitting pad, a new design approach was chosen as shown in Figure 3-7. By winding the coil around a ferrite bar, a so-called

flux pipe, flat solenoid or H-core pad is created [165], [166], [167]. Due to the increased flux path height, the coupling between transmitter and receiver side is higher. In comparison to the circular design, the flux pipe has a better lateral misalignment tolerance. The windings must be carefully designed, to reduce the overall amount of material used. Budhia *et al*. split the windings and used two separate coils connected in series per pad [165]. Whereas [166], used split cores to reduce the weight and cost of the pads. One major problem of these designs is the double-sided nature of the magnetic flux. Because the windings are on both sides, a leakage flux is produced on the backside of the pad, which lowers the coupling and reduces the transfer efficiency. It is possible to use an aluminium shield on the backside to reduce interactions between flux and surroundings. However, there will be losses associated with the eddy currents produced in the shield and the interactions between the shield and coil.

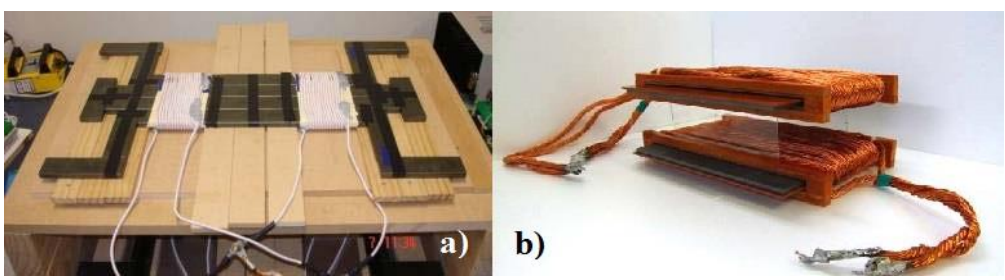

Figure 3-7 Flux pipe/ flat solenoid coil configuration a) flux pipe by [165] b) flat solenoid by [166]

As shown, the tolerance against lateral misalignment is a key factor in designing the coil structures in WPT-systems. Commonly, there is a null in the power distribution as the lateral offset increases regardless of the coil design. Elliott *et al.* designed a multiphase pickup coil (quadrature coil) that uses two windings, combining a horizontal winding and a vertical winding, wound on top of each other around a ferrite E-core [168], [169]. Using two windings, one is compensating the power null of the other and vice versa, alleviating the problem, while achieving similar power levels as conventional coil structures. However, it uses twice the amount of copper wire.

The feature of producing a single sided flux sparked new research on advanced coil structures. Popular examples are the DD and DDQ pads [170], [171], the bipolar pad [172], [173], tripolar pad [174], [175], and a novel design called ZigZag [176]. A DD-pad uses a similar approach as the flux pipe design, but instead of winding the coil around the core material, it is wound like a circular spiral coil on top of the core material. It channels the magnetic flux and re-directs it to the front. Therefore, this design does not produce flux on the backside of the coil. As shown in Figure 3-8a) the flux that links the pads, is the flux produced by the coupling between both coils in one

pad. In order to maximise the coupling, the ‘flux pipe’ length has to be maximised. One drawback of the DD design is it only couples the horizontal flux. By adding the quadrature coil designed in [168], the vertical components can be utilised and a DDQ structure is created as shown in Figure 3-8b). The DDQ pad uses more wire as it combines two windings but creates twice the flux height of a circular coil. Bosshard *et al.* compared the performance of rectangular and DD charging systems with each other [177]. A rectangular WPT-system has a marginally higher mass and surface area related power density, but the DD pads create a lower magnetic leakage field. Recently, new adaptations of the DD pads have emerged, including an overlapped DD array [178] and a crossed DD coil [179]. The crossed DD coil setup uses two rectangular coils next to each other similar to the conventional DD coil. In contrast, one coil is shifted by half a coil length in longitudinal direction. The system improves misalignment tolerance if multiple coils are placed next to each other. To guarantee minimal changes in mutual inductance, two coil pairs have to be excited at the same time. As multiple coils are energised, the magnetic field of the uncovered coils needs to be shielded. An overlapped DD array uses multiple stacks of DD coils on top of each other with an offset between the different layers [178]. It optimises the transfer efficiency and aims at very low-speed dynamic power transfer.

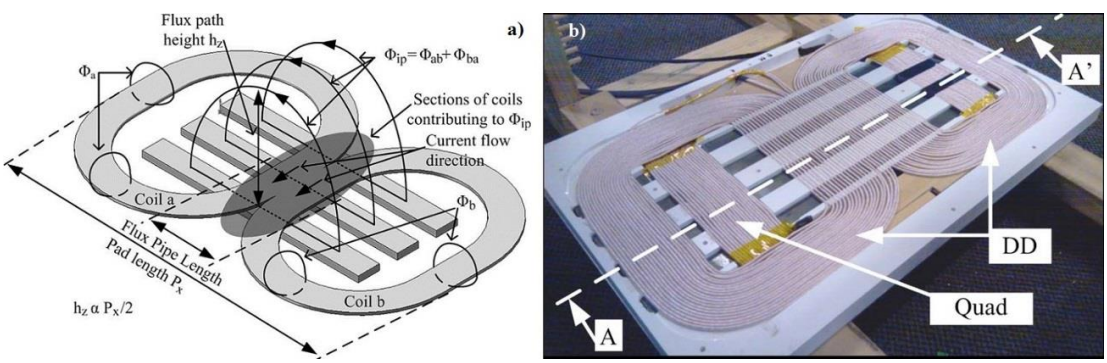

Figure 3-8 Single-sided flux coil designs a) DD- and b) DDQ-pad [171]

The bipolar pad design is similar to the DD pad, but the individual coils overlap. It has similar power transfer capabilities but uses approximately 25% less wire material [173]. Furthermore, both coils require an independent converter, which are synchronised [180].

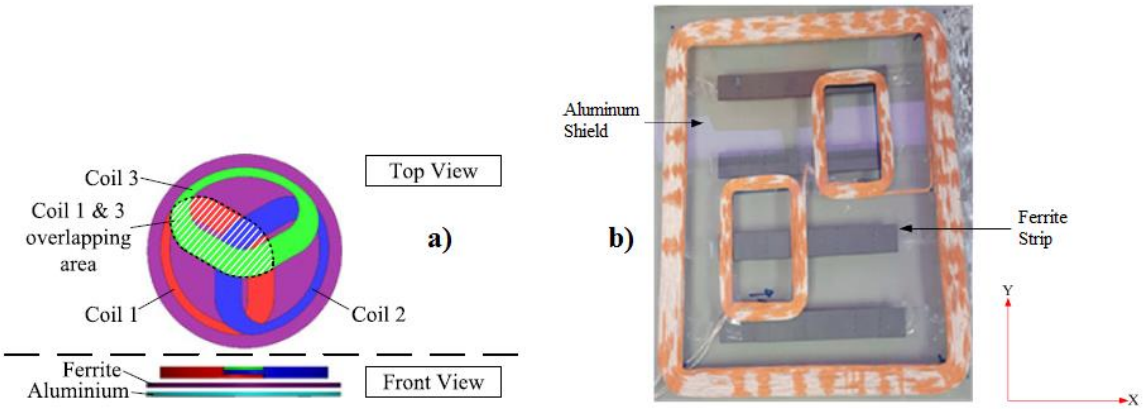

Figure 3-9 Three-coil design pads a) circular-shaped tripolar pad [175] b) ZigZag pad [176]

In contrast to the two coils used in a DD-pad, the tripolar design uses three coils similar to the DDQ pad [174]. The three oval-shaped coils are decoupled from each other and overlap at the centre of the coil as shown in Figure 3-9a). Decoupling is achieved by adjusting the overlapping area to minimise the induced field in the adjacent coil [181]. By adopting multiple coils, the pad provides a high non-directional misalignment tolerance and therefore a larger effective area to transfer rated power [182]. In addition, the leakage field is significantly reduced in comparison to a circular pad. One disadvantage is the complex control scheme required. Furthermore, each coil is driven independently by an individual inverter, leading to increased costs. Figure 3-9b) shows another design that uses three coils per pad, one large coil wound as a rectangle containing two smaller rectangular coils in the area enclosed [176]. It has a uniform magnetic flux distribution in the smaller coils. The output power provided to the load changes only slightly over a wide range of misalignments. Again, a large amount of wire material is used. Furthermore, a hexagonal coil is introduced in [183]. While the performance of the proposed coil geometry is similar to that of a circular spiral coil (about 1-1.6% higher misalignment tolerance), its main improvement is the reduction in weight by about 26%. It is also possible to use intermediate coils between the main transmitting and receiving coils to further increase the transmission distance [184]. However, intermediate coils are not addressed in this review. Finally, a bifilar Archimedean coil is proposed in [185]. The coil comprises two spiral arms which are oriented 180° relative to each other. The stray capacitance between the two arms is used to form a series resonance circuit. Table 3-1 summarises the differences in achievable misalignment tolerance and if the design is subject to a null in the power distribution, as well as flux path height for various coil designs. As shown in the review, the aim of future coil designs is the increase in misalignment tolerance as well as transfer

distance while maintaining a high transfer efficiency. Both factors are important with respect to the feasibility of such systems and their flexibility and usability in a real-world scenario. The short comings of earlier designs are alleviated through careful routing of the copper wire or even through the introduction of additional (smaller) coils within the main coil area. Nevertheless, space requirements must be kept in mind as vehicles themselves are being optimised to reduce free space within the chassis and overall weight.

Table 3-1 Comparison of different coil design approaches

Coil design	Misalignment tolerance	Flux path height	Reference
Circular	Null at 40% of diameter	¼ of coil diameter	[158]
Flux pipe/ flat solenoid	Good tolerance in one direction	½ of coil length	[165], [166]
DD	Null at 34% of length of pad (in x-direction)	½ of coil length	[171]
DDQ	Null at ca. 95% of length (in x-direction)	Twice of circular	[171], [173]
Bipolar	Null at ca. 95% of length (in x-direction)	Twice of circular	[173]
Tripolar	Non-symmetric tolerance	N/A	[182]
Hexagonal	Similar to circular	N/A	[183]
Zigzag	No null	1/(2.5) of coil length	[176]

3.2.3.1 High temperature superconductors (HTS) as coil material

So far, coils are conventionally made of copper wire due to its high conductivity, while still being cheap and easy to manufacture. To reduce the impact of proximity and skin effects at higher frequencies, copper in form of Litz wire is used. While copper has a good balance between performance and cost/availability, new materials emerge to improve the performance of WPT-systems. One of these new materials are high temperature superconductors (HTS) [40]. Even though HTS are more expensive than copper, they are already used as coil material in other systems e.g. power generators for wind turbines [186], [187] or fault current limiters [188], [84], but are not as prevalent in WPT. In addition, HTS-capacitors for WPT are proposed but are not

part of this review [189]. HTS provide virtually no resistance and high current densities, when operated in critical state. Incorporating HTS in a WPT-system can increase transfer efficiency due to the smaller resistance and therefore higher quality factor *Q*. Furthermore, higher current densities lead to smaller dimensions of the system, while maintaining high power levels. Another positive effect is the increase in possible transmission distance as the magnetic field density is higher. The critical state is dictated by the temperature, current density and magnetic field. Each of these critical values depends on the type of HTS used. Outside of this critical state, the superconductor 'quenches' and converts back to a normal conductor. Additionally, HTS lose their superconductivity if bent too far [190], [191].

One requirement for the use of HTS material is an additional cooling system that cools the coils below critical temperature. The coolant required depends on the critical temperature of the HTS. Conventionally, rare-earth barium copper oxide (REBCO) superconductors are used, which are cooled with liquid nitrogen to 77K. The additional need for cooling leads to further space demand and increased cost which ultimately can offset benefits obtained from using HTS material. Furthermore, handling cryogenic material raises safety concerns which need to be addressed. This is particularly true for HTS in receiving coils mounted underneath a vehicle. If HTS are used in transmitting coils, specially trained personnel are required for the installation of the transmitting pads/ rails, while space concerns are not a key driver.

Compared to regular copper, HTS material has interesting AC loss characteristics [192], [193], [194]. Operating at higher frequencies causes increased AC losses in HTS, which has direct influence on the power transfer efficiency. AC losses in HTS contain transport losses, hysteresis losses, and eddy-current losses [195]. It is important to quantify and minimise these losses, as heat is dissipated proportionally to the losses, which puts an additional burden onto the cooling system. Because of the lower resistance, HTS coils have a higher Q-value compared to conventional copper coils and therefore support a higher transfer efficiency. Like a typical coil system, HTS-WPT systems require resonance to achieve maximum power transfer efficiency. Therefore, bifurcation can occur as well and must be considered by the controller [195].

In general, using HTS as coil material on both sides can increase the power transfer capabilities as shown in Figure 3-10a). The transfer efficiency for conventional copper systems increases when the coils are cooled, as the resistance decreases [196]. HTS-coils on both sides require cooling systems in both pads as well, which might not be possible due to space constraints and cost. Chung

et al. and Kim *et al*. stated that a receiver coil with high *Q*-value and low impedance is advantageous over a transmitting coil with high *Q*-value [196], [197]. Conversely, as shown in Figure 3-10b), the impact of using HTS in the transmitting coil is greater than for HTS in the receiving coil.

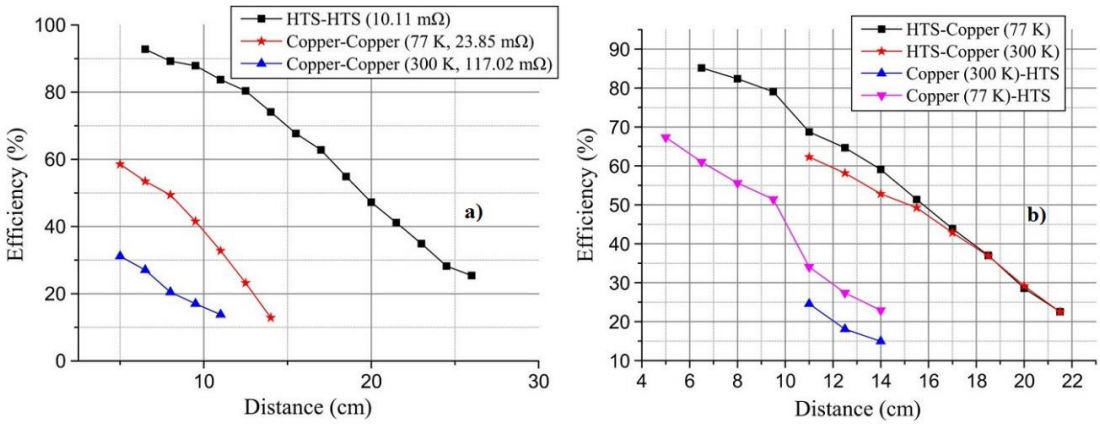

Figure 3-10 Power transfer efficiency for different coil materials at a resonance frequency of 3 kHz a) same material is used for receiving and transmitting coil b) different materials for receiving and transmitting coil [195]

Traditional WPT-charging systems use single coil sub-systems. Some DWPT-systems, particularly chargers using power supply rails, can supply multiple receiving coils with a single transmitting coil. Multi-coil systems are investigated, where one copper coil is substituted with an HTS-coil [198]. Kim *et al*. proposed a system with four coils, two made from HTS [199]. It has a power coil connected to the power supply and a transmitting coil coupled to the power coil, on the transmitting side. Both made of copper wire and operated at room temperature. The receiving system contains an HTS receiving coil and an HTS load coil that is connected to the load. Power and load coil have one turn and an air gap length of 3 cm to the transmitting and receiving coil, respectively. At an air gap length of 0.3 m a current transfer efficiency of 50% was achieved. A key aspect of the experiments was the impedance matching between the load and the transmitting coil pair. The experiments conducted in this study used a resonance frequency of 13.56 MHz, which is not viable for charging EVs. However, it shows the general principle of using multiple HTS and copper coils within one system

Chung *et al*. suggested using a resonator coil between transmitting and receiving coil [200]. Three different arrangements were tested and are shown in Figure 3-11. At a frequency of 370 kHz the system, using two HTS-coils in the transmitting sub-system had the highest transfer efficiency with 79% compared to 67% achieved by the three-coil system with cooled coils. A total of 4 litres

of liquid nitrogen per hour of testing was consumed by the cooled copper coil system whereas approximately 2 litres were consumed by the HTS system while supplying 400 W to the transmitting coil. This consumption can be reduced by adopting and optimising different cooling systems, instead of using a batch approach without covering the cooling vessel. One issue of using an additional resonator coil is the varying air gap length between resonator and receiving coil. As the gap length varies, the resonance coupling between the coils changes, which introduces reactive power losses and therefore thermal losses that need to be compensated by the cooling system. An improved transfer efficiency, when using HTS resonator coils compared to copper coils was reported in [201].

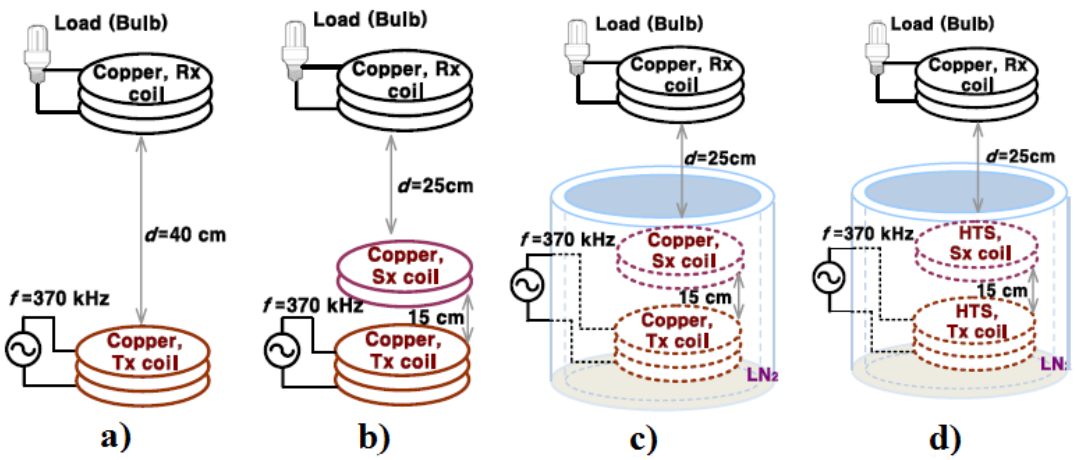

Figure 3-11 Different coil arrangements for a three coil WPT-systems incorporating HTS a) conventional system with copper coils at room temperature, b) copper coil resonator in conventional system, c) three-coil system with cooled transmitting and resonator coil (77K), d) HTS-three-coil system with HTS transmitting and resonator coil cooled to 77K [200]

A study conducted by Inoue *et al*. investigated the impact of low-frequency operation on the power transfer efficiency [202]. It has been shown that at low resonance frequencies, the HTS-system has a much higher transfer efficiency due to the higher quality factor of HTS-coils compared to traditional copper-systems. Furthermore, the HTS-system presents a higher robustness against frequency variation compared to copper-systems. This allows more leeway in the frequency control. A summary of experiments conducted with HTS-systems is presented in Table 3-2.

While losses occurring in the pavement material are negligible [203], the material of the cooling vessel has great impact on the coil-to-coil efficiency. Jeong *et al*. compared multiple vessel materials under varying air gap lengths [204]. The system comprised source and load coils made from copper and two YBCO-coils (Yttrium barium copper oxide) in the transmitting sub-system.

Amongst the tested vessel materials were fibre reinforced plastics (FRP), Bakelite, polystyrene, aluminium, and iron. While FRP, Bakelite and other plastics have high wave penetration characteristics, aluminium and iron have high electrical conductivity and are used as shielding and core materials. While increasing the air gap length, the reflection parameter was measured and compared. The plastic materials have only minor impact on the power transfer, with FRP achieving the highest unaffected transmission distance with 2 m. Hence, FRP is the most favourable cooling vessel material amongst the tested ones. Instead of absorbing or reflecting incident magnetic waves, it does not affect them. In addition, its durability is very high, and it has a very low thermal conductivity with 0.5 W/(m*°C) [205]. On the other hand, iron and aluminium are the least favourable materials as they absorb magnetic flux and cause losses. Other investigated plastics had good properties regarding power transfer efficiency, but low durability and therefore are not suitable for WPT-systems. Kang *et al*. investigated the effect of steel and Styrofoam material as cooling vessel material for the HTS-receiving coil [206]. Styrofoam has a similar magnetic permeability to air and liquid nitrogen, and therefore does not affect the magnetic field. Whereas steel channels the magnetic field inside the cooling vessel and lowers the incident magnetic field on the HTS-coil. Hence, metallic materials should not be used as cooling vessel materials for WPT-systems, as they severely affect the magnetic field and cause losses. While experiments investigate the effect of vessel materials on the power transfer, they do not outline practical solutions for real world systems and do not consider safety regulations. The effect of rain or water between the charging pads was investigated in [207]. Different containers, surrounding the coils, were filled with fresh water or salt water with a salinity of 3.4%. The results show that fresh water reduces the transmission efficiency by up to 5%, even when only one coil is surrounded. If salt water is used, the efficiency decreases significantly with a maximum efficiency decrease of 30% when both containers are filled. This is due to the shielding effect of the salt element in the water.

Table 3-2 Summary of experiments using HTS coils

Power level [W]	Separation distance [m]	Frequency [kHz]	Coil specifications, diameter [m]	Reference
500	0.3	370	HTS Tx: 0.3m Copper Rx: 0.3m	[196]
200	0.5-1.5	13560	Copper Tx: 0.28m HTS Rx: 0.28m	[197]
11	0.05-0.22	3	HTS Tx: 0.29m Copper Rx 0.29m	[195]
N/A	0.03-0.18	63.1	HTS Tx: 0.3m Copper Rx: 0.2-0.3m	[190]
<10	0.02	10	HTS-system: 0.09m Copper-system: 0.09m	[202]
N/A	0.3	370	Copper Tx: 0.3m HTS Rx: 0.3m	[206]
60	0.4	370	HTS Tx: 0.3m Copper Rx: 0.3m	[208]

3.2.3.2 Track layout

Not only has the geometry of the charging pads an impact on the system performance but also the system layout, particularly on the primary side. While the layout for stationary system is straight forward, there are different options available for DWPT mostly related to the dynamic nature of the charging process. Main challenge associated with DWPT is the short time period in which the transmitting and receiving pad can interact with each other and transfer power. As the vehicle is approaching the transmitting pad from one side and moves across it, the magnetic flux intercepted by the receiving coil and therefore the magnetic coupling changes. This causes power and transfer efficiency fluctuation and increased stress on the power electronics. To reduce the impact on the charging system and grid connection, charging pads must have a high degree of misalignment

tolerance. Depending on the layout of the transmitting coil and power supply, two designs can be distinguished and are shown in Figure 3-12.

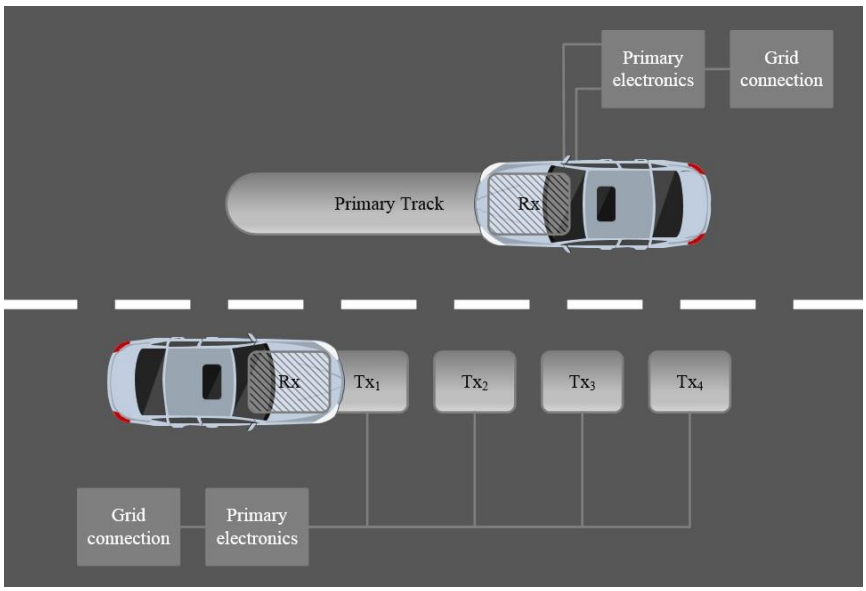

Figure 3-12 Different track layout options for DWPT

While in stationary charging a single power supply can power one or multiple separate transmitting pads, another option is considered for DWPT charging. Instead of using multiple segmented transmitting pads for DWPT, a long transmitter rail is widely used [209], [210]. Both designs have advantages over the other approach, but also their own disadvantages. Using a long transmitter track minimises the amount of system components and reduces control complexity, as it produces a constant power output and current once the receiving pad is located above the track. However, it increases the ratings of each component if supplied by a single power source and if a fault occurs, the whole system must be switched off, decreasing the system reliability. In addition, the efficiency is low during part load operation as the whole track always needs to be energised and the coupling is lower, as the receiving coil is much smaller. The electromagnetic field produced by the parts that are not in use must be supressed to reduce harmful radiation. Furthermore, the consumption of coolant is higher if HTS-coils are used [211]. On the other hand, if the transmitting sub-systems contains multiple segmented pads [212], [213], it requires a multitude of components like power sources and high-frequency inverters, as every pad has to be connected separately. By using multiple inverter-pad sub-systems, the reliability of the system increases through redundancy, as the charging system is still functional, when faults occur within one segment. It is also possible to connect multiple pads together and instead of using several

inverters, one high power inverter is connected via switches to the transmitter pads [214]. Each of the pads switches off as soon as the vehicle passes over it, reducing the electromagnetic field radiation and alleviating the reduced coupling. In addition, each transmitter pad has a compact low weight structure, which simplifies deployment. Disadvantages of this layout are the increased cost and control complexity to increase efficiency and lower the grid impact due to power fluctuations. The inter-pad spacing needs to be optimised as it affects the system performance [215], [216]. If the pads are too close together, coupling between the transmitting pads can occur, which produces negative current stress and it would increase the number of pads per given length. The coupling between the transmitting coils can be reduced by placing them farther apart, but this will eventually result in discontinuous power transfer and has negative effects on the grid network.

3.3 Control Methods

For controlling the power throughput and output of the system, multiple control methods can be used. The most fundamental methods are primary side control [217], [218], secondary side control [219], [220], [221] or both combined [17], [222], [223]. A primary control method cannot be used for power supply tracks with multiple pickup coils. It is necessary that one supply is connected to only one receiver [224]. The primary current and the frequency are controlled to regulate the power output on the secondary side. Using this strategy provides higher efficiencies at lower loads compared to secondary control [225]. One requirement for primary control strategies is a communication link between transmitting and receiving pad. The battery management system (BMS) is transmitting information about the battery e.g. SoC etc. to the primary pad. By controlling the transmitting pad, the secondary electronics can be simplified, thus reducing complexity and cost.

Two important strategies are considered for inverter control, namely phase shift control and frequency control. When phase shift control is used, the phase difference at constant switching frequency between inverter legs is varied [226]. While varying the phase shift, the pulse width of the voltage output signal changes. This causes the amplitude of the voltage fundamental to change accordingly and controls the power output. However, it compromises soft switching as bifurcation during operation close to resonance can occur, which can lead to non-inductive conditions and high switching and conduction losses. Phase shift control does not require a communication link between transmitting and receiving pad, but it is only usable for full-bridge inverters [227]. During frequency control, the phase shift between inverter legs is constant and the switching frequency is varied [228]. This affects the DC output voltage feeding into the battery on the receiver side. The

controller constantly monitors the switching conditions and updates the inverter frequency and switching signals. A range of possible switching conditions needs to be pre-defined so that the controller can limit the frequency to achieve ZVS. To reduce losses, the WPT-system has to operate under inductive conditions and the actual resonance frequency must be measured in real time.

Secondary side controllers keep the supply current and the frequency constant and each receiving system adjusts the power it draws according to their load [229]. If multiple receiving pads are connected to the primary, an active rectifier in each secondary system is required. The power drawn by the secondary system can be controlled by varying the Q-value. As the whole supply rail must be powered, efficiency under part load is low. A combination of control methods on both sides can vary the current and the power demand according to the load on the secondary side. Hence, it requires the same power electronics as primary and secondary control. Highest efficiency is achieved by controlling current and *Q*-values, to match primary and secondary side losses [230]. Advantages of primary and secondary side control can be combined. Diekhans & De Doncker proposed a dual-side controlled WPT-system with a full-bridge inverter on the primary side and an active rectifier on the secondary side [231]. The lower half of the rectifier consisted of switches instead of diodes. By varying the pulse width of the secondary voltage, the fundamental output voltage to the battery can be adjusted. At the same time, the inverter is phase shift controlled. The primary current is controlled by the secondary rectifier pulse width, while the primary inverter pulse width affects the secondary current. A control strategy is developed that uses this additional degree of freedom to maximise the overall efficiency by adjusting the point of operation. While the frequency is limited to 35 kHz it is not clear to what extend the system behaviour changes when a higher switching frequency of 85 kHz is used. A bidirectional frequency control is proposed in [222]. It uses the system frequency to control the supplied power. A new controller is demonstrated in [232], which uses active and reactive power, measured at the resonant circuit of the secondary side, to regulate the bi-directional power flow. The new controller does not require a dedicated communication link between primary and secondary side. However, the system has reduced efficiency in the part load regime.

3.4 Communication in WPT-systems

Equally important to the power transfer system is the communication link between GA and VA. This also includes the communication to the grid connection of the GA to manage the demand based on the grid status. Communication between the sub-systems is required throughout the

charging process in a stationary environment as well as under dynamic charging conditions. The VA needs to detect and request charging from the GA. At the same time, the GA must approve or deny the request. In addition, the GA must detect any foreign objects on the road, which might affect the charging process. Once the charging request has been approved, the VA transmits its charging requirements. These include SoC, power level, misalignment and ground clearance. To ensure optimal charging conditions the VA has an alignment assistance to maximise transfer efficiency. During the charging process, SoC and position of the vehicle are monitored [233]. After the charging process, the method of payment must be communicated between the parties. Wireless communication for stationary charging systems is possible, particularly for smart charging purposes [234], [235]. Key technologies for communication systems under review for stationary WPT include Zigbee, Wi-Fi, Bluetooth and cellular [236]. However, conventional off-the-shelf communication systems i.e. Wi-Fi or Bluetooth are not well suited for wireless communication in WPT-systems, as one of the key requirements is a two-way link with simultaneous data transfer (duplex) [237].

For DWPT there are additional requirements that are caused by the speed of the vehicle and the potential to charge multiple vehicles at the same time. Problems like priority charging and queuing, as well as the potential of speed limitations on the stretch of road arise. Therefore, commonly used technologies in stationary wireless charging cannot be used for DWPT systems. Special requirements for the dynamic system include low latency to ensure stable real-time communication at higher velocities, an increased communication range to reduce roaming between charging zones and the potential to support multiple vehicles [238]. Furthermore, a high bandwidth and reliability are required to safely incorporate real-time control mechanisms and transfer of information [239]. The SAE J2954 guideline outlines Wi-Fi, Dedicated Short Range Communication (DSRC) or RFID as potential communication technology for WPT-systems. RFID communication is suitable for stationary charging, but not usable under dynamic conditions due to latency issues. Furthermore, the signal strength after propagating through concrete to reach the transmitting coil might not be sufficient enough [240]. A study conducted by Gil, *et al.* compared DSRC, radio communication, cellular communication, satellite communication and WiMAX [238]. It concluded that DSRC and cellular communication are the most favourable options. DSRC has a very low latency while maintaining a reasonable high data rate. However, the effective maximum coverage is limited to around 300 m, which might not be enough depending on the length of the charging lane. Cellular communication has a very high coverage

area in which it can transfer with high data rates but with higher latency than DSRC. An additional benefit of DSRC is its current utilisation in safety applications, hence providing a secure communication link [241].

Echols *et al.* proposed a hybrid communication system based on wireless and wired communication [242]. The infrastructure uses a wireless communication link (cellular and DSRC) between VA and GA to process the detection of the approaching vehicle, and the charging request. After the charging request has been approved the information are transmitted to a roadside unit (RSU) and the vehicle is tracked via GPS. The communication between RSU and GA is realised via optical cables to provide low latency, real-time exchange of information. So far, the communication with a single EV has been tested but the impact of multiple vehicles charging at the same time has not been investigated. Another hybrid system based on two different wireless communication links is suggested in [243]. It uses DSRC for the communication between VA and GA, providing a low latency and low jitter link. A Fog management system manages and supervises the DSRC-system. Information gathered during the VA-GA communication are stored in a cloud network and can be accessed by users without disturbing time-sensitive communication. Hybrid systems provide a valuable alternative to single technology communication. However, increased complexity of the communication link could raise additional problems like user accessibility. Another technology that might be viable for future wireless communication in DWPT is 5G, as it provides fast data transfer between multiple parties with low latency [244], [245]. Currently, 5G technology is still in the early stage of deployment [246].

3.5 Foreign object detection and EV detection

Foreign object detection (FOD) is a key auxiliary system required to enable widespread application of wireless charging. It covers the detection of living objects (LOD) and non-living objects e.g. conductive objects and approaching EVs. If the system detects objects between the charging pads it immediately shuts down and prevents any power transfer. By doing so, it prevents heating of conductive objects, which can cause safety hazards. Furthermore, it prevents that living matter e.g. people or animals are subject to magnetic and electric fields. On the technical side, it also prevents system losses and switches off the power transfer when the receiving coil is not near the transmitting pad.

Multiple methods are known to date and mostly rely on sensors i.e. inductive or capacitive, optical, and mechanical [247]. A simple and cheap way is the comparison of power losses in the system

with and without the presence of a conductive object between the pads [248]. Unfortunately, as WPT-systems transfer high powers, the losses generated are small and difficult to detect [247]. Another approach uses the quality factor Q of the secondary pad [249]. This method is viable for stationary systems that include an alignment mechanism. If the pads are misaligned the quality factor of the receiving system changes, disguising the change due to an object. The same is true for DWPT-systems as the receiving coil is constantly moving, causing a changing quality factor. Jang *et al.* proposed an FOD-system based on the change of the magnetic field [250]. It uses multiple non-overlapping coils in the transmitting pad, to detect an object and the voltage difference in the sensing coils across the pad area. The detection of living objects uses similar technologies. By using the capacitive coupling between the transmitting pad and the ground, an approaching living object e.g. animals or humans can be detected [251]. The presence of the living object alters the coupling, but changes are minimal and require careful tuning of the sensor.

Vehicle detection is a special form of metal object detection and is mainly used for switching the transmitting pad *on* and *off* depending on the presence of the receiving pad. It is possible to incorporate the vehicle detection into the FOD-system [252]. Figure 3-13 shows the detection coils for a combined system for stationary charging. It comprises two sets of coils, one for lateral direction and one for longitudinal direction. The system uses the difference in induced voltage in each of the detection coils to locate the object, while the impact on the power loss characteristic is widely minimised. Due to the additional coils, the material usage of the system is high.

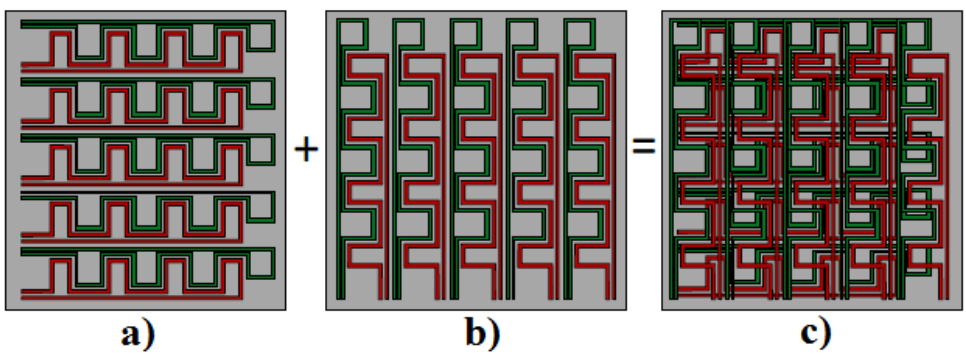

Figure 3-13 Detection coils for a) longitudinal direction b) lateral direction and c) combined [252]

Vehicle detection for DWPT-systems is a main research area within wireless charging systems. A wide range of detection systems exists. Multi-coil systems are commonly proposed e.g. [253] and [240]. In [240], the transmitting pad includes two coils with an offset in the direction of travel and a single detection coil is incorporated in the receiving pad. The detection coil in the receiving pad

is energised, which induces a voltage in the detection coil in the transmitting pad as the EV approaches the charger. Due to the longitudinal offset of the coils, the voltage profile is different, and the phase difference can be used to detect the vehicle. One drawback of this method is that only vehicles approaching along the direction of travel are detected. In general, neighbouring transmitting pads should be decoupled to reduce the negative impact on the transfer efficiency. However, there is a small, often negligible coupling between the pads depending on the pad spacing. Here, this coupling is used to detect the approaching vehicle [254]. As the EV approaches the transmitting pads, the ferrite in the receiving coil affects the coupling and allows a voltage to be induced in the latter transmitting coil. If the primary pad resonates with its tuning capacitor, a current flows and is measured and utilised to detect the vehicle. While the current sensor is already part of the transmitting pad, the system is only applicable to segmented DWPT-systems that uses closely spaced transmitters. Other approaches include phase differences between voltage and current in the transmitting pad [255] or RFID [256]. These systems are limited to a single vehicle per pad and limit the vehicle speed. A new type of detection system uses ferrite position identification (FPID), which locates the vehicles position based on the detection of specifically arranged ferrite cores [257]. An extension to this system employs a ferrite core counter and a FPID messaging unit, that can actively correct errors and does not need information from the source coil or the inverter [258]. For stationary charging systems in particular, position correction is viable option to maximise the transferred power. In [259], the transmitting coil position is adjusted based on the magnetic coupling between Tx and Rx.

3.6 Health & Safety of WPT-systems

The use of time-varying currents and voltages, particularly at higher power levels, brings certain risks and concerns for health and safety (H&S) with it. However, these risks are well known due to usage in other fields and can therefore be addressed. They include electromagnetic field exposure, electrical shock, and fire hazards [260]. Hence, the bigger challenge with H&S in WPT is the public perception of the safe employment rather than an actual challenge for the system [261]. The high-frequency currents in the system produce varying magnetic and electric fields. Due to the low coupling between the coils, the share of leakage fields is high. It causes unwanted electromagnetic interference and field exposure, which not only lowers the system efficiency, but also leads to safety risks. To limit the impact of magnetic and electric fields on employees and for the public in general, the International Commission on Non-Ionizing Radiation Protection

(ICNIRP) proposed a guideline for field limitations [262], [263]. The reference levels for electric and magnetic fields for public and occupational exposure are shown in Figure 3-14.

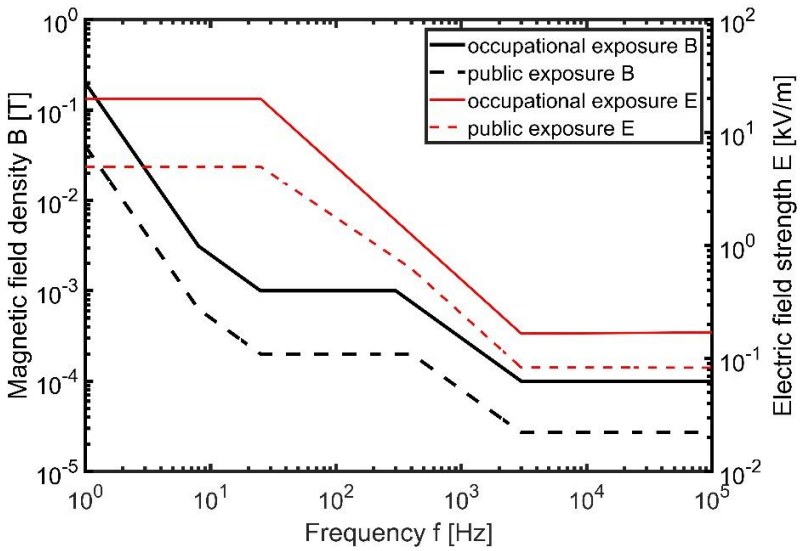

Figure 3-14 ICNIRP reference levels on magnetic and electric fields for occupational and public exposure [262]

In the late 2000s, the World Health Organization (WHO) presented a report that stated, that there is a lack of scientific evidence for health risks caused by fields with a frequency below 100 kHz [264]. Since then, the amount of research on low-frequency magnetic and electric fields has increased but it is difficult to study the long-term effects of magnetic radiation. Short-term effects and biological response can be studied by using experiments on mice and other animals [265]. A study conducted by Nishimura, *et al*. could not observe any changes in reproductive organs of rats during and after magnetic field exposure with frequencies of 20 kHz and 60 kHz [266]. The investigated magnetic fields had a higher field intensity but a lower frequency than currently present in WPT. It is therefore difficult to gauge possible impacts on the human body.

With the aid of anatomical models of humans, it is possible to assess the impact of external magnetic field exposure on humans [267], [268], [269]. These models are based on MRI-scanned human bodies and include properties of multiple different tissues, organs, and body fluids [270]. By coupling the anatomical model and the magnetic field generated by the WPT-system, a tool is obtained to investigate the impact of magnetic field exposure. A person can interact with the wireless charging system and its most delicate areas in multiple ways. Due to the proximity to the transmitting coil, the area underneath the vehicle has the highest magnetic field strengths and is

most likely to exceed the reference levels of the guidelines [271]. Other areas that need further investigation include the area surrounding the vehicle and the inside of the vehicle. The inside is particularly important for future DWPT-systems.

A study conducted by Shimamoto, *et al*. investigated the effect of a 7 kW WPT-system operating at 85 kHz on a human body [272]. The magnetic field distribution around the vehicle, generated by a two-coil system under misalignment (0.2 m later and 0.1 m front-to-back) is modelled using ANSYS HFSS. To mimic the field incident to the human MRI-model, the results are extracted and the magnetic vector potential that would yield the same magnetic field is calculated. This is done to ensure that the resolution of the incident field distribution is equal to the MRI-model. After that, four cases are investigated. A kneeling person touching the vehicle chassis, a person lying next to the vehicle with his right arm stretched towards the coils, a person standing on the transmitting coil (neglecting receiving coil) and a person sitting on the driver's seat were simulated. The induced electric field distribution for the person sitting on the driver's seat is shown in Figure 3-15.

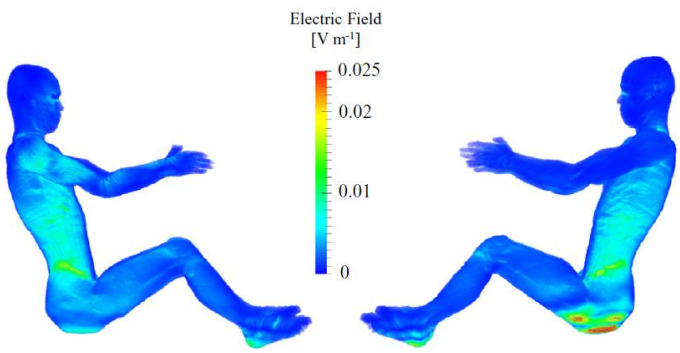

Figure 3-15 Induced electric field distribution of the human model sitting on driver's seat [272]

The maximum induced electric fields for all scenarios are shown in Table 3-3. The highest values are obtained when the person is lying on the ground, next to the vehicle where the magnetic field is the greatest. ICNIRP limits the maximum internal electric field in the frequency range of 3 kHz-10 MHz to $1.35*f*10^{-4}$, which limits the electric field to 11.39 V/m at 85 kHz [262]. All the investigated scenarios are within the guideline. It has been shown that the system complies with current guidelines even under misaligned conditions. However, only a single pair of primary and receiving pad is investigated, neglecting the effect of supply rails and the increased magnetic field due to lower coupling and greater area coverage. In addition, the power during the absence of the

receiving pad was reduced to 5 W, ignoring the case when rated power is transferred during open circuit operation.

Table 3-3 Maximum induced electric fields for each scenario after [272]

Posture and position	99.9th percentile *in-situ* E-field (V/m)	Site of maximum E-Field	Tissue types of the highest E-field
Stand next to the vehicle	0.4	Ankle	Fat (71%), bone (26%), other (3%)
Crouch toward the vehicle	0.92	Thigh	Fat (78%), bone (21%), other (1%)
Lie on the ground	2.3	Chest	Fat (67%), bone (26%), muscle (7%)
Lie on the ground (arm stretched)	5.95	Hand/forearm	Fat (41%), bone (21%), muscle (38%)
Sit on driver's seat	0.024	Buttocks	Fat (90%), bone (8%), other (2%)
Stand on transmitting coil	0.55	Foot	Fat (76%), bone (12%), muscle (12%)

Park used a 3.3 kW WPT-system that operates at 85 kHz, to evaluate the electromagnetic exposure [273]. A two-stage process to solve the bio-electromagnetic problem in the human model proposed in [274] was used. The equivalent currents radiated by the WPT-system are resolved using the equivalence principle. With the known incident fields, the internal electric fields in the human body are calculated by using the quasi-static finite-difference time-domain method. Three different positions of the human model relative to the WPT-system were considered. A person standing next to the WPT-system (case 3 foot), one lying in front of it with the head pointing towards the system (case 3 head), and the WPT-system is positioned at half the height of the human model (case 3). In addition, the system is covered with a 1.5 m x 1.5 m x 1 mm metal plate to mimic the vehicle floor panel, while a person is standing next to it (case 3 metal). The lateral distance between the system and the human was always 0.1 m. As the magnetic field changes with the relative position of the coils to each other, the perfectly aligned case as well as the misaligned case were investigated. Figure 3-16 shows the normalised results for the misaligned case, which is the worst-case scenario. By simulating the vehicle chassis, the induced field is much smaller

than in the other case. The induced current in the head is the largest, as the conductivity of the tissue was the largest. Nonetheless, all results were below the ICNIRP guidelines. The case of operating at rated output during absence of the receiving coil, as well as a receiving pad supplied by a power rail were not investigated. Similar models were built with human models of children and the induced electric field was smaller, due to the smaller cross-sectional area of the body [270].

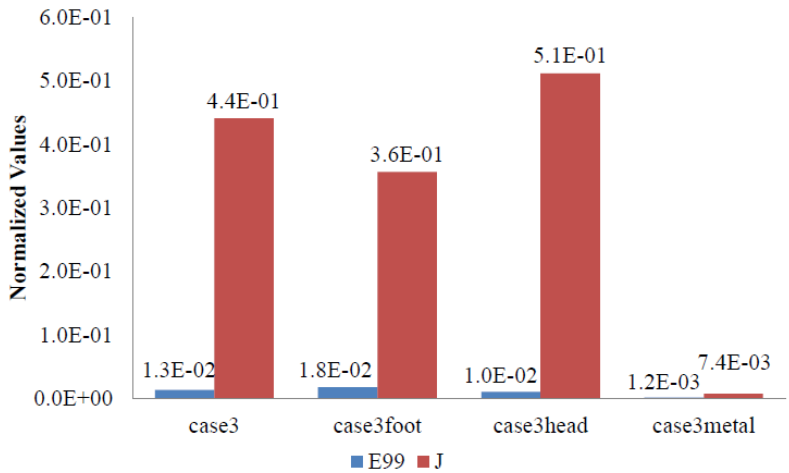

Figure 3-16 Internal electric field normalised to basic restrictions from ICNIRP guidelines of 1998 (J) and 2010 (E99) for the cases where the WPT-system is placed in the middle of the human model (case 3), next to the feet (case 3 foot), next to the head (case 3 head) and covered by metal plate (case 3 metal) [273]

Campi *et al.* investigated the magnetic field produced by a 22 kW WPT-system operating at 85 kHz [275]. 3D FEA-modelling was used to calculate the magnetic flux inside a vehicle and its surroundings. The WPT-system was compliant with ICNIRP reference levels for the fully aligned case. However, under large misalignments small areas around the vehicle were reported in which the magnetic field exceeded the limits. Passengers located within the vehicle were not subject to increased magnetic fields. The highlighted areas around the vehicle were investigated further in [276], with the potential coupling between a pacemaker and the charging system of an EV. As demonstrated, the induced voltage in the pacemaker lead drastically exceeds the limits when outside of the EV and underneath the chassis. While there are protective measures in place to prevent foreign/living objects between the charging pads while the EV is actively charged, bystanders next to the vehicle are at risk as there is no such measure. On the other hand, passengers inside the vehicle are safe as they are shielded by the chassis. However, the materials used in the

chassis are an important factor. Metallic materials such as aluminium and iron have better shielding properties than carbon fiber reinforced plastic (CFPR) [277].

These studies were conducted for light-duty EV and their power requirements. In contrast to the research conducted for light-duty vehicles, the early adopters for WPT also include electric busses for public or freight transport [278]. This is particularly true for DWPT [279]. Research on high power systems for charging busses is limited. Tell *et al*. measured the magnetic and electric field emitted by a WPT-system designed for charging buses with 60 kW at 20 kHz [280]. With a maximum magnetic field of 7.98 µT and maximum electric field of 1.17 V/m inside the bus, when the coils are perfectly aligned, the exposure levels were similar to the magnetic field generated by a video display terminal. Again, the ICNIRP guidelines were not exceeded.

In general, the use of pacemakers and other AIMDs is not considered in these studies. The leakage field can interfere with the medical equipment of the operator or people nearby and negatively affect its operation. In addition, implants can contain metallic parts and wires, which are affected by induced currents and can form local temperature 'hot spots' [281], [282]. To make WPT-systems accessible to everybody, including people using AIMDs, the system must be in accordance with the ISO 14117:2012 standard that limits fields even further [283]. These limits are used in the standards regarding WPT for vehicle charging purposes to limit the fields inside the vehicle and above the ground clearance.

In recent research, only stationary charging was investigated. Due to the constant change in coupling and the higher power levels of DWPT-systems, the magnetic leakage field can be significantly higher. The influence of the dynamic behaviour needs to be investigated to allow safe operation of such systems. Nevertheless, it has been shown, that there is no immediate threat to the health of the person operating or using a WPT-system based on the electromagnetic emission. However, conducting objects e.g. cans, between the coils can be a safety concern due to the increase in temperature caused by eddy currents [284]. Consequently, such charging systems require foreign object detection as presented in chapter 3.5 to interrupt power transfer immediately in the event of a foreign object between the charging pads.

To reduce the radiated fields and losses, shielding and magnetic field cancellation methods can be employed [285], [286]. Such shielding systems can be categorised as passive or active methods [287]. In passive shielding, ferromagnetic materials are used to guide the magnetic flux. By redirecting the magnetic flux, the system performance can be improved while the leakage field is

limited. However, there are limits depending on the material used, as hysteresis losses occur with increasing frequency. Ferrites with high permeability should be employed to reduce the negative impact on the system performance. Passive shielding is an effective way to reduce the leakage field [288], [289]. Passive cancellation methods use conducting materials like aluminium sheets to establish a magnetic field that opposes the original field. The incident magnetic field induces eddy currents within the material, which produce magnetic fields with opposite direction. These fields cancel incoming fields and reduce the net magnetic field. Furthermore, active methods for field cancellation have been introduced in the past. These rely on the same principles as passive methods as they create a magnetic field with opposite direction but provide a more effective way to reduce the leakage field. At higher power levels, an additional power source for the cancellation coil is required, which increases the weight, size, and overall complexity of the sub-system [290]. Kim *et al*. and Moon *et al.* designed a reactive resonant current loop that generates an opposing magnetic field from the original magnetic field [291], [292]. The resonant circuit consists of a capacitor in series with a shield coil. By adjusting the capacitor, the coil current can be tuned to generate a magnetic field that is equal in magnitude but opposite in direction to the incident field. Hence, reducing the overall leakage field [293]. The impact of the cancellation coil on the transfer efficiency depends on the coupling between the shielding coil and the receiving coil. With increasing coupling, the transfer efficiency decreases, so the shielding coil has to be decoupled from the transfer system. Zhu *et al.* proposed a similar shielding mechanism relying on the null in the mutual inductance profile of two coupled coils [294]. By shifting the shielding coil in the transmitting pad to the null position of the receiving coil, it is uncoupled from the receiving coil. Therefore, it can shield the transmitting pad's leakage field. One advantage is the applicability of this approach as it can be used in both pads. The adverse effect on the transfer efficiency is reduced, compared to that of an aluminium shield.

A different approach is used in [295], where a handheld stationary charging system is proposed. It utilises the same approach as plug-in chargers, but it uses two separated sub-systems. The transmitting coil is inserted into the receiving coil. Therefore, it supports a safe way of operation in any weather conditions and lower magnetic field exposure. However, this approach is only applicable to stationary charging.

3.7 Standards for WPT systems

Since the first appearance of WPT for charging purposes, there was the need for standardization. Low-power appliances like mobile phones, toothbrushes and laptops were at the forefront of the

adoption of WPT and standardization for these power ranges emerged first. Currently there is a multitude of standards for these applications, mainly formed through consortia between industrial partners. The QI standard was defined by the Wireless Power Consortium (WPC) for applications in the power range of 5-15 W [296]. It limits the maximum air gap length for power delivery to 4 cm and its operating frequency range to 87-205 kHz. Another standard is the Rezence standard designed by the Alliance 4 Wireless Power Transfer (A4WP) [297]. It is designed for power delivery of up to 50 W at a frequency of 6.78 MHz.

As the power transfer levels required for vehicular applications are much higher than for small scale applications these standards cannot be used. However, consumer and manufacturer require standards for a commercialisation and rapid market uptake. Up to 2016, there was no standard for wireless charging of EVs. This hindered large-scale deployment of WPT technology within the automobile industry, as vehicle manufacturer see it as risk to invest into not market-ready technologies. Standards ensure a minimum quality of the charging system, safe operational conditions and allow comparison between multiple systems from different manufacturers. With the introduction of the SAE J2954-2016, 'Wireless Power Transfer for Light-Duty Plug-In/ Electric Vehicles and Alignment Methodology' guideline in May 2016, updated in 2019 [298], a first attempt was made towards standardisation of WPT for EVs [99]. The usage of this guideline is not mandatory but provides a thorough overview of possible targets. Criteria mentioned in the guideline include interoperability, electromagnetic compatibility, minimum requirements on performance and safety, communication, as well as testing of charging systems for light-duty EV.

Currently the guideline is limited to stationary charging systems within the three power levels of 3.3 kVA, 7.7 kVA, and 11.1 kVA. DWPT and stationary WPT with higher power levels for heavy-duty vehicles and buses will be part of future guidelines. It classifies multiple ground clearances between 100 mm and 250 mm as well as maximum misalignment tolerances a proposed system should comply with. The maximum lateral offset a system can transfer rated power at is ±100 mm, whereas the allowable longitudinal offset is ±75 mm. Additional performance parameters are shown in Table 3-4. Electromagnetic compatibility and EMI levels are defined as in the ICNIRP guideline presented in chapter 3.6. Furthermore, it outlines interoperability between different modules. The efficient coupling between any type of transmitting and receiving system, regardless of manufacturer and home/office applications, within a certain power class and ground clearance must be guaranteed. In addition, systems must be able to charge various battery systems for a wide range of EVs. On one hand, private systems i.e. home chargers or garage chargers can

be surface mounted. On the other hand, publicly available systems and DWPT systems should be embedded in the road surface to allow safe operation and protect the system from mechanical impacts. A feature that is not covered by the guideline is the bi-directional power transfer between EV and grid.

Table 3-4 Proposed power classes and system performances [99]

Power Classes	Maximum input [kVA]	Minimum transfer efficiency [%]	Minimum transfer efficiency with offset [%]	Frequency [kHz]
WPT1	3.7	>85	>80	Nominal 85 Within range 81.38-90
WPT2	7.7	>85	>80	
WPT3	11.1	>85	>80	
WPT4	22	TBA	TBA	

At the beginning of 2017, the International Organization for Standardization (ISO) has published a Publicly Available Specification (PAS) in response to the increasing interest in WPT for EVs. ISO/PAS 19363:2017 ‘Electrically propelled road vehicles – Magnetic field wireless power transfer – Safety and interoperability requirements’ defines criteria for safety requirements and initial classification of charging systems for light-duty vehicles and passenger vehicles [299]. It is structured similar to the SAE guideline, but due to the nature of the PAS, it is less detailed. Once technical experience with WPT for EVs is acquired, the PAS will be converted into a fully operational and binding ISO standard. A list of key standards applicable for WPT-systems for EV charging is summarised in Table 3-5.

Table 3-5 Important standards for WPT-systems

Standard	Description	Ref.
SAE J2954	Wireless Power Transfer for Light-Duty Plug-In/ Electric Vehicles and Alignment Methodology	[99]
SAE J2894/1	Power Quality Requirements for Plug-In Electric Vehicle Chargers	[300]
SAE J2847/6	Communication between Wireless Charged Vehicles and Wireless EV Chargers	[301]
SAE J2931/6	Signaling Communication for Wirelessly Charged Electric Vehicles	[302]
ICNIRP 2010	ICNIRP Guidelines for limiting exposure to time-varying electric and magnetic fields (1 Hz-100 kHz)	[262]
ISO 14117:2012	Active implantable medical devices – Electromagnetic compatibility – EMC test protocols for implantable cardiac pacemakers, implantable cardioverter defibrillators and cardiac resynchronization devices	[283]
ISO/PAS 19363:2017	Electrically propelled road vehicles – Magnetic field wireless power transfer – Safety and interoperability requirements	[299]
ISO 15118	Road vehicles – Vehicle to grid communication interface	[303]
IEC 61980-1	Electric vehicle wireless power transfer (WPT) systems – Part 1: General requirements	[304]

3.8 Grid impact

With the potential large-scale deployment of EVs, a new way to introduce renewable energy sources into our daily lives is possible. However, the change from conventional ICE that rely on fossil fuels, to EVs that use electricity as ‘fuel’ puts an additional burden on the electricity network. Due to the increased number of EVs and the current lack of public charging infrastructure, most EV-user will charge their vehicle at home. EVs are active loads that, once connected to the grid, increase the demand on the line. An increase in demand load influences the line voltage, network frequency, harmonic content, and losses of the distribution grid. By increasing the demand on a particular line, the network approaches its maximum load capability, which causes voltage drops

and can ultimately lead to failures within the network. The same is true for the frequency and its effect on the network. Network operators coordinate the power distribution from large power stations towards the consumer and try to mitigate negative impacts on the network. Even though, the additional load due to EV charging is somewhat deterministic, it is difficult to predict as the decision to charge an EV is based on the driving pattern of the user, initial charge of the vehicle, and potential short-term charging. The mode of charging has an additional impact on the grid. Slow charging processes have a small impact on the grid as a small current is used to charge the vehicle. On the other hand, fast chargers use high currents, and have a bigger impact on the grid [305]. Conventionally, home systems use plug-in chargers, but stationary WPT-system are commercially available. Stationary WPT-systems provide safer charging but have the same grid impact compared to conventional plug-in chargers if they use the same charging power level. Most EV-users charge their vehicle at home, usually after work. This increases the already high demand during the evening peak. Current distribution networks are not capable of allowing large numbers of EV-chargers to draw power at the same time, especially not during peak hours of the day [306]. Smart charging methods can reduce or prevent such impacts [307]. Shifting the charging process from the evening to the night can help reducing the impact by a significant margin, as the base demand during night-hours is very low, compared to peak hours. Therefore, the load on the grid network still follows the conventional two-peak curve, but the trough in the early morning hours is increased and the loading on each line is kept below maximum loading [308]. Zhang *et al.* used the IEEE radial distribution network with 13 nodes and investigated the impact of shifting the charging process to the night-hours [309]. At 30% EV penetration, the grid losses were reduced from 3.7% to 3.1%. Additionally, EVs provide frequency control and help regulating the network frequency [310]. The impact analysis shows positive results for a small network but relies on the installation of smart meters and the possibility to control the EVs directly. While smart meters gain popularity, a widespread deployment is yet to be achieved.

In comparison to conventional stationary (wireless) charging, DWPT-systems introduce highly variable load profiles. Due to the nature of the charging process and depending on the vehicle speed, the charging process consists of a series of very short (in the range of few to several milliseconds), high power charging pulses. This characteristic directly transfers to the electricity network and can cause voltage and frequency fluctuations if no intermediate power storage is used. As shown in [311] and [312], the change in power drawn from the network can change drastically in short timescales e.g. several MWs in tenths of seconds. Additionally, non-continuous charging

pads cause higher fluctuations as continuous charging tracks. There is a high demand for information on the grid impact of these systems, driving research in recent years [313], [314] but it is limited to medium and long-term effects in the range of hours and longer on the network. The impact of DWPT and fast stationary chargers on the distribution network in a Greek city has been investigated in [315]. Two approaches for stationary charging were used. The conventional home charging at power levels of 3.6 kW or 11 kW and a fast-inductive charger with a power level of 30 kW. Using real data from implemented fast chargers, the probability distribution of a charging event occurring within a one-hour period and its charging time was calculated. DWPT-systems were used for emergency charging during the day and the possibility of a charging event occurring on a DWPT-system depends on the amount of EVs on the street and the probability of a charging event. A total of four scenarios were investigated and are outlined in Table 3-6.

Table 3-6 Scenarios for grid network impact analysis in [315]

Scenario	# of vehicles charging at home	EVs using fast chargers	DWPT
A	0	0	No
B	1000	0	No
C-I	1000	100	No
C-II	1000	300	No
D-I	1000	100	Yes
D-II	1000	300	Yes

In scenario C-I, 6 additional fast chargers are required, whereas in C-II 19 are used. The same number of stationary chargers is required for D-I and D-II, with an additional 68 and 61 dynamic chargers. The maximum number of operating chargers is determined based on the likelihood of a charging event and the number of vehicles currently on the roads. Figure 3-17a) shows the power demand profiles of the different scenarios. An increase of approximately 28% in evening peak demand is caused by the home charging of 1000 EVs. This additional demand is present in the rest of the scenarios. Using fast chargers increases the demand in the morning and mid-day hours, causing an increase of 10% when 300 vehicles use the chargers. However, the impact of fast chargers on the evening peak is minor compared to the increase of the morning peak demand. Figure 3-17b) depicts the demand increase due to DWPT-systems. DWPT introduces high demands over the course of the day and creates an additional peak before the evening peak in scenario B, as these systems get used more frequently during the evening rush hour. This rush

hour peak coincides with the beginning of home charging and both combined cause an increase of 44% in a very short period of time between 18:45 and 19:00. While investigating the additional demand, the authors do not consider the impact of the EV usage on the network frequency and voltage.

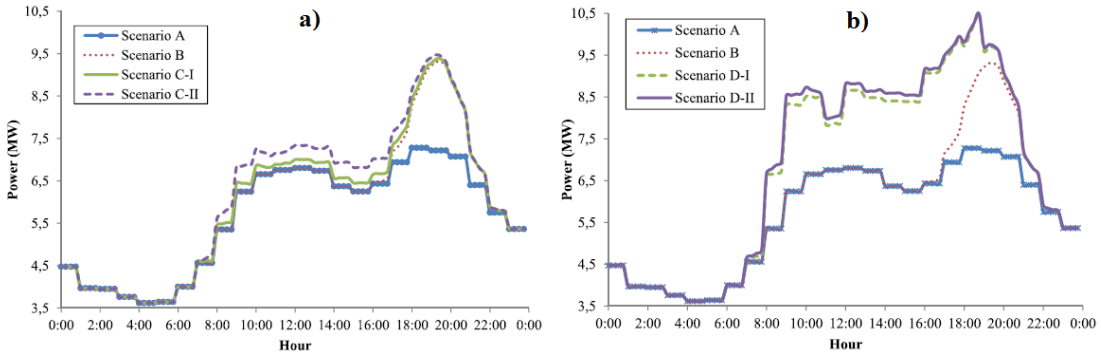

Figure 3-17 Demand power curves for different cases of EV penetration a) scenarios C-I and C-II, b) D-I and D-II [315]

Garcia-Vazquez *et al.* examined the effect of DWPT-systems in Spain. Real traffic data from an 11.3 km long stretch along a highway with a speed limit of 100 km/h, a 75.3 km long motorway with a speed limit of 120 km/h and an urban road with a length of 2.4 km and a speed limit of 50 km/h were used [316]. The DWPT-system comprised multiple transmitter pads of 8 m length and 5 m inter-pad spacing. Three transmitter pads are connected to one power source and form one segment of the DWPT-system. Each segment can transfer up to 40 kW to a single EV. As EV, a Nissan Leaf is used with a 24 kWh Li-Ion battery. The vehicle uses regenerative braking and uses air conditioning (AC) for 94% of the time it is driving. It is assumed that 25% of the vehicles driving on these roads are EVs. While driving with 100 km/h on the highway the SoC of the battery increases by 1%. Whereas the SoC would decrease by up to 10% without DWPT charging. The load profile shows morning and evening peaks depending on the direction the vehicles are travelling as illustrated in Figure 3-18a). On the motorway, the DWPT-system cannot increase the SoC of the battery, but still has a positive effect on the maximum driving distance. The annual average power drawn from the grid is shown in Figure 3-18b). While driving in the urban area the highest increase in SoC is realised with up to 12.7%, this is due to the reduced speed of the vehicle and the longer charging times per pad. Without the DWPT-system, the SoC would decrease by approximately 2%. As shown in the previous study and Figure 3-18c) the power demand profile within a city follows the daily demand curve.

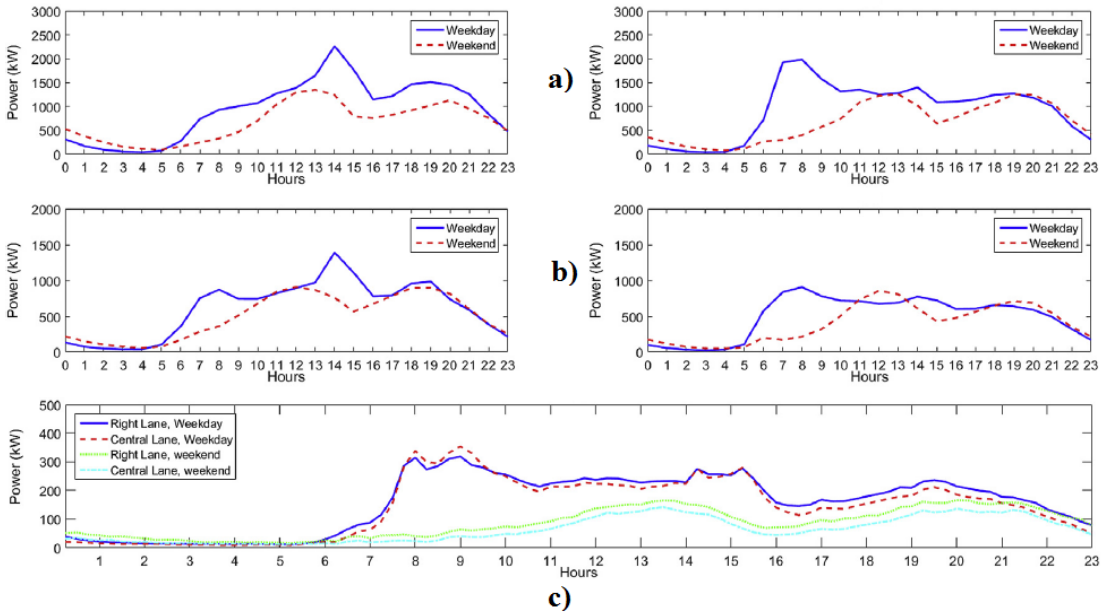

Figure 3-18 Annual average load profiles on DWPT-system during weekdays/ weekends for a) highways: right: from Cadiz, left: from San Fernando b) motorways: right: from Las Cabezas de San Juan, left: from Jerez and c) urban road [316]

It has been shown that any form of WPT-system puts an additional burden onto the electricity network. While stationary charging can be controlled in such a manner that there is no increase in peak demand, DWPT-system will most likely follow the daily demand curve.

3.9 Costs of wireless charging systems

Commercial solutions are available for stationary WPT-systems. Stationary wireless chargers are more expensive than conventional conductive chargers, as they include the cost of charging pads and inverters to produce the high-frequency coupling between transmitting and receiving coils. However, due to the novelty of dynamic wireless charging technology, the economic feasibility has not been fully investigated and literature is scarce. Available literature and costs analysis mainly focus on research projects. Currently EVs are more expensive than conventional ICE-vehicles due to the large on-board battery pack. While using stationary wireless charging, the conventional plug-in charging system is substituted with a charging pad installed in the ground. Compared to a conventional charging system, this means that the vehicle battery pack must have the same size and capacity. One advantage of DWPT is that the vehicle can be charged while it is driving. Hence, the change in SoC of the battery pack while driving is reduced, and the total on-board battery capacity can be reduced [317], [318]. This leads to a significant reduction in initial

cost of the EV [319], [320]. On the other hand, to support the reduced storage capacity DWPT-systems need to be deployed at a large scale. However, construction and maintenance of the transmitter structure result in high capital costs. Recent global trends show that a large portion of driven mileage is located on a small number of roads i.e. highways and motorways. For example, between 2016 and 2017, 65% (212 billion miles) of the driven miles in the UK were located on 13% (~32,000 miles) of the road length [321]. This means that much of the daily driven mileage can be covered by installing DWPT on these key roads. In general, the economic feasibility of a DWPT-system depends on the road coverage, the power level of the system, and the EV penetration rate and battery size [322].

From the few DWPT systems built and tested so far, the costs of some components of the system can be estimated. The third generation OLEV used a W-type transmitter rail to transmit 100 kW and the system cost were 1.069 M$/km [323]. In the following fourth generation (I-type rail) the total costs were reduced by about 21% to 0.85 M$/km. Shin *et al.* estimated the cost of the power supply system to be 0.235 M$/km [324]. Based on these costs, multiple case studies have investigated the economic feasibility of DWPT. Shekhar *et al.* used a set of linear equations to estimate the SoC of an on-board battery pack depending on the mass, frontal area, auxiliary power demand of a vehicle and road coverage as well as charging power level of a DWPT-system [325]. With the aid of this model, a case study based on a bus service in North Holland was investigated. The bus service included 25 buses, five of which were kept as redundancy. Each bus was equipped with a 500 kWh battery pack and was expected to drive 400 km/day, split into ten 40 km long services with six minute breaks between the journeys. Along the service, there were 24 stops of 20 s each. The Urban Dynamometer Driving Schedule (UDDS) standard driving cycle was utilised and a climate model predicted the auxiliary power consumption of each bus to be 25 kW. Under these conditions, the SoC dropped to 68.66% after the first 40 km. The required SoC of the on-board battery to achieve a total of 400 km was calculated to be 87%. A combination of stationary charging and dynamic charging was used to remove the discrepancy between actual and required SoC. Figure 3-19 depicts the variation in the final SoC and achievable driving range of the bus depending on the stationary charging power on each stop. The SoC can be increased to 77.7% when a 200 kW stationary system is used. As this is still below the required SoC, an additional DWPT system must be deployed.

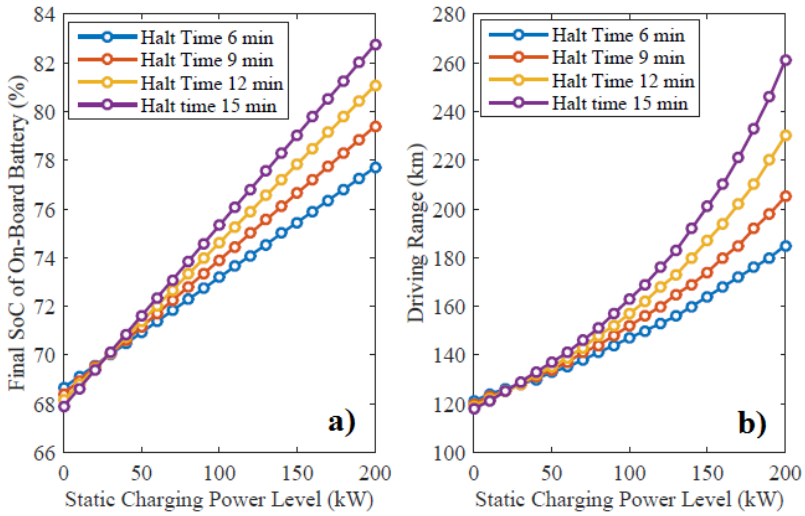

Figure 3-19 a) SoC and b) achievable driving range variation depending on stationary wireless charging power [325]

The required length of transmitter coils and therefore the cost of the DWPT-system depend on the charging power level of the system. As shown in Figure 3-20, the required road coverage decreases with increasing power level. This is because a higher amount of power can be transferred in a shorter period of time, which therefore means that less road needs to be covered with the charging system. On one hand, the system cost of the charger increases with increasing power level. On the other hand, as the construction and infrastructure cost are very high, a reduction in road coverage can lower the total cost. An urban environment with low vehicle speeds and frequent stops was assumed for this study. The effect of other driving cycles e.g. Highway Fuel Economy Test (HWFET) or hybrid cycles with higher speeds intermitted by stops was not investigated.

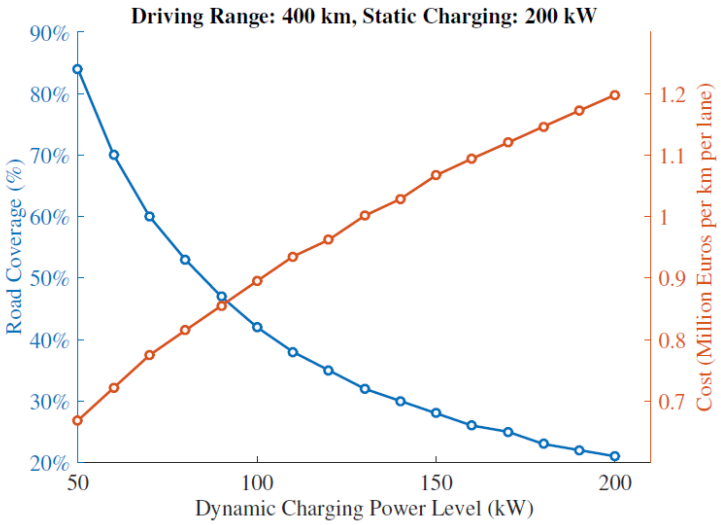

Figure 3-20 Cost estimates and road coverage for various DWPT power levels [325]

Currently there are two OLEV-buses in use within the public transport system of Gumi City. The buses are powered via DWPT and travel about 34.5 km per service. To date, the buses use a 100 kWh battery pack and the authors in [326] have investigated the economic impact of DWPT compared to stationary charging and by how much the battery capacity can be reduced, when DWPT is used. An economic model is built, based on the SoC of the battery pack and the real driving cycle of the buses. The model evaluates the cost of the charging system when 18 buses with 50 kWh battery packs are operating on the route. It would require seven charging pads with a maximum length of 372 m and a charging power level of 80 kW to always achieve a SoC above 50%. Figure 3-21 shows the total cost of the DWPT-system over a ten-year period. The total cost of the DWPT system is approximately 20% lower than the system cost of a stationary charging system. Due to the lack of charging possibilities for the stationary charging system a higher on-board battery capacity is required. In this case study, the battery capacity is assumed to be 100 kWh. After the battery has reached the end of its life, it must be replaced. By employing DWPT and reducing the battery capacity, the life of the battery can be extended as the depth of discharge is limited and shallow charge-discharge cycles are used [327]. In future research, the authors will focus on including a stochastic approach to the driving cycle including traffic and driving uncertainties. Bi *et al.* conducted a life cycle cost assessment between ICE-, plug-in, hybrid, and wirelessly charged busses [328]. The wireless system has the lowest cumulative cost over its lifetime, confirming previous findings. Key uncertainties influencing the total cost of

wireless charging are the battery price, price of electricity and the installation cost of the charging pads.

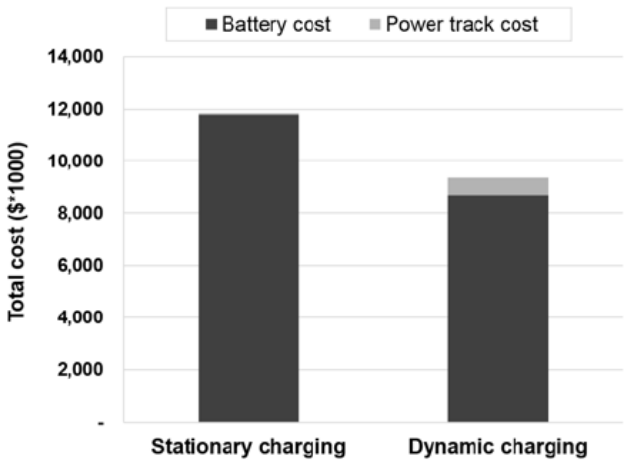

Figure 3-21 Total cost comparison over 10 years between stationary and dynamic charging systems [326]

Battery swapping and DWPT target a similar market i.e. electric taxi [329]. Chen *et al.* conducted a cost-competitiveness analysis of dynamic charging lanes, charging stations and battery swapping stations [330]. An empirical analysis using real world data from a bus rapid transit corridor in Los Angeles, USA was used to evaluate the total cost of each infrastructure. The transit corridor is 35.2 miles long, with a service frequency of 16 busses per hour and an average vehicle speed of 19.9 mph. Battery swapping stations are the most cost competitive, followed by the dynamic charging lane. DWPT has the highest infrastructure cost but the lowest fleet cost. As there is no recharging delay for DWPT, busses do not experience any downtime and less busses are required. In comparison, battery swapping has more balanced costs. While additional batteries are required, the infrastructure cost is lower due to smaller construction space. Furthermore, swapping batteries only introduces little downtime to the service. The same design model is used for a large number of transit corridors from all over the world and the majority of the proposed infrastructures are DWPT-systems. Driving distance, vehicle speed and service frequency are the key factors determining the cost competitiveness. High service frequency and low vehicle speeds favour DWPT due to reduced specific infrastructure cost. While high vehicle speeds, medium driving distance, and service frequency aid battery swapping stations.

Another important factor that affects the feasibility of DWPT systems is the EV fleet penetration. Limb *et al*. and Quinn *et al*. investigated the societal payback time for two different DWPT

systems and their large-scale deployment on primary and secondary roads in the USA [331], [332], [333]. Societal payback time is the time required for savings associated with WPT-EV usage to break even with the initial deployment cost of the charging infrastructure. Vehicles drive according to the Highway Fuel Economy Test (HWFET) when they use motorways and according to UDDS for urban roadways. As a large portion of total mileage is being driven on a fraction of the roads, a total of 83.5% of the motorways and 2.6% of the urban roadways need to be covered with 25 kW charging pads to maintain the SoC. Figure 3-22 depicts the societal payback time for a deployment cost of 2.4 M$/(mile*lane) and an electricity price of 0.127 $/kWh. Battery replacement cost is not considered, and the maintenance cost of DWPT-system is assumed to be similar to conventional road maintenance cost.

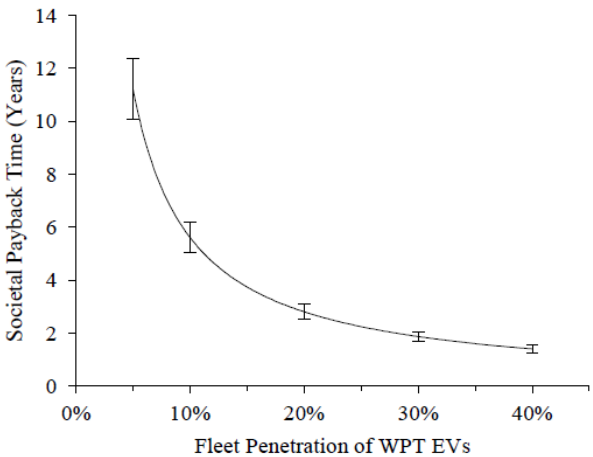

Figure 3-22 Societal payback time for different fleet penetrations [332]

Fuller *et al.* estimated the cost for installing 626 miles of roadways in California with 40 kW DWPT-system to be $2.5 billion [334]. This would be sufficient to allow a 200-mile EV to reach destinations within California on a single battery charge. Aiming at a payback time of 20 years, with a total number of EVs of 300,000, the costs per vehicle and year would be $512. An increase to 1 million EVs would further reduce the costs to $168 a year per vehicle. Moreover, DWPT would still be more cost effective for extending driving range than increasing the battery capacity even at very competitive battery prices of $100 per kWh. It has been demonstrated that WPT and particularly DWPT-system require a large upfront investment due to high construction and instalment costs. However, the costs across the society are comparably small and can be further reduced by a higher adoption of EVs. The cost-effectiveness of DWPT depends greatly on multiple factors and therefore has significant uncertainties associated with it. However, the fast

development and recent improvements can drastically reduce these. Furthermore, conductive chargers have been in mass production for an extended period, whereas WPT is at the beginning of its market readiness. Mass production will positively affect the cost of WPT-technology.

3.10 Conclusion

This chapter presents an in-depth review of the key topics related to WPT-systems for EV charging. It gives an overview of the components used in a WPT-system and major research interests and findings within each component. The coil structure and compensation topology are the most studied parts within a wireless charging system and research focusses on increasing transfer efficiency, misalignment tolerance, and reduced component stress. While copper is conventionally used as coil material, new materials such as HTS with advantageous properties are proposed. However, HTS-coils introduce additional design criteria with their need to be cooled below a critical temperature. Auxiliary topics such as communication and foreign object detection are reviewed. While stationary charging can draw on communication technologies from conventional plug-in chargers, DWPT-systems cannot employ these technologies. DSRC communication is a viable way of allowing wireless communication between GA and VA in a dynamic environment. As EVs are a key pillar of the transition towards a clean and low-carbon society, it is necessary to present that WPT-charging has no negative impact on its users and surroundings. It has been shown that all currently used WPT-systems have electromagnetic emissions below the limits determined by ICNIRP. Tougher limits have been introduced for vehicular applications to protect AIMD-user. Since 2016, a voluntary guideline for design and testing of EV WPT-chargers is in circulation and a PAC forms the beginning of a binding standard for stationary chargers. Further standards covering dynamic wireless charging will be added. While shifting towards electricity ‘fuelled’ vehicles brings the advantage of reducing the CO_2 emissions at the application, its effect on the distribution network needs to be addressed. Stationary wireless chargers have a similar impact on the network as conventional conductive chargers, with demand peaks in the evening. They also provide the option to shift demand to later hours of the day and night. On the other hand, the demand of dynamic chargers follows the conventional daily load profile. Wireless charging requires substantial upfront investment into the infrastructure. However, due to the novelty of the technology, the economic feasibility of such a system is difficult to evaluate. Research on WPT for EVs is becoming increasingly popular, resulting in a rapidly growing community of academia and industry. To achieve market readiness several

challenges, have to be overcome, while exploring potential prospects. Table 3-7 summarises challenges and opportunities of WPT-charging for EVs discussed in this chapter.

Table 3-7 Summary of challenges and opportunities of WPT-technology for EV charging

Challenges	Opportunities
Misalignment tolerance of the charger	Application for HTS and other new materials
Timing of power transfer at high speed	Range and battery life extension of current EVs
Charging multiple vehicles per transmitter	Driverless vehicles
Lifespan of charger, durability under real conditions	Energy storage for renewable energy sources
Grid impact	Frequency control at grid connection
Expensive infrastructure & large-scale deployment	Cost reduction of EVs
Interoperability between multiple manufacturers	Environmental benefits if electricity is renewable
Policies for WPT introduction	
Fast charging	
Universal standards	

4 Range modelling for EV

4.1 Introduction

Main reasons for the lacking widespread adoption of EVs result from the battery technology and charging infrastructure used, causing higher investments, longer charging times, and lower driving capacity often named ‘range anxiety’, with respect to conventional ICE-vehicles. To overcome these drawbacks, more charging stations and faster charging cycles are required. Conventionally, EVs use conductive charging stations to recharge. However, due to the small number of dedicated charging stations for EVs and the long waiting times it is difficult to fully exploit the potential of EV integration. In addition, handling high power cables, particularly in adverse weather conditions, can be dangerous.

This chapter aims at investigating the effect of quasi-dynamic, dynamic wireless charging as well as combined charging on the battery SoC of an electric vehicle. Accurate and easy to implement vehicle and battery models are used to emulate main vehicle components and battery characteristics. Well known driving cycles for urban, highways, and combined driving are used to simulate the driving behaviour. Several scenarios and sensibility analyses are used to demonstrate the change in SoC and minimum requirements for unlimited range are derived to aid policy making. Section 4.2 presents the charging pad structures of a wireless charging system that can be used in stationary and dynamic environments. The vehicle model is introduced in section 4.3, while section 4.4 proposes an extended battery model to simulate the SoC of the on-board accumulator sub-system. Different scenarios for an electric vehicle are shown in section 4.5. A sensitivity analysis in chapter 4.6 investigates the impact of ambient temperature, charging efficiency, and life-cycle on the state of charge profile. Finally, a discussion on human safety concerns is provided in chapter 4.7. This section has been published in [3].

4.2 Charging pad structure

In SWPT systems, a single power supply can power one or multiple separate transmitting pads. A similar approach is used in QDWPT systems. Conventional charging pad structures incorporate circular, rectangular, and double-D coils [162]. Most coils are made from copper but new materials such as HTS are investigated due to favourable characteristics [40] [335]. A single vehicle uses one transmitting pad.

On the contrary, in DWPT systems multiple options are considered. Similar to the approach used in SWPT systems, multiple separate transmitting pads are used to charge a driving vehicle. On the other hand, a long transmitter rail can be used too [210]. Both designs come with advantages over the other approach, but also with their own disadvantages. Using a long transmitter rail minimizes the number of system components in use and therefore reduces control complexity. It produces a constant power output and current once the receiving pad is in the vicinity of the rail. One disadvantage is its need for higher component ratings if the rail is supplied by a single power source, which increases costs. If a fault occurs, the entire system must be shut down, decreasing the system reliability. Furthermore, the efficiency of the system is low during part load operation as the entire track is always energized and the coupling between rail and VA is low due to the size difference. While the ratio of coil size and air gap length influences the coupling between the submodules, the mutual inductance also depends on the coil size ratio. The bigger the difference in coil size is, the lower the coupling between the coils in a WPT system. The coupling, which is influenced by coil size and air gap, also depends on the size difference between coils. The coupling between the coils in a WPT system may vary when the size difference of coils changes. This is because the change of magnetic flux linkage caused by the size difference [336] [337] [338]. The electromagnetic field produced by the parts not in use must be suppressed or shielded to prevent contact with living matter and limit human exposure [263] [339].

On the other hand, using multiple transmitting pads increases the number of required components, such as power sources and connections, as well as high-frequency inverters [213]. However, the large number of components increases the system reliability through redundancy, as the system is still functional, even if a fault occurs in one of the segments. The number of components can also be reduced if multiple transmitting pads are connected to one high power inverter via switches [214]. Having multiple segments creates an additional degree of freedom, as single pads can be switched off as soon as the vehicle passes over it, reducing the electromagnetic radiation and boosting the coupling. Furthermore, each GA is compact, simplifying deployment. Disadvantages of having multiple segments are increased cost and control complexity to increase transfer efficiency and reduce power fluctuations. One key parameter for system performance is the inter-pad spacing, which needs to be optimized [216]. Coupling between transmitting pads can occur if spacing is too small, producing negative current stress and increasing number of pads required for a given length. This coupling can be reduced by increasing the spacing between pads, however

this can result in a discontinuous power transfer profile, which has negative impacts on the grid network.

4.3 Vehicle model

The achievable range of an EV depends on a multitude of internal and external factors. Internal factors include the capacity of the on-board battery system, driving style and the usage of auxiliary components, while external conditions are temperature, terrain and weather. A well-established force-based vehicle model is used to determine the power supplied to and drawn from the battery [340]. Using such a model allows for easy and accurate prediction of system behaviour based on the overall external forces acting on the vehicle, either as resistance against the movement of the vehicle, e.g. drag, or as force produced by the electric motor to propel it. Applied forces are resolved in 2D and are assumed to be constant over the width of the vehicle. The forces acting on a vehicle are shown in Figure 4-1 and include the following:

- Rolling resistance of tires P_r, owing to interaction between tires and road surface, is calculated using Eq. 4.1. The type of tires used on the vehicle affects the load due to rolling resistance.
- Aerodynamic drag P_d, due to interaction between the air volume and the vehicle chassis. It depends on the geometry and frontal area of the vehicle. The load can be calculated using Eq. 4.2.
- Weight load of the vehicle P_h, caused by the weight of the vehicle and affected by the gradient of the road. The weight load is determined by Eq. 4.3.
- Linear acceleration P_{la}, is affected by the acceleration of the vehicle and computed using Eq. 4.4.
- Auxiliary power demand P_{aux}, due to on-board electronics and HVAC (heating, ventilation, and air cooling).

Forces are multiplied by the vehicle's velocity (v) to calculate the power load related to the force. Thus, the resultant power demand P_t required to propel the vehicle is determined by Eq. 4.5. In this study, the 2018 version of the Nissan Leaf is used and given vehicle parameters are listed in Table 4-1.

$$P_r = F_r * |v| = \mu_{rr} mg \cos\theta * |v| \quad (4.1)$$

$$P_d = F_d * |v| = \frac{1}{2} C_d \rho A |v|^3 \quad (4.2)$$

$$P_h = F_h * |v| = mg \sin\theta * |v| \quad (4.3)$$

$$P_{la} = F_{la} * |v| = ma * |v| \quad (4.4)$$

$$P_t = F_t * v = (F_r + F_d + F_h + F_{la}) * |v| + P_{aux} \quad (4.5)$$

To reduce the complexity of the model while still ensuring real world applicability, some assumptions were made including:

- Temperature is set to 20°C as baseline and is constant over one cycle. A wide range of possible temperatures will be investigated in chapter 4.6.3.
- Auxiliary power demand depends on the ambient temperature and the driving style. The power demand is extracted from experimental data of 7375 trips of a Nissan leaf at various temperatures [341]. At 20°C, the auxiliary power consumption is 924 W.
- Air density is 1.23 kg/m³ and constant, neglecting elevation and temperature effects.
- Standard driving cycles, used by car manufacturers, use flat terrain to evaluate vehicle performance and emissions. Therefore, flat terrain i.e. no gradient (θ=0) is assumed.
- Conventional regenerative braking is used throughout the journey. The maximum practical efficiency of 40% is chosen [342]. The effect of regenerative braking will be examined in chapter 4.6.2.
- Total efficiency of the electric drive train, including motor, controller, converter etc. is 80%.
- The mass shown in Table 4-1 is the total weight of the vehicle with driver, passenger, and receiving pad [162].
- According to SAE J2954 the WPT-efficiency for power levels up to 11 kW is at least 85% without any displacement and 80% with lateral misalignment [99]. Therefore, assuming no misalignment between transmitting and receiving pad, the efficiency is set to 85%. Furthermore, maximum power is transferred as soon as the WPT-pads overlap. Misalignment effects and reduced transmission efficiency are studied in chapter 4.6.1.
- A wide range of wireless charging powers is possible. However, for light duty vehicles, designs of up to 50 kW are investigated [162].

- During stops, the total time is spent on the charging pad. Reduced idle times are considered in chapter 4.6.2.

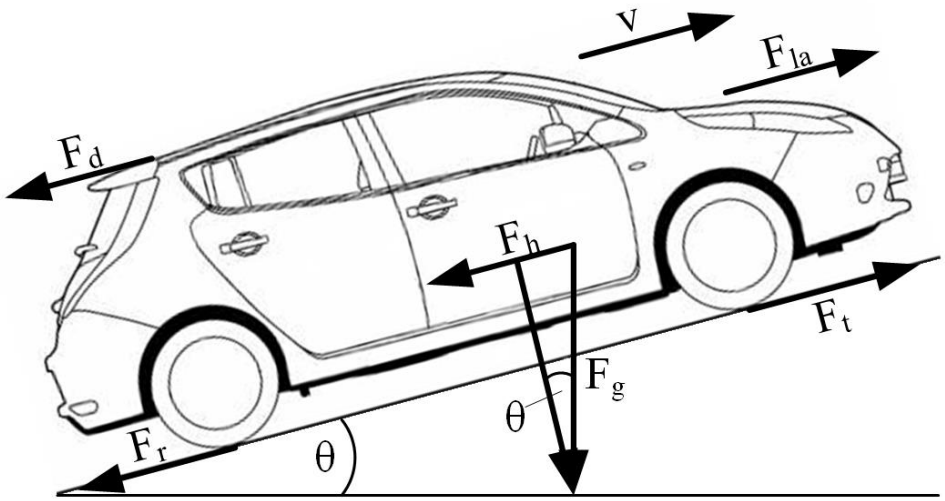

Figure 4-1 Forces acting on a vehicle

Table 4-1 Electrical vehicle parameters [343]

Parameter	Nissan Leaf
Mass *m* [kg]	1700
Frontal Area A [m^2]	2.7
Coeff of rolling μ_{rr}	0.1
Coeff. of drag C_d	0.28
Air density ρ [kg/m^3]	1.23
Rated battery capacity *C* [kWh]	40

Advantages of using this model is the easy implementation into Matlab as well as its modularity in terms of adding more detailed features such as battery models and correction functions. Furthermore, this model can be applied to different vehicle types such as lorries and electric scooters and as shown to a multitude of driving cycles. However, the model is limited by the data acquisition and readily available data for such vehicle types. Particularly, auxiliary power and battery performance data of electric vehicles are scarce. In addition, the electric drive train is modelled as black box with an overall efficiency rather than each component separately to reduce complexity.

4.4 Battery model

With the aid of the vehicle model, it is possible to quantify the loads on the vehicle and subsequently on the drivetrain. The battery is connected to the drivetrain and supplies the electrical power used to propel the vehicle. It is therefore necessary to illustrate the electrical characteristics of the battery. A wide range of parameters can affect the performance of a battery, e.g. capacity, SoC, temperature, state of health, and age. Consequently, a variety of models exists, with varying degrees of complexity and each targets a specific purpose. Those models include, but are not limited to, electrochemical models, electrical models, and mathematical models [344] [345] [346] [347] [348] [349] [350] [351].

Electrochemical models [344] [345] [346], are used to couple the fundamental mechanisms of porous electrodes and concentrated solutions with the electrical behaviour of the battery [347]. Due to the nature of this correlation, electrochemical models are very complex and computationally expensive.

Mathematical models [348] [349], demonstrate system behaviour, but are not practical. Instead, electrical models [350] [351], use equivalent electrical circuits, based on resistors and capacitors, to model batteries in conjunction with other systems. A key advantage of electrical models is their reasonably low complexity and easiness of implementation in circuit simulators. They are commonly used in SoC estimation.

As the SoC is used to evaluate the effectiveness of the WPT system, an electrical model is implemented. Furthermore, extensions for input parameters can be implemented easily. An important feature of the battery model is the dependency of the open circuit voltage and internal resistance on the SoC of the battery. Figure 4-2 depicts the electric equivalent battery model used. It is a combination of a Thevenin-based model and a runtime-based model. In comparison to the simplest equivalent battery model comprising of a single resistor and capacitor, the model employs two resistor-capacitor pairs increasing its accuracy while maintaining a reasonable complexity [350]. In this way, it is also possible to study the transient response. The I-V-characteristics, such as open circuit voltage and resistances, are extracted from experimental data of multiple Li-ion batteries. For an in-depth overview of the model, the reader is referred to [350]. Open circuit voltage and resistance of the battery are calculated for each time step using the battery model. The battery power is determined by the power required to propel the vehicle as shown in Eq. 4.5 and

the power obtained from the charging pad. Terminal voltage and resistance of the battery pack are paired with the battery power, to calculate the current drawn from or supplied by the battery.

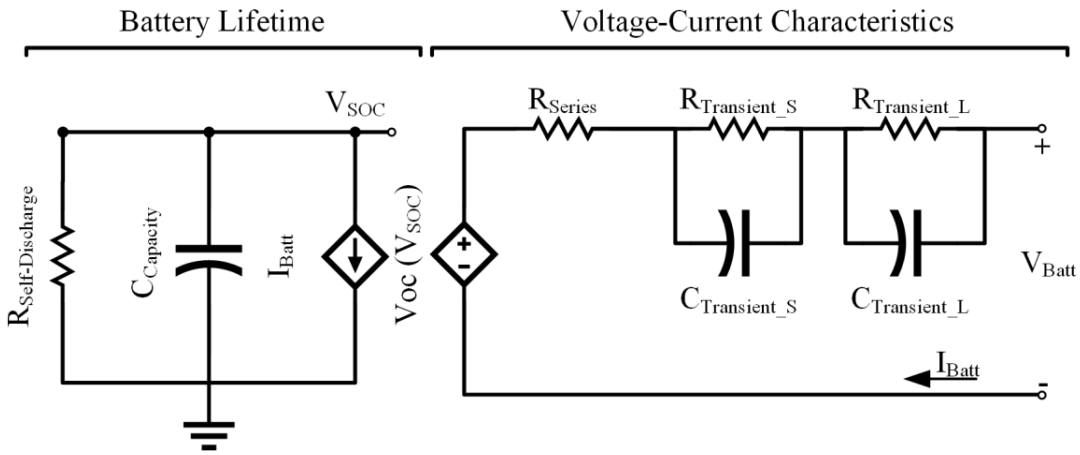

Figure 4-2 Electrical battery model [350]

To increase the versatility of the model, it is expanded to account for temperature and cycle life effects on the capacity via correction functions. Currently there is no data, addressing these characteristics of the actual on-board battery of the Nissan leaf, available. Therefore, experimental data from other Li-ion batteries with a similar chemistry is used to determine the correction functions. For the effect of the cycle life, the available battery capacity after N charging cycles is used. One cycle is defined as an initial discharging of the battery from 100% to 0%, followed by a charging phase back to 100%. In order to increase battery life, car manufacturers limit the available range of batteries and use 20% safety margins on either end of the discharge-charge cycle. The battery is therefore cycled between 80% and 20%. Overall, the available capacity decreases linearly with number of cycles [352].

The available battery capacity is also affected by the temperature. At low temperatures, e.g. -20°C the available capacity is limited to a fraction of the rated capacity, whereas at higher temperatures, i.e. 20-40°C, the available capacity is close to rated capacity [353]. The discharge rate (C-rate) also affects the delivered capacity. However, the previous on-board battery design of earlier Nissan Leaf models only showed minor variation with increasing C-rate. In addition, temperature affects batteries differently depending on their cycle number but due to simplicity, this inter-dependency was not investigated [354] [355].

After applying the correction functions, the final SoC was derived with the aid of Coulomb counting (Ampere-Hour counting) by using Eq. 4.6 where C_n is the total capacity, affected by temperature and number of cycles and I is the battery current:

$$SoC = SoC(0) - 1/C_n \int_{t_0}^{t} I\, dt \tag{4.6}$$

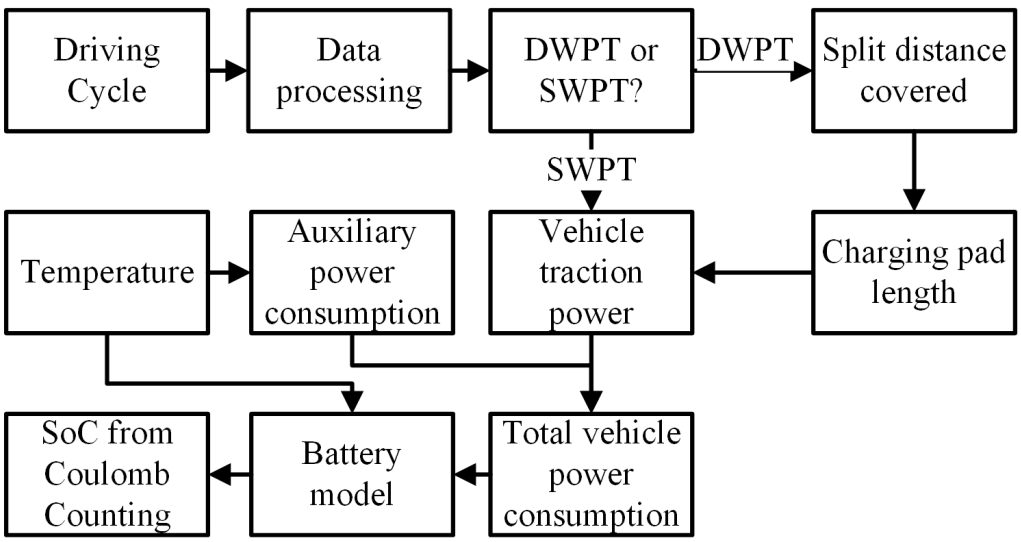

Figure 4-3 Model flowchart

4.5 Scenarios for EV light duty vehicle

The aim of the presented scenarios is to investigate the effect of wireless charging on the state of charge of a light-duty electric vehicle and therefore on the achievable driving range. Furthermore, conclusions regarding the achievement of unlimited range are derived. On-road wireless charging can be applied in two different environments. In the first scenario, only quasi-dynamic charging is applied at traffic lights. Quasi-dynamic charging is referred to by the subscript SWPT. Secondly, only dynamic wireless charging is used to transfer power to the on-board battery system. The final scenario combines both, quasi-dynamic and dynamic charging.

Different standardized driving cycles simulate journeys in different environments most suitable for wireless charging. Car manufacturers commonly use such cycles to demonstrate compliance with emission regulations and to indicate vehicle performance. Each driving cycle, i.e. Urban Dynamometer Driving Schedule (UDDS), HighWay Fuel Economy Test (HWFET) and

Worldwide harmonized Light vehicles Test Cycles (WLTC), is presented in their respective scenario and key information are listed in Table 4-2.

The velocity and acceleration profiles are processed and fed into the vehicle model. Depending on the ambient temperature, the auxiliary power consumption is determined and combined with the power drawn from the battery. Both outputs are fed into the battery model, which computes the battery current profile, the charge removed and the SoC of the battery. The overall layout of the model is illustrated in Figure 4-3.

Table 4-2 Drive cycle characteristics

Parameter	UDDS	HWFET	WLTC
Total time [s]	1369	765	1800
Total distance [m]	11997	16503	23266
Average speed [km/h]	31.6	77.7	46.5
Maximum driving speed [km/h]	91.2	96.3	131.3
Standing time [s]	189	0	235
Number of stops	14	0	7
Average stop time [s]	13.5	0	33.6

4.5.1 Quasi-dynamic WPT

In the first scenario, the EV utilizes quasi-dynamic wireless charging. SWPT charging is most effective in urban areas, due to number of stops and lower average and maximum velocities. The UDDS, depicted in Figure 4-4, simulates urban driving. It contains 14 stops in total and has an average velocity of 31.6 km/h. A velocity of 0 km/h indicates the stops. The SoC profile over one UDDS cycle with different power levels of SWPT is shown in Figure 4-5. Without SWPT, denoted by 0 kW, the SoC decreases by 5.2%-points. This drop can be alleviated by incorporating SWPT at various power levels during each stop, installed at traffic lights to enable charging while waiting. As mentioned in chapter 4.3, the total time idle is used to charge the battery system. Deployed pads are identical and applied power levels range from 0 kW to 50 kW. Assuming a WPT efficiency of 85% and a power level of 10 kW, the SoC decreases by 2.84%-points, which is equivalent to a range increase of 83%. At a charging power level of 20 kW, the loss in SoC is only 0.27%-points, achieving nearly unlimited driving range under given conditions. Higher power levels will not only compensate for the consumption during the cycle but will also charge the battery. The highest power level investigated, 50 kW charges the battery to about 88%, increasing its SoC by 8%-points.

In reality, the change in SoC might be lower as it is likely that the charging pads are misaligned, and the vehicle will not spend 100% of the waiting time on the charging pad. However, according to SAE J2954, the minimum efficiency, even under maximum misalignment must not be below 80%. The effect of different transfer efficiencies and duration spent charging is investigated in chapter 4.6.1.

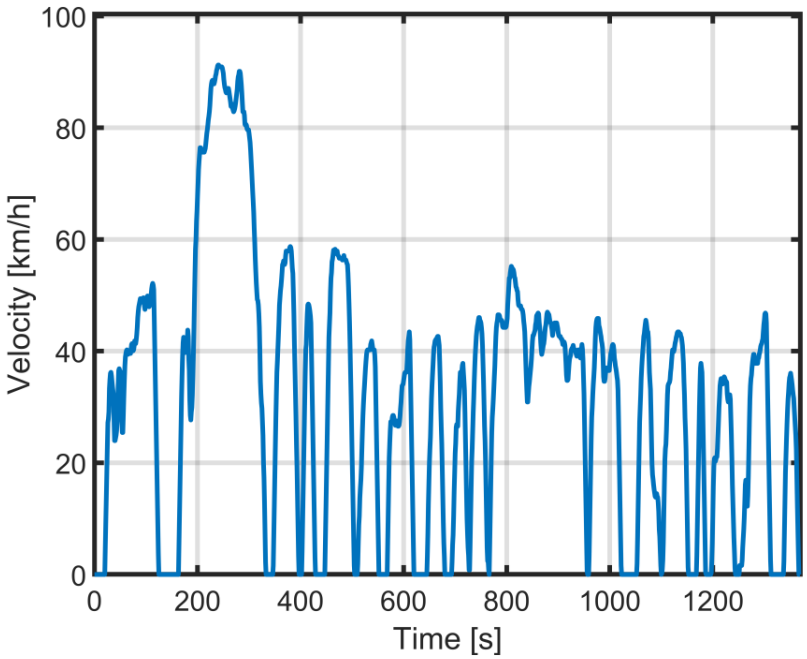

Figure 4-4 Velocity profile of the UDDS driving cycle

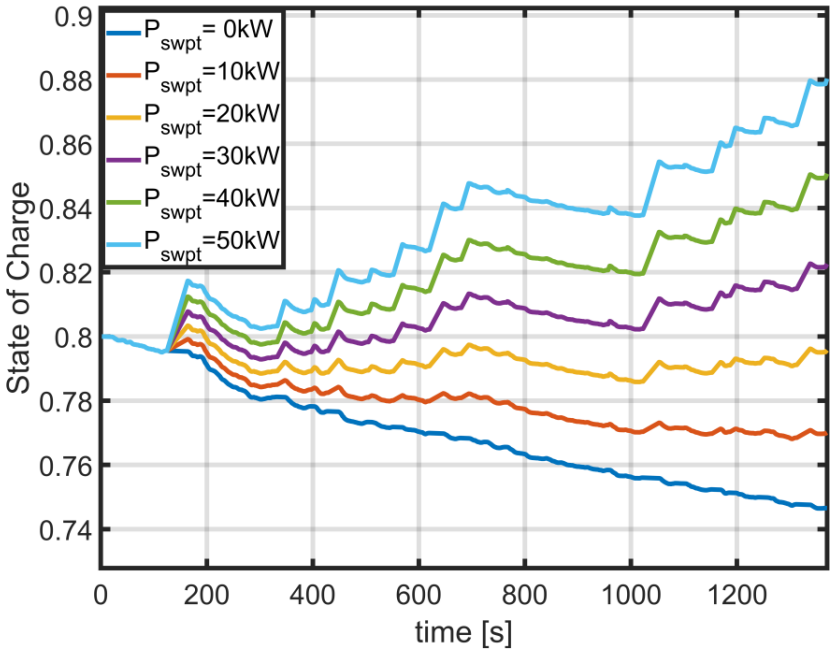

Figure 4-5 SoC profile over one UDDS cycle at stationary power levels between 0 kW and 50 kW

4.5.2 Dynamic WPT

During a conventional highway journey, the EV is never idle. Hence, stationary or quasi-dynamic charging cannot be applied. Therefore, the second scenario deals with dynamic charging or on-road charging at velocities above 0 km/h. Highways comprise a high margin of total driving mileage. In 2017, 66% (215 billion miles) of the total mileage driven in the UK were located on 13% (~32,000 miles) of the road length [356]. This means that the majority of the daily driven mileage can be covered by installing DWPT on these key roads. The HWFET, shown in Figure 4-6, emulates a journey on a highway. It is characterized by a high average and maximum velocity without any stops, shown in Table 4-2. To apply DWPT on highways, a considerable share of road must be covered by the transmitting pad or rail. The ratio of total pad length to road length is called coverage and it is a key parameter that affects the effectiveness and cost of the DWPT system. The distance travelled during one cycle is split into ten equally sized segments, in which the charging pads are located in the centre. The coverage determines the length of each pad as shown in Figure 4-7. In the DWPT scenario presented, coverages up to 50% and power levels up to 50 kW are considered. Other assumptions can be found in chapter 4.3.

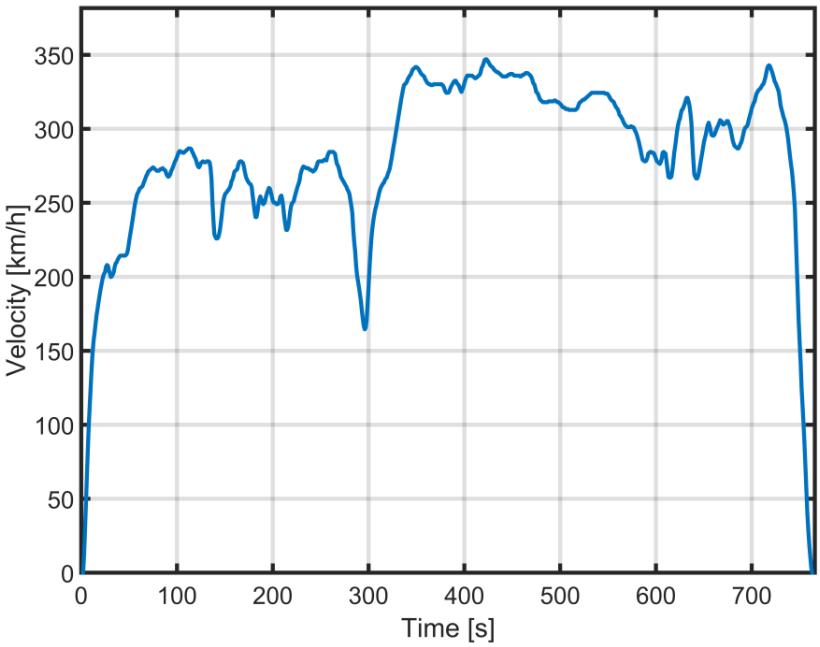

Figure 4-6 Velocity profile of the HWFET driving cycle

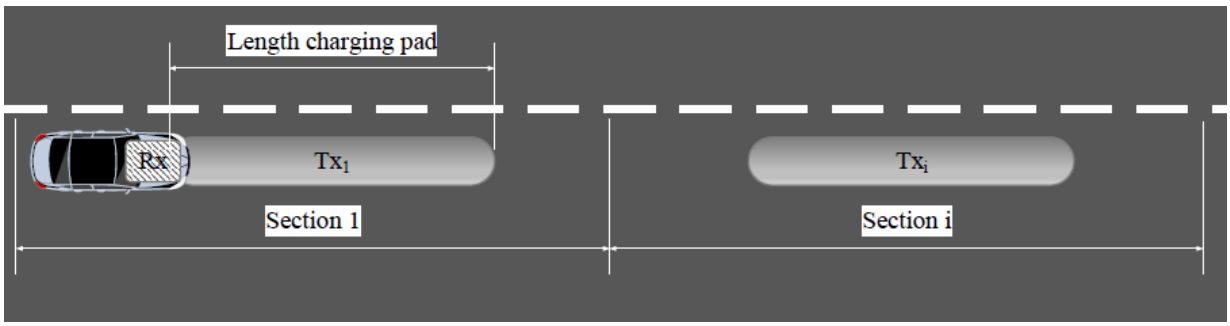

Figure 4-7 Dynamic charging pad allocation

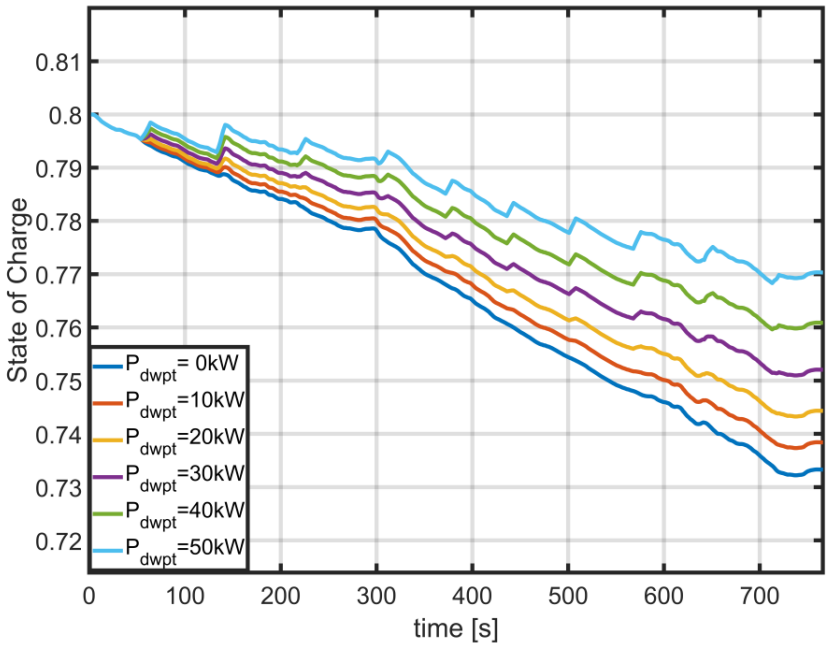

Figure 4-8 SoC profile over one HWFET cycle at dynamic power levels between 0 kW and 50 kW at 10% road coverage

Table 4-3 Minimum dynamic charging power level required for unlimited range in HWFET cycle

Road coverage [%]	DWPT power level [kW]
5	111.5
10	78.5
15	58
20	47.5
25	39.5
30	35
35	31
40	28
45	25.5
50	24

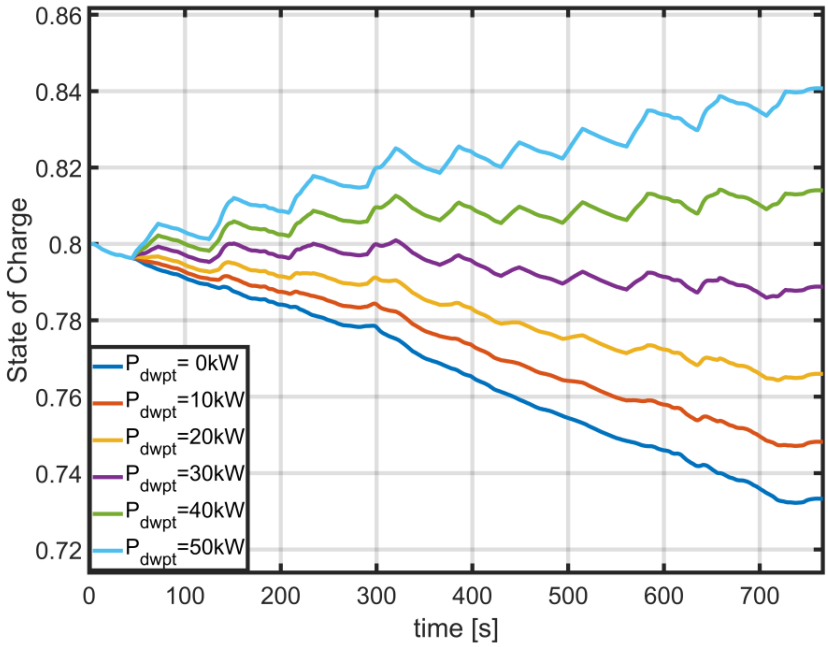

Figure 4-9 SoC profile over one HWFET cycle at dynamic power levels between 0 kW and 50 kW at 30% road coverage

Figure 4-8 illustrates the SoC profile over one HWFET cycle for different charging power levels at 10% coverage. Without on route charging, the battery loses 6.7%-points. Overall, the gain in SoC is small and in contrast to SWPT, a net positive change in SoC, i.e. unlimited range, cannot be achieved with 10% coverage (1.65 km), and power levels up to 50 kW. However, the effect of the charging pads and their location can clearly be seen. The moment the EV is traversing a charging pad is characterised by an increase in SoC, with larger increases at higher charging power levels. At 10 kW the achievable range is extended by 8.2% and at 20 kW by circa 20%. Highest increase in range with 125% is realized at 50 kW.

To increase the effectiveness of DWPT, the coverage is tripled to 30% (4.95 km) and the SoC profile is depicted in Figure 4-9. With 30% coverage the gain in SoC is higher than with 10% as the time spent on the charging pad and therefore to transfer energy is increased drastically. A net positive change in SoC can be achieved, meaning that the EV can be charged to a higher SoC at the end of the cycle than the SoC it started with. Power levels above 30 kW increase the range indefinitely. Lower power levels i.e. 10 kW extend the range by 29% and 20 kW by 96%. Increasing the coverage even further to 50% allows EVs unlimited range at power levels of 24 kW.

Table 4-3 shows the minimum power levels required for various road coverages to achieve unlimited range. The required charging power level decreases rapidly with increasing road coverage but slows down with coverages above 30%.

Figure 4-10 shows the effect of increasing the power level and coverage. As shown before, extending the range is possible by either increasing the charging pads length or by increasing the power level. For example, 30 kW at 10% coverage achieves similar results as 10 kW at 30% coverage. However, increasing the charging power level for a given coverage has a greater impact on SoC than increasing the coverage. In Figure 4-10, the increase in range for 50 kW at 10% coverage is greater than for 10 kW and 50% coverage. This is also advantageous as increasing the coverage involves a large amount of construction works and cost. Furthermore, the effect of coverage increases at higher charging power levels. This is due to the stacking of additional energy transferred per charging pad.

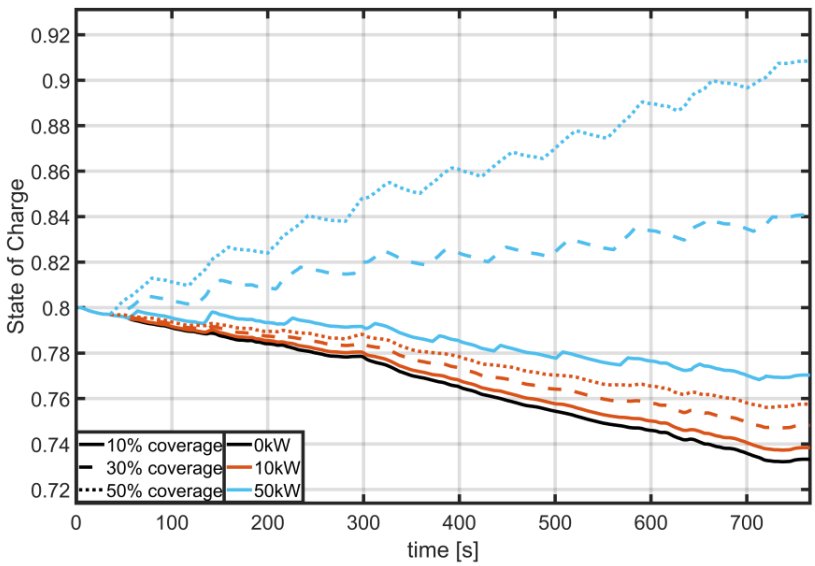

Figure 4-10 SoC profile over one HWFET cycle with dynamic charging at different power levels and various coverages

4.5.3 Combined SWPT and DWPT

The final case study combines both SWPT and DWPT charging in a single cycle. It uses the WLTC to simulate urban driving followed by a highway section as indicated in Figure 4-11. The WLTC cycle is characterized by a high maximum and average velocity but it also includes stops, particularly in the first section. Key characteristics are shown in Table 4-2.

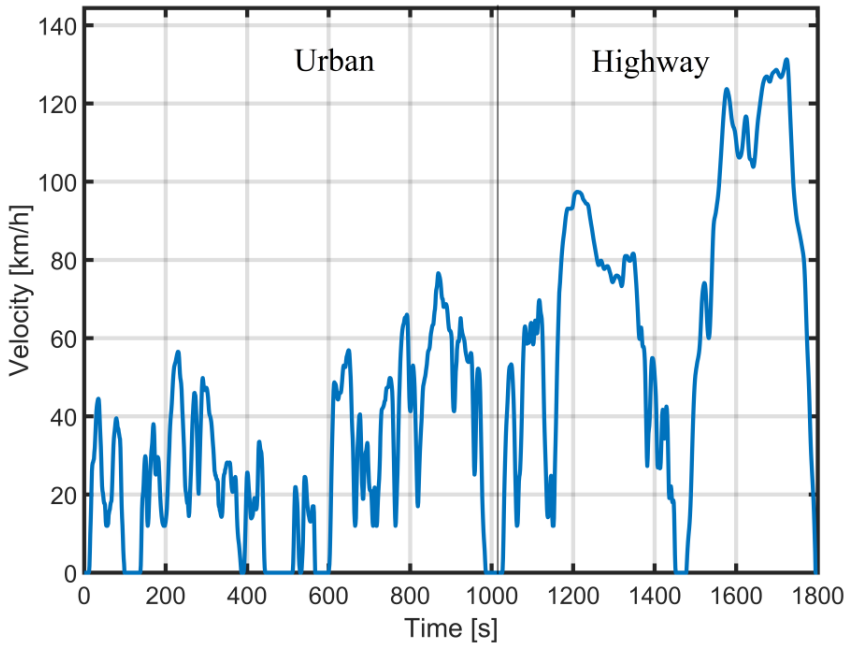

Figure 4-11 Velocity profile of the WLTC driving cycle

Initially, SWPT and DWPT are investigated separately for the WLTC cycle. Figure 4-12 shows the impact of SWPT on the SoC profile. Without any on-road charging the SoC decreases to approximately 68%. The change in SoC decreases with increasing charging power level e.g. at 10 kW the range extends by 23.7% and for 20 kW by approximately 67%. It is possible to achieve unlimited range with solely SWPT charging, however, very high power levels of 50 kW or greater are required.

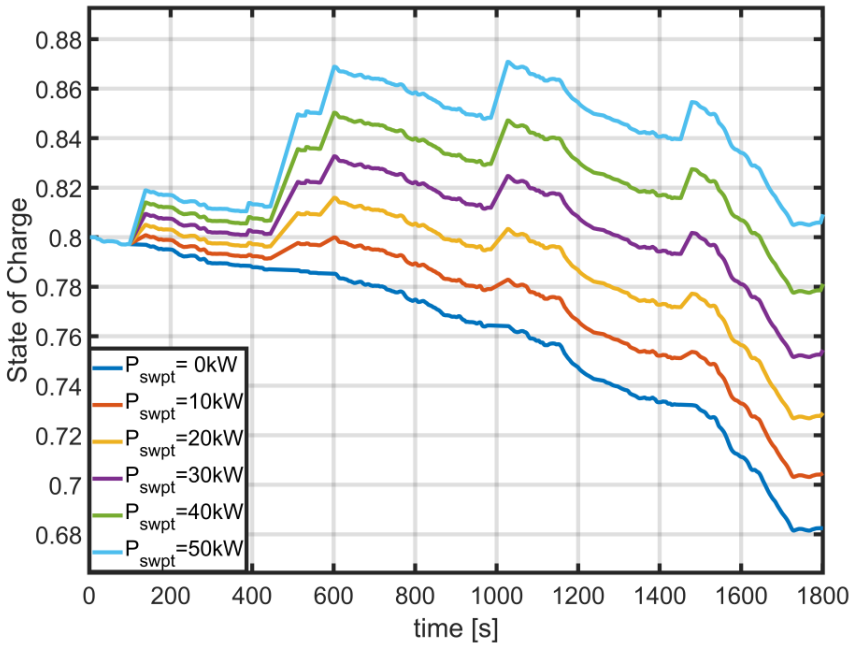

Figure 4-12 SoC profile over one WLTC cycle at stationary power levels between 0 kW and 50 kW

Dynamic wireless charging only at different coverages is investigated in Figure 4-13 and 4-15. At a coverage of 10%, dynamic charging extends the range by up to approximately 170% at 50 kW. It is not possible to realize unlimited range with a coverage of 10% as the energy transferred in the short periods of time is not sufficient to offset the power consumption of the vehicle. By increasing the lengths of the on-road charging pads, the net time spent on the pads and therefore charging time is drastically increased. This leads to a substantial increase in energy transferred, even at lower power levels. In addition, it reduces the burden on the electricity network as short-term pulses are extended.

At a road coverage of 30%, power levels of 30 kW and higher can achieve unlimited range under given circumstances. Power levels of 10 kW and 20 kW can increase the range by circa 38% and 155% respectively. For coverages of 50%, the charging power level threshold for unlimited range is further reduced to 20 kW. In addition, high power levels at coverages of 50% have the potential to overcharge the battery. This means an appropriate control mechanism is required to switch off the charging system once the battery is fully charged to avoid damage to the accumulator system. Similarly, to dynamic charging during the HWFET cycle, an increase in charging power level is more beneficial than an increase in charging pad length.

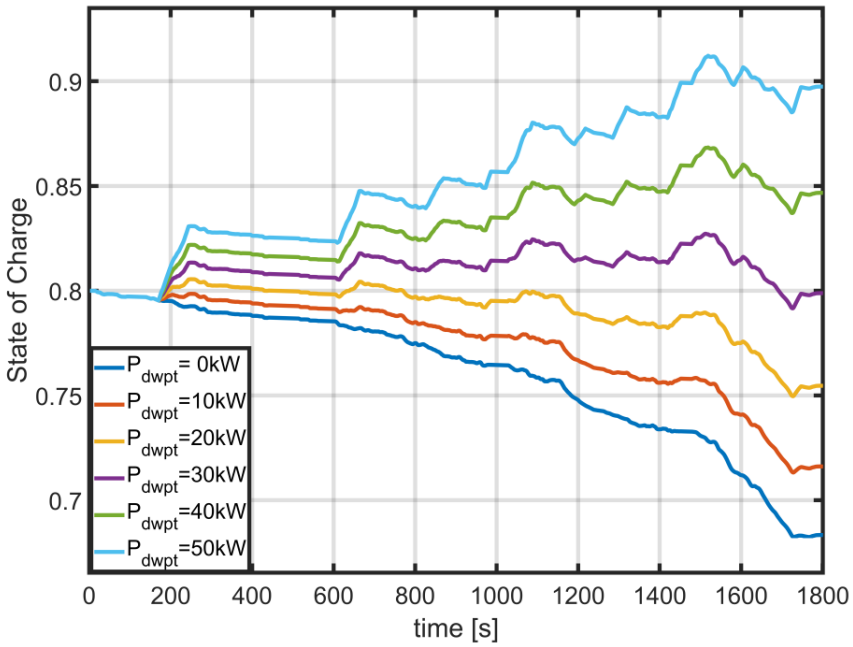

Figure 4-13 SoC profile over one WLTC cycle at dynamic power levels between 0 kW and 50 kW and 30% coverage

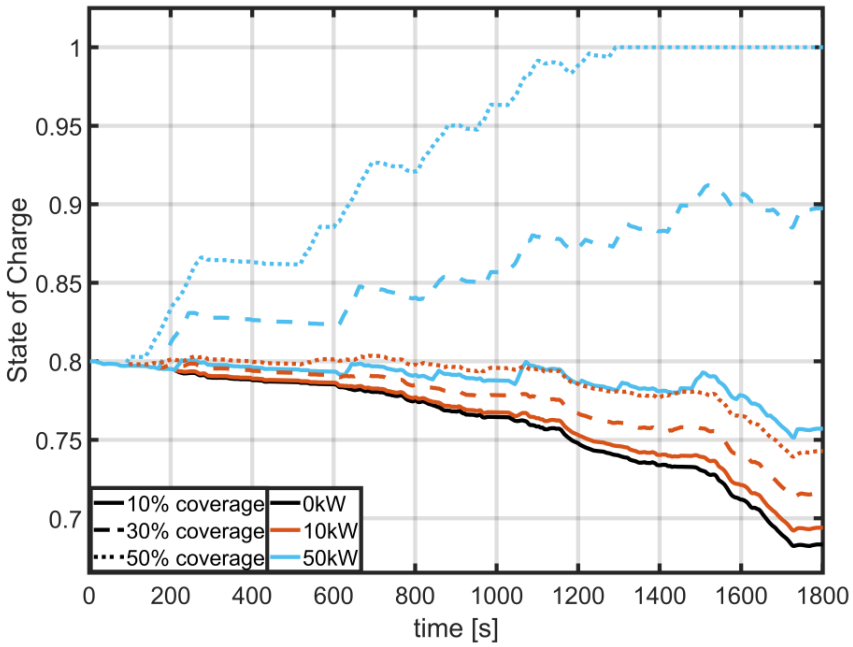

Figure 4-14 SoC profile over one WLTC cycle with dynamic charging at different power levels and various coverages

A combination of both, stationary and dynamic charging, can help reducing the high requirements

for both systems to achieve unlimited range independently. Figure 4-15 to 4-18 show the change in SoC over one WLTC cycle for a wide range of SWPT and DWPT combinations. The graphs also include the cases of using SWPT charging and DWPT charging as standalone options for comparison. SWPT charging combined with 10 kW of DWPT charging can achieve a net positive change in SoC. In comparison to stationary charging as standalone option, the power requirement for unlimited range can be reduced significantly from 50 kW to 30 kW. As shown in Figure 4-11, the majority of stops is located in the first section of the cycle, limiting the use of stationary charging. However, Figure 4-12 indicates that two-thirds of the energy consumption occurs in the second section i.e. on the highway. It is therefore possible to reduce the power level of stationary charging pads if used in conjunction with dynamic charging. Nevertheless, high coverages or high stationary charging power levels are required to offset the energy consumption during the cycle.

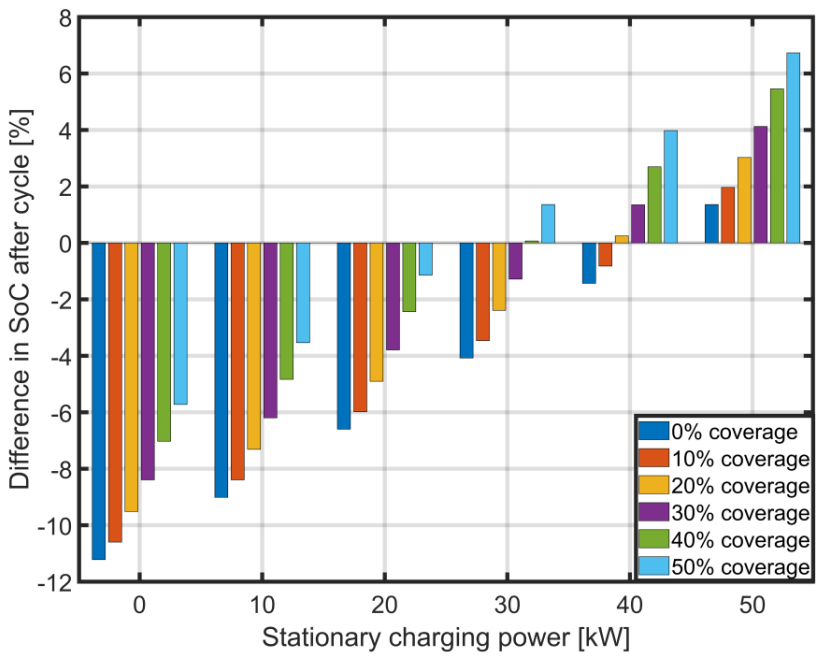

Figure 4-15 Change in SoC over one WLTC cycle with combined stationary and dynamic charging at different stationary power levels and coverages of 10 kW dynamic charging

With an increase in dynamic charging power level to 20 kW, the required combination to achieve unlimited range shifts towards medium stationary charging power levels and medium road coverages. Figure 4-16 shows that there is a trade-off between stationary power level and DWPT coverage. The required coverage for DWPT charging at 20 kW can be reduced by 10%-points if the stationary power level is increased by 10 kW.

The impact of increasing the dynamic charging level to 50 kW is shown in Figure 4-17. Nearly all combinations result in unlimited range. Furthermore, many combinations, particularly with high coverages, overcharge the battery and require switch off mechanisms. The trade-off between stationary charging level and coverage has increased and a reduction of 10%-points in coverage is achieved by increasing the stationary power level by 20 kW until SWPT charging alone can realize unlimited range.

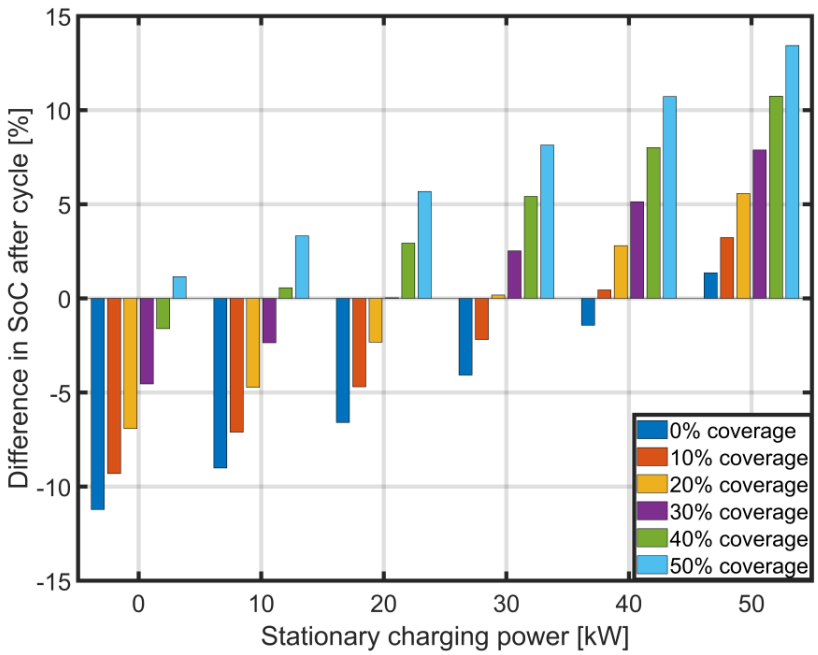

Figure 4-16 Change in SoC over one WLTC cycle with combined stationary and dynamic charging at different stationary power levels and coverages of 20 kW dynamic charging

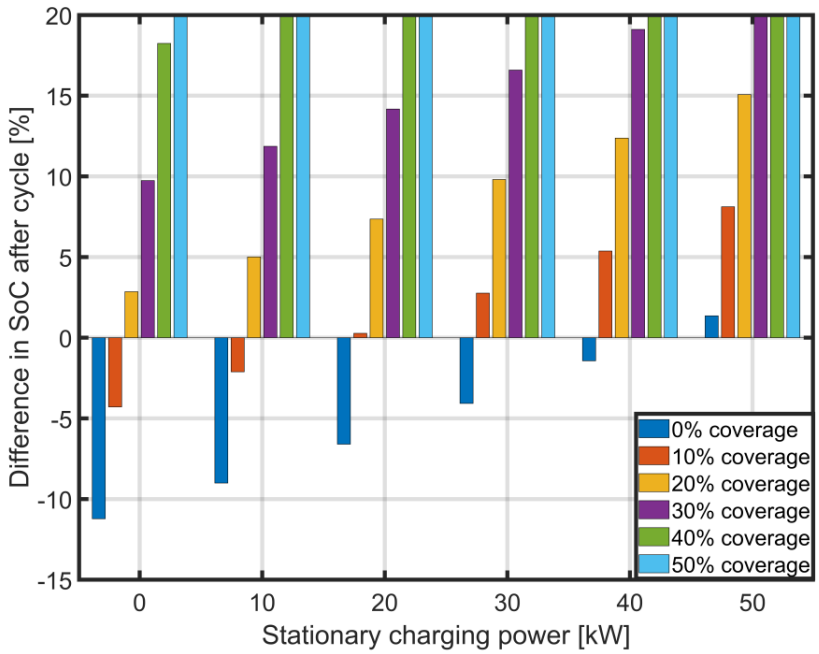

Figure 4-17 Change in SoC over one WLTC cycle with combined stationary and dynamic charging at different stationary power levels and coverages of 50 kW dynamic charging

4.6 Sensitivity analysis

The effectiveness of wireless charging depends on a wide variety of internal and external factors. This chapter examines the impact of the wireless transfer efficiency and the time spent idle on the charging pad, the temperature and age of the battery. In addition, the effect of regenerative braking is shown. All three scenarios are investigated.

4.6.1 WPT-efficiency and time spent idle

Before 2016, there was no standard or guideline specifying key system parameters for WPT for EV charging. With the introduction of SAE J2954 [99] and the sub-sequent ISO/PAS 19363 [299], the first step towards a regulated utilization of this technology was made. SAE J2954 introduces 85% as a minimum transfer efficiency for perfectly aligned charging pads. Furthermore, under the maximum misalignment, the minimum efficiency achieved by the system must be 80% [99]. Although this guideline is for stationary charging at power levels up to 11 kW, it is currently the only official guideline for wireless charging of EVs.

Hence, it is used here to define the lower limit of the wireless charging system efficiency. The upper limit is taken from experimental work on WPT for charging purposes [17] [357]. However, under practical conditions this limit is difficult to achieve.

The WPT efficiency considered does not specify whether the charging pads are misaligned or a WPT system with lower achievable maximum efficiency is used. It corresponds to an overall loss in efficiency, potentially attributed to lateral misalignment, longitudinal misalignment as the EVs traverses the charging pad or sub-optimal operation.

The effect of different charging efficiencies for SWPT charging is depicted in Figure 4-18. There is a linear correlation between the change in SoC and the WPT efficiency. At higher charging power levels, the influence of the charging efficiency is greater as more energy is transferred at each charging pad.

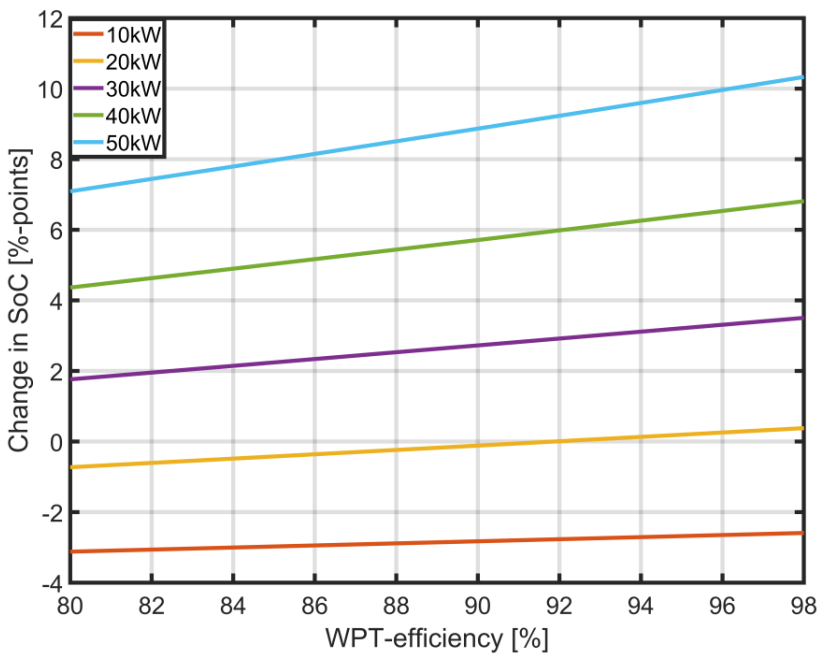

Figure 4-18 Effect of varying charging efficiencies on change in SoC over one UDDS cycle with stationary charging at different power levels

Table 4-4 Relative increase in achievable range [%] for various wireless transfer efficiencies at 10kW and various driving cycles

Charging efficiency [%]	UDDS (SWPT)	HWFET (DWPT at 30% coverage)	WLTC (combined charging at 30% coverage)
80	66.4	26.6	76.3
85	273.0	28.7	86.2
90	2083.7	31.0	97.3
95	92.2	33.6	109.7

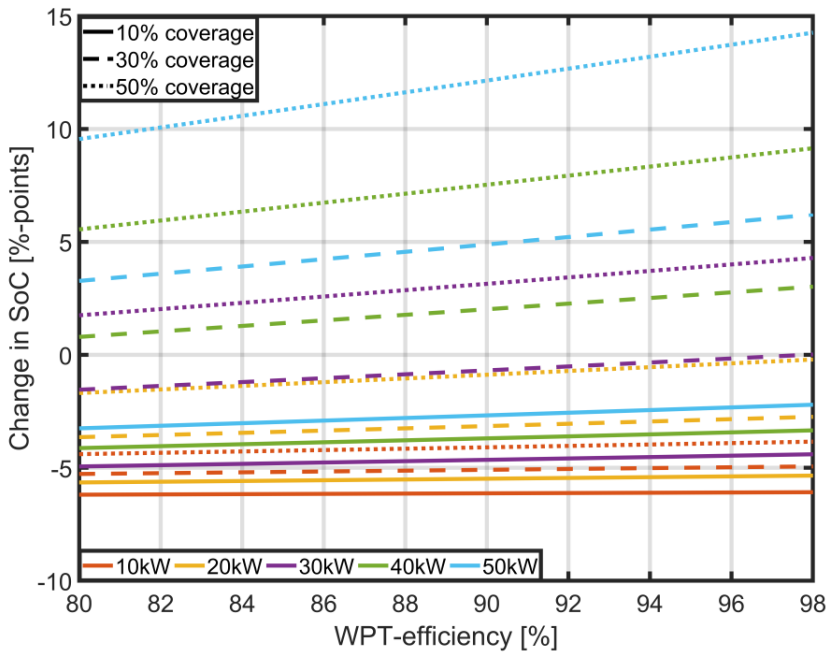

Figure 4-19 Effect of varying charging efficiencies on change in SoC over one HWFET cycle with dynamic charging at different power levels and coverages

Similar results are obtained for dynamic charging for the HWFET cycle. One factor that reinforces the benefits of higher charging efficiency is the road coverage as shown in Figure 4-19. At higher coverages, the effect of increased charging efficiency is more pronounced as energy is transferred for a longer periods per charging pad. On the other hand, for a coverage of 10% and low charging power levels, the effect is almost negligible. Only at higher power levels, a higher efficiency is beneficial.

Due to the large number of combinations for the WLTC cycle and combined charging, the case of 20 kW SWPT and 20 kW at 30% coverage of DWPT was chosen in the following sensitivity analysis. As previously shown, this case achieves no change (±0%) in SoC over one cycle,

meaning the charging system transfers as much energy as the EV uses. It is therefore a good scenario to investigate the impact of mentioned factors.

Figure 4-20 shows the impact of different charging efficiencies on the SoC over one WLTC cycle. An increase in charging efficiency from 80% to 85% results in unlimited range of the EV. Nevertheless, an efficiency of 80% is still sufficient to increase the available range drastically. Higher efficiencies can reduce the power level or coverage required to achieve unlimited range as energy is transferred more effectively. Table 4-4 summarizes the gain in achievable range for different driving cycles using 10 kW of stationary and/or dynamic wireless charging. The highest impact is in the WLTC scenario as 10kW of stationary and 10kW of dynamic charging is used. Contrary, dynamic charging used in the HWFET scenarios has the least effect on the achievable range.

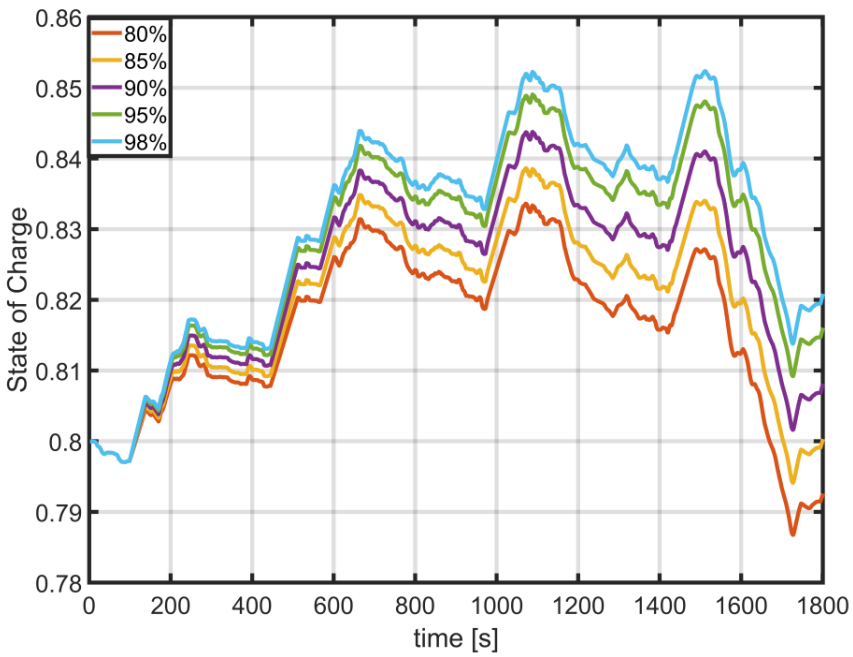

Figure 4-20 Effect of varying charging efficiencies on SoC profile over one WLTC cycle for combined charging at 20 kW stationary and 20 kW at 30% coverage dynamic charging

Particularly for stationary and quasi-dynamic charging, the time spent idle on the charging pad influences the potential of the charging system. It represents the availability of the charging pad on e.g. a traffic light and the duration waiting for the light to switch. It is therefore, considered for the UDDS and WLTC cycles. The time spent idle linearly affects the SoC during the UDDS cycle

(Figure 4-21). At higher power levels, more energy is transferred per second spent on the charging pad, resulting in a greater change in SoC. Therefore, it is crucial to maximize usage of high power WPT charging pads in a quasi-dynamic fashion, as the feasibility is strongly influenced by the utilization.

In Figure 4-22, the black line shows the SoC profile for DWPT (20 kW and 30% coverage) charging only. Using SWPT, the final SoC approaches the initial SoC, representing unlimited range. The change in SoC is linearly dependent on the time spent idle on the charging pad, similar to the UDDS case. However, for this special case the achievable range exponentially approaches infinite for increasing shares of time spent idle.

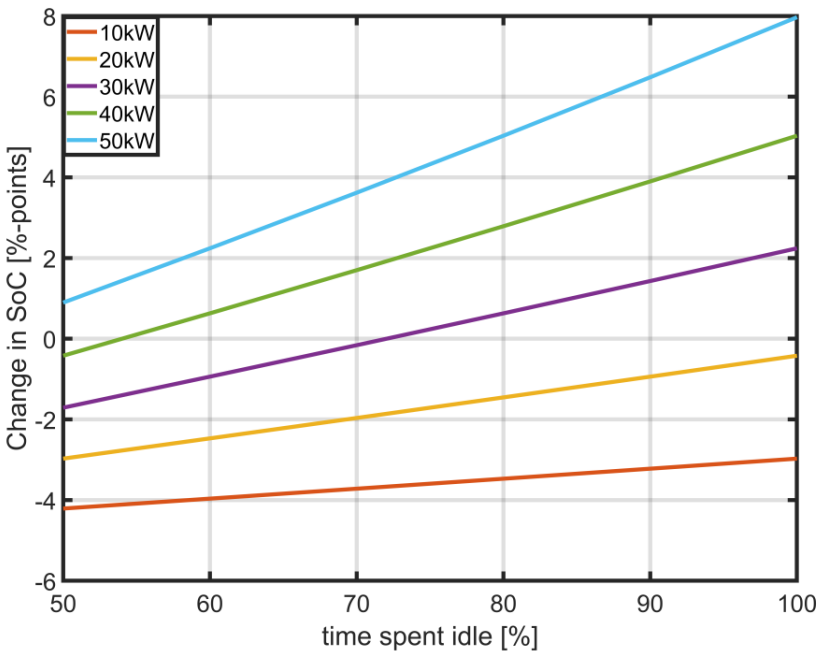

Figure 4-21 Effect of varying shares of time on change in SoC over one UDDS cycle with stationary charging at different power levels

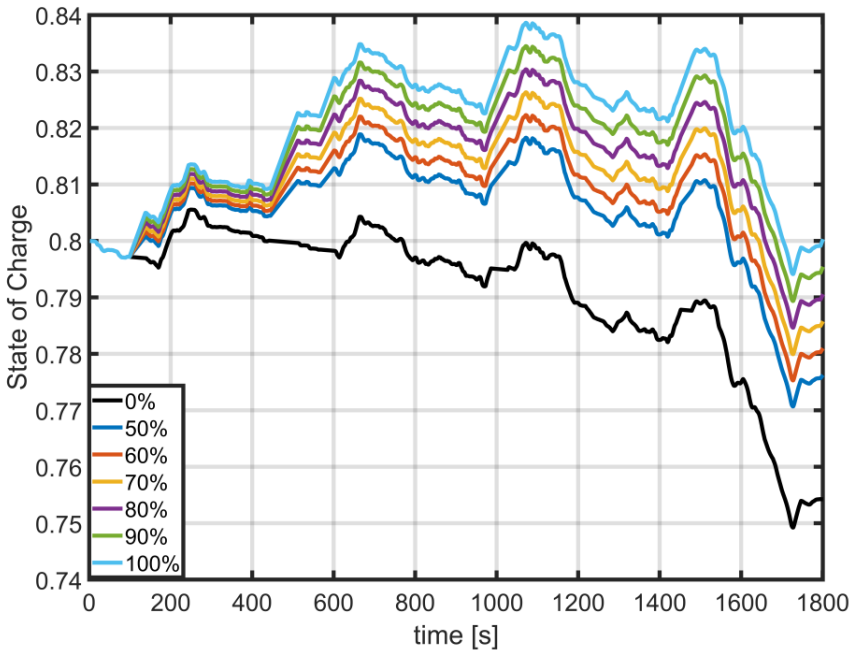

Figure 4-22 Effect of varying shares of time spent idle on SoC profile over one WLTC cycle for combined charging at 20 kW stationary and 20 kW at 30% coverage dynamic charging

4.6.2 Regenerative braking

One additional advantage of EVs is the re-utilization of energy conventionally wasted in ICE-vehicles, by implementing regenerative braking. In this chapter, the effect of regenerative braking on the achievable range is explored. During regenerative braking, the kinetic energy of the vehicle slowing down is converted to electrical energy that charges the on-board battery. Using the given vehicle and an assumed drive train efficiency of 80%, the theoretical maximum of the regenerative braking efficiency is 64%.

Regenerative braking is independent of the charging technology used. Therefore, the suitability for each driving cycle is shown in Figure 4-23. It extends the achievable range even at low efficiencies. The range increases linearly for a HWFET cycle. For UDDS and WLTC, the range increases in a non-linear manner. The improvement in range is highly dependent on the driving style and the route driven. Amongst the chosen scenarios, it is most effective for the WLTC cycle, due to the high deceleration rates and large number of stops. On the other hand, the impact for the HWFET cycle is only minor due to the high average velocity and low deceleration rates. Nevertheless, it enhances the achievable range and offers an additional benefit over conventional ICE vehicles.

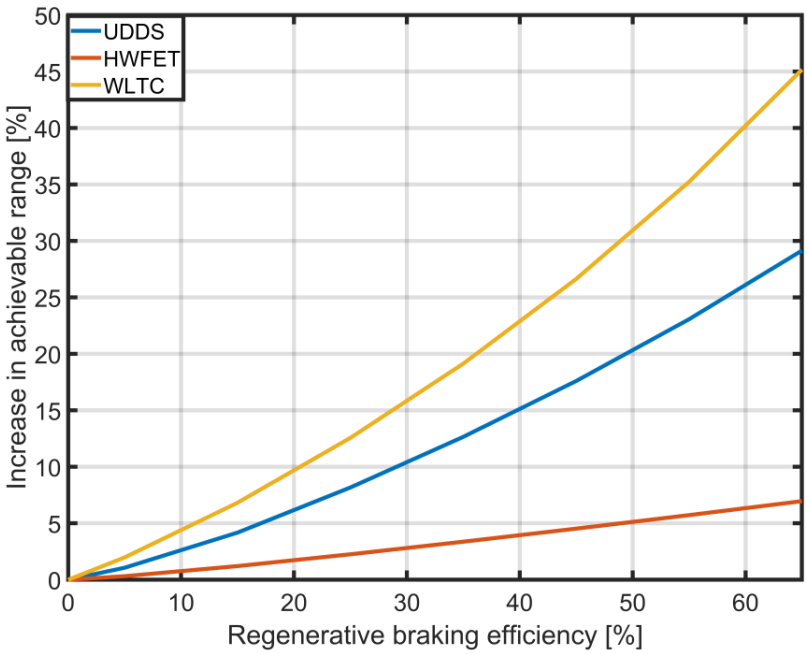

Figure 4-23 Effect of regenerative braking on achievable range at different driving cycles

4.6.3 Temperature

Battery performance and auxiliary power usage are highly dependent on the ambient temperature. At high temperatures, air conditioning and ventilation are used in vehicles to cool the cabin temperature to a pleasant level. While heating is used at low ambient temperatures. In both cases, the battery must supply power for auxiliary systems. Furthermore, conventional battery systems are designed to operate at temperatures between -10°C to 45°C [358]. At lower temperatures, the internal resistance increases while the available capacity decreases. Increasing the temperature reduces the internal resistance, however, the capacity is limited to rated capacity. Contrary to the capacity, the possible power output increases with temperature due to increased reactivity on the battery nodes. Both cases significantly reduce the battery life. In the presented scenarios, the temperature is varied between -20°C and 40°C to account for a wide range of common ambient temperatures.

Figure 4-24 shows the effect of temperature on the change in SoC over one UDDS cycle for different SWPT charging power levels. The effect of lower temperatures on the change in SoC is greater than at higher temperatures. Low temperatures e.g. - 20°C increase the change in SoC as the available capacity is reduced while a higher amount of energy is drawn from the battery due

to heating. The auxiliary power demand is up to three times higher than at 20°C. This behaviour is shown in a more pronounced negative change in SoC compared to the positive change at higher power levels. To achieve ±0% after one cycle, the required SWPT power level at low temperatures is with 30 kW higher than 20 kW at 20°C.

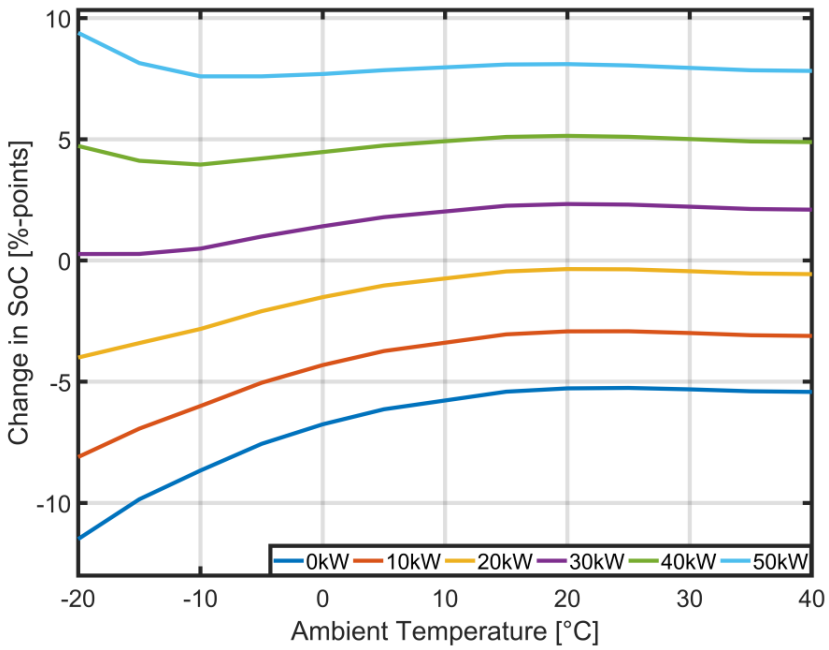

Figure 4-24 Effect of varying ambient temperatures on change in SoC over one UDDS cycle with stationary charging at different power levels

In contrast, at higher temperatures above 20°C, the increase in auxiliary power demand due to cooling and ventilation is only minor. Additionally, the available capacity is not negatively affected by the temperature and the rated capacity is fully available. At 20°C, the change in SoC has a maximum as the auxiliary power demand is at its lowest. However, at a charging power level of 50 kW, the maximum is located at lower temperatures as more energy is transferred to the battery then removed, overcoming the effect of the maximum in auxiliary power demand. Furthermore, the share of energy added is higher as the available capacity at lower temperatures is reduced.

Figure 4-25 illustrates the change in minimum charging power level to achieve unlimited range through stationary charging over one UDDS cycle with respect to transfer efficiency and temperature. In general, the minimum power level decreases linearly with increasing transfer

efficiency. The required charging power can be reduced by approximately 1 kW for every 4%-points increase in transfer efficiency, independently of ambient temperature. At higher efficiencies, the energy is transferred more effectively resulting in a lower minimum charging power. As the temperature decreases, the auxiliary power consumption increases and therefore a higher charging power level is required to negate the additional demand. Similar observations can be made at higher temperatures. However, the energy demand increases more rapidly at lower temperatures.

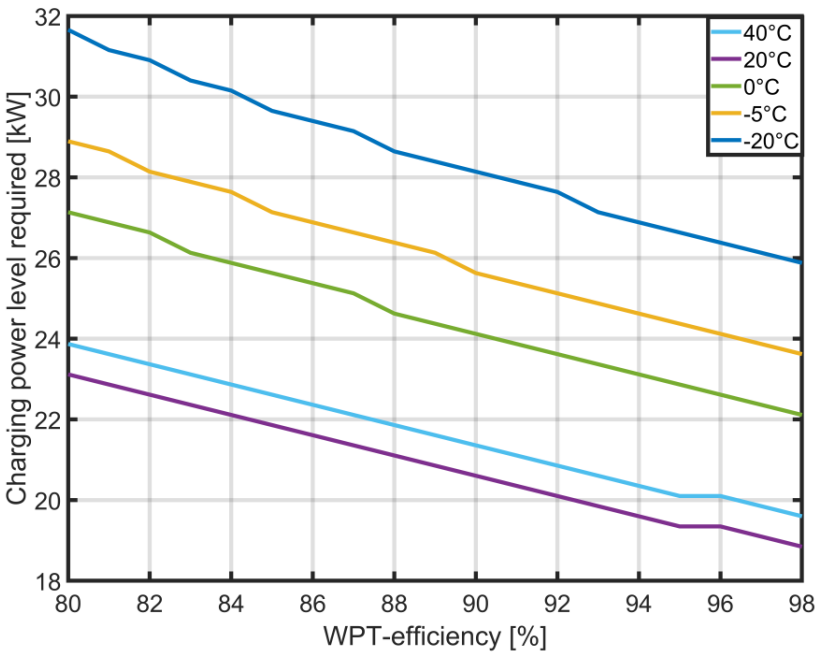

Figure 4-25 Minimum stationary charging power level required for unlimited range at different temperatures and transfer efficiencies in UDDS cycle

The effect of temperature for DWPT charging is presented in Figure 4-26. Overall, the change in SoC for DWPT shows similar trends as in SWPT charging. The change is more pronounced at lower temperatures than at higher temperatures, with a shallow maximum at 20°C because of reduced available capacity and higher auxiliary power consumption. For a road coverage of 10%, the change in SoC increases with rising temperatures independently from charging power level. A combination of medium charging power levels and road coverages of 30% or 50% cause widely constant changes in SoC. Higher power levels paired with 50% coverage result in decreasing change in SoC with rising temperature. This is due to a combination of low available battery capacity and high auxiliary power consumption at low temperatures. High power levels and

coverages result in the transmission of larger quantities of energy over one cycle, which create bigger changes in SoC. As the temperature increases, the available capacity increases and the auxiliary power decreases causing a relative decrease in change of SoC.

A change in SoC of ±0% can either be achieved by a higher power level or by increasing the road coverage. The ability of coverage to offset the change in SoC increases at higher power levels, however, the effect of power level is larger for smaller coverages e.g. 10% of 50 kW achieves better results than 10 kW at 50% and 20 kW at 30%.

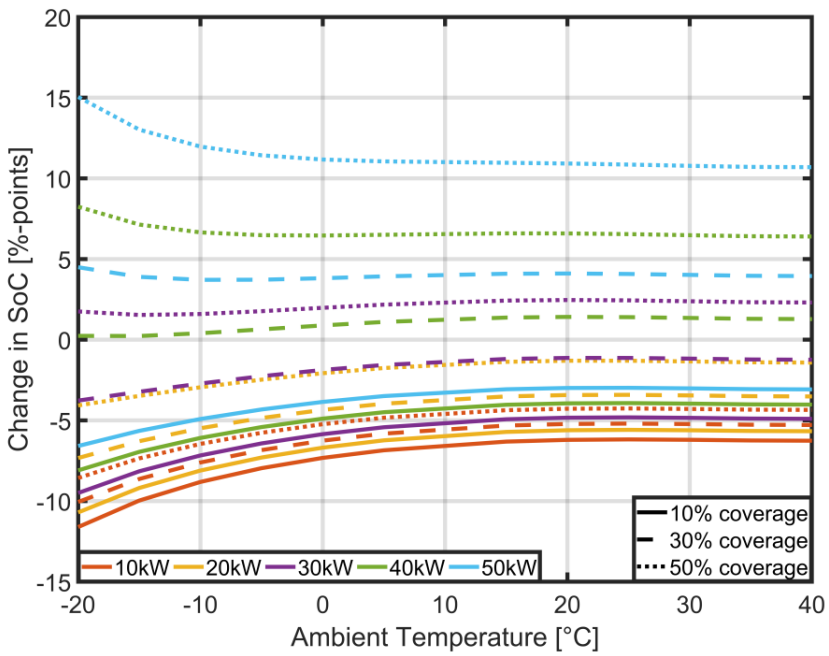

Figure 4-26 Effect of varying ambient temperatures on change in SoC over one HWFET cycle with dynamic charging at different power levels and coverages

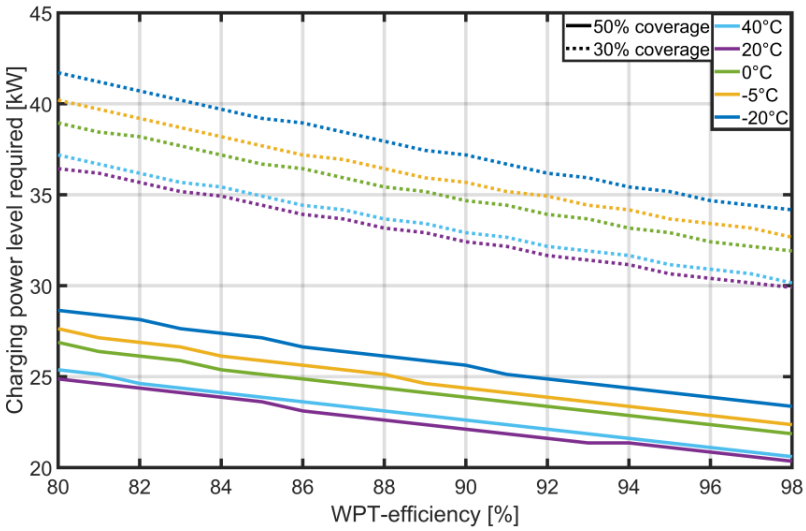

Figure 4-27 Minimum dynamic charging power level at 30% and 50% coverage for unlimited range at different temperatures and transfer efficiencies in HWFET cycle

The minimum charging power level to achieve unlimited range within the HWFET cycle depending on the transfer efficiency and temperature is depicted in Figure 4-27. As previously shown, it is not possible to realize unlimited range with 10% road coverage. However, it is achievable at higher road coverage e.g. 30% and 50%. The impact of a higher transfer efficiency is more pronounced at 30% coverage. On average, the charging level can be reduced by 1 kW for every 2.5%-points increase in transmission efficiency. At 50% coverage, the trade-off is slightly higher with 1 kW every 3-4%-points.

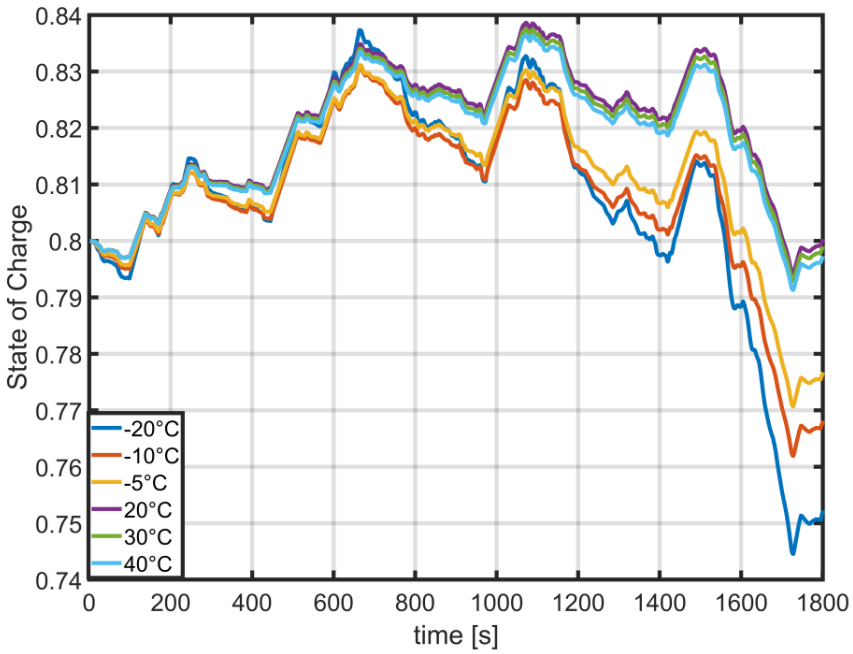

Figure 4-28 Effect of varying ambient temperatures on SoC profile over one WLTC cycle for combined charging at 20 kW stationary and 20 kW at 30% coverage dynamic charging

Figure 4-28 displays the SoC profile for the combined charging scenario of 20 kW stationary and 20 kW at 30% coverage dynamic charging at the WLTC cycle. The change in SoC reaches its maximum at 20°C and achieves unlimited range. At temperatures above 20°C, the SoC profile shows only minor differences to the maximum. This is attributable to the slight increase in additional HVAC power consumption. Temperatures below 0°C seriously affect battery performance while increasing the auxiliary power consumption. Consequently, the SoC at the end of the cycle is much lower than at higher temperatures. This results in a shorter achievable range. The range is extended in comparison to no charging at lower temperatures.

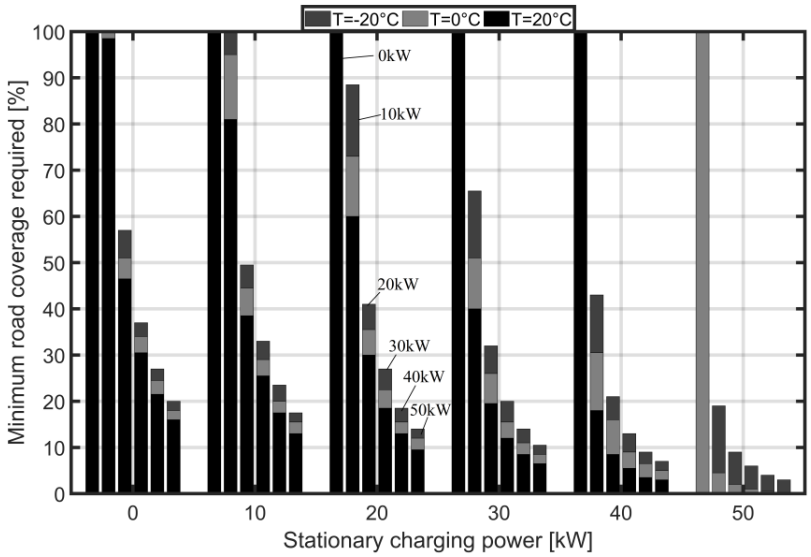

Figure 4-29 Minimum road coverages for various stationary and dynamic charging power levels (0-50 kW) illustrated as blocks and columns respectively at temperatures of -20°C, 0°C and 20°C in WLTC cycle

Figure 4-29 portrays the minimum road coverage required to achieve unlimited range within the WLTC cycle for a wide range of stationary and dynamic power levels depending on the temperature. Dynamic power levels of 0-50 kW are illustrated by columns from left to right. As indicated with the black leftmost bars of each column, it is not possible to achieve unlimited range with stationary charging alone (implied by a road coverage of 100%), except at 20°C and a power level of 50 kW. At other temperatures, the auxiliary power demand as well as the change in available capacity cannot be offset by lower charging power levels.

On the contrary, it is possible to achieve unlimited range with DWPT alone at very high coverages or medium coverages and power levels. The required coverage is also the lowest at 20°C, followed by 0°C, and the highest at -20°C. This is due to the additional energy consumption of the HVAC system, which can lead to negating the positive effect of higher charging power levels. In general, with increasing dynamic power level, the required road coverage decreases. An initial increase of dynamic charging power from 10 kW to 20 kW has the greatest influence on the coverage required and additional power level increases have diminishing returns as the coverage approaches a minimum. Similarly, coverage required reduces with increasing stationary power levels in a linear manner. However, due to the limited number of stops, the effect of dynamic charging power level on the required road coverage is bigger than that of the stationary charging power. In addition, the main energy consumption occurs in the second half of the cycle i.e. the highway part. As shown,

the ambient temperature has a direct impact on the system performance as it affects the available battery capacity but also increases additional power consumption due to HVAC operation.

4.6.4 Cycle life

The final parameter considered is the age or cycle life of the battery system. Over time the reactivity of the solutions used in batteries as well as the anode and cathode materials degrade. In addition, the amount of charging and discharging cycles influences the available capacity. Conventionally, a battery has reached its end of life when the available capacity reaches 80% of the initial rated capacity. Taking two journeys a day, simulated by the driving cycles without recharging until the SoC reaches 20%, the battery system goes through one cycle every five days for UDDS, every three days for HWFET, and every two days for WLTC, respectively. Assuming that the battery can cycle through 1000 discharging-charging cycles before reaching its end of life, the expected lifetime would be 13.7 years for UDDS, 8.2 years for HWFET and 5.5 years for WLTC, respectively.

The effect of the cycle life for SWPT charging for one UDDS cycle is shown in Figure 4-30. Up to 200 cycles, the change in SoC stays constant, independently of the charging power level. The change in SoC increases with increasing age of the battery as the available capacity decreases, amplifying the ratio of added and removed charge. Charging power levels below 20 kW are not enough to compensate for the reduction in available capacity, while power levels above 20 kW can lead to higher added charge.

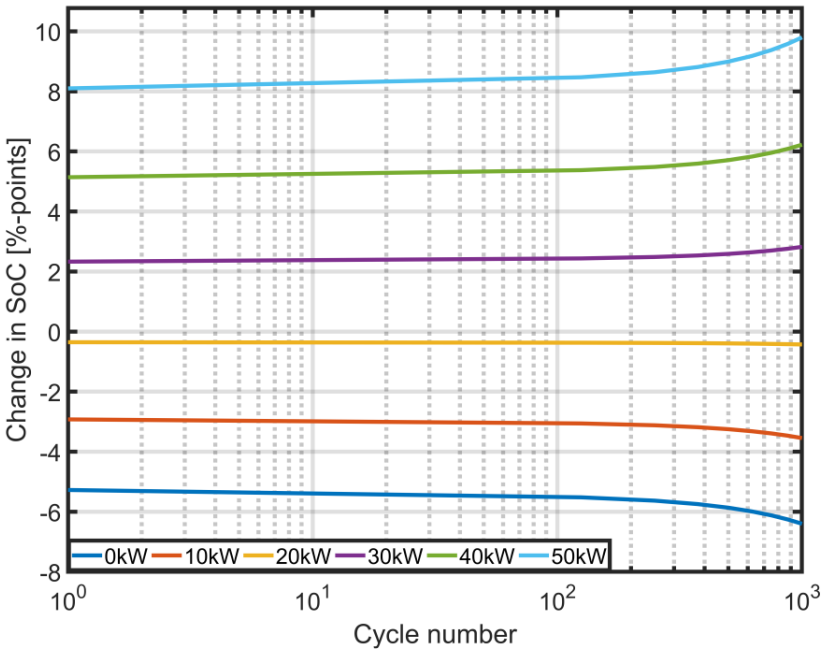

Figure 4-30 Effect of varying cycle numbers on change in SoC over one UDDS cycle with stationary charging at different power levels

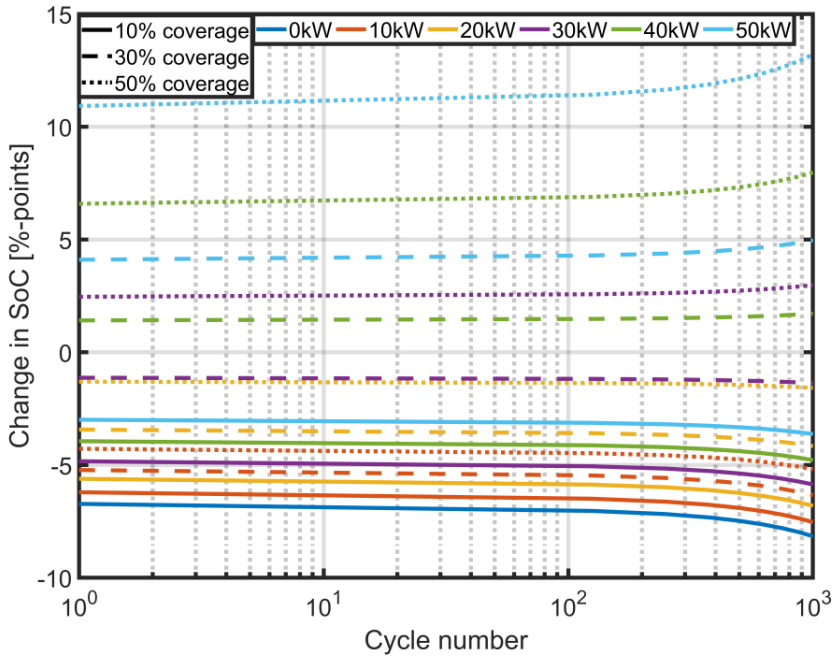

Figure 4-31 Effect of varying cycle numbers on change in SoC over one HWFET cycle with dynamic charging at different power levels and coverages

For DWPT charging during a HWFET cycle, depicted in Figure 4-31, a similar trend is shown. The benefit of WPT, especially DWPT is even greater for aged batteries as the available capacity is further reduced by the cycle life. There are combinations of charging power level and coverage that are sufficient to offset the negative effects of aging batteries.

The initially used combination of 20 kW SWPT combined with 20 kW at 30% coverage DWPT charging shows no change in SoC profile over the investigated selection of cycle numbers. Therefore, Figure 4-32 illustrates the SoC profile for 50 kW SWPT in tandem with 20 kW at 30% coverage DWPT charging. The change in SoC increases with increasing age of the battery system. In summary, wireless charging cannot only increase battery life, as it reduces the number of deep discharge cycles but also help assuaging the negative effects of aging batteries.

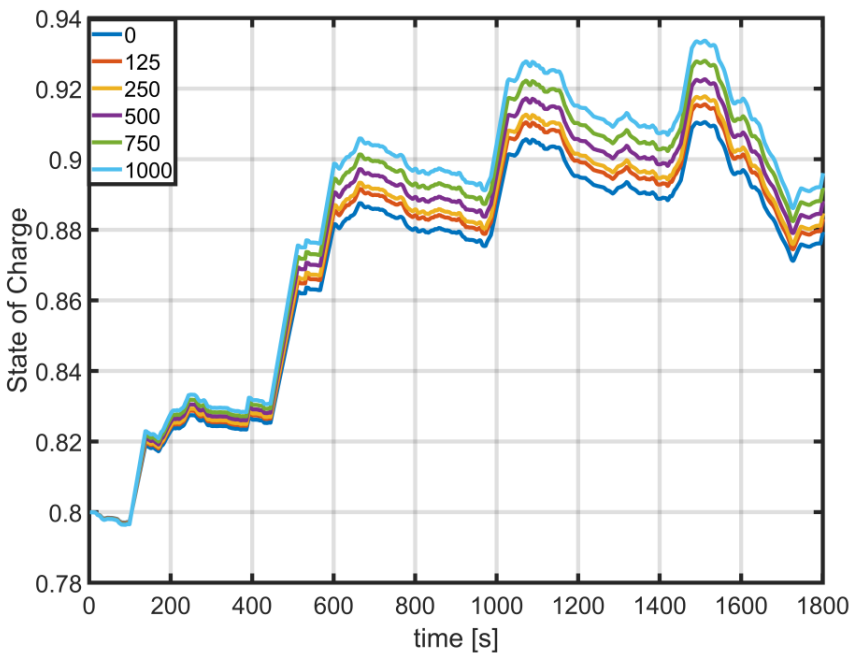

Figure 4-32 Effect of varying cycle numbers on SoC profile over one WLTC cycle for combined charging at 50 kW stationary and 20 kW at 30% coverage dynamic charging

4.7 Human exposure

One of the main concerns about WPT technology applied to recharge EVs is due to the electromagnetic field (EMF) emission in the environment. This emitted field must be compliant with EMF safety standards regarding the human exposure [263] [339]. While the SWPT has been largely investigated [359] [360] fewer studies are available for the DWPT systems. The SAE

J2954 provides specifications for power levels up to 11 kW even though today's EV power transfer systems can reach up to 50 kW. This is a quite high power level considering the 85 kHz standardized frequency and therefore the magnetic field cannot be neglected around the vehicle. Checking the compliance with guidelines, recommendations or legislation, will become mandatory. Thus, in order to avoid any compliance issues and minimize the exposure to humans a good trade-off between charging efficiency and EMF safety concerns should be found. The proposed medium power (20-30 kW) SWPT combined with an intermediate power (20-30 kW) DWPT system is found to be the best solution also on this aspect.

4.8 Conclusions

In this chapter, the driving range of electric vehicles charged by static, quasi-dynamic, dynamic or combined WPT systems has been investigated. To this aim, an easy to implement extended battery model was coupled with a force-based vehicle model to study the impact of WPT charging on the onboard battery system of an EV. Three different driving cycles, i.e. urban (UDDS), highway (HWFET) and combined (WLTC), were used to simulate wireless charging in different environments. Moreover, a multitude of external and internal factors, such as the ambient temperature and the age of the battery system were for the first time taken into account to evaluate the impact of WPT technology on the battery SoC.

The analysis of the obtained results has shown that a deviation from the rated temperature of the battery system has a high impact on the change in SoC due to the reduction in available capacity and change in auxiliary power demand. It has been observed that lower temperatures have a stronger impact compared to higher temperatures. With regards to the second aspect, it has been outlined as the WPT effectiveness increases with the battery age due to the limited driving range and amplified ratio of added and removed charge.

When combining the above-mentioned battery parameters together with the several driving cycles the following conclusions can be drawn. WPT technology will definitely alleviate the range anxiety issue by extending the achievable range significantly or even achieving unlimited range. While SWPT is best employed on busy roads, DWPT should be used on highways. However, when combining both systems, the size and power level can be reduced significantly. This benefits the overall system as a higher power level requires a careful design to limit the EMF emission and reduce its impact on passengers and bystanders. By reducing the SWPT power to a medium level (20-30 kW) in combination with DWPT we can achieve unlimited range and alleviate health and

safety concerns regarding EMF emissions. This result is of outmost importance for policy makers since the deployment of WPT systems are still under investigations. It is also worth mentioning that the results hereto shown are specific to the considered scenarios. However, the proposed models can be extended in the future to find optimal system parameters for given routes and driving cycles.

5 WPT experiments with HTS coils

5.1 Introduction

The first standard addressing WPT for EVs, SAE J2954 was published in 2016 and outlined the operating frequency of wireless charging systems to be between 81.39 and 90 kHz with a nominal operating frequency of 85 kHz [302]. Recent literature on superconducting wireless power transfer systems focusses on low input power and operating frequencies in the range of several kHz to tens of kHz [195], [198], [361], [190], 370 kHz [206], [208], [335] or 13.56 MHz [197], [362]. Many of the above-mentioned studies rely on analytical equations for HTS tapes to estimate the AC loss of HTS coils and miss the opportunity to combine AC loss modelling for HTS coils with experimental measurements. Furthermore, the applied equations are not applicable in the high frequency regime, up to 85 kHz, used in WPT [4], [8], which leads to incomplete comparisons. Therefore, this chapter combines finite element analysis (FEA) simulations with a circuit model to simulate the system performance of (HTS) WPT-systems. Obtained results are compared with experimental results. Conventionally used copper coils are compared with HTS coils as well as hybrid systems, using HTS and copper coils within the same transfer system are researched. Additionally, the performance of cooled copper coils at 77K is shown. A frequency range of 11-85 kHz, commonly used for wireless charging, was chosen for the comparison.

Section 5.2 presents the 2D axisymmetric multilayer model used to investigate the AC losses and equivalent resistance of HTS coils for WPT. The experimental set up is introduced in section 5.3 and results are discussed in chapter 5.4.

5.2 Simulations

In the following chapter a combination of FEA-simulations and a circuit model in Simulink is used to evaluate the performance of HTS coils in a WPT-system following the process outlined in Figure 5-1. The input currents of the experiments are used as input for the FEA simulations. In the first step, the magnetic fields produced by the coils, carrying their respective current, is modelled. Together with the currents obtained from the experiments, the magnetic fields are used as input parameters for the AC loss model to obtain the equivalent resistance of the HTS coils. Subsequently, the system efficiency is calculated using a circuit model. The FEA-model used here is introduced in-depth in chapter 6.

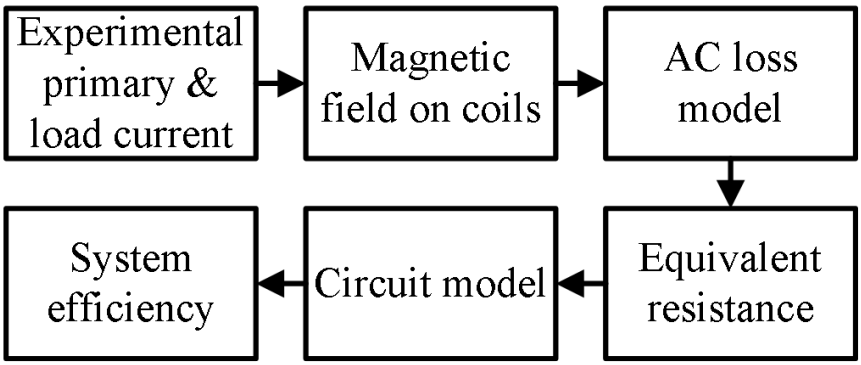

Figure 5-1 Simulation flowchart

5.2.1 ***H***-formulation

To evaluate the AC losses and the equivalent resistance of the HTS coils, when carrying an AC current while located within a varying external magnetic field, the 2D axisymmetric multilayer model presented in chapter 6.2 has been used. Furthermore, the tape parameters outlined in Table 6-1 are used. Each layer of the HTS tape is modelled as an individual domain. After calculating the total AC loss, the equivalent resistance can be obtained from Eq. 5.1 with the magnitude of the transport current *I*.

$$R_{\mathrm{eq}} = \frac{Q_{\mathrm{total}}}{I^2} \tag{5.1}$$

5.2.2 Circuit analysis

The results obtained from the FEA model are used as inputs for the circuit model laid out in Figure 5-2. It shows a circuit diagram of an SS compensation which is used in the experiments. L_1 and L_2 are the primary and secondary coils, R_1 and R_2 are the coil resistances, while C_1 and C_2 are the primary and secondary compensation capacitors, respectively. R_{L} is the load resistance. Using Kirchhoff's Law, the loop-currents i.e. the primary and load current, I_1 and I_{L}, for the circuit can be resolved using Eq. 3.1.

The equivalent total impedance of the circuit, Z_{tot}, within an SS-compensated circuit is the sum of primary circuit impedance Z_1 and secondary reflected impedance Z_{r} derived in Eq. 3.2. The secondary reflected impedance is the ratio of reflected voltage and primary current. The current that supplies the load is shown in Eq. 3.4. Input power and output power are calculated using Eq. 3.5-3.6. It is assumed that power is supplied with unity power factor into the primary compensation network. At zero-phase-angle frequency, the reactive power flow is zero. To form a resonance circuit with maximum power transfer capability, this frequency must be equal to the resonance

frequency ω_0, where the reactive parts in Eq. 3.1-3.7 cancel out. With the aid of the input and output power, the efficiency at resonance frequency can be expressed by Eq. 3.9 with the quality factors Q for each coil in Eq. 3.10. It can be seen that a high quality factor is advantageous for system efficiency. Assuming identical coils in the primary and secondary circuit, the resonance frequency can be calculated using Eq. 3.8. For the simulation it was assumed that the parasitic resistances of wires, connectors and capacitors are negligible. However, it should be noted that for future research these resistances should be considered as the equivalent resistance of the HTS coils is very small and therefore such parasitic resistances must be considered to improve applicability and accuracy of the models.

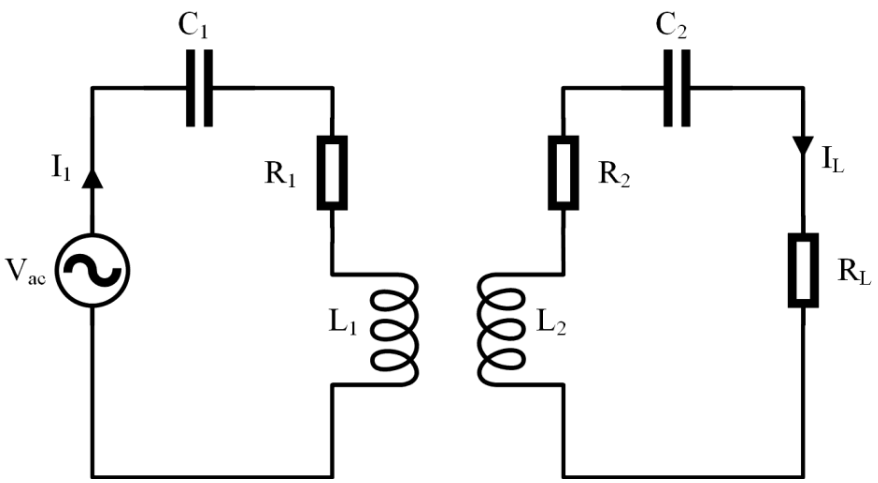

Figure 5-2 SS compensation topology for primary and secondary resonance circuit.

Table 5-1 Coil parameters

Parameter	HTS coils	Copper coils
Tape width [mm]/ Litz wire	4	0.1x200
Turn number	8	8
Inductance [µH]	18.5	15.6
Winding type	Double pancake	Solenoid
Coil diameter [m]	0.125	0.125
Inductance [µH]	18.5	15.6
Load [Ω]	0.4	0.4

5.3 Experimental set-up

The system outlined in Figure 5-2 comprises two coils made from either copper Litz wire (0.1×200) or HTS tape. Litz wire is conventionally used in WPT systems due to their reduced AC loss characteristics at elevated frequencies. Both types of coils are depicted in Figure 5-3 and key parameters are summarised in Table 5-1. While the copper coils are wound as an eight-turn solenoid, the HTS coils are wound as double pancake coils with two layers of four turns each, totalling eight turns. Therefore, both systems use the same turn numbers and system components All coils are wound on glass-fibre reinforced plastic (GRP) formers and have a diameter of 0.125 m. Kapton tape was used as insulation on the HTS coils and each turn was insulated separately.

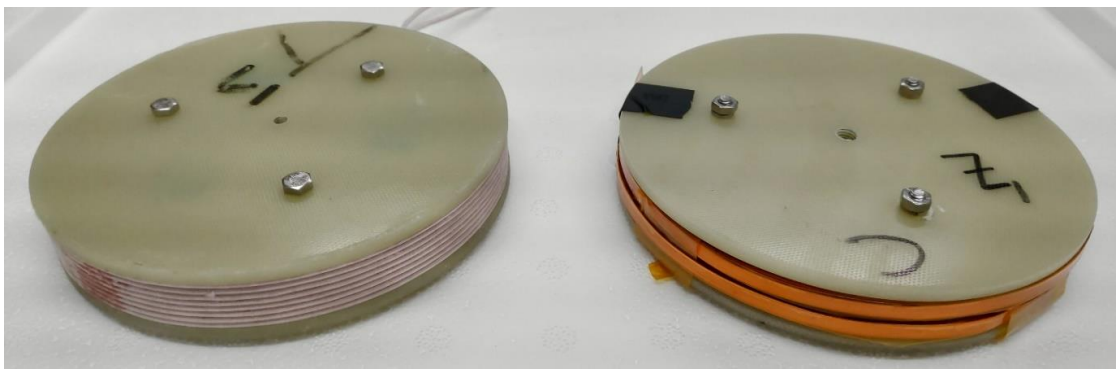

Figure 5-3 Copper Litz wire solenoid (left) and HTS tape double pancake coil (right)

The self-inductance $L_{1/2}$ and mutual inductance M between the primary and secondary coil was measured using the Impedance/Gain-Phase Analyser ZGA5905. Both, open secondary inductance L_o and short secondary inductance L_s were measured and the coupling coefficient k was calculated by the analyser as Eq. 5.2 and converted to the mutual inductance in Eq. 5.3.

$$k = \sqrt{1 - \frac{L_s}{L_o}} \tag{5.2}$$

$$M = k\sqrt{L_1 L_2} \tag{5.3}$$

In addition, the mutual inductance was calculated using the FEA model and it is rapidly decreasing with increasing air gap length and the trend is illustrated in Figure 5-4. It largely depends on the air gap between the coils and the results for double pancake and solenoid are similar. In the FEA model, the individual coil turns where approximated by a lumped coil cross-section.

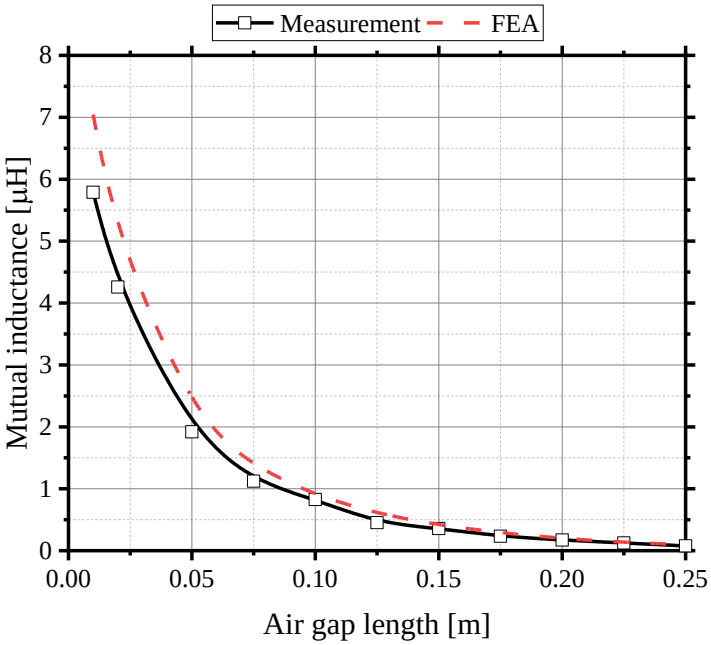

Figure 5-4 Mutual inductance between primary and secondary coil vs air gap length

Furthermore, resistance R and quality factor Q of the copper coils were measured using the Impedance Analyser and the FEA model was used to calculate the equivalent resistance R_{eq} and the quality factor Q of the HTS coils. The copper coils were not only measured at a room temperature of 300K but also at the boiling point of liquid nitrogen (LN_2) at 77K, the same operating temperature of the HTS coils. All results are displayed in Figure 5-5 and Figure 5-6.

As shown, the HTS coils have the lowest resistance and therefore highest quality factor. Particularly, at the lowest frequency investigated of 11 kHz. In comparison to the copper coils measured at room temperature, which exhibit the highest resistance, the cooled copper coils have a much lower resistance as the temperature-dependent resistivity is decreased. Nevertheless, not as low as the HTS coils. All coils experience increased resistances as the frequency increases due to the skin effect. The effect of frequency is the greatest for the HTS coils, which is approaching the copper coils rapidly.

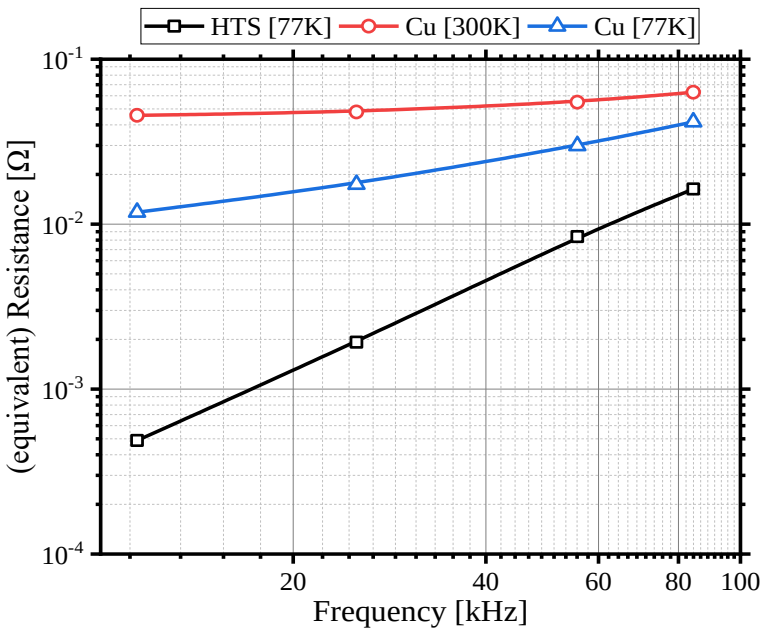

Figure 5-5 Resistance and equivalent resistance of copper coils at room temperature, copper coils at 77K and HTS coils

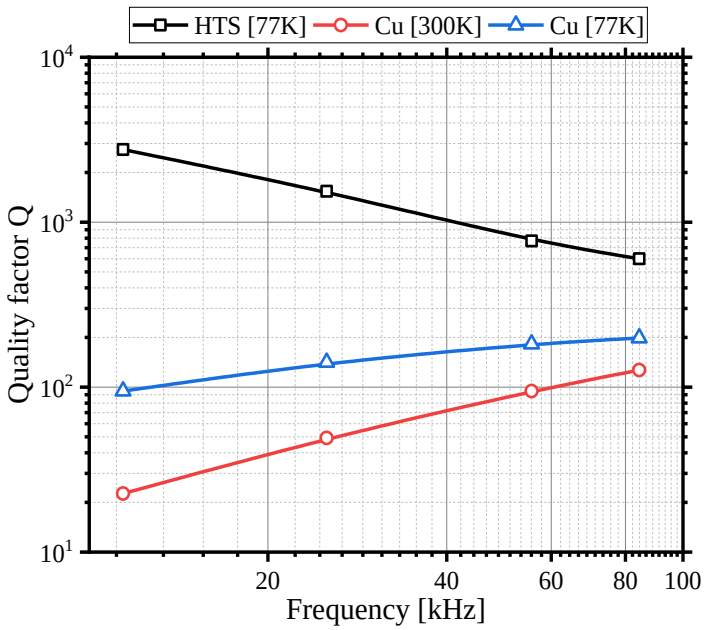

Figure 5-6 Quality factor of copper coils at room temperature, copper coils at 77K and HTS coils

Figure 5-7 shows the experimental setup used to measure the transfer efficiency of the WPT-system. A high-frequency power supply controlled via a PC supplied the system with a square voltage waveform. The capacitor banks were connected in series with the Tx and Rx coils and comprised several high-frequency, high-voltage capacitors with capacitances between 0.01 µF to 2 µF (±5%), joint by copper plates. Depending on the coils and the frequency investigated, different arrangements of capacitors were made to achieve the desired resonance frequency according to Eq. 3.8. The phase angle of the resonance circuit was measured before the experiments to ensure resonance, as depicted in Figure 5-8 a resonance frequency of 85 kHz was achieved. Two light bulbs, each with a resistance of 0.2 Ω, were used as load. All measurements regarding voltages, current and powers were conducted using the YOKOGAWA PX8000 Power Analyser. Experiments were conducted on a small scale WPT system and the input power was approximately 10 W.

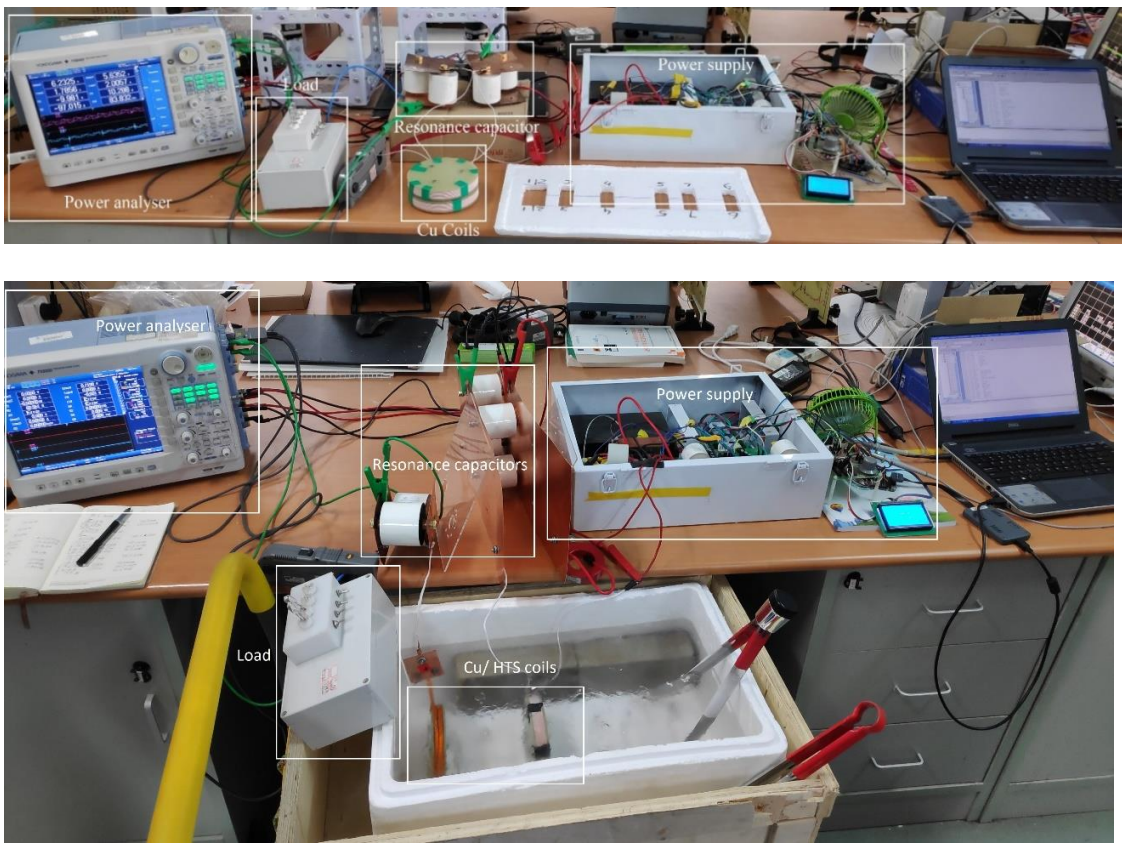

Figure 5-7 Experimental setup with a power supply, resonance capacitors, copper and HTS coils, resistive load and a power analyser. Setup for copper coils at room temperature at the top and cooled copper and HTS coils at the bottom

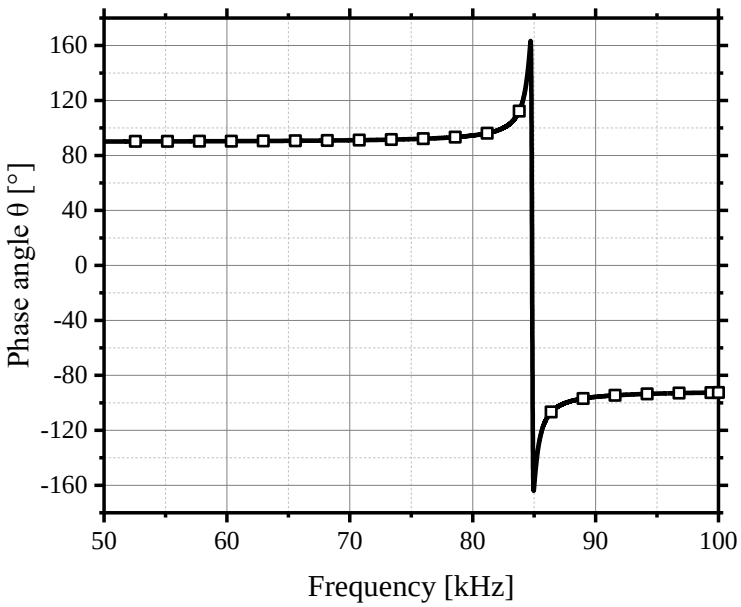

Figure 5-8 Phase angle of the copper resonance circuit at a resonance frequency of 85 kHz

Figure 5-9 illustrates the different combinations of coils that were measured. In total five different cases were investigated, including a) Cu-Cu coils at room temperature, b) Cu-Cu in LN_2, c) HTS-HTS, d) HTS-Cu in LN_2 and e) Cu-HTS in LN_2. Measurements that included the use of LN_2 were conducted in a Styrofoam cooling vessel. Additional copper plates were used to achieve solder-free connections between the HTS coils and other circuit components.

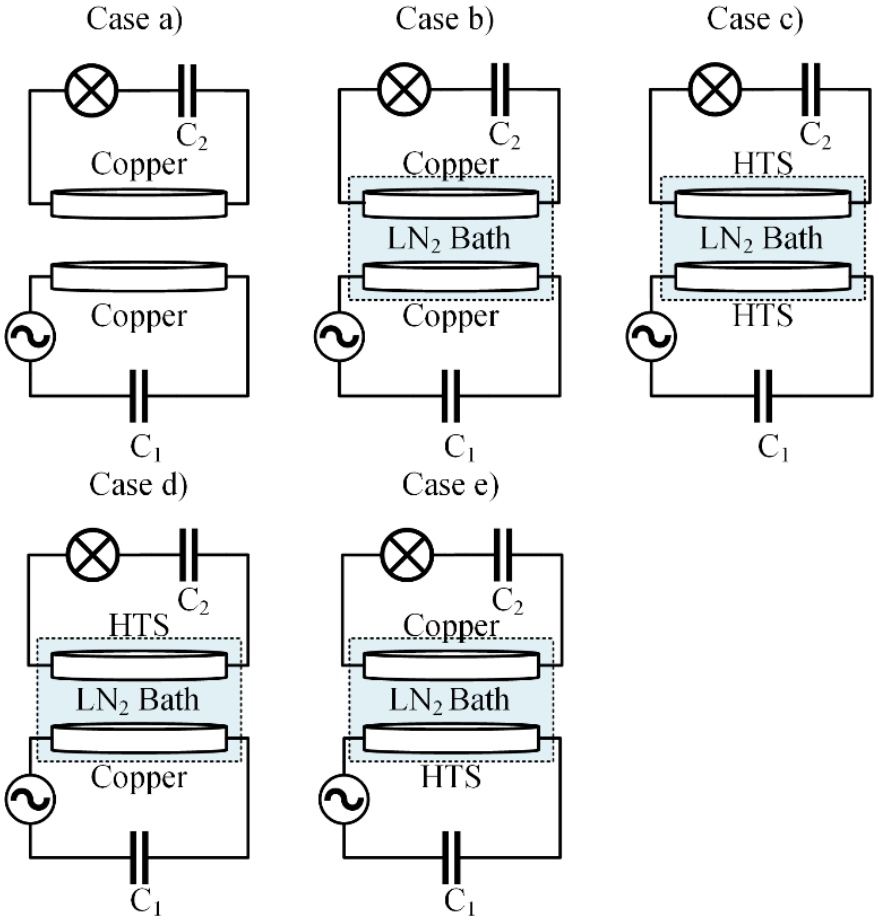

Figure 5-9 Coil arrangements for different cases investigated including case a) Cu-Cu coils at room temperature, b) Cu-Cu in LN2, c) HTS-HTS, d) Cu-HTS in LN2 and e) HTS-Cu in LN2

5.4 Results and discussion

The transfer efficiencies for the different cases for frequencies of 11 kHz, 25 kHz, 55 kHz and 85 kHz are shown in Figure 5-10. It can be clearly seen that the transfer efficiency increases drastically with operating frequency as a higher voltage is induced in the receiving coil. An increase from 11 kHz to 25 kHz shows the highest increase in efficiency and a change from 55 kHz to 85 kHz the lowest. In addition, the transfer efficiency decreases rapidly and linearly (frequencies above 11 kHz) with air gap length e.g. from 97% at 1 cm to approximately 30% at 12.5 cm for 85 kHz in the HTS-HTS system. Particularly for 11 kHz and 25 kHz, the effect of the distance is more pronounced than for higher frequencies. Furthermore, at large air gaps of 7.5cm and larger, the Cu-Cu system exhibits an efficiency close to 0%.

Furthermore, Figure 5-10 shows a comparison of the different cases at the four frequencies investigated. Firstly, the transfer efficiency for the different cases increases with frequency. In addition, the shape becomes extremely linear as the frequency increases. At the lowest frequency of 11 kHz, the efficiency initially decreases linearly to about 7.5 cm, an equivalent of 60% of the coil diameter, before remaining generally constant with increasing air gap length. It can also be clearly seen that the Cu-Cu has the lowest efficiency at 11 kHz and 25 kHz due to the lower resistance and therefore higher quality factor of the HTS coils as well as the reduced resistivity of the Cu coils when submerged in LN_2. However, as the frequency increases, the difference between the achieved efficiencies becomes smaller and at a frequency of 55 kHz, copper coils achieve a similar efficiency as the HTS coils. Similar results were obtained for a frequency of 63 kHz [363]. This is caused by the rapidly increasing AC loss and therefore equivalent resistance of the HTS coils, which approaches the resistance of the copper coils. Furthermore, a comparison between single HTS coil systems, namely Cu-HTS and HTS-Cu was made. Given the experimental results, none of the two systems has a better transfer efficiency, which is in line with conflicting findings of other research [195], [196], [197]. Nevertheless, when comparing other advantages, the HTS-Cu system is favourable due to tighter space limitations on the VA compared to the GA. This is in line with literature as advantages of either system are discussed controversially [364], [365], [366]. However, as discussed earlier, the absence of an impedance matching system influences results obtained as primary and secondary systems become mismatched and there is a phase shift between waveforms, negatively affecting the results. It is necessary to underline, that even though HTS systems achieve similar transfer efficiencies as copper systems, the transferred power can be much higher, which is required for applications such as fast charging.

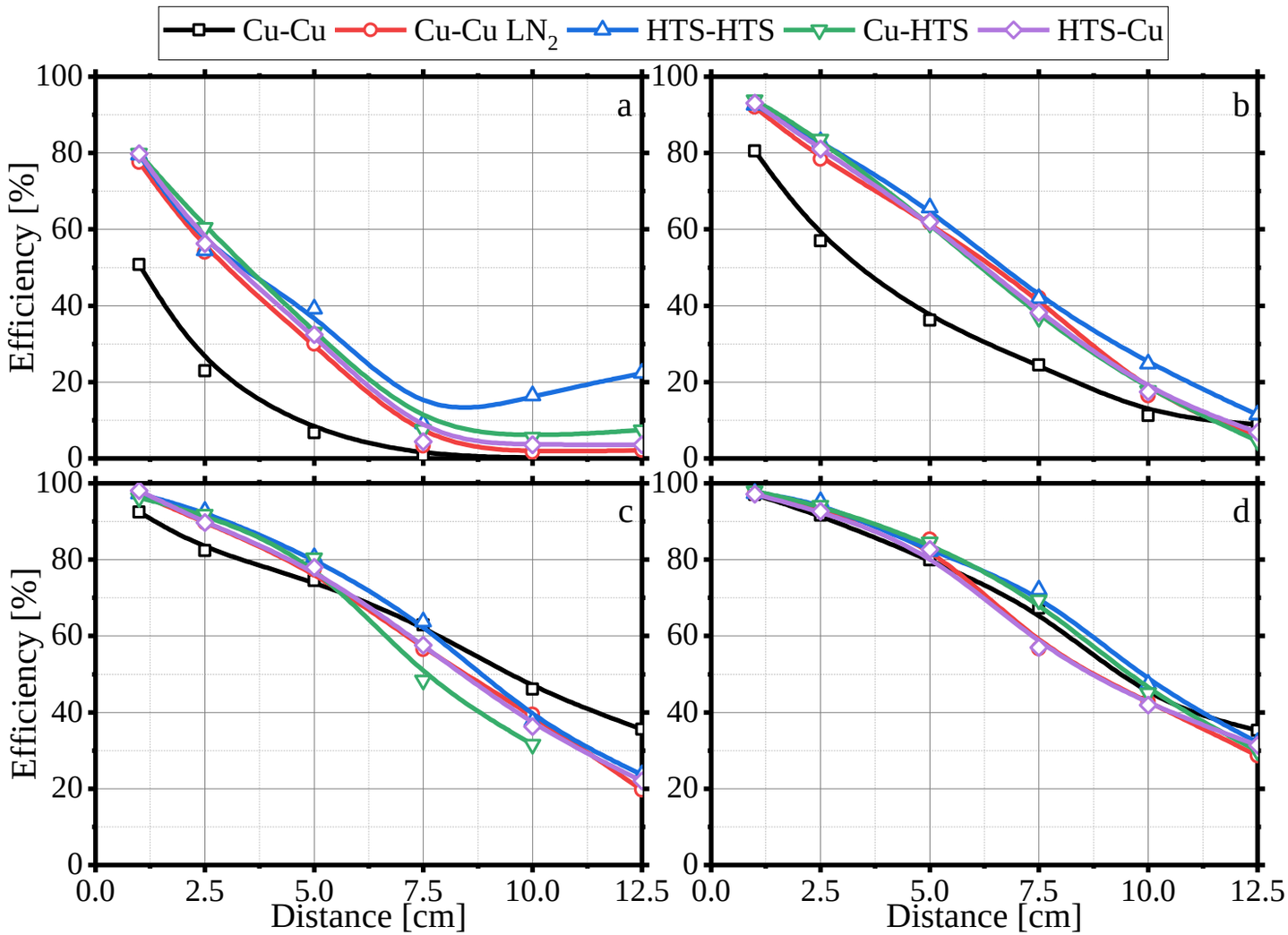

Figure 5-10 Transfer efficiency of various coil combinations for different operating frequencies a) 11 kHz, b) 25 kHz, c) 55 kHz and d) 85 kHz

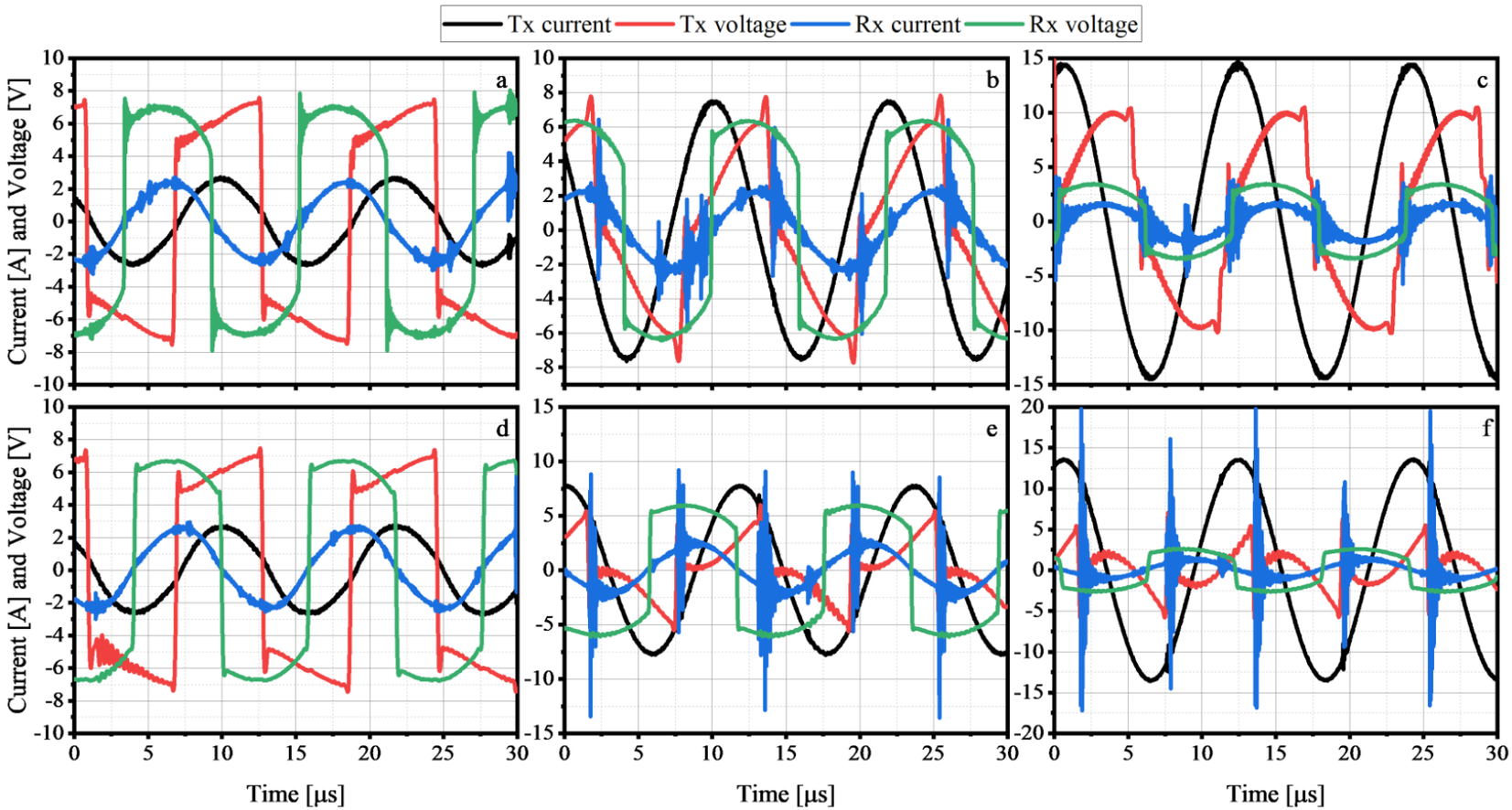

Figure 5-11 Current and voltage waveforms of Tx and Rx coils for HTS-HTS a)-c) and Cu-Cu d)-f) at 85 kHz and different air gap lengths of 0.01 m (left), 0.05 m (centre) and 0.125 cm (right)

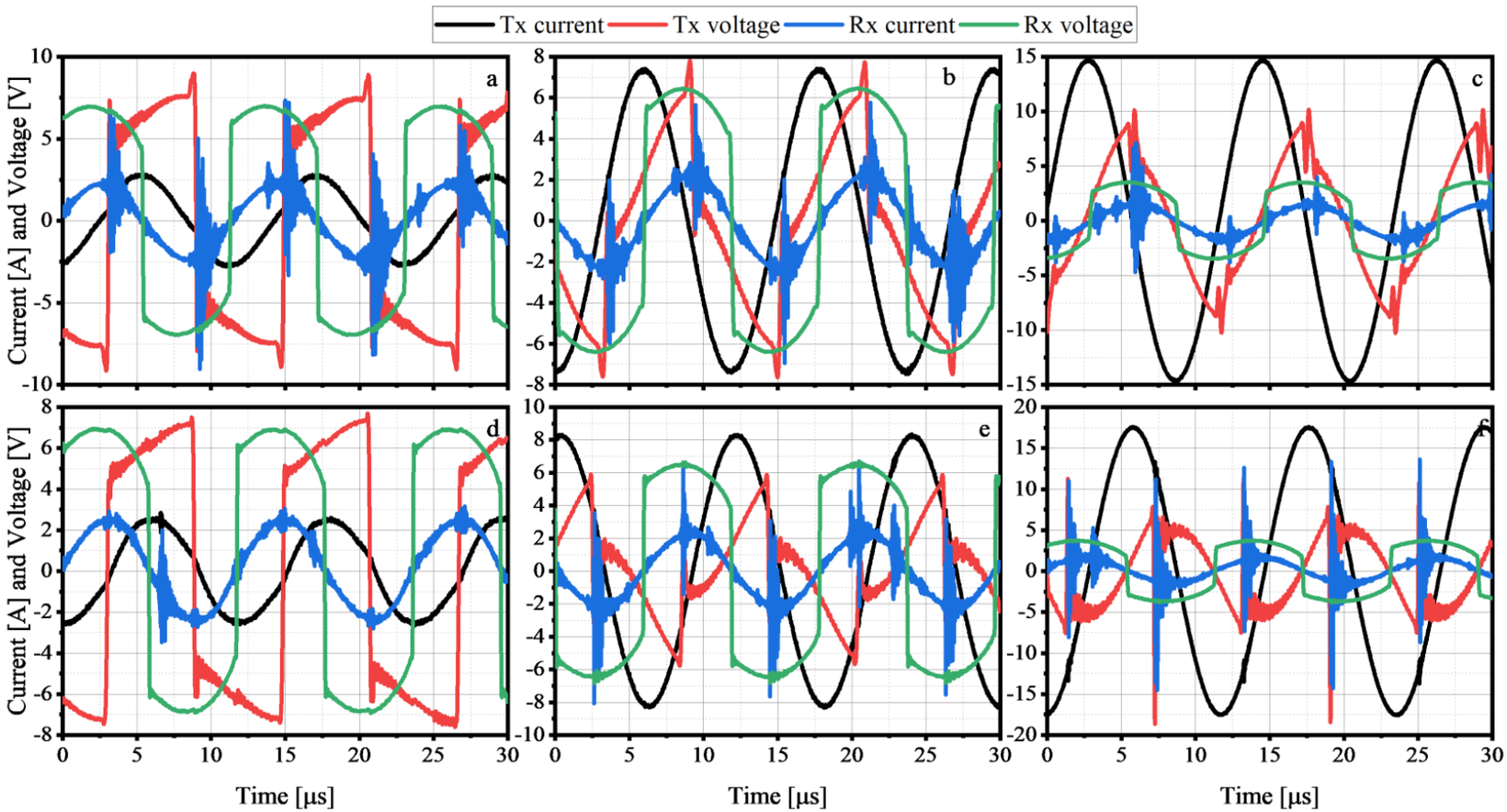

Figure 5-12 Current and voltage waveforms of Tx and Rx coils for HTS-Cu a)-c) and Cu-HTS d)-f) at 85 kHz and different air gap lengths of 0.01 m (left), 0.05 m (centre) and 0.125 m (right)

The current and voltage waveforms of transmitting and receiving coils for cases a) HTS-HTS and cases c) Cu-Cu at air gap lengths of 1 cm, 5 cm and 12.5 cm are depicted in Figure 5-11. In addition, the waveforms for case d) Cu-HTS and case e) HTS-Cu are shown in Figure 5-12. As the air gap length increases, the voltage and current amplitudes of the Tx coil increase too. This is due to the increase in reflected impedance. On the contrary, the current and voltage on the receiver side decrease with increasing distance, indicating a reduction in overall power transfer, as the magnetic field linking both coils becomes weaker. Furthermore, a phase shift can be seen particularly at large air gap lengths. An impedance matching circuit is commonly used to match input and output impedance and maximise power transfer. However, it was not used in the experiments conducted here. Furthermore, as the air gap increases the waveforms become increasingly distorted and move away from being a voltage square waveform as the resonance circuit loses resonance and the reactive part of the impedance is not fully cancelled.

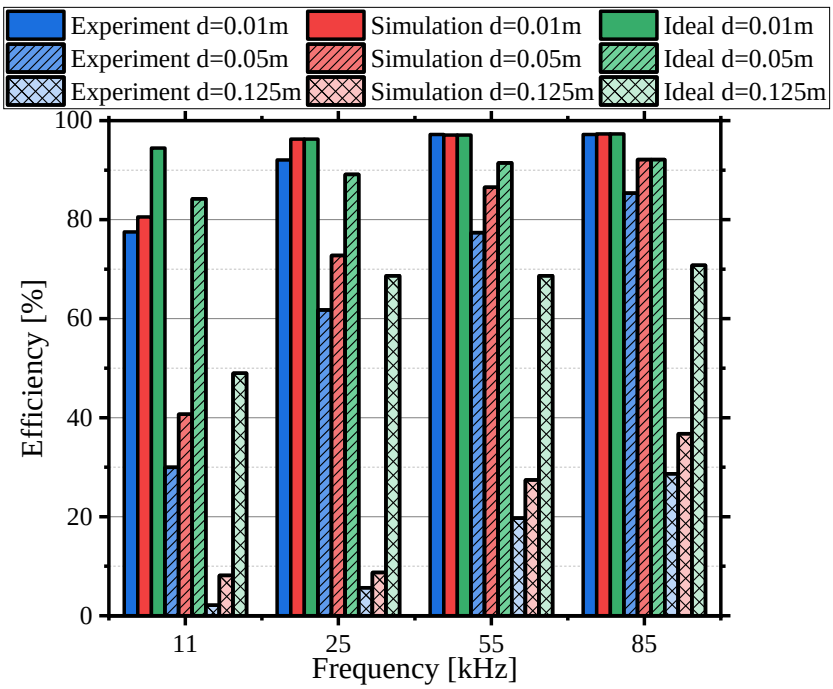

Figure 5-13 Cu-Cu in LN2 efficiency measurement vs simulation and ideal case for air gap lengths of 0.01 m, 0.05 m and 0.125 m

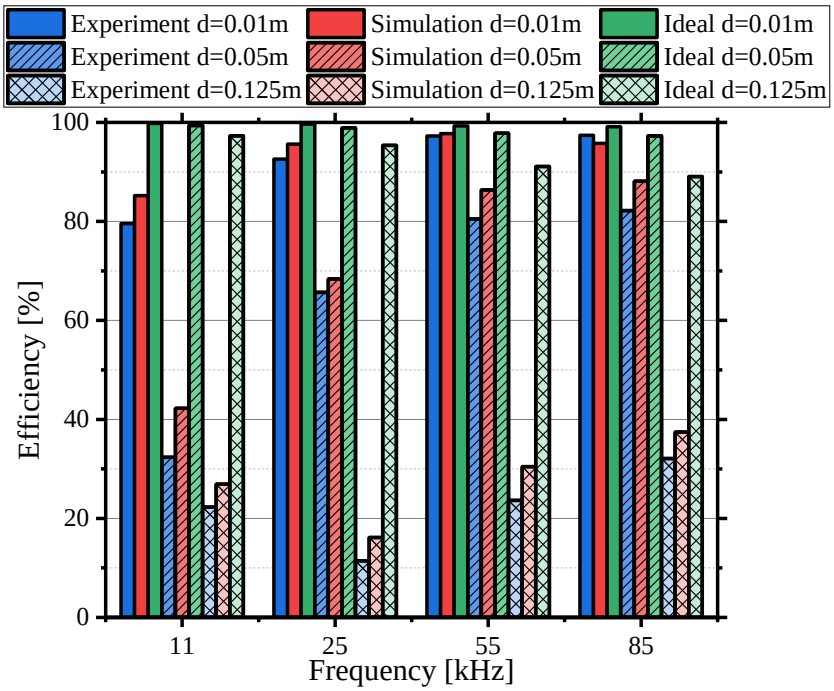

Figure 5-14 HTS-HTS efficiency measurement vs simulation and ideal case for air gap lengths of 0.01 m and 0.05 m and 0.125 m

The obtained experimental results for Cu-Cu in LN_2 and for HTS-HTS were compared with the simulations according to Figure 5-1 and results are illustrated in Figure 5-13 and Figure 5-14. Furthermore, an ideal case is included using Eq. 3.9. Experimental results for 1 cm, 5 cm and 12.5 cm are highlighted in blue, while the corresponding modelling results are depicted in red and the ideal efficiency in green. It should be noted that the cooling system was not considered for the efficiency calculation. In general, the simulations are in good agreement with the experimental results but tend to overestimate the achievable efficiency. Moreover, as the frequency increases, the difference between simulations and experiments decreases. This is especially true for the HTS-HTS system. As the frequency decreases, the losses in the HTS coils become very small, resulting in a very low equivalent resistance, which is used as input for the circuit model. The overall system efficiency declines with frequency as the induced voltage decreases rapidly.

In general, losses in the copper leads used to connect the HTS coils as well as the connecting wires and the capacitors banks and their copper plates were not considered. While the circuit model accounts for small mismatches in resonance and unity power factor, such general system losses are not accounted for in the circuit model. Nevertheless, the proposed model reasonably emulates the system performance. As seen from the comparison with the ideal case, the systems operate not

under ideal conditions, particularly at large air gaps, highlighting that higher efficiencies can be achieved with proper impedance matching. While for the Cu-Cu system the efficiency increases with frequency, the opposite is true for the HTS-HTS system as the AC losses decrease significantly with frequency.

5.5 Conclusions

In this chapter, the transfer efficiency of multiple WPT systems using copper coils, HTS coils and copper coils submerged in LN_2 was investigated. The systems operated in a frequency range relevant for EV wireless charging from 11 kHz up to 85 kHz. The measurements showed that HTS-HTS systems have superior transfer efficiency over Cu-Cu systems at frequencies below 50 kHz. As the frequency increases, the difference between the HTS and copper systems becomes negligible. In addition, hybrid systems such as HTS-Cu and Cu-HTS show a similar performance to HTS-HTS systems. However, no clear advantage in terms of efficiency of one hybrid system over the other crystallised. Given the low power input and the very small equivalent resistance of the HTS coils, the parasitic resistances of connectors etc must be considered. Furthermore, the resonance condition must be observed carefully to avoid distortion in the waveforms and a reduced performance of the system.

The measured efficiency was, for the first time, compared with simulation results obtained from a combination of FEA modelling and circuit modelling. A 2D axisymmetric numerical multilayer FEA model was used to simulate AC losses of the investigated HTS coils, as conventional HTS film models and analytical equations for HTS tapes are not suitable for high frequency applications using HTS coils. Subsequently, the losses were converted to an equivalent resistance. The simulation results are in good agreement with the experiments. Parasitic losses in coil connectors, connecting wires and capacitor banks have not been included causing the difference between simulation and measurements. Furthermore, the cooling system when operating at 77K was not considered. When comparing achieved results to ideal conditions, higher systems efficiency can be expected. This chapter provides a comparison of power transfer efficiencies of copper, HTS and hybrid WPT-systems. Additionally, a practical numerical method to estimate the power transfer performance of the wireless charging systems is proposed. On one hand, it should be noted that, if the cooling system losses are included, the overall efficiency of the HTS system could possible decrease largely and become unfeasible. On the other hand, although at higher frequency bands the HTS based WPT-systems do not have a distinct advantage over copper systems, in

regards to efficiency, the transferred power of HTS systems is much higher than of copper systems, which is extremely important in some specific power-demand cases, such as fast charging.

6 AC loss modelling of superconducting coils

6.1 Introduction

Current systems use copper as coil materials, as it provides high conductivity and high availability at low cost. However, new materials emerge such as HTS. Sedwick conducted initial tests with HTS coils in 2010 and demonstrated improved system efficiency [367]. This is mainly due to the higher quality factor Q, compared to copper coils. HTS coils provide virtually zero DC resistance, while also being able to carry large amounts of current resulting in a higher power density compared to copper coils, allowing for a higher magnetic flux density. When subjected to a time varying current or magnetic field, HTS coils still experience AC losses [55].

With the introduction of the first standard addressing WPT for EVs, SAE J2954-2016, the operating frequency of such charging systems is set to be between 81.39 and 90 kHz with a nominal operating frequency of 85 kHz [99]. Therefore, 'high frequency' refers to the above-mentioned range. AC losses in HTS tapes and coils have been investigated extensively, however, limited only to low frequencies up to several kHz [368], [369], [370], [371], [372]. One important aspect for the use of HTS coils in WPT systems is the loss characteristic at high frequencies. For low frequencies, the main loss component is the hysteresis loss within the HTS layer. However, at higher frequencies, eddy current losses, particularly in the copper layers and ferromagnetic losses in the substrate become more pronounced and cannot be neglected.

In this chapter, a 2D axisymmetric multilayer model for the most commonly used coil configurations in WPT i.e. double pancake, circular spiral and solenoid coils is derived using $\boldsymbol{H}$-formulation in COMSOL. Initially, the model is outlined where different approaches to the field-dependency of the critical current density and geometry approximations are compared. The most suitable option is then chosen and validated with experimental data. Lastly, different scenarios for the losses are presented including transport current loss, magnetisation loss and combined losses. Parts of this chapter have been published in [2] and [4].

6.2 AC loss model

6.2.1 Model outline

To evaluate the losses occurring in the HTS coil when supplied by an AC current or located within a varying external magnetic field, a 2D axisymmetric model has been constructed. A 2D axisymmetric model was chosen as it provides a reasonable approximation for rotationally

symmetric coil configurations such as investigated here, while minimising the computational time required for solving a 3D model. In addition, the aspect ratio of the investigated multilayer model is very large, particularly for full scale systems, which makes it difficult to simulate. Furthermore, the applied external magnetic field is centrosymmetric, thus does not have one fixed direction.

The model uses the commonly applied ***H***-formulation and comprises the equations presented in chapter 2.3.3, namely Ampere's law Eq. 2.6, Faraday's law combined with constitutive law Eq. 2.7, *E-J* power law Eq. 2.8 and Ohm's law Eq. 2.9. The simulation was performed in COMSOL and Eq. 2.6-2.9 can be rewritten as general form in Eq. 6.1.

$$\frac{\partial(\mu_0\mu_r\mathbf{H})}{\partial t} + \nabla \times (\rho\nabla \times \mathbf{H}) = 0 \tag{6.1}$$

The general model layout can be found in Figure 6-1. Three different coil structures are investigated. A solenoid configuration, i.e. stacking turns along the z-direction, a spiral coil, i.e. stacking turns in r-direction, and finally, a double pancake configuration, commonly used in WPT systems. To apply a time-varying external magnetic field, Dirichlet boundary conditions have been used.

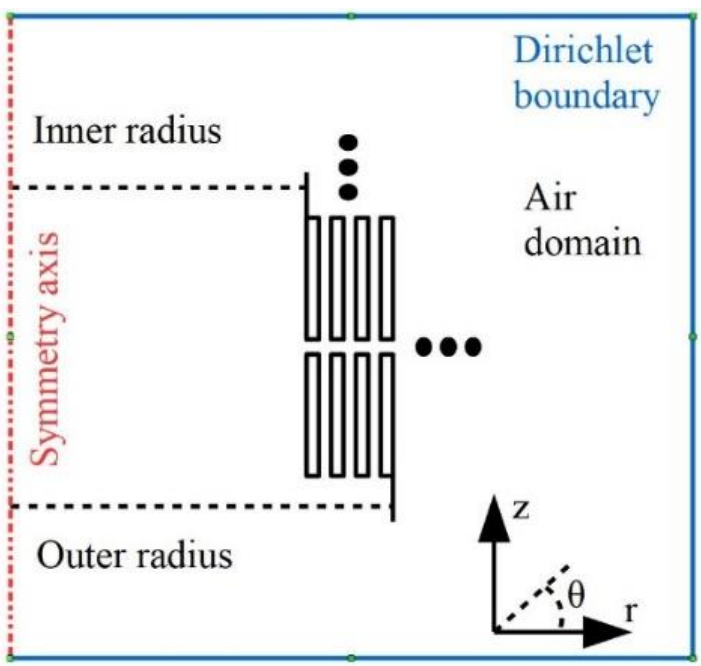

Figure 6-1. 2D axisymmetric model layout

To incorporate the magnetic field dependency on the critical current density $J_c(\mathbf{B})$, an anisotropic Kim-like model shown in Eq. 2.3-2.4 was adopted. Eq. 2.3 uses only the perpendicular magnetic

field component while Eq. 2.4 uses both, the perpendicular and the parallel component of the magnetic field to adjust the critical current density. Commonly Eq. 2.3 is used for tapes as the effect of the perpendicular magnetic field component onto the critical current density is greater than that of the parallel field [373]. However, for coils, particularly those used in WPT systems, displacement between the coils frequently occurs as EVs traverse over the transmitting pad. Furthermore, so far only multilayer coils are used for WPT systems, causing additional parallel cross-turn effects. Therefore, it suggests that the influence of the parallel field cannot be neglected and should be included. Both models are compared in the next section. As shown in Figure 6-2 and Figure 6-3, the difference between full field dependency and using only the perpendicular field component is small. Nevertheless, both field components are considered in the following.

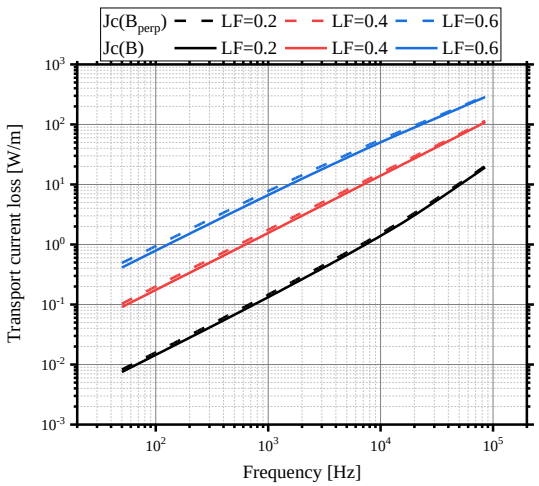

Figure 6-2 Comparison of transport current loss of eight-turn double pancake coil model using full and perpendicular field components

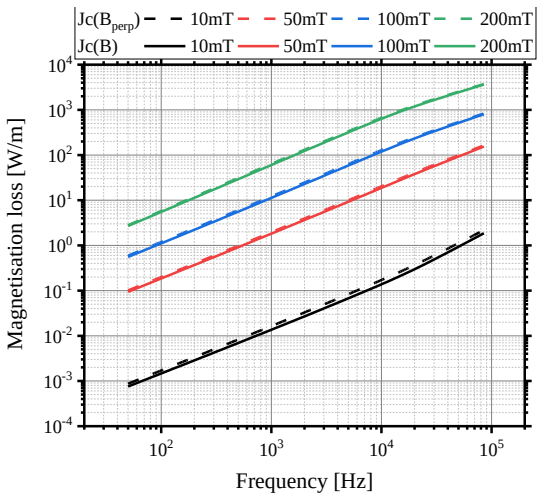

Figure 6-3 Comparison of magnetisation loss of eight-turn double pancake coil model using full and perpendicular field components

The model uses real geometric data from Fujikura FYSC SCH04 outlined in Table 6-1. A cross-sectional view of the HTS-CC is depicted in Figure 6-4. The GdBCO superconducting layer thickness is 2 µm, copper stabiliser thickness is 20 µm (located on top and bottom of the tape), silver layer thickness is 2 µm and the non-magnetic substrate (Hastelloy®) thickness is 75 µm. Each coil investigated has an inner radius of 0.0625 m and is comprised of 8 turns with an intra-turn spacing of 200 µm due to the Kapton tape insulation. A common technique to increase computational speed is to approximate the HTS coil turns through homogenisation as presented in [374]. The critical current of the multilayer turn is adjusted by the volume fraction of the superconducting layer f_{HTS} according to $J_{\mathrm{c,Eq}}(\mathbf{B}) = J_{\mathrm{c}}(\mathbf{B}) f_{\mathrm{HTS}}$. However, this approach is only

viable for low operating frequencies as other layers such as the copper stabilisers will significantly contribute to the losses [8]. Therefore, separate HTS coil turns are approximated by a multilayer structure including copper stabilisers, silver overlayer, HTS layer and substrate. The multilayer structure allows for considering different loss mechanisms in the layers. Transport current and magnetisation loss in coils at various transport current load factors (LF), external magnetic fields (B_{ext}) and frequencies are calculated. The LFs are defined as the ratio of transport current I_t to self-field critical current I_{c0} of the tape used.

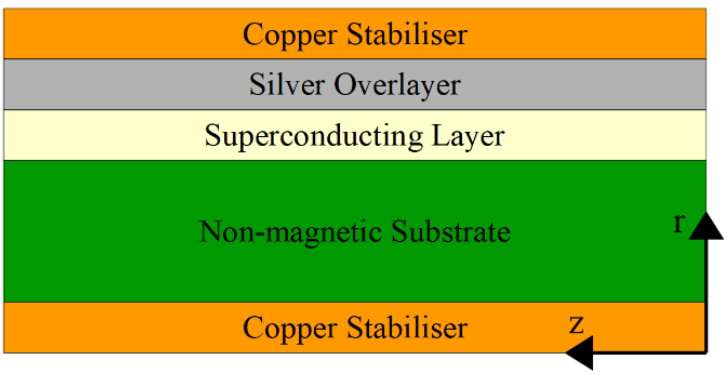

Figure 6-4. Cross-section of HTS coated conductor

Table 6-1 HTS tape parameters [375], [376]

Parameter	Value
YBCO tape width	4 mm
YBCO film thickness	2 μm
Copper thickness	20 μm
Silver thickness	2 μm
Substrate thickness	75 μm
Copper resistivity at 77K	1.97×10^{-9} Ω/m
Silver resistivity at 77K	2.7×10^{-9} Ω /m
Substrate resistivity at 77K	1.25×10^{-6} Ω /m
Free space permeability	$4\pi \times 10^{-7}$ H/m
Power-law exponent	25
k	0.67
α	0.6
Critical current in self field	245 A
Characteristic E-field	10^{-4} V/m
Magnetic field constant	0.2 T
Coil radius	0.0625 m
Turn number	8
Winding width [mm]	1.076
Operating temperature [K]	77

Each layer of the HTS tape is included in the model and treated as an individual domain. The different layers are connected in parallel and carry the transport current I_t with the peak current I_P, see Eq. 6.2. For a sinusoidal input signal, the AC loss Q_n within each layer can be calculated by integrating the power density of the layer over the domain Ω and the second half of the steady state period T as described by Eq. 6.3 [377]. Finally, the total AC loss Q_{total} of the HTS coil can be calculated from Eq. 6.4. All parameters used for the coil simulation are summarised in Table 6-1.

$$I_t = I_p \sin(2\omega t) = \int_\Omega \boldsymbol{J}(t)\, d\Omega \tag{6.2}$$

$$Q_n = \frac{2}{T} \int_{0.5T}^{T} \int_\Omega \boldsymbol{E} \cdot \boldsymbol{J} d\Omega dt \tag{6.3}$$

$$Q_{total} = \sum_{n=1}^{5} Q_n \tag{6.4}$$

6.2.2 Model validation

In this section, simulation results are compared with experimental measurements [368] and other reference models [378] obtained from literature for single HTS tapes and multilayer coils. The 2D multilayer tape model [8] was extended to include geometrical features of a coil in an axisymmetric environment. Initially, transport current loss results for a HTS tape and a double pancake coil using the homogenisation approach are shown in Figure 6-5 and Figure 6-6. The obtained results agree with measured results, however, there is some difference. As the conductivity of the superconducting layer is much larger than for the other layers, most of the losses will be generated here. However, as the frequency increases and the losses shift towards other layers, the homogenisation approach loses its applicability. In case of an HTS coated conductor with magnetic substrate such as used in [368], the homogenisation model must be adapted to accommodate the substrate and its μ_r. Other layers can still be modelled using the homogenisation approach.

Transport current losses and magnetisation losses for the multilayer model are depicted in Figure 6-7 to Figure 6-9. As displayed, the simulated results are in very good agreement in the case of single tapes at higher frequencies as well as for coils, subject to AC transport current and time varying external magnetic field. Furthermore, the losses in each of the layers of the HTS tape are shown. As the frequency increases, the losses in the copper layers cannot be ignored. Hence, the multilayer approach will be used in the proceeding chapters to minimise errors and to investigate the impact of the copper layer further.

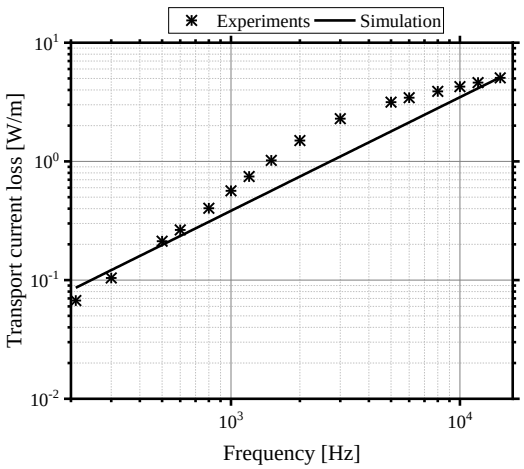

Figure 6-5. Comparison of AC transport current loss simulation (homogenisation) and experimental data [368] for an HTS tape at frequencies up to 15 kHz and a transport current of I_0= 45A.

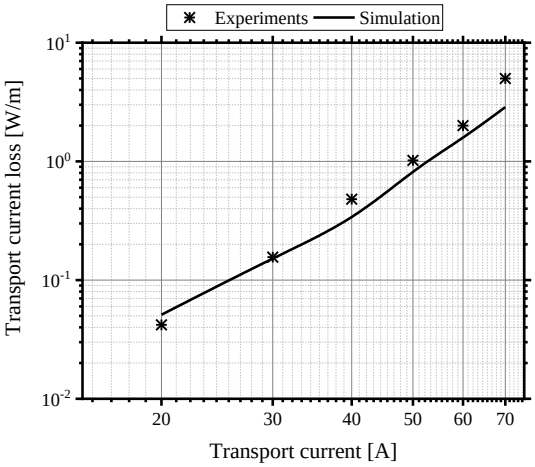

Figure 6-6. Comparison of AC transport current loss simulation (homogenisation) and experimental data [378] for a 36-turn double pancake coil at 200 Hz and different transport currents I_0.

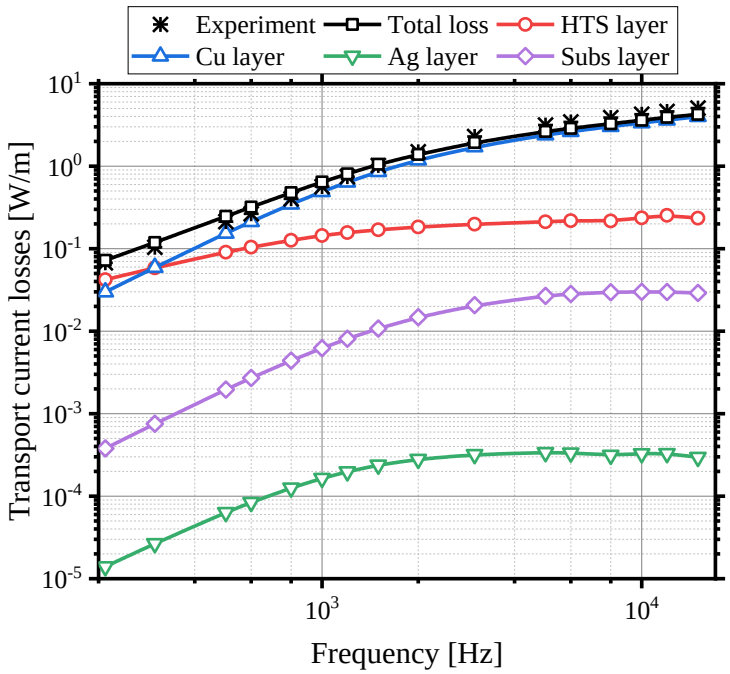

Figure 6-7. Comparison of AC transport current losses simulation and experimental data [368] for a single HTS tape at frequencies up to 15 kHz at I_t =45 A

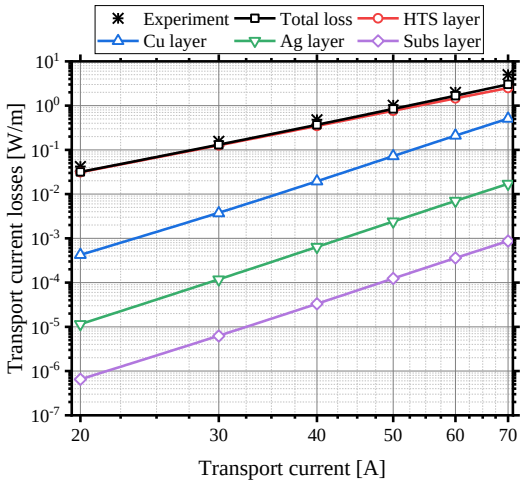

Figure 6-8. AC transport current loss measurements [378] and simulations for a 36-turn double pancake coil at 200 Hz

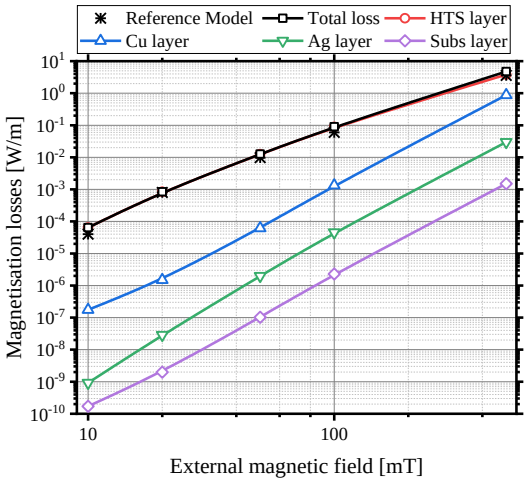

Figure 6-9. Comparison of AC magnetisation loss of the proposed model and [378] for a 36-turn double pancake coil at 200 Hz

6.3 Transport current loss

Initially, the transport current loss for the three coil configurations is investigated. Key loss characteristics involve the hysteresis loss in the HTS layer, which is the main loss mechanism at lower frequencies, coupling and eddy current losses. The tape under investigation uses Hastelloy®, a non-magnetic substrate and there are no superconducting filaments involved. Hence, ferromagnetic losses and coupling losses are neglected. To evaluate the transport loss, a sinusoidal AC current with different frequencies, between 50 Hz and 85 kHz, is applied to the coil and there is no external magnetic field. The transport current is quantified by LF and ranges from 0.1 to 0.8, equivalent to up to 80% of the critical current of the coil.

Figure 6-10 shows the total transport current loss of eight-turn coils wound as double pancake, spiral and solenoid, respectively. In general, the loss increases with rising frequency and higher LF. The impact of LF increases with frequency, as more current is pushed into a smaller current carrying area, confined by the skin effect [8]. This effect can clearly be seen in Figure 6-11, which shows the magnetic field distribution in the HTS tape as well as the current density in the HTS layer of a double pancake coil at the negative peak of the sinusoidal transport current.

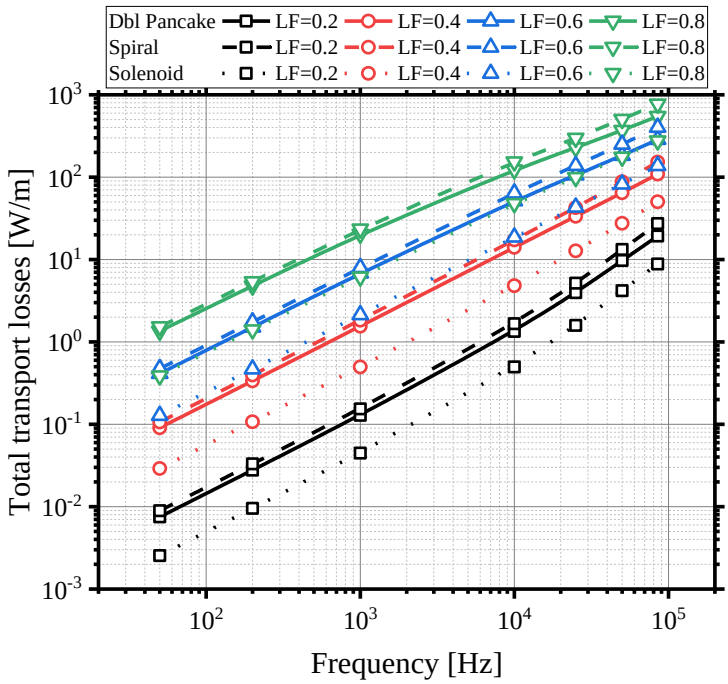

Figure 6-10. Total transport current loss of eight-turn coils (double pancake: full line, spiral: dashed line, solenoid: dotted line) at different LF and frequencies up to 85 kHz

Comparing the different loss characteristics of the presented coil configurations, it is evident that the spiral coil experiences the highest total transport current loss, closely followed by the double pancake configuration. Resulting from the multilayer nature within the double pancake coil, each tape only faces high magnetic fields on the outer edges of the turn, this is paired with a similar occurrence of high current densities, leading to high transport current losses as shown in Figure 6-11 for the case of a LF of 0.5. However, the current penetrates deeper into the tape with increasing load factor offsetting the benefits of the multilayer structure. On the other hand, within the solenoid structure, magnetic field hotspots are localised in the gaps between each turn and on the outer edges of the first and last turn. Here, the highest magnetic fields occur at the top and bottom of the coil and decreases towards the gaps in the centre of the coil until the fields cancel each other in the centre of the winding (along *z*-direction). Furthermore, only one side of the turn experiences a high magnetic field, while the magnetic field on the other side gets cancelled by the previous turn. In the spiral configuration, there is no field cancellation, resulting in high magnetic fields on each side of the tape. Nevertheless, there is a slight shielding effect, limiting the magnetic and electric fields in tapes in the middle of the winding.

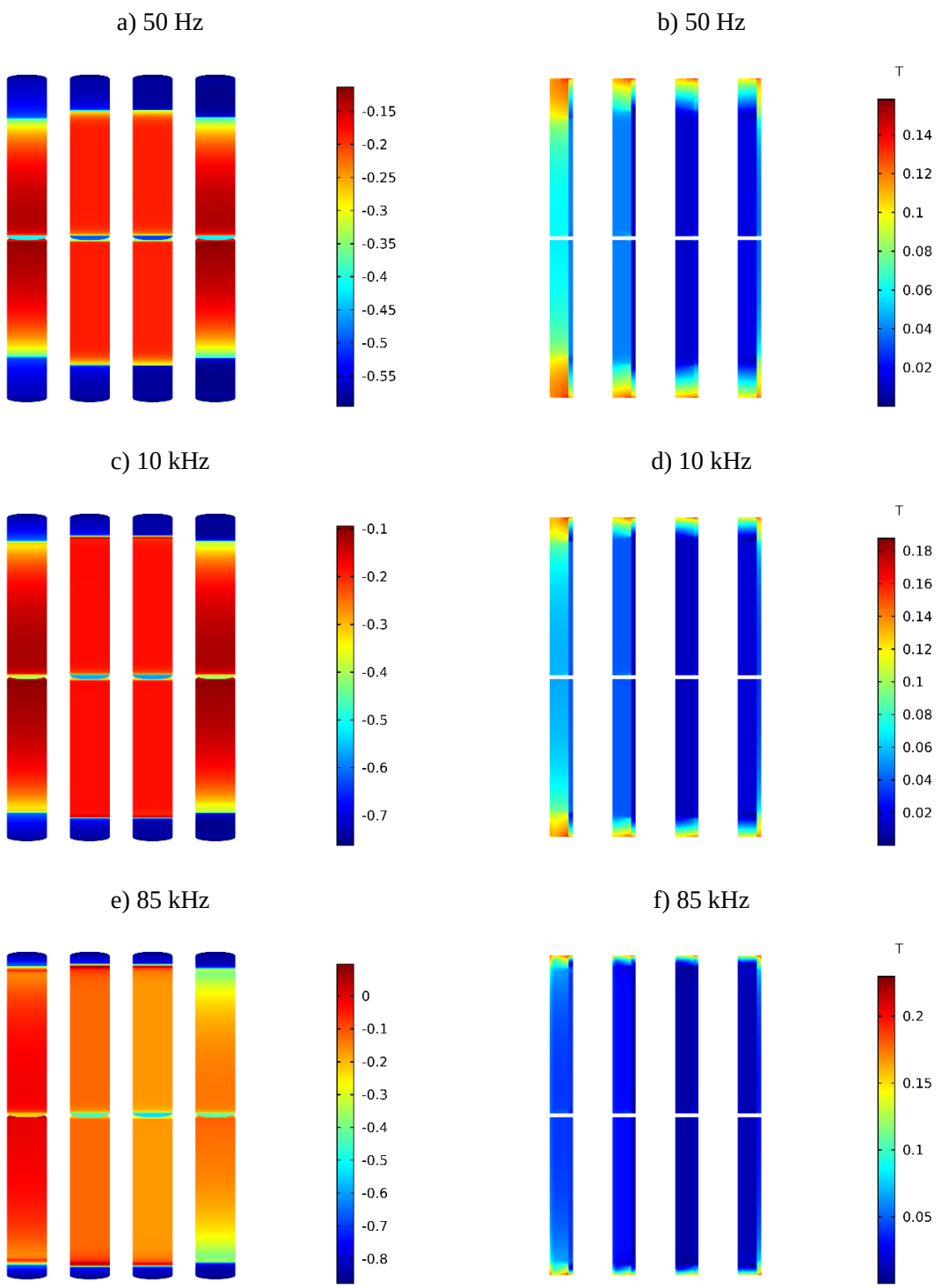

Figure 6-11 Current density distribution J/J_c a),c),e) in the HTS layer and magnetic field distribution b),d),f) at $3\pi/2$ for a double pancake coil subject to a LF=0.5 at 50 Hz, 10 kHz and 85 kHz, respectively. To improve visualisation the HTS layer thickness has been increased.

To achieve the required overall system efficiency of 85% for WPT-systems [99], the losses in the coils must be reduced. The losses generated by the HTS coils are extremely high for LF and frequencies targeted by such systems, particularly taking into account that the operating temperature is 77K. Viable option for loss reduction will be explored in chapter 7.

Each HTS tape comprises several different layers and Figure 6-12 shows the contribution of each of the layers on the total loss with changes in frequency for a LF of 0.5. As shown, the HTS layer itself has the highest contribution towards the losses of the HTS tape, followed by the copper. Losses within the silver and the substrate layer are several magnitudes smaller than other losses. The substrate considered here is non-magnetic and even though it has the highest volume fraction, its limited electric conductivity results in the lowest loss contribution. With increasing frequency, the contribution of the HTS layer decreases and the share of the copper layer increases. This is due to the skin effect pushing the current into the outer layers of the tape i.e. the copper layers [8]. An additional factor that influence the losses is the critical current of the coil. When transitioning from single tapes towards stacks and coils, the interaction between individual turns and tapes cannot be neglected as the self-field lowers the critical current compared to single tapes. A self-consistent model was used to determine the influence of subsequent turns onto the critical current of each individual turn [379]. It uses the voltage drop per unit length as criterion in each tape to determine the new critical current of the coil. Results obtained are displayed in Figure 6-13. As shown, the configuration has great influence on the critical current of a coil. The two extremes considered are the solenoid and spiral configuration. In a solenoid configuration, the critical current is widely stable and only reduces by a small fraction compared to an individual tape. However, in a spiral coil, the effect of subsequent turns is much higher, resulting in a much lower critical current. Additionally, the double pancake configuration, ranks between the two previous structures as it combines features of spiral and solenoid configuration.

To take into account the different critical currents of the coils, the applied transport current, resulting from LF of the HTS tape, was adjusted to fit the actual LF of the coil. Figure 6-14 shows the adjusted total transport current of the three coil layouts. The overall losses are for double pancake and spiral coils smaller as the applied current is lower. In addition, the gap between the solenoid structure and the remaining layouts has shrunken.

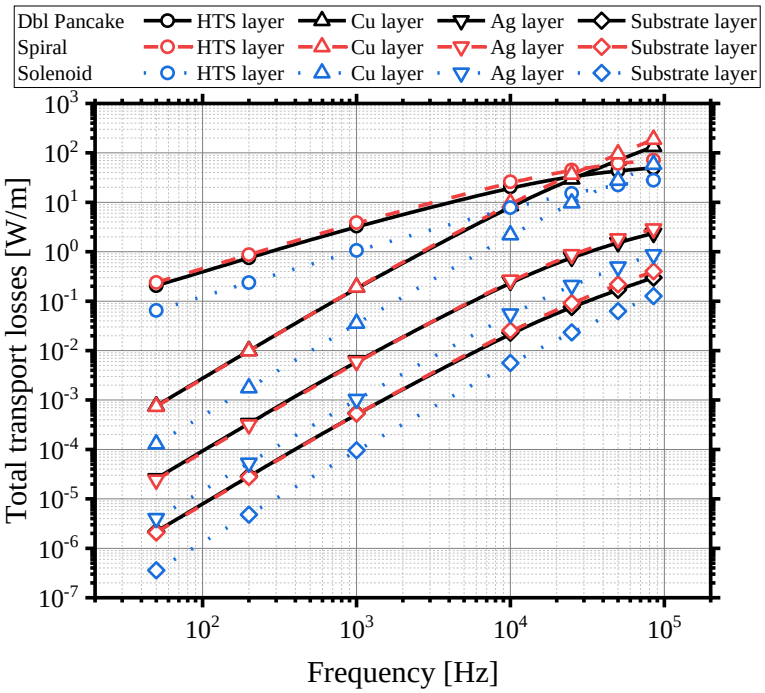

Figure 6-12. Total transport current loss contribution of pancake (black), spiral (red), solenoid (blue) at LF=0.5 and frequencies up to 85 kHz

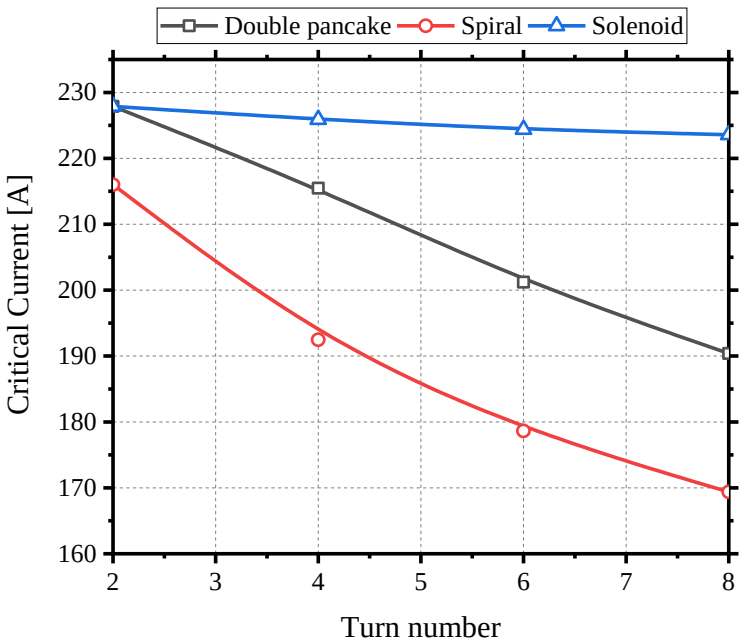

Figure 6-13. Critical current for different coil configurations and turn numbers.

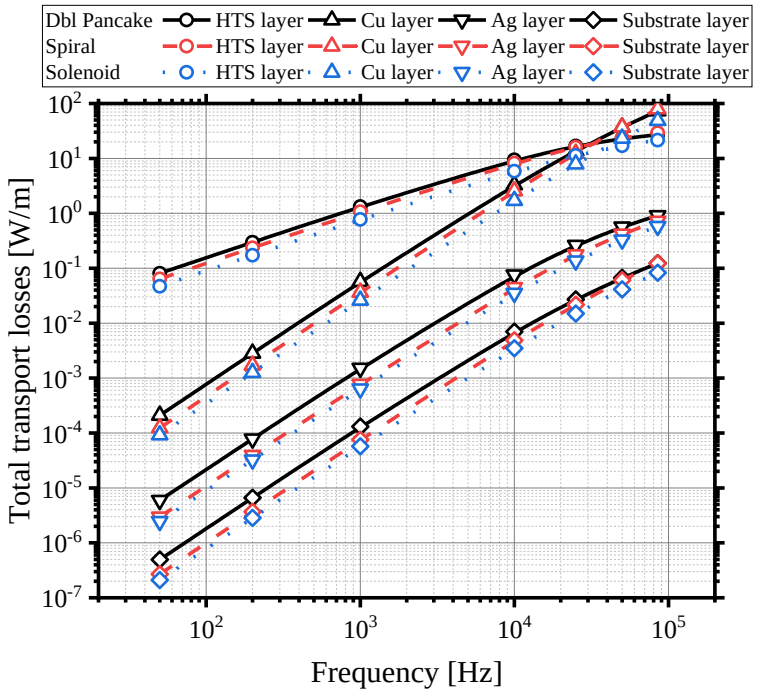

Figure 6-14. Total transport current loss contribution of pancake (black), spiral (red), solenoid (blue) at adjusted LF of 0.5 and frequencies up to 85 kHz

As verified, the main driver for transport current losses at higher frequencies is the skin effect [8]. This phenomenon occurs in all three coil configurations. Therefore, a transition frequency is defined where $Q_{HTS}=Q_{Cu}$. It changes depending on the configuration and applied transport current as illustrated in Figure 6-15. For a single HTS coated conductor, the losses in the HTS are prevalent up to 100 kHz [8]. Generally, due to the interaction between the different windings within a coil, the transition frequency for coils is much lower and therefore limits the use of HTS film models for HTS coils operating at higher frequencies. When comparing the different transition frequencies, it is noteworthy that for LF below 0.3 the difference in coil configurations is small. At high LF, the transition frequency for double pancake and spiral coils are similar, while it is much higher for the solenoid coil. A higher transition frequency represents a later shift from the HTS layer towards the copper stabilisers as main contributor of the transport current losses. The interaction between the loss shares of the HTS and copper layers for the double pancake coil and the solenoid coil are shown in Figure 6-16 and Figure 6-17, respectively. The loss distributions are similar for lower frequencies and LF. However, as the LF increases the shift is delayed for the solenoid configuration, which can be explained by the field cancellation, reducing the impact of

the magnetic field on J_c of the HTS layer and the reduced local current density in the conducting area.

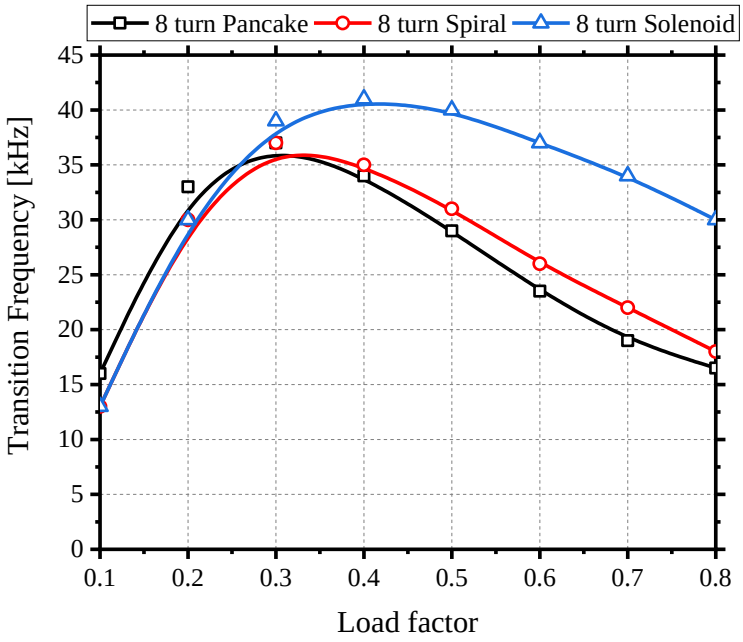

Figure 6-15. Transition frequency for different coil configurations over a range of load factors

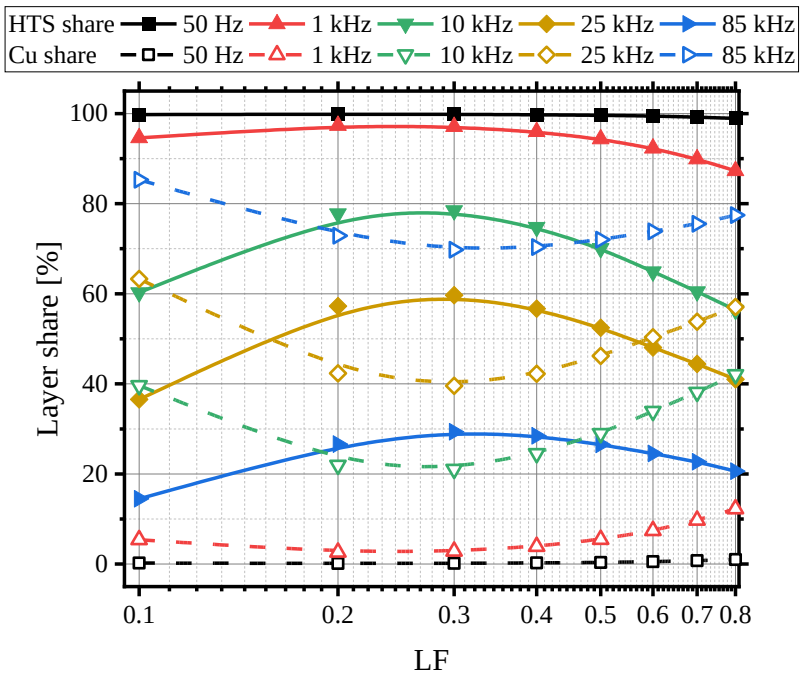

Figure 6-16 HTS/ Cu share of the transport current loss of an eight-turn double pancake coil at different frequencies and LF

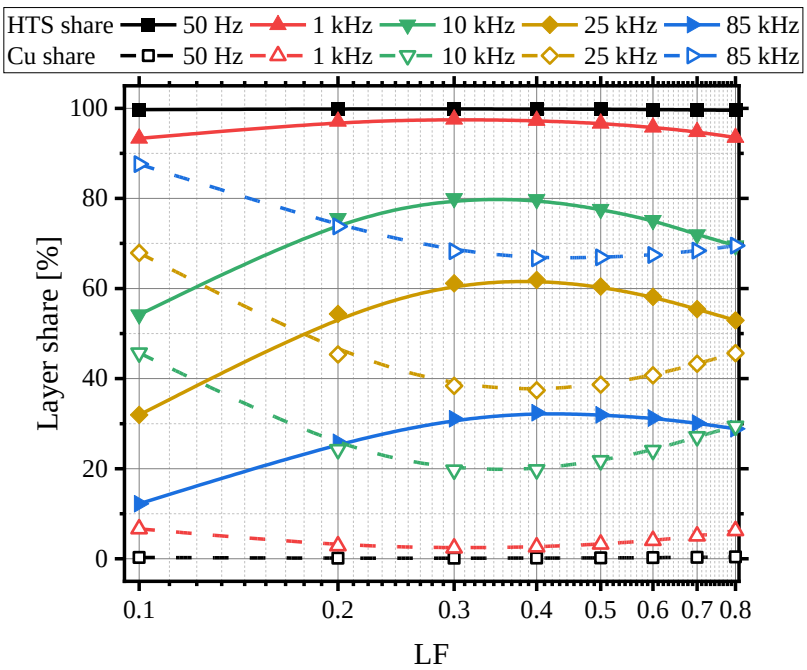

Figure 6-17 HTS/ Cu share of the transport current loss of an eight-turn solenoid coil at different frequencies and LF

When designing the cooling system used for HTS coils, it is of interest where local temperature hot spots occur. Therefore, Figure 6-18 to Figure 6-20 depict the share of each turn on the total transport loss for a LF of 0.5 and frequencies between 50 Hz and 85 kHz. L1-L8 denote the turn from left to right or top to bottom for the spiral and solenoid configuration, respectively. While T1-T4 are the top turns and B1-B4 are the bottom turns from left to right in the double pancake coil. As one can see, the double pancake and spiral coils have comparable distributions, while the solenoid coil has vastly different characteristics. At low frequencies e.g. 50 Hz and 1 kHz, the loss distribution amongst the turns is mostly even for pancake and spiral coils. As the frequency increases to 10 kHz and later 85 kHz, innermost turns are subject to the highest losses. This is due to the increased magnetic field in the centre of the coil. The increase is compensated by a reduction in the share of the outer turns, while the second last turn for the pancake and the second and third last turns of the spiral coils experience the lowest loss. Subsequent coil turns are shielded from the magnetic field and the transport current penetration depth is lower, resulting in an overall decrease of the combined electric and magnetic field and therefore loss.

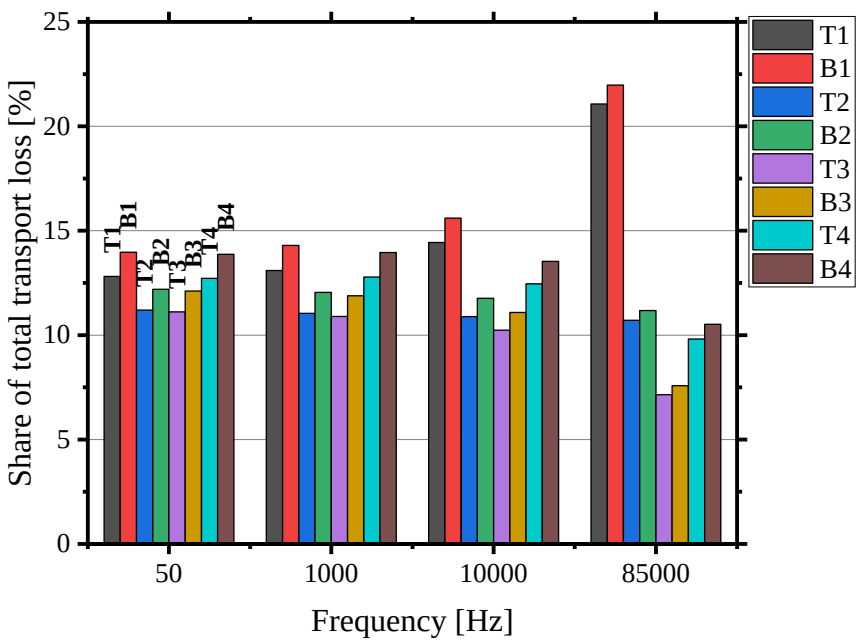

Figure 6-18. Turn loss contribution in an eight-turn double pancake coil for different frequencies at a load factor of 0.5

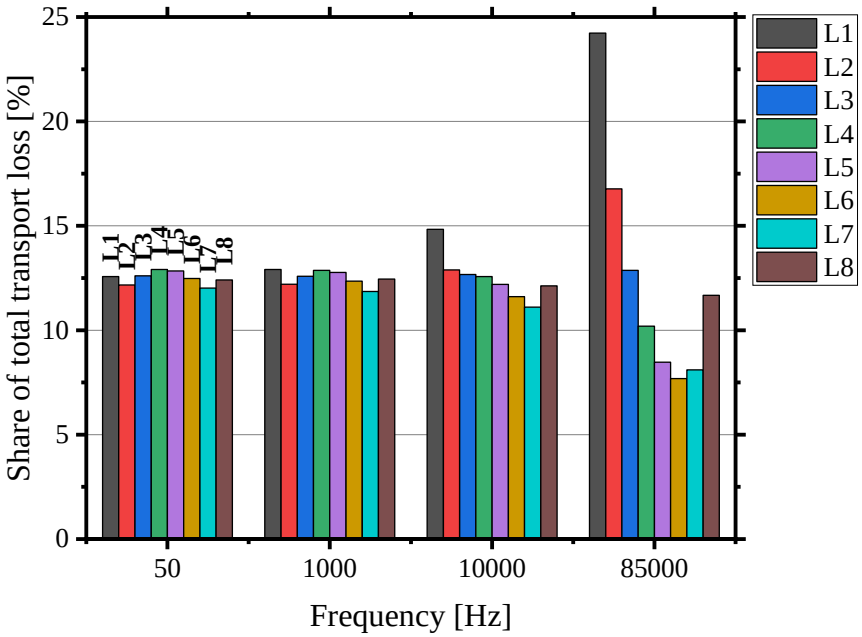

Figure 6-19. Turn loss contribution in an eight-turn spiral coil for different frequencies at a load factor of 0.5

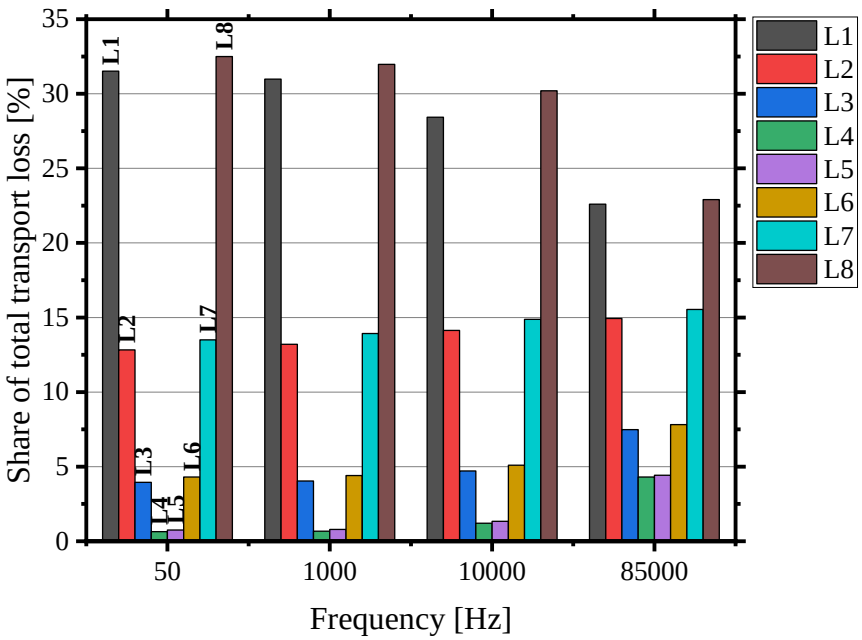

Figure 6-20. Turn loss contribution in an eight-turn solenoid coil for different frequencies at a load factor of 0.5

The loss distribution within the solenoid coil is vastly different to the previous two configurations. All turns are subject to the same local magnetic field, while each turn contributes to the field cancellation between the turns. The outermost turns do not experience this cancellation and therefore experience the highest loss. With increasing frequency, this trend weakens, and the loss contribution of the innermost turns increases. As the frequency increases the losses in the copper layer increase and dominate at frequencies above the transition frequency. The solenoid layout is clearly advantageous when considering transport current loss characteristics for WPT systems. Particularly, when considering the magnetic field distribution above the centre of the coil as shown in Figure 6-21, which is an important parameter for a WPT-system and its performance.

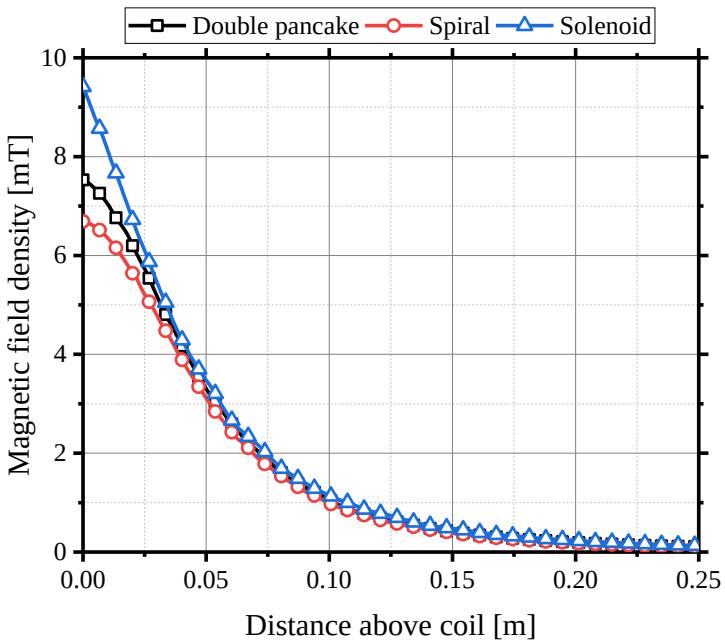

Figure 6-21. Magnetic field distribution above the centre of the coil at adjusted LF=0.5

6.4 Magnetisation loss

6.4.1 Magnetisation loss at different external magnetic fields

In this chapter the magnetisation loss is investigated. All external fields are alternating at frequencies up to 85 kHz and perpendicular to the wide tape surface, demonstrating the worst case for a WPT-system. Applied AC magnetic field densities range from 10 mT to 200 mT and there is no additional current applied to the coils.

Figure 6-22 illustrates the magnetisation loss for the previously introduced coil configurations. In general, the magnetisation loss per unit length increases with stronger external magnetic fields. Lower external magnetic fields are not strong enough to penetrate the HTS layer due to the shielding current produced, repelling the external field. The effect of the magnetic field increases rapidly with frequency. The magnetic field distribution of the double pancake coil and the current density in the HTS layer at the negative peak of the sinusoidal external magnetic field (at $3\pi/2$) are depicted in Figure 6-23. Similarly, to the transport loss scenario, the magnetic field and current density forms local 'hotspots' characterised by very large peaks. The area of such hotspots decreases with frequency while the magnitude of the local magnetic field and current density increases. The middle windings i.e. turn pairs two and three show a more drastic shift from the hotspots towards the centre of the tape, whereas the innermost and outermost windings experience a more gradual transition. This is due to the higher magnetic field generated within the centre of the coil and the shielding of the middle windings through the outermost turns.

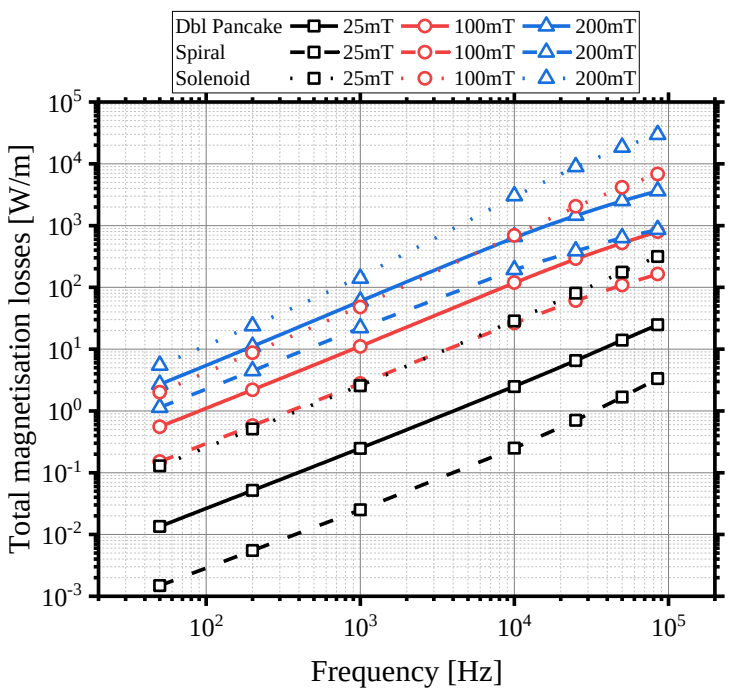

Figure 6-22. Total magnetisation loss of eight-turn coils (double pancake: full line, spiral: dashed line, solenoid: dotted line) at different magnetic field densities and frequencies up to 85 kHz

Contrary to the results obtained for the transport current loss, the solenoid configuration experiences the highest loss, while the spiral coil has the lowest losses. This is due to the shielding effect. In a spiral coil, the outermost turns shield subsequent turns, resulting in higher than per-

turn-average losses for the first and last turn, while other turns experience lower than average losses. A similar mechanism causes reduced loss in the double pancake coil. However, in a less pronounced fashion. In contrast, all turns in a solenoid layout are subject to the same field, without any shielding. It is therefore possible to use the shielding effect and change the layout of the windings to shield as many turns as possible, hence reducing the overall influence of external magnetic fields. Nevertheless, one still has to account for the critical current in the outermost turns which will experience a proportionally higher magnetic field. Additionally, stabiliser-free tapes can be used to eliminate one of the loss sources.

a) 50 Hz

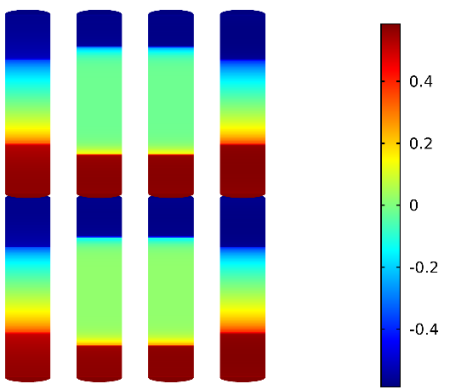

b) 50 Hz

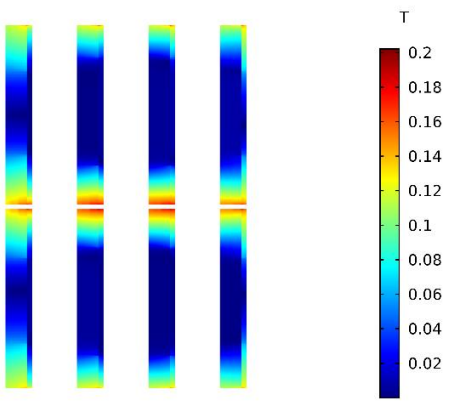

c) 10 kHz

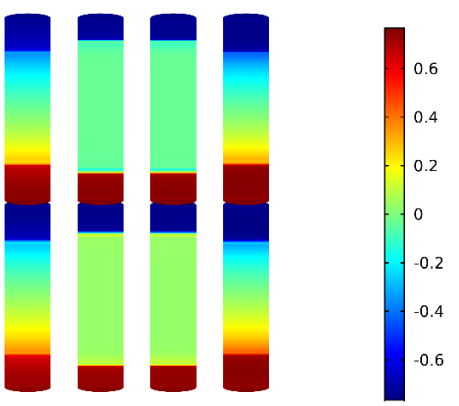

d) 10 kHz

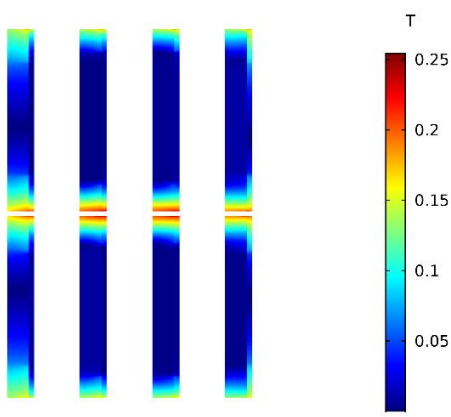

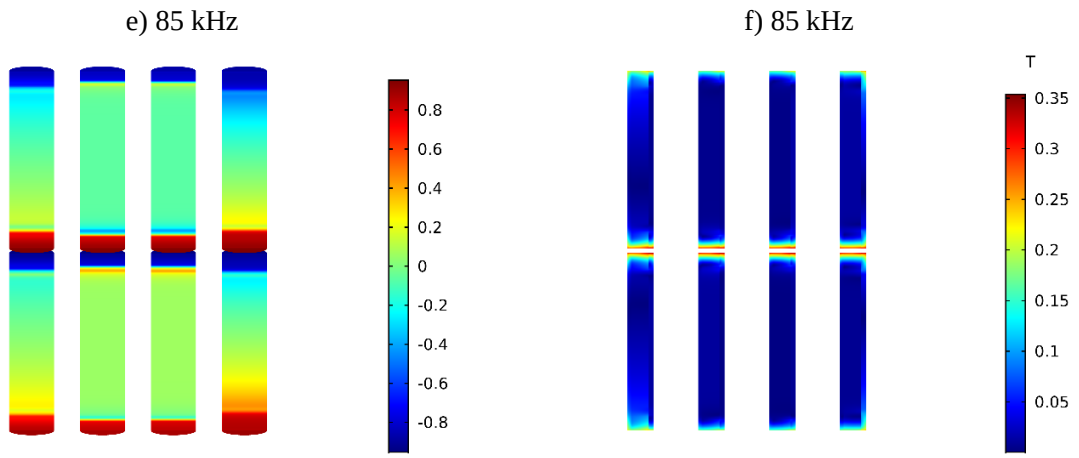

Figure 6-23 Current density distribution J/J_c a),c),e) in the HTS layer and magnetic field distribution b),d),f) at $3\pi/2$ for a double pancake coil subject to an external magnetic field B_{ext}=100 mT at 50 Hz, 10 kHz and 85 kHz, respectively. To improve visualisation the HTS layer thickness has been increased.

When looking at the contribution of the different layers depicted in Figure 6-24, a similar tendency as for the transport loss is shown. HTS and copper layers largely dominate the magnetisation losses in the HTS coil, while silver and substrate layer have only minor contribution.

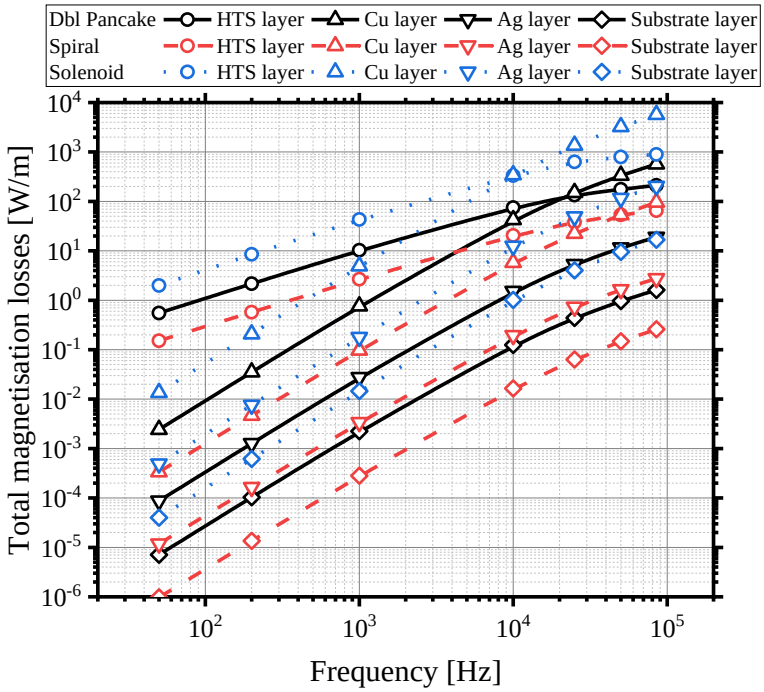

Figure 6-24. Total magnetisation loss contribution of pancake (black), spiral (red), solenoid (blue) at Bext =100 mT and frequencies up to 85 kHz

The loss in the HTS layer increases with frequency up to 50 kHz and stagnates at higher frequencies. On the other hand, the losses in the copper layers rapidly increase. This is a direct result of the skin effect, causing the current to be pushed into the copper layers as well as to the outer edges of the HTS tape. Similarly, the magnetic field is greatly increased at the outer edges of the tape. Figure 6-25 to Figure 6-27 show the interaction between the HTS layer and the copper stabilisers of the different coils. The overall trend is similar for all three coils, but the curves are shifted towards higher B_{ext} when comparing solenoid, double pancake and spiral. The shift is caused by the shielding effect in the spiral and double pancake coil whereas it is absent in the solenoid coil. There exists a maximum and minimum for the loss share in the HTS layer and the copper stabilisers, respectively. At a frequency of 50 Hz, almost all losses occur in the HTS layer for double pancake and solenoid coils, independently of the external magnetic flux density. However, as the frequency increases, the penetration depth of the magnetic field decreases and the magnetic field becomes weaker the farther it penetrates into the HTS tape according to the Beer-Lambert Law. Yet, the magnetic field penetrates the copper layer, generating the majority of the losses. As soon as a stronger magnetic field penetrates the HTS layer, most of the losses will occur there, until the skin effect pushes the magnetic field and current into the copper layer and the outer edges of the turn. Before reaching the maximum/minimum, frequency and B_{ext} have the same relationship and higher frequencies result in higher external magnetic fields to transition from higher copper to HTS losses. After the maximum is reached there is an inverse relationship between frequency and B_{ext} dictating the transition from HTS layer losses towards copper layer losses. Higher frequencies push the cross over point towards lower magnetic field densities. At a frequency of 85 kHz, neither spiral nor solenoid configuration, go through the described trend as the copper losses are always higher than the losses in the HTS layer.

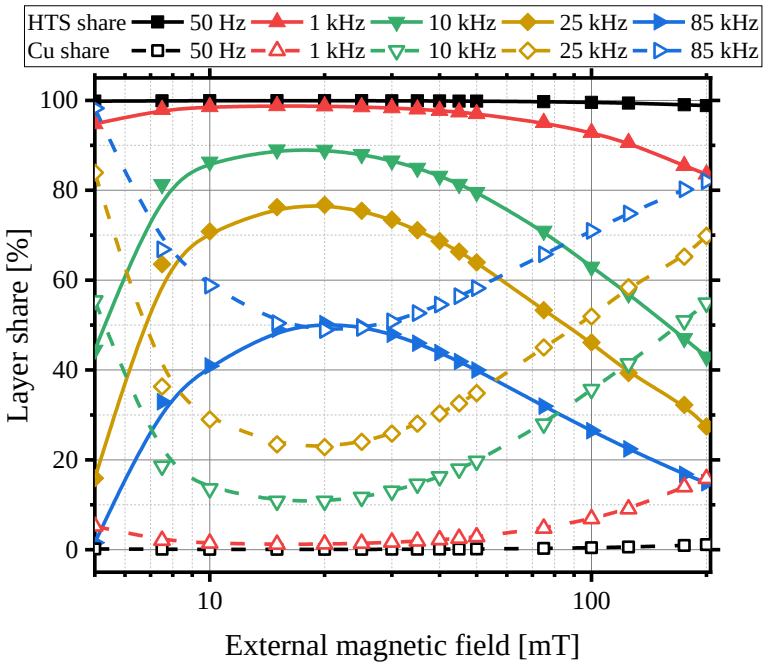

Figure 6-25. HTS (solid line) and copper (dashed line) layer loss contribution of an eight-turn double pancake coil for different frequencies and external magnetic field up to 200 mT

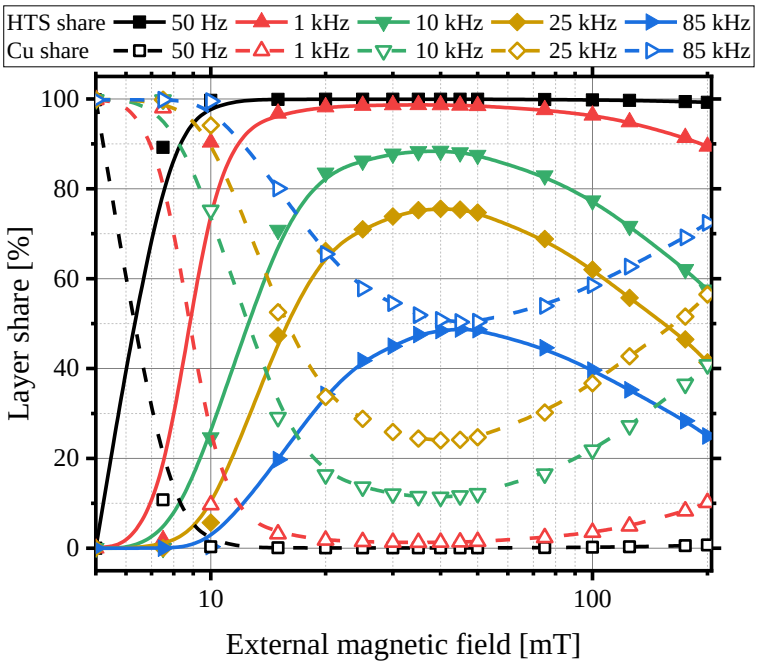

Figure 6-26. HTS (solid line) and copper (dashed line) layer loss contribution of an eight-turn spiral coil for different frequencies and external magnetic field up to 200 mT

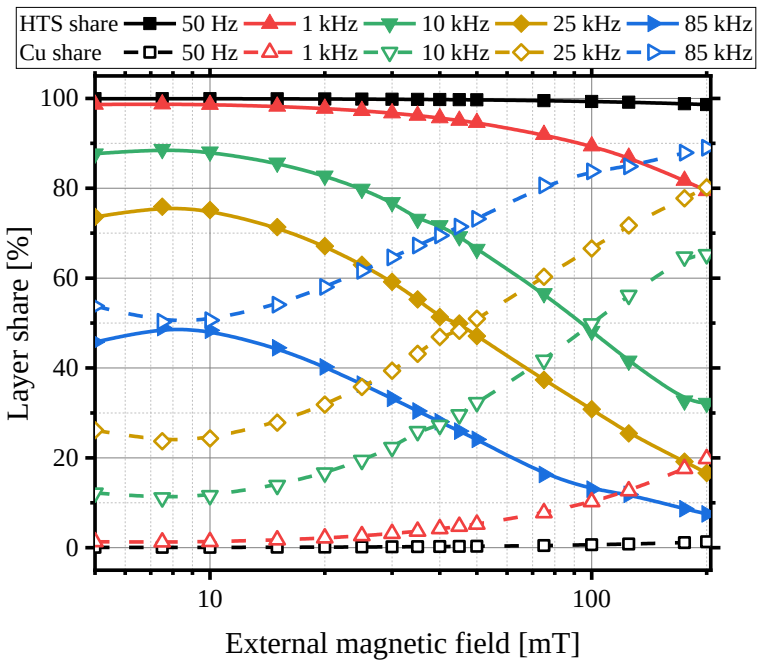

Figure 6-27. HTS (solid line) and copper (dashed line) layer loss contribution of an eight-turn solenoid coil for different frequencies and external magnetic field up to 200 mT

The cross over point i.e. transition frequency when $Q_{Cu}=Q_{HTS}$ is depicted in Figure 6-28. As shown, all three coil configurations exhibit similar trends in their transition frequency. It is characterised by a sharp parabolic trend, however, the maximum is shifted depending on the coil structure. The solenoid coil reaches its maximum transition frequency of circa 83 kHz at a magnetic field of approximately 7.5 mT, just shortly after reaching the threshold field. As each turn is subjected to the same external magnetic field, the solenoid configuration is extremely prone to magnetic fields above its threshold field, which affects the critical current density and has great impact on the loss distributions. Similarly, to the maximum transition frequency of the solenoid coil, the spiral coil reaches its peak at a magnetic field of 45 mT. Its transition frequency is attained at greater external fields, as inner turns are shielded. The double pancake coil has the highest transition frequency with almost 90 kHz, which it reaches at a magnetic field of 20 mT. It achieves the highest transition frequency as it combines shielding and cancelling effects.

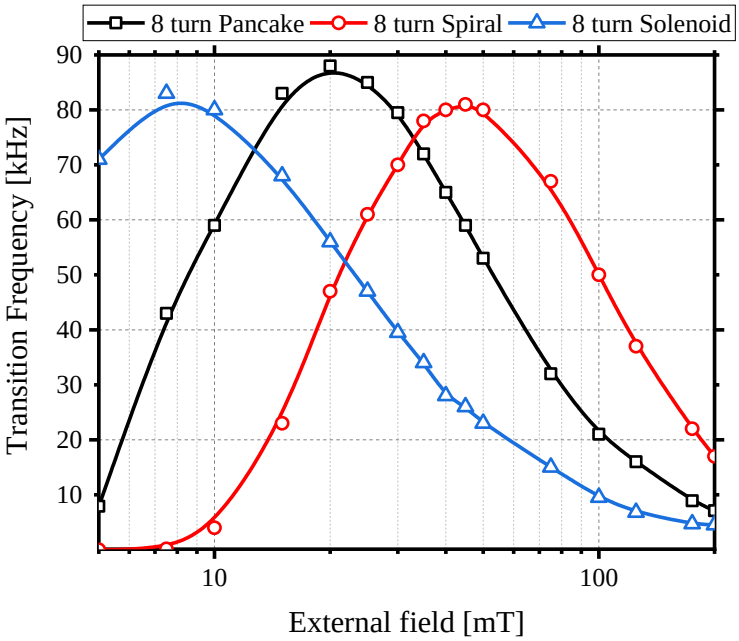

Figure 6-28. Transition frequency for different coil configurations over a range of external magnetic field densities

When looking at the magnetisation loss contribution of each turn for an external magnetic field of 100 mT, as shown in Figure 6-29 to Figure 6-31, the results are generally not skewed towards the innermost turns of the coil. While the turns in the middle of the coils are still shielded in the case of spiral and double pancake coil, the difference between inner and outermost turns is smaller. Nevertheless, the difference still increases with frequency providing further evidence of the skin effect. The opposite is true for the solenoid structure. While at frequencies below 10 kHz, the loss contribution amongst the different turns is stable, the discrepancy between the innermost and outermost turns increases with frequency and the outermost turns contribute less to the total loss than the innermost turns. This is due to a channelling effect enhancing the external magnetic field in the gaps between turns and the local magnetic field in the turns themselves. While the innermost turns are subject to this effect on either side, the outermost turns only face it on one side, reducing the overall loss in the turn compared to the other turns. The spiral layout is favourable when considering magnetisation loss characteristics in WPT systems.

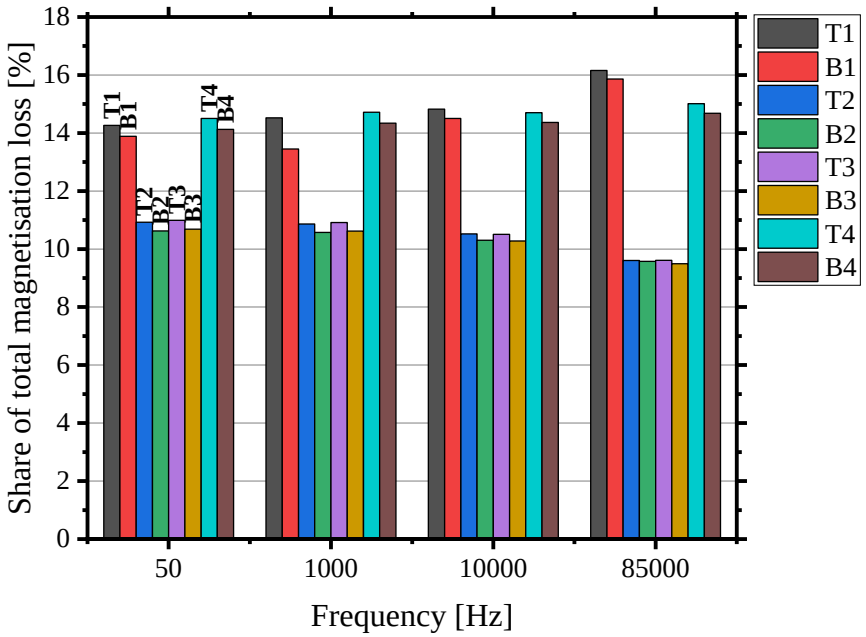

Figure 6-29. Turn loss contribution in an eight-turn double pancake coil for different frequencies with an external magnetic field of 100 mT

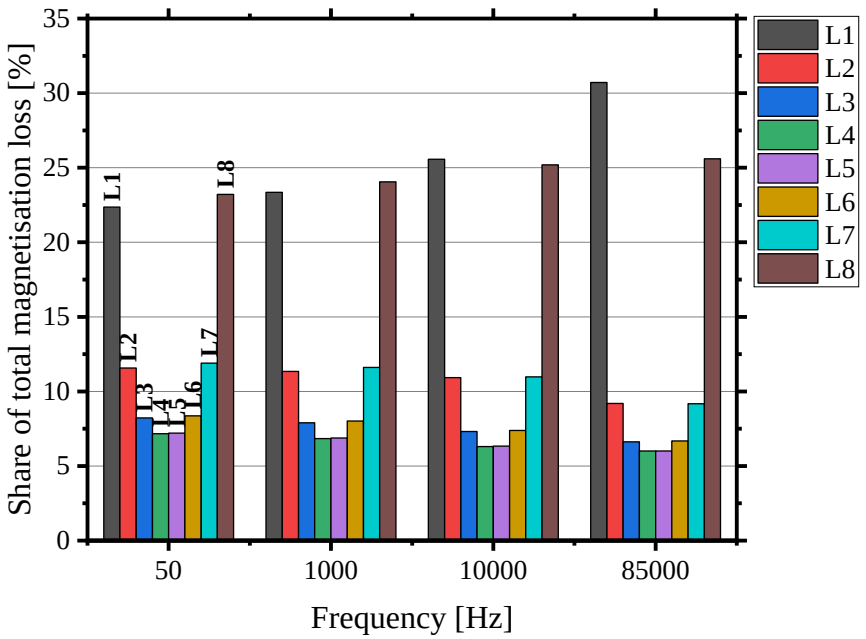

Figure 6-30. Turn loss contribution in an eight-turn spiral coil for different frequencies with an external magnetic field of 100 mT

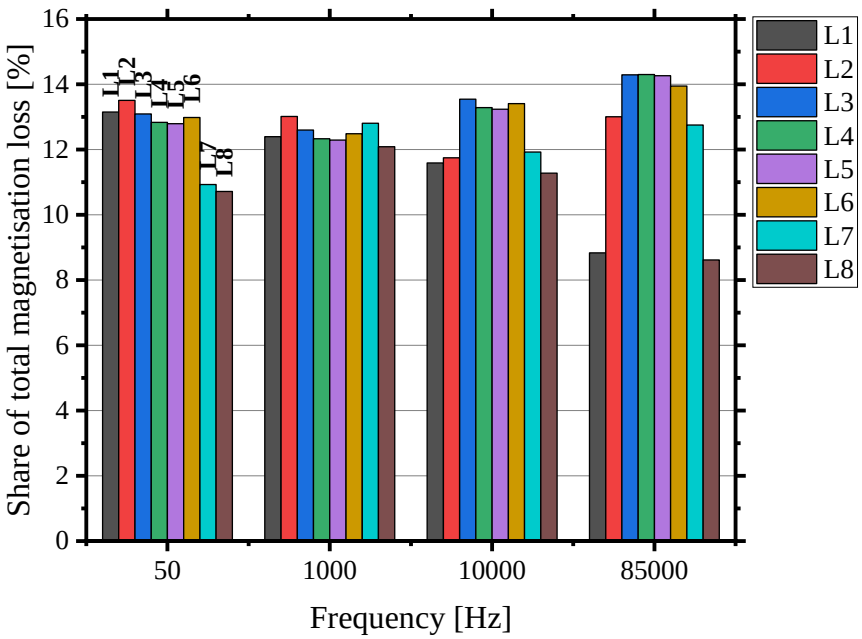

Figure 6-31. Turn loss contribution in an eight-turn solenoid coil for different frequencies with an external magnetic field of 100 mT

6.4.2 Magnetisation loss at different angles

WPT-systems operate at the highest capacity when the two charging pads are perfectly aligned. However, this is not always the case and particularly for DWPT-systems, the charging pads must link when the vehicle is not fully aligned with the charging pad. Operating under these conditions changes the angle of the external magnetic field onto the wide side of the tape. Hence, in this chapter the angular dependency of the magnetisation loss is investigated.

Figure 6-32 shows the angular dependency of the magnetisation loss for different coil layouts at 50 Hz and 85 kHz subject to an external magnetic field of 100 mT. As outlined in the previous chapter, the solenoid configuration experiences the highest loss, while the spiral coil has the lowest losses. All three different coil geometries exhibit the same trend for a frequency of 50 Hz. As the angle increases towards 60°, the magnetisation loss changes only marginally. At higher angles, the loss drops significantly until it reaches a minimum when the magnetic field is parallel to the wide surface of the tape. The losses drop significantly as the perpendicular field component is the main driver for the critical current density and therefore losses in the HTS layer. Hence all losses occur in the copper layer as shown in Figure 6-33 to Figure 6-35. When comparing the share of the HTS layer and copper layer, it can clearly be seen that the HTS share reaches a maximum at

0° and trails off with increasing angle. However, this is not the case for a solenoid coil as seen in Figure 6-34. As the angle increases, the total loss decreases too. But the copper losses decrease more rapidly until the external magnetic field is parallel to the tape, where the losses in the HTS layer become negligible. As the frequency increases, more losses occur in the copper layer. This phenomenon is independent of the angle. For a frequency of 85 kHz the different coil geometries have increased losses but vastly different loss characteristics. In the case of the solenoid, the overall trend does not change. However, the initial range of small changes is less pronounced and losses stay mostly constant up to an angle of approximately 30°.

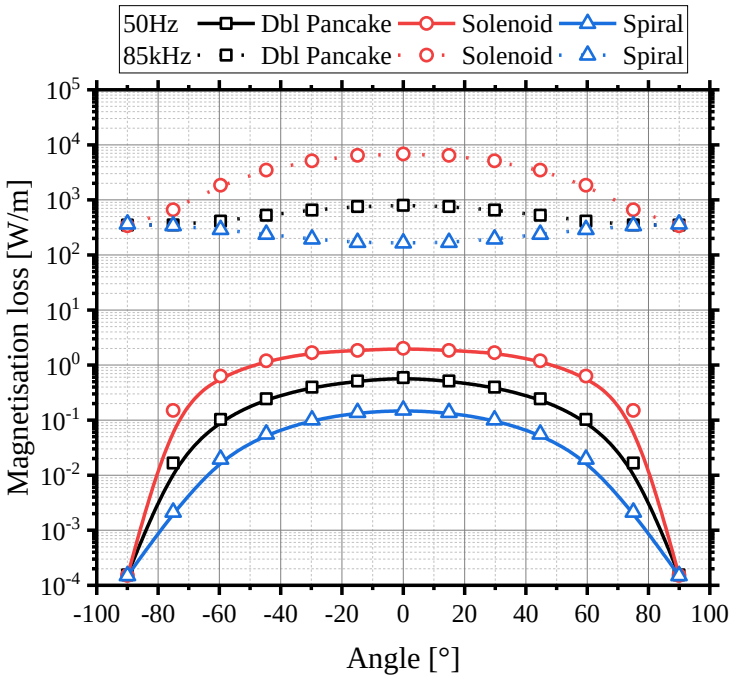

Figure 6-32. Angular dependency of magnetisation loss for different eight-turn coil configurations at 50 Hz and 85kHz at 100 mT.

On the contrary, the loss of the spiral coil slightly increases with angle. The increase in loss is due to the fact that the copper layer is responsible for the main share of the losses at 85 kHz and as the angle increases the shielding of the turns in the middle is lost, subjecting all copper layers to a high external magnetic field. Furthermore, eddy currents have a greater area to loop around. While the losses with B_{ext}=100 mT in the HTS layer reduce by two orders of magnitude, the losses in the copper layer quadruple as the orientation of the external magnetic field changes. For the double pancake configuration, the magnetisation loss is roughly independent of the angle, while there is a slight maximum when the external magnetic field is perpendicular to the wide tape surface. The

double pancake coil combines characteristics of the spiral and solenoid coil, which partly cancel out. The overall trends shown in Figure 6-32 also apply to other magnetic field densities.

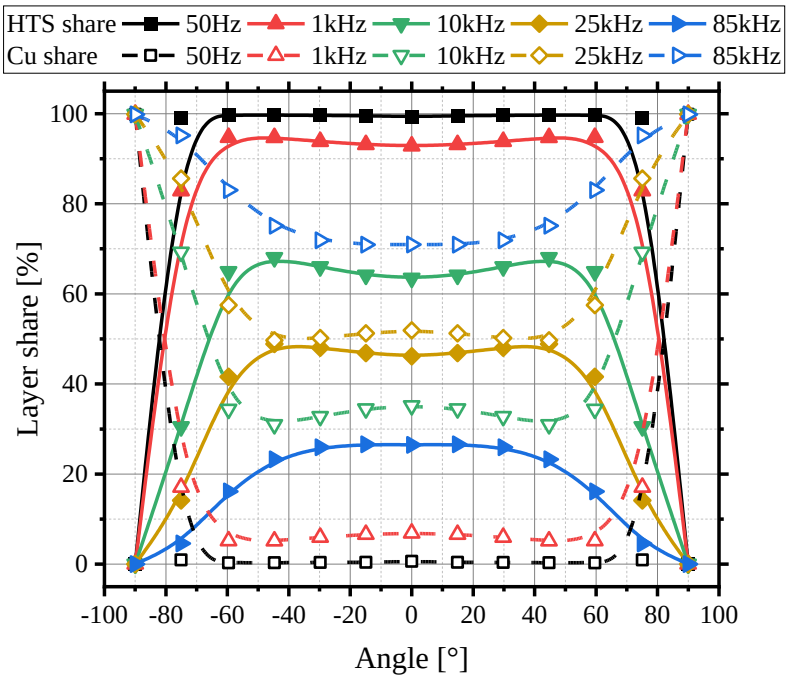

Figure 6-33 HTS and copper share vs angle of external magnetic field for an eight-turn double pancake coil at different frequencies at Bext= 100mT

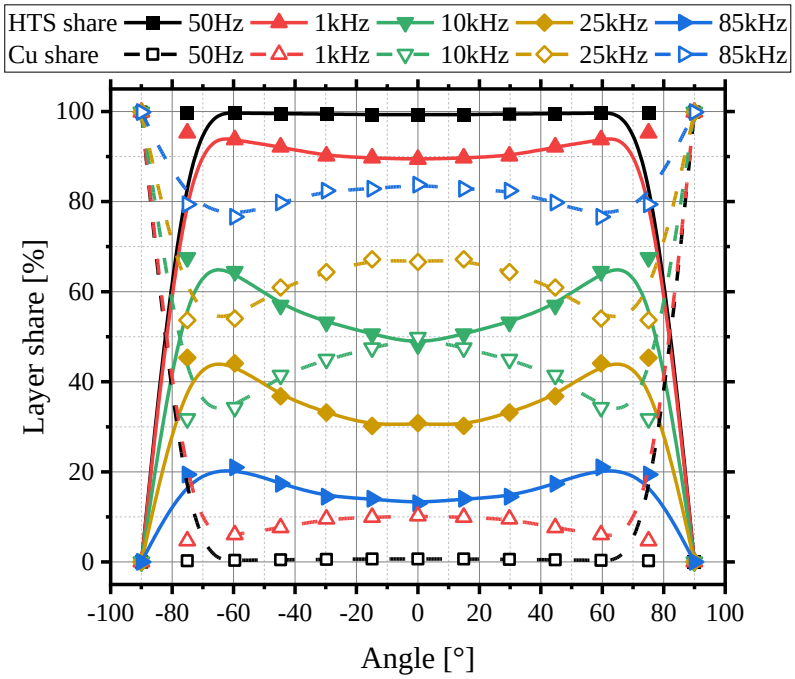

Figure 6-34 HTS and copper share vs angle of external magnetic field for an eight-turn solenoid coil at different frequencies at Bext=100 mT

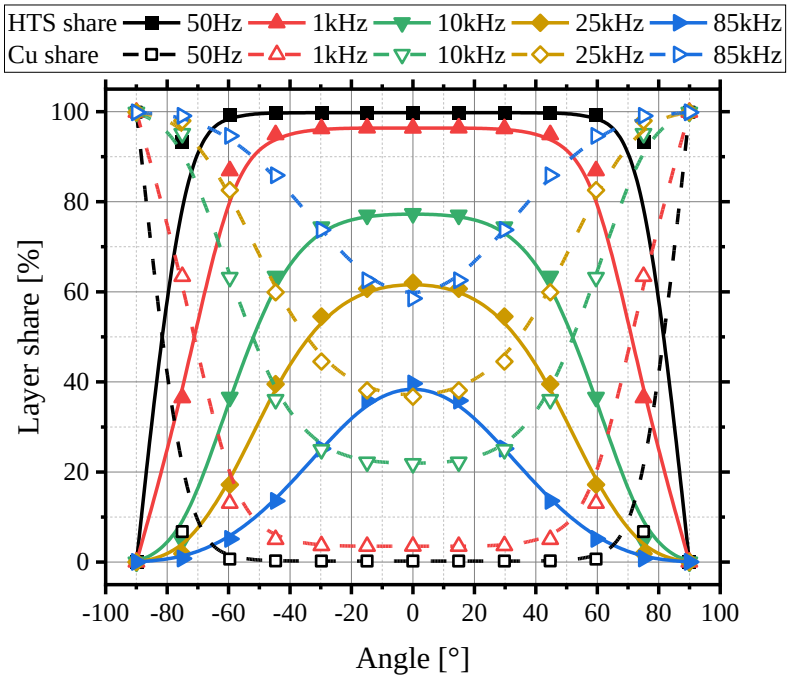

Figure 6-35 HTS and copper share vs angle of external magnetic field for an eight-turn spiral coil at different frequencies at Bext=100 mT

Figure 6-36 to Figure 6-38 show the evolution of the layer contributions for different external magnetic field densities at frequencies of 50 Hz, 10 kHz and 85 kHz for a double pancake coil. As seen, at 50 Hz the majority of the losses are generated in the HTS layer for a wide range of angles. As stated earlier, there is a sharp transition between the copper and the HTS layer shares. However, as the external magnetic field becomes stronger, the maximum angle before the transition from HTS to copper layer increases e.g. from just over 40° for 7.5 mT to approximately 75° at 200 mT. With increasing frequency e.g. 10 kHz, the transition loses its sharpness and losses are not primarily generated in one of the two layers but rather both contribute a large portion of the losses. For small angles, most losses occur in the HTS layer, while large angles lead to a higher contribution of the copper layer. If the frequency is even higher e.g. 85 kHz, the majority of the losses will be generated in the copper layer due to the skin effect. Furthermore, as the magnetic field density increases beyond 45 mT, the losses in the copper layer increase more rapidly than in the HTS layer, this results in the relative decrease in the magnitude of the HTS share with magnetic field density and the flattening of the peak.

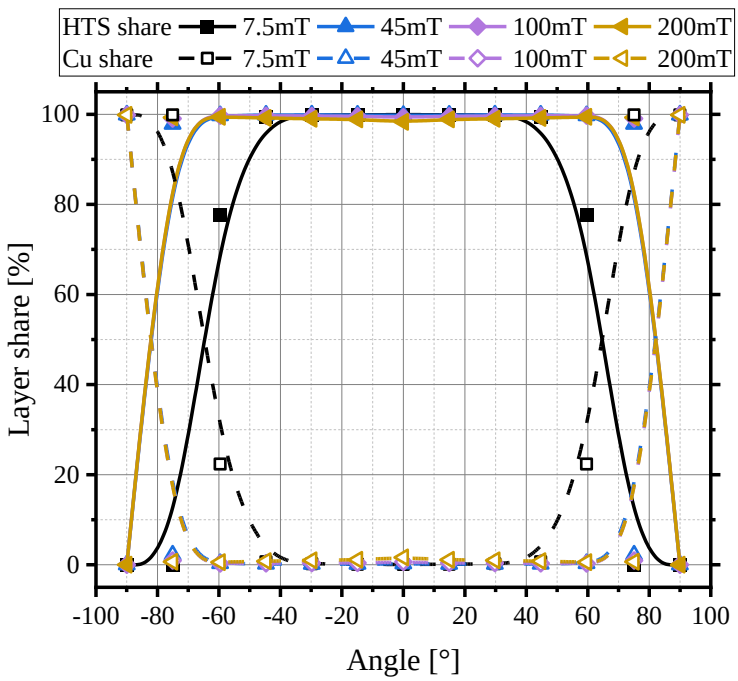

Figure 6-36 HTS and Cu share vs angle of external magnetic field for an eight-turn double pancake coil at different Bext at 50 Hz

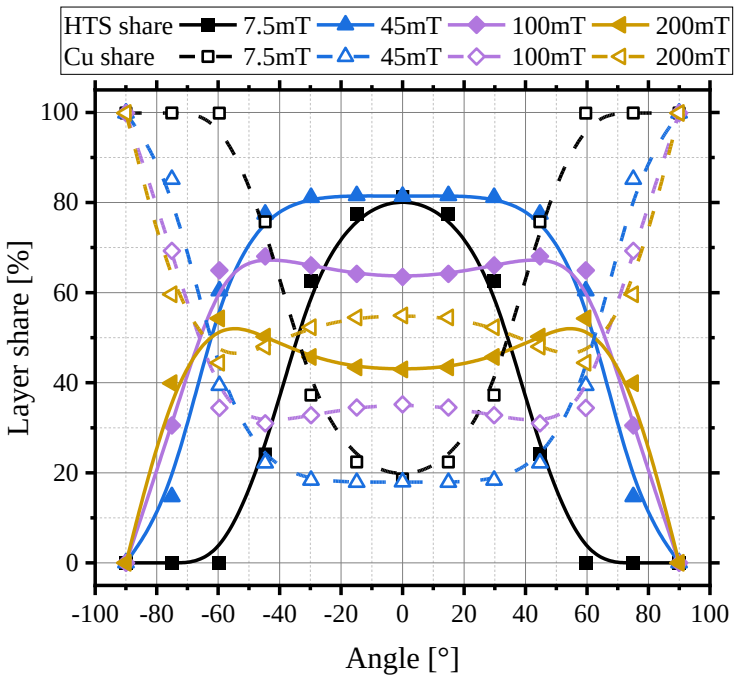

Figure 6-37 HTS and Cu share vs angle of external magnetic field for an eight-turn double pancake coil at different Bext at 10 kHz

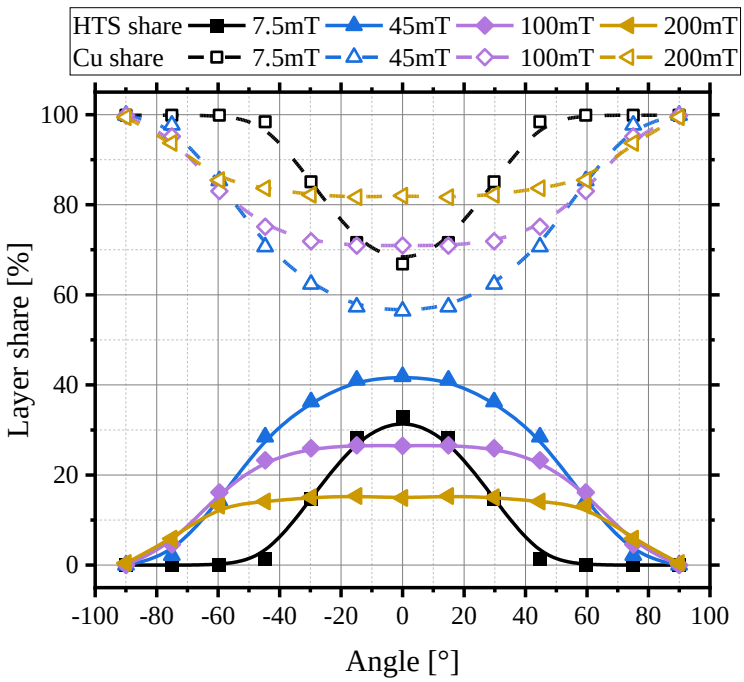

Figure 6-38 HTS and Cu share vs angle of external magnetic field for an eight-turn double pancake coil at different Bext at 85 kHz

6.5 Combined losses

6.5.1 Transport current and magnetisation loss

This chapter discusses the effect of applying a time varying transport current while also being subject to an external AC magnetic field, posing as real scenarios encountered by HTS WPT-systems. Transport current and external magnetic field have the same frequency and there is no phase shift (Ps) between the two. In general, there will be a 90° phase shift between the external magnetic field linking both coils and the induced current in the receiving coil. Figure 6-39 shows the difference between in-phase AC transport current and external magnetic field and 90° out of phase current and magnetic field. The losses generated by the HTS coils are slightly reduced when a 90° phase shift is introduced as the peak of the transport current does not coincide with the peak of the external magnetic field anymore. As there is only a minor difference the phase shift will be neglected in this chapter, but it should be included for a proper system design.

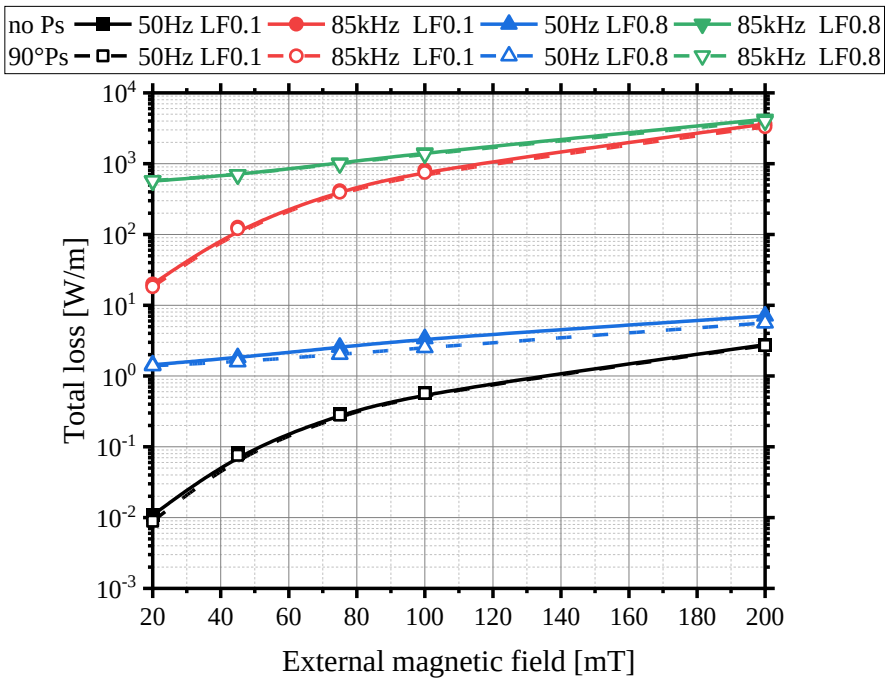

Figure 6-39 Comparison of combined losses for an eight-turn double pancake coil with and without phase shift (Ps) for 50 Hz and 85 kHz and LF of 0.1 and 0.8 with B_{ext}=100 mT

The total loss for the simultaneous application of AC transport current and AC external magnetic field for a double pancake coil, spiral and solenoid coil is depicted in Figure 6-40 to Figure 6-42. Two load factors, namely 0.1 and 0.8 are considered and the effect of the external magnetic field density is investigated. As shown in Figure 6-43 and Figure 6-44 for a double pancake coil, the

impact of the magnetic field changes depending on the load factor and frequency. The magnetic field distribution and current density distribution shrinks with frequency and is confined to a smaller area. Compared with Figure 6-23, a low LF, such as 0.1, shows only a minor impact on the distribution as it is dictated by an external magnetic field. However, as the LF increases, the distribution shows the strong interaction between the self-field due to the transport current and the external magnetic field. In addition to the interactions, each coil configuration reacts differently. The losses of the double pancake coil operating at LF=0.1 increase slowly with magnetic field density up to circa 15 mT. Afterwards, the losses increase linearly. Here the transition point is independent of the frequency. If the load factor is increased to 0.8, the losses are approximately constant up to a magnetic field density of 50 mT and then increase linearly as well. At higher magnetic field densities e.g. 200 mT the losses generated for the two load factors are approaching each other and the difference decreases with frequency. It can be concluded that the loss due to the transport current dominates at lower magnetic field densities, whereas the loss becomes increasingly independent of the load factor at higher field densities and frequencies. Lower magnetic field densities have only a minor effect on the overall self-field along the HTS turns. However, as the external field becomes stronger, the self-field along the windings of the coil increases and causes higher losses. One should also note that, the magnetic field in general is enhanced on one side of the windings, while it is reduced on the other side according to the right-hand rule (see Figure 6-43). The spiral and solenoid coils exhibit a similar behaviour, however, the transition between a minor increase in losses due to the magnetic field and linear increase is at a higher field density for the spiral and at a lower field density for the solenoid.

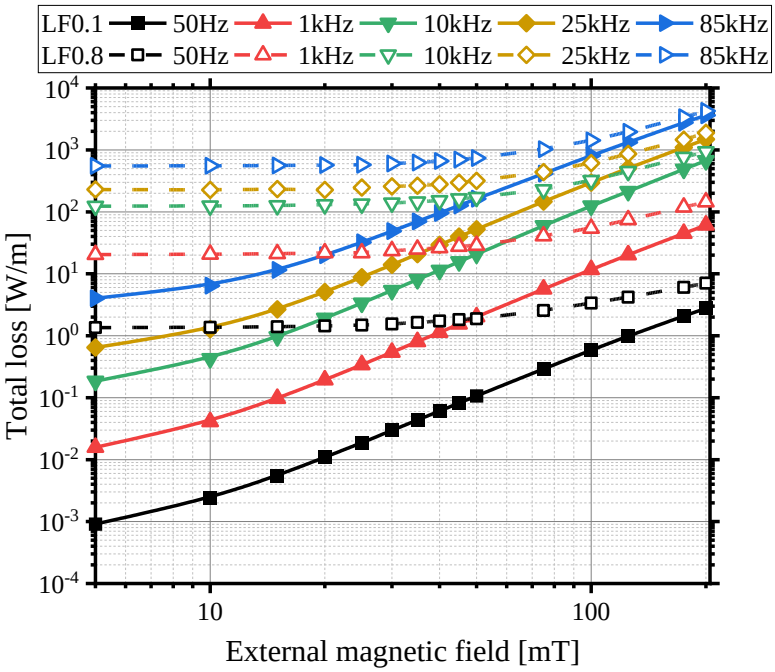

Figure 6-40 Combined losses for an eight-turn double pancake coil vs B_{ext} for various frequencies and a LF of 0.1 and 0.8, respectively

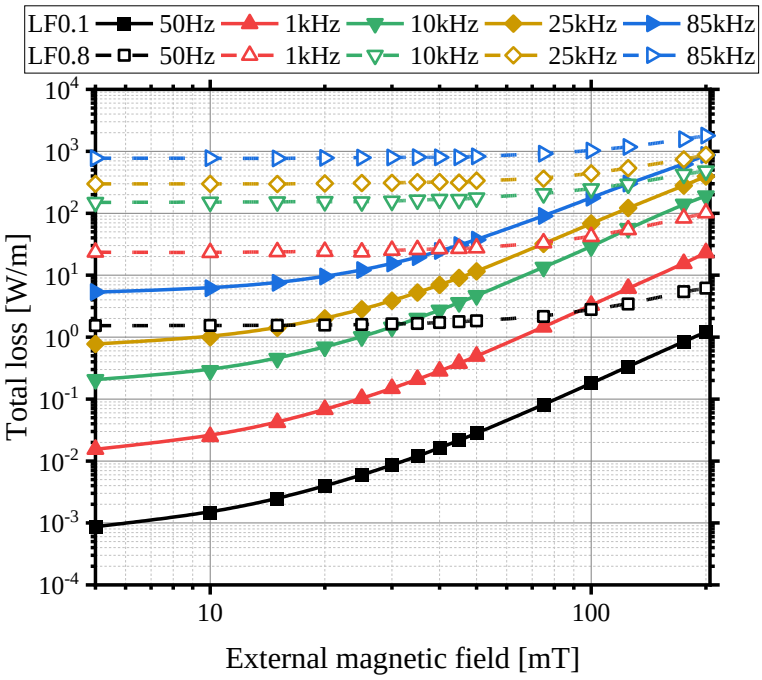

Figure 6-41 Combined losses for an eight-turn spiral coil vs B_{ext} for various frequencies and a LF of 0.1 and 0.8, respectively

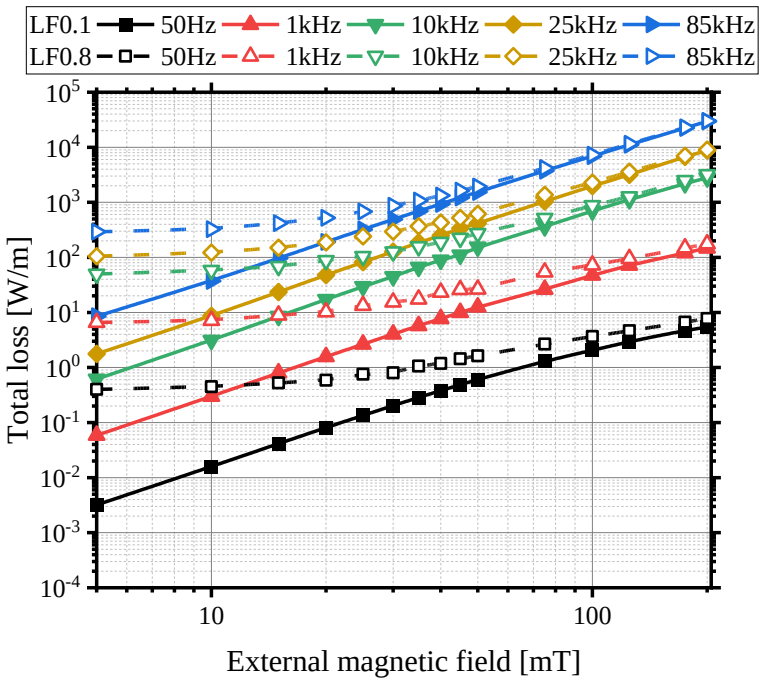

Figure 6-42 Combined losses for an eight-turn solenoid coil vs B_{ext} for various frequencies and a LF of 0.1 and 0.8, respectively

a) 50 Hz LF=0.1

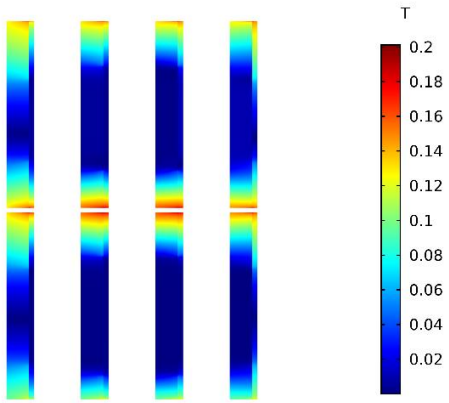

b) 50 Hz LF=0.8

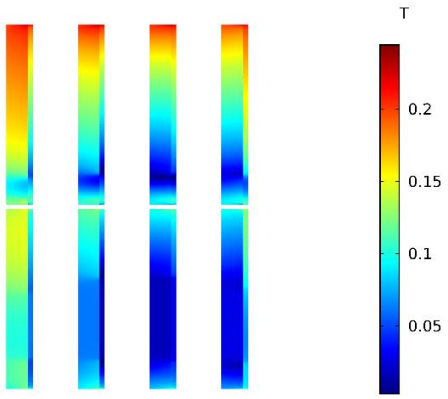

c) 10kHz LF=0.1

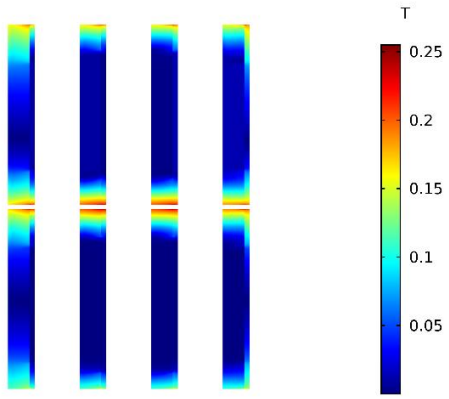

d) 10kHz LF=0.8

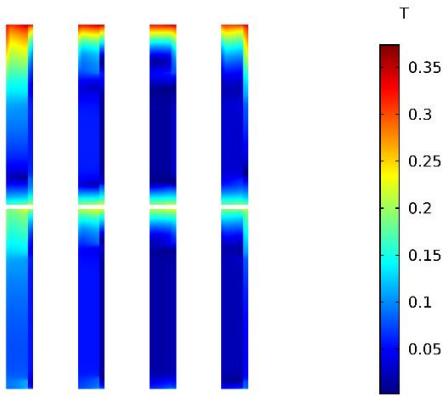

e) 85kHz LF=0.1

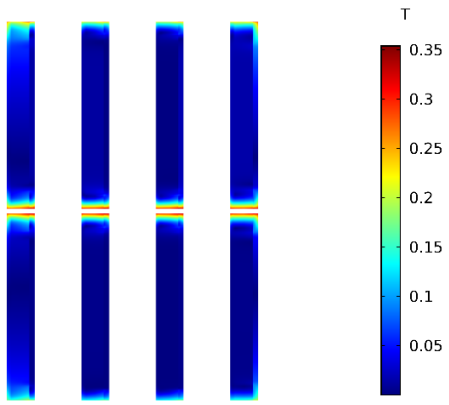

f) 85kHz LF=0.8

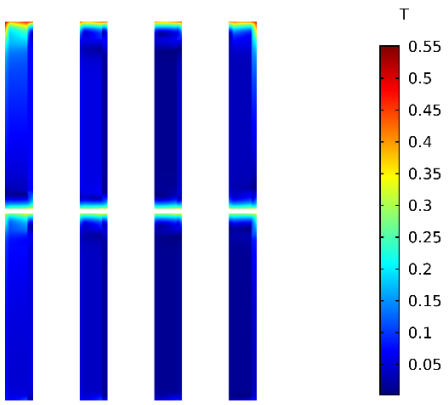

Figure 6-43 Magnetic field distribution in the HTS tapes of a double pancake coil at $3\pi/2$ subject to an external magnetic field B_{ext}=100 mT and a LF=0.1 a),c),e) and LF=0.8 b),d),f) at 50 Hz, 10 kHz and 85 kHz, respectively

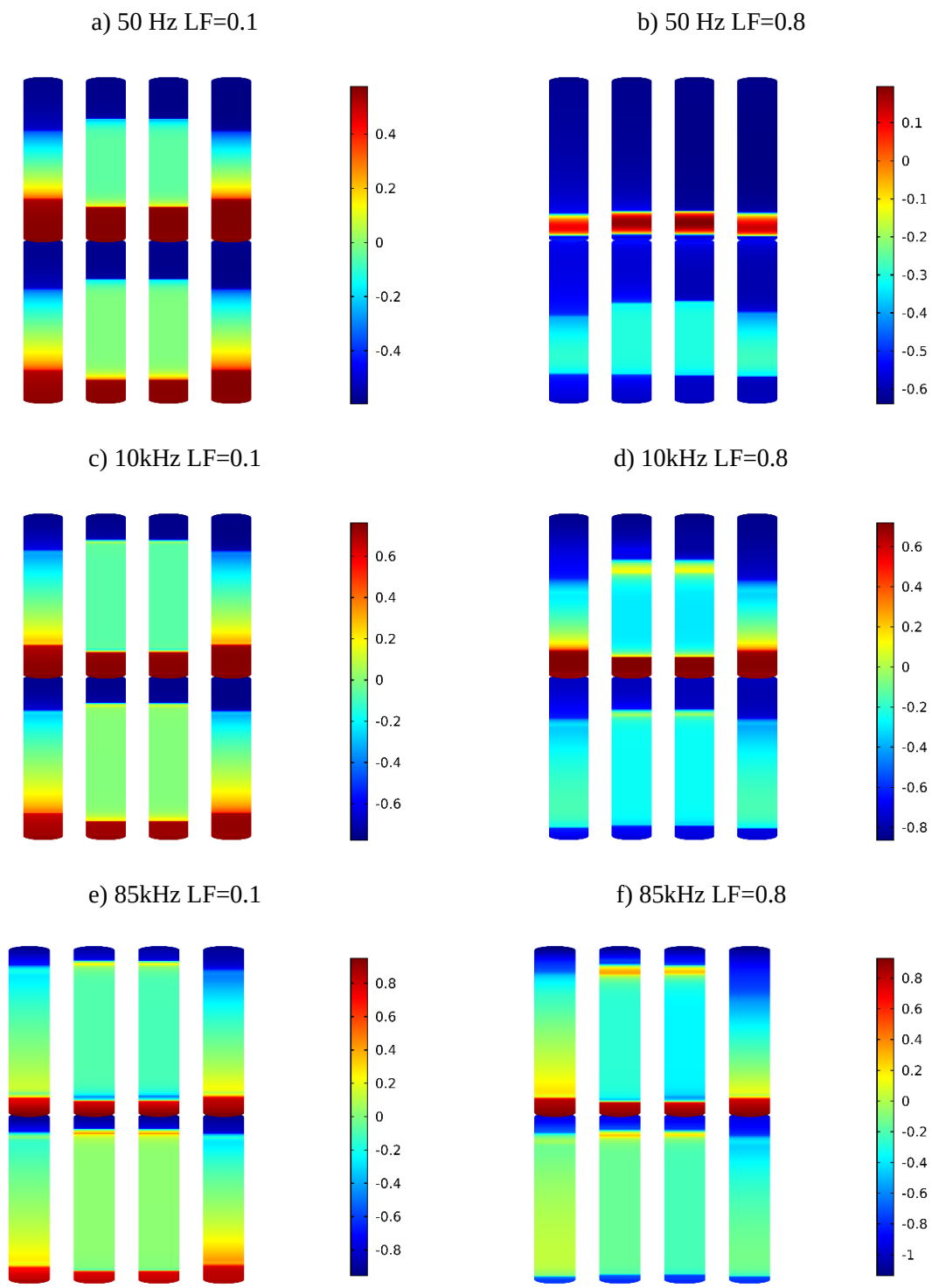

Figure 6-44 Current density distribution J/J_c in the HTS layer of a double pancake coil at $3\pi/2$ subject to an external magnetic field. B_{ext}=100 mT and a LF=0.1 a), c), e) and LF=0.8 b), d), f) at 50 Hz, 10 kHz and 85 kHz, respectively. The thickness of the HTS layer has been scaled to improve visibility.

The transition frequencies for different load factors between LF=0.1-0.8 of the coil geometries investigated are displayed in Figure 6-45 to Figure 6-47. As shown, the initial parabolic trend is flattened with increasing load factor irrespective of the coil structure. For smaller external fields, the transport current loss in the HTS layer dominates the transition frequency. This results in an increase in transition frequency for low external magnetic field densities. For load factors smaller than LF=0.4, an overall peak in transition frequency exists, similar to the LF=0 case. However, the transition frequency is much lower. As the load factor increases to ultimately LF=0.8, the transition frequencies widely remain constant, particularly for external fields up to circa 50mT, as the loss share for the HTS and copper layers stay constant. The transport current dictates the transition frequencies for small and medium external magnetic field densities. While at large external fields, the transition frequency is reduced further due to the skin effect and the increased magnetic flux that penetrates the HTS layer and therefore lowering the critical current density.

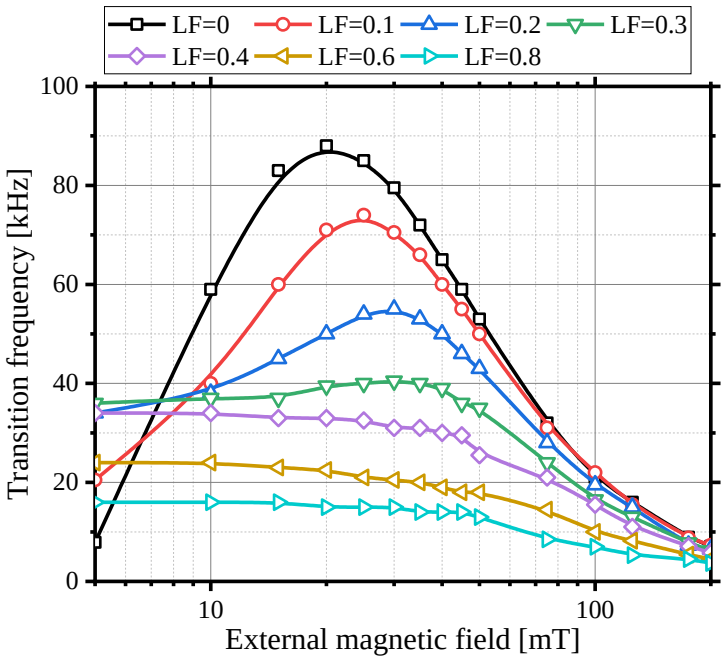

Figure 6-45. Transition frequency for eight-turn double pancake coil over a range of external magnetic field densities and various load factors

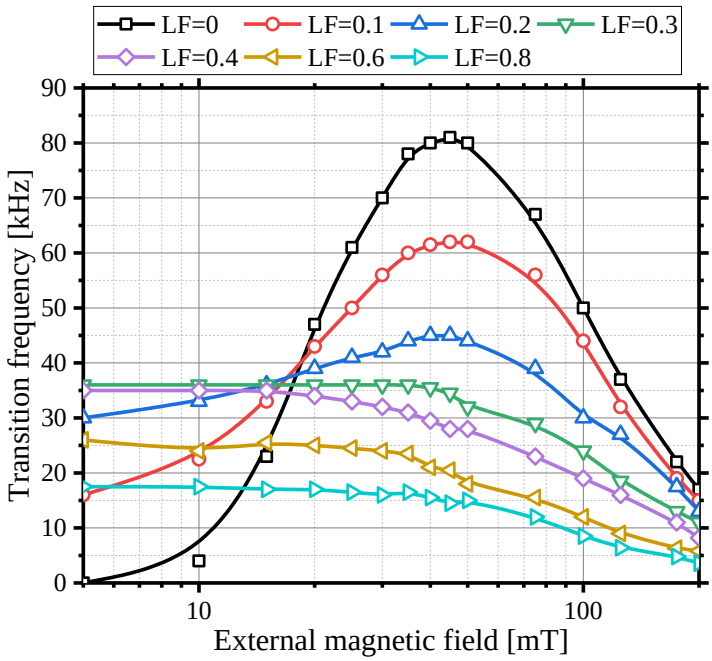

Figure 6-46. Transition frequency for eight-turn spiral coil over a range of external magnetic field densities and various load factors

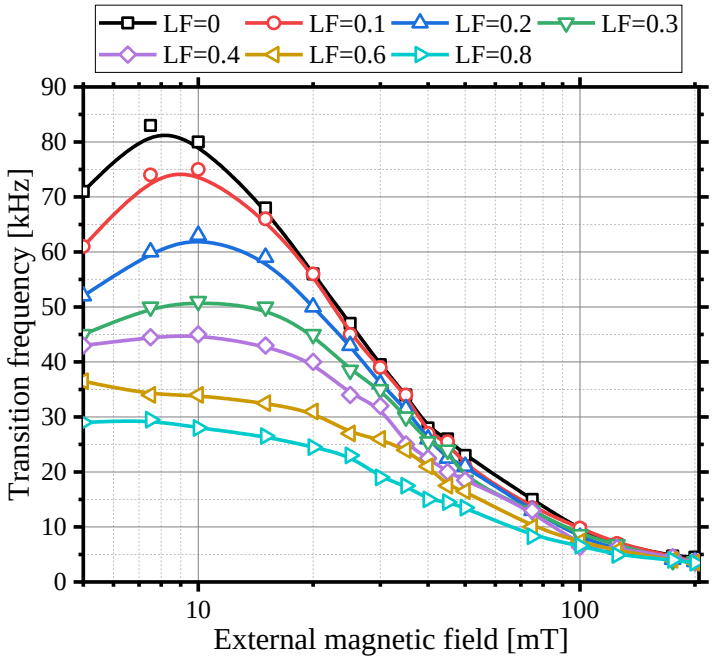

Figure 6-47. Transition frequency for eight-turn solenoid coil over a range of external magnetic field densities and various load factors

For small load factors e.g. 0.1, the loss distribution is very similar to the distributions of the magnetisation loss (Figure 6-29 to Figure 6-31). Some turns have a higher share than for the case of no transport current, which is mainly based on the interaction between the transport current and the external magnetic field. As the load factor increases, the top layer of turns in the double pancake coil have a ten times higher contribution than the bottom layer (Figure 6-48). Independent of the frequency, both layers of the double pancake coil behave similarly and the only distinction is the magnetic field enhancement in the top layer and the partly cancelled field in the bottom layer, which leads to a higher loss and lower loss, respectively. On the contrary, the spiral coil was previously characterised by a symmetric loss distribution, where the outermost turns have the highest losses and the turns in the middle have the lowest. As the load factor increases to 0.8 (Figure 6-49), this symmetry is lost and all turns generate approximately the same loss for frequencies below 10 kHz. The magnetic field above the spiral coil is enhanced, while the field at the bottom is widely reduced to about half the magnitude of the topside. At 50 Hz the magnetic field is evenly distributed at the top, yet as the frequency increases, the skin effect sets in and current as well as the magnetic field gets pushed towards the edges of the tape reinforcing the interaction between external and self-field and above 10 kHz the original symmetry is re-established and the outermost turns contribute the highest loss. The loss distribution for the solenoid coils is depicted in Figure 6-50 and had a symmetric distribution, similar to the spiral coil, but more pronounced. Conversely, the solenoid coil is very susceptible to the external magnetic field and with the introduction of it, the loss distribution shifts dramatically to the side of the winding where the external magnetic field enhances the self-field generated by the transport current. This shift increases with frequency up to 85 kHz, but at 85 kHz, the highest loss is not in the outermost turn but rather in the second turn. As the frequency increases, the transport current is pushed towards the outer edges of the turns through the skin effect. This leads to an increase of the local magnetic field in the inter-turn spacing, which coincides with the local maximum of the current density. However, the outermost turn is only partly affected by this local magnetic field in the gap, whereas the second turn is subject to such maxima on either side. Even though one of the maxima is smaller than the outermost, it is still sufficient to boost the loss beyond the loss in the outermost turn.

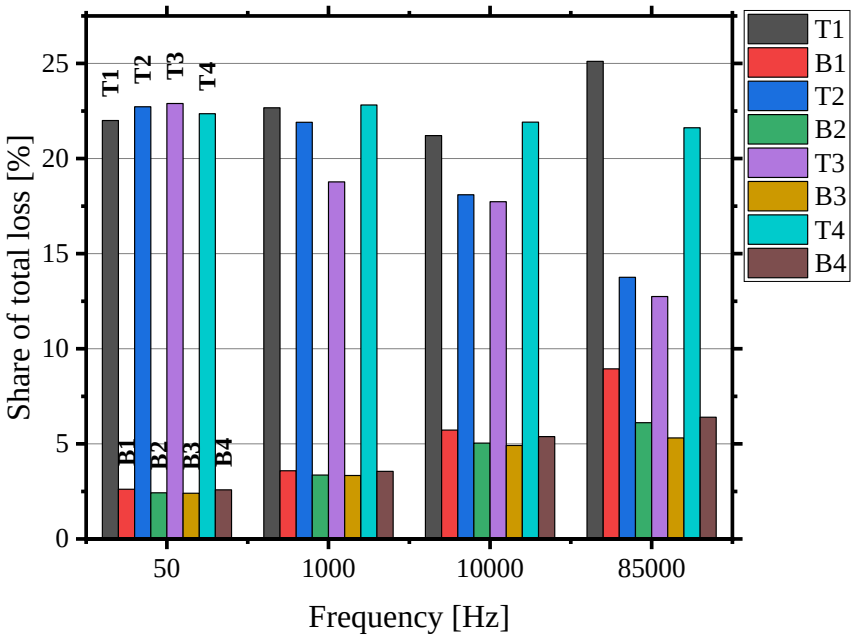

Figure 6-48 Turn loss contribution in an eight-turn double pancake coil for different frequencies at a LF=0.8 and B_{ext}=100 mT

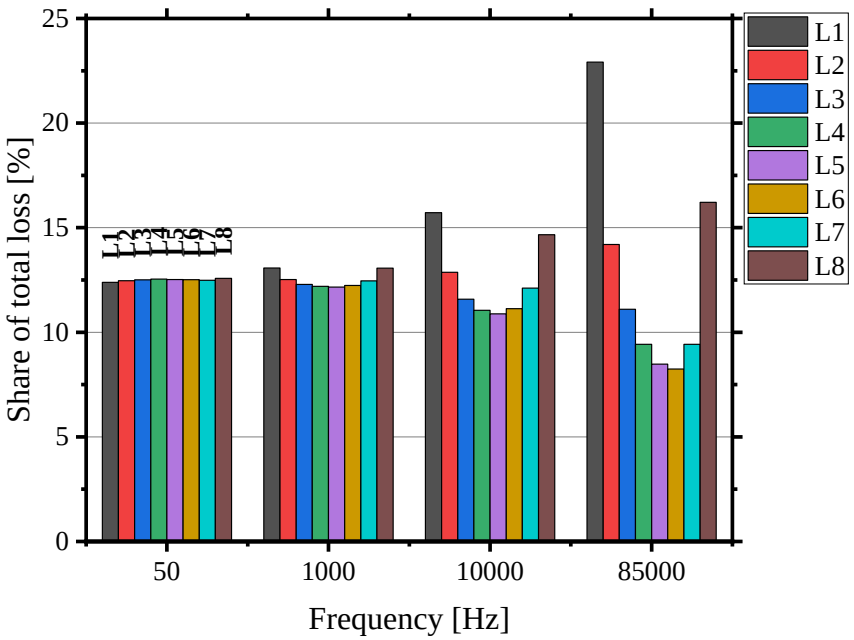

Figure 6-49 Turn loss contribution in an eight-turn spiral coil for different frequencies at a LF=0.8 and B_{ext}=100 mT

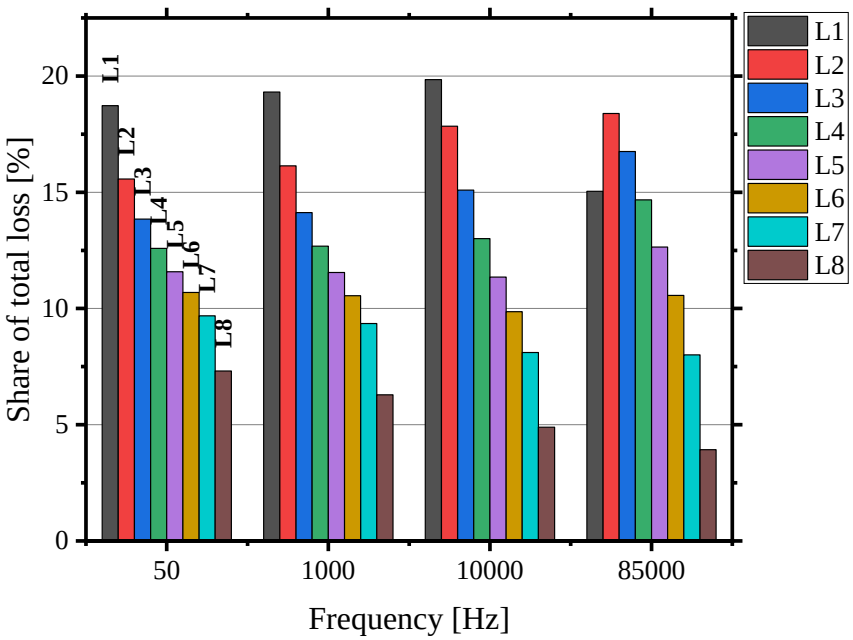

Figure 6-50 Turn loss contribution in an eight-turn solenoid coil for different frequencies at a LF=0.8 and B_{ext}=100 mT

6.5.2 Transport current and magnetisation loss under angular external field

In this chapter the angular dependence of the combined losses is investigated. An AC transport current is applied to the different coil geometries while they are being subjected to an AC external magnetic field with several angles between perpendicular and parallel to the wide surface of the tape. The angular dependence is depicted for a frequency of 50 Hz in Figure 6-51 and for 85 kHz in Figure 6-52. The investigated load factors are 0.1, 0.4 and 0.8. Similar to the angular dependence of the magnetisation loss, the introduction of an additional transport current does not alter the characteristics. At 50 Hz, the losses drop sharply with increasing angle. The sharp decrease is partly offset by the increasing load factor and the peak is less pronounced for LF=0.4 and 0.8. As the load factor increases more current is within the HTS layer and therefore, the effect of the external magnetic field and the shift towards a minimum in the perpendicular field component is offset. This is also the case for higher frequencies such as 85 kHz. However, the impact is different for the separate geometries, with a very small change with higher load factors for the solenoid coil and a large change in the spiral coil.

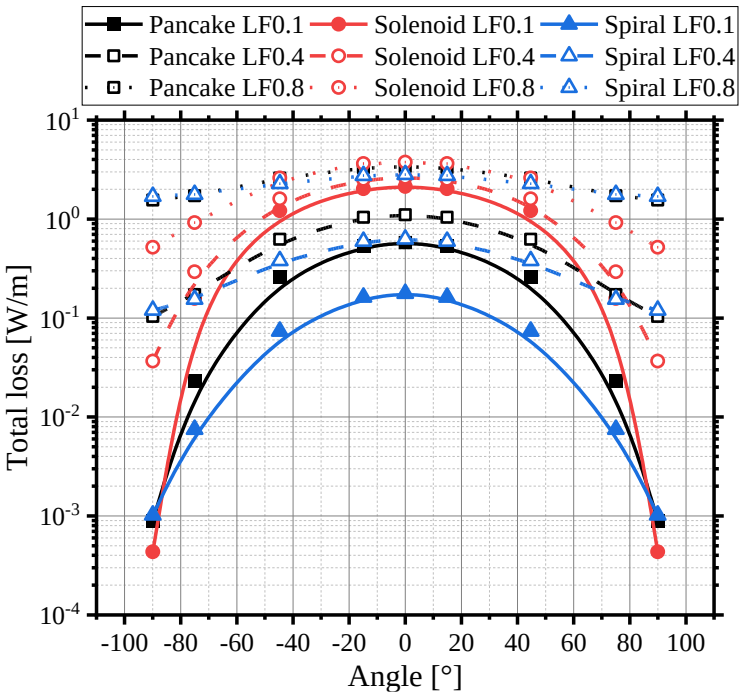

Figure 6-51 Angular dependency of the combined losses of different coils subject to an external magnetic field Bext=100 mT at 50 Hz and various LF

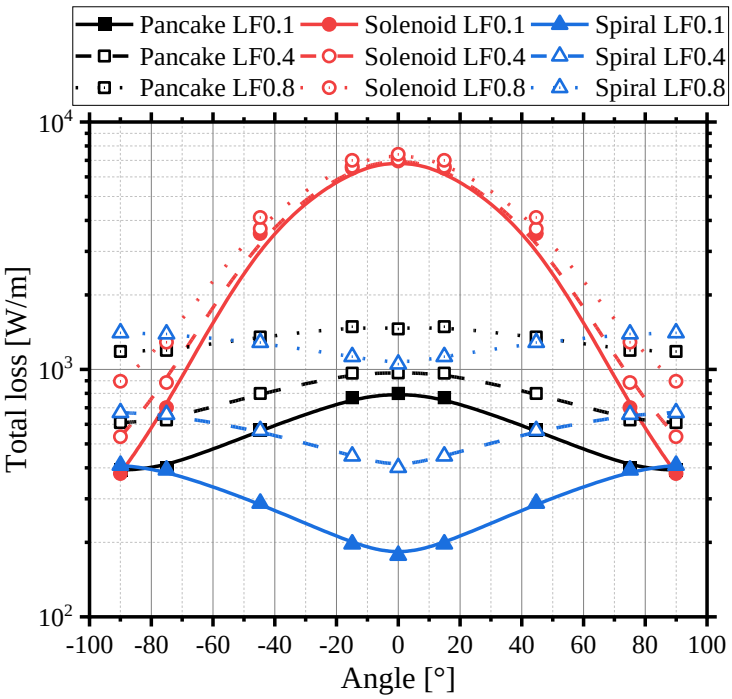

Figure 6-52 Angular dependency of the combined losses of different coils subject to an external magnetic field Bext=100 mT at 85 kHz and various LF

6.6 Conclusion

For the first time, an investigation of the transport current loss, magnetisation loss, combined loss and their angular dependence of HTS coils in the frequency relevant to WPT (up to 85 kHz) for EVs has been carried out. The study used a 2D axisymmetric multilayer coil model, resolving the overall loss distribution in the turns and showed that, the loss in the copper layer surpasses the loss generated by the HTS layer at higher frequencies. Three different coil configurations were used, including spiral, solenoid and double pancake. In addition, a comparison between the full anisotropic dependency of the critical current and only considering perpendicular field components for HTS WPT coils was conducted. Results show that the effect of the parallel field is only minor even in (multilayer) HTS coils. Hence, can be neglected for coils.

Key findings include:

1) Investigation of transport current losses in various HTS coil structures in the frequency range from 50 Hz to 85 kHz with the aid of a multilayer model taking skin effect into account. In general, the frequency has a great impact on the transport current loss and its effect increases at higher load factors. Solenoid coils have the lowest transport current loss, while spiral coils have the highest.

2) The magnetisation loss increases with increasing magnetic field densities and frequency. Contrary to the results obtained from the transport current loss calculations, the spiral configuration has the lowest magnetisation loss, while the solenoid layout has the highest. Depending on the frequency, the main contributor towards the magnetisation loss shifts between the copper and the HTS layer. At higher frequencies, the penetration depth of the external magnetic field changes and the field cannot penetrate the HTS layer, subjecting the copper stabilisers to high losses. For medium external magnetic fields, the HTS layer generates the main share of losses before it shifts back into the copper stabilisers depending on a high enough magnetic field. The range of magnetic field densities, causing the highest loss to occur in the HTS layer, decreases with increasing frequency until the losses in the copper stabilisers are always higher than the HTS layer losses.

3) The angular dependence of the magnetisation and the combined losses are investigated. At low frequencies such as 50 Hz all three geometries exhibit similar trends. However, as the frequency increases, up to 85 kHz, their respective characteristics differ drastically. While the solenoid behaves the same, the losses in the spiral coil increase with angle due to the loss of shielding of the turns in the middle of the winding and the greater area of the eddy current. As the double

pancake coil combines the characteristics of the other two geometries, its losses have a more subtle trend compared with the solenoid configuration.

4) The impact of the magnetic field on the combined total loss changes depending on the load factor, frequency and winding layout. Initially, the losses increase slowly with magnetic field density up to a specific field density, dependent on the coil configuration. Afterwards, the losses increase linearly. For low magnetic field densities, the load factor dictates the losses and for high field densities the losses generated become independent of the load factor as the frequency increases. Compared to the double pancake layout, the spiral transitions at higher field densities between a minor increase in losses due to the magnetic field and linear increase is at a higher field density and the solenoid at a lower field density.

5) A transition frequency was introduced, at which copper losses are equal to the losses in the HTS layer. Due to the interaction between the different turns, the transition frequency for coils is much smaller than for single tapes. Below a LF of 0.3 there was no significant difference between the coil structures. At higher LF, the solenoid coil had a much higher transition frequency.

The transition frequency for the magnetisation loss is vastly different than in the case of transport current loss. It is characterised by a sharp maximum, which is shifted depending on the coil arrangement. The spiral coil reaches its transition frequency at the highest external field densities, while the double pancake coil has the marginally highest frequency.

When combining transport current and external magnetic field, the transition frequency is mainly influenced by the transport current and its associated loss. For low external fields, the transition frequency increases when compared with cases where only the external field is applied. On the contrary, at high external fields, the transition frequency is reduced further due to skin effect and the reduced critical current density.

6) Examination of loss contribution of individual turns within the coil. The transport current loss contribution of single turns within the coils showed that losses are heavily generated in the innermost turns. While the trend increases with frequency for the spiral and double pancake configuration, it decreases for the solenoid coil. The magnetisation loss contribution of individual turns was not skewed towards the innermost turns, particularly for the solenoid structure. Within the solenoid coil, the outermost turns have the lowest contribution as the magnetic field is enhanced in the gaps between subsequent turns.

7 AC loss reduction measures

7.1 Introduction

The losses generated by the HTS coils are extremely high for LF and frequencies targeted by wireless charging systems, particularly taking into account that the operating temperature is 77K. Therefore, the reduction of the AC losses of HTS coils is a key research topic to increase viability of such coils in high frequency applications up to 85 kHz. To reduce the overall losses of the system two main methods can be utilised. On one hand, another tape or superconductor can be used such as MgB_2 or stabiliser-free tape. On the other hand, additional components such as flux diverters can be implemented to reduce the magnetic field and therefore losses. Both approaches will be discussed in this chapter and a more in-depth analysis of flux diverters and their viability at high frequencies will be given. The work on flux diverters has been submitted for publication as [5].

Furthermore, improvements to the manufacturing process can be made to enhance flux pinning and other intrinsic properties. However, such techniques can be used in the future and not with currently available HTS tapes. Therefore, while being a powerful tool and research will progress in these areas, they are not discussed here.

7.2 Different tapes and materials

Other superconductors such as MgB_2 can be used to reduce the overall AC loss of the coil. It is widely used in superconducting applications for its lower AC losses due to its multifilamentary structure as depicted in Figure 7-1 [380], [381], [382], [383].

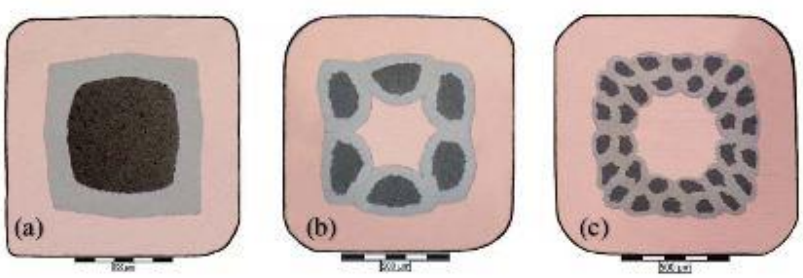

Figure 7-1 Cross-sections of typical rectangular MgB_2 wires [384]

MgB_2 wires comprise of several different materials and therefore all loss mechanisms introduced in chapter 2.4 must be accounted for when analysis and calculating AC losses. Analytical

equations to estimate such losses exists and are listed below and are applicable for a cylindrical conductor. The average hysteresis loss P_h can be calculated using either Eq. 7.1 or 7.2 depending on the relationship between the penetration field H_p and the external magnetic field H_0 [385]. Where, j_c is the critical current density, λ is the superconductor fill factor, f is the frequency, V is the volume and a is the radius of the MgB_2 filament.

$$\frac{P_h}{V} = \lambda f \frac{16}{3\pi} a \mu_0 H_0 j_c \qquad \text{for } H_0 \gg H_p \tag{7.1}$$

$$\frac{P_h}{V} = \lambda f \frac{256 \mu_0 H_0^3}{18\pi a j_c} \qquad \text{for } H_0 \ll H_p \tag{7.2}$$

The average eddy current loss P_e can be obtained using Eq. 7.3, where σ_m is the conductivity of the metallic matrix [386]. However, eddy current loss is only significant at high magnetic field amplitudes [387].

$$\frac{P_e}{V} = (\pi f a \mu_0 H_0)^2 \lambda f \frac{\sigma_m}{6} \tag{7.3}$$

To be able to calculate the coupling losses, a new conductivity σ_{perp} of the matrix must be obtained [385]. Afterwards, the average coupling loss P_c can be found with Eq. 7.4, where ω is the angular frequency, L is the twist pitch of the MgB_2 filaments and r_0 is the radius of the filament region.

$$\frac{P_c}{V} = \omega^2 \frac{\sigma_{perp} (\mu_0 H_0)^2}{2} \left[\left(\frac{L}{2\pi} \right)^2 + \frac{r_0^2}{4} \right] \tag{7.4}$$

Finally, the ferromagnetic loss P_f can be calculated using the Steinmetz equation [388] (Eq. 7.5) with the material specific constants k_h, n and the specific fill factor λ_{fe} of the metal and the maximum magnetic field density B_m.

$$\frac{P_f}{V} = \lambda_{fe} f k_h B_m^n \tag{7.5}$$

The above listed equations are only applicable to slowly changing magnetic fields transverse to the length of the superconducting wire as they are based on full flux penetration. Even though the losses are widely researched, there is no literature on the use of MgB_2 in the frequency range used in WPT, which makes it difficult to gauge feasibility. FEA simulations, such as [389], are therefore required to estimate the losses of multifilamentary superconducting wires correctly and accurately at high frequencies. In addition, MgB_2 has a lower critical temperature and therefore higher cooling penalty, which can be disadvantageous when compared with YBCO tapes.

Another approach to reduce AC losses can be the use of stabiliser-free tapes. As shown in chapter 6, the copper stabilisers can have the highest contribution to the overall losses, particularly at high frequencies. It is therefore possible to assume that removing the copper stabilisers, can reduce the losses. Stabiliser-free tapes are commercially available but literature on their use is limited [390]. A comparison between the transport current loss and magnetisation loss of stabiliser-free HTS tapes and conventional HTS tapes is shown in Figure 7-2 and Figure 7-3. It is assumed that the stabiliser-free tapes have similar characteristics and parameters than the conventional tapes. This might not be true for real cases, however it allows for a general comparison of the best case scenario. The performance of stabiliser-free tapes changes with load factor and frequency. For low frequencies up to 1 kHz there is no difference between the two types of tape as the majority of the losses will be generated in the HTS layer. However, as the frequency increases, the stabiliser-free tapes have lower losses for load factors below 0.5. The copper layer interacts with the self-field of the HTS coil, partially shields the HTS layer and is subject to eddy currents. Therefore, the loss of the HTS layer is slightly reduced. However, the eddy current losses in the copper layer are of comparable magnitude. On the other hand, if the load factor is above 0.5, the conventional tapes generate fewer losses. Similarly, the copper losses increase with load factor, but the additional losses are offset by the relative decrease in losses in the HTS layer.

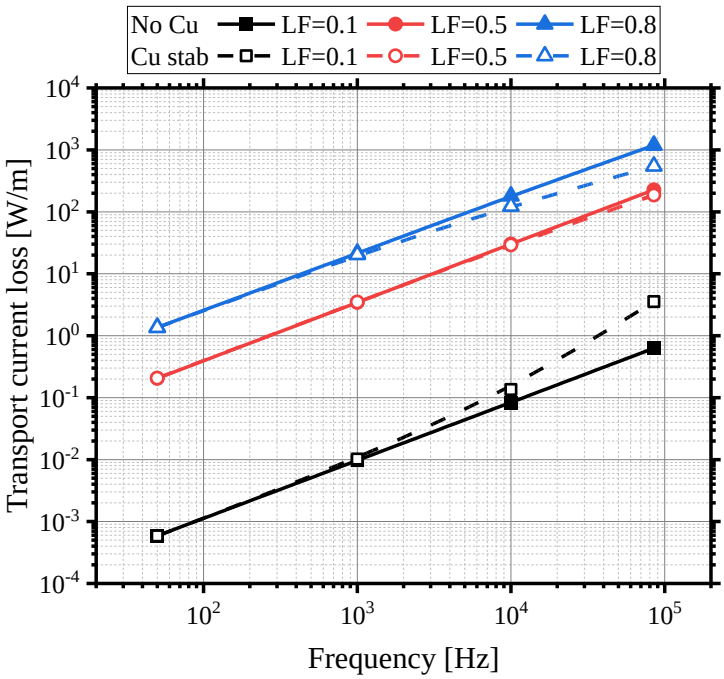

Figure 7-2 Comparison of the transport current loss of an eight-turn double pancake coil using stabiliser-free (No Cu) and conventional HTS tape (Cu stab)

In the case of magnetisation loss, the lack of the copper stabilisers only has a small effect on the loss characteristic. The interaction between the copper and the HTS layer is offset by the increased penetration depth of the current in the HTS layer of the stabiliser-free tape and therefore increased losses in the HTS layer itself compared to the shared losses in the conventional tape. Therefore, from a loss reduction standpoint, it is not viable to use stabiliser-free tapes over conventional tapes that incorporate copper stabilisers as the loss characteristic is only slightly better in some case.

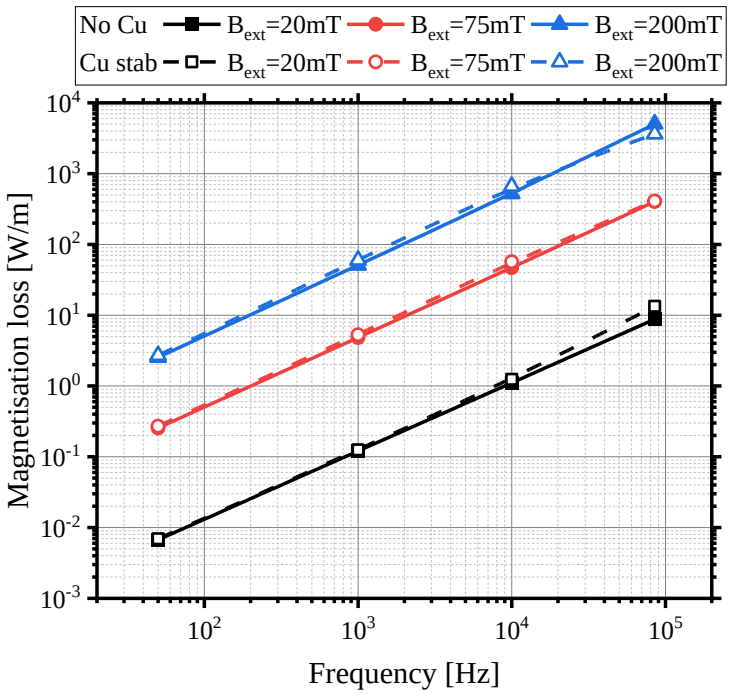

Figure 7-3 Comparison of the magnetisation loss of an eight-turn double pancake coil using stabiliser-free (No Cu) and conventional HTS tape (Cu stab)

7.3 Flux diverters

Finally, the impact of flux diverter on the loss properties of HTS coil is examined. Flux diverters have gained increased attention in recent years [391], [392], [393], [394], [395]. However, their viability for high frequency application has not yet been explored. To evaluate the AC losses of the HTS coil and the flux diverter, when carrying an alternating sinusoidal current, the 2D axisymmetric multilayer model introduced in chapter 6.2 is modified and shown in Figure 7-4. Flux diverters are conventionally used to reduce the overall losses in the HTS coils as the flux is guided away from the HTS layer/tape and therefore the critical current is preserved. To be able to divert the flux properly, the diverter should have a high magnetic saturation field. As soon as the material is saturated, the magnetic flux within the material caps out and μ_r decreases. Here a strong magnetic Ni-alloy with a saturation field of 1.66 T was used [94]. The diverter is characterised by its thickness h_d, its width h_b (h_b is half the width difference between diverter and coil) and the air gap g between the diverter and the coil. The relative permeability can be modelled using Eq. 7.6, which was generated from experimental results [94]. While for a weakly magnetic substrate the relative permeability is temperature dependent, a strongly magnetic substrate, like the one used here, only experiences a small different between room temperature and 77 K [396]. Nevertheless,

the experimental results used to generate Eq. 7.6 were taken at 77 K. With the aid of the relative permeability the losses within the flux diverter can be calculated. Generally, two loss mechanisms can be distinguished, namely, eddy current loss and ferromagnetic loss. Both can be accounted for by the power density as shown in Eq. 6.3. Therefore, Eq. 6.3 includes all losses generated by the different components.

$$\mu_r = 1 + 1200000 * \left[1 - \exp\left(-\left(\frac{H}{70}\right)^{3.2}\right)\right] * H^{-0.99} \tag{7.6}$$

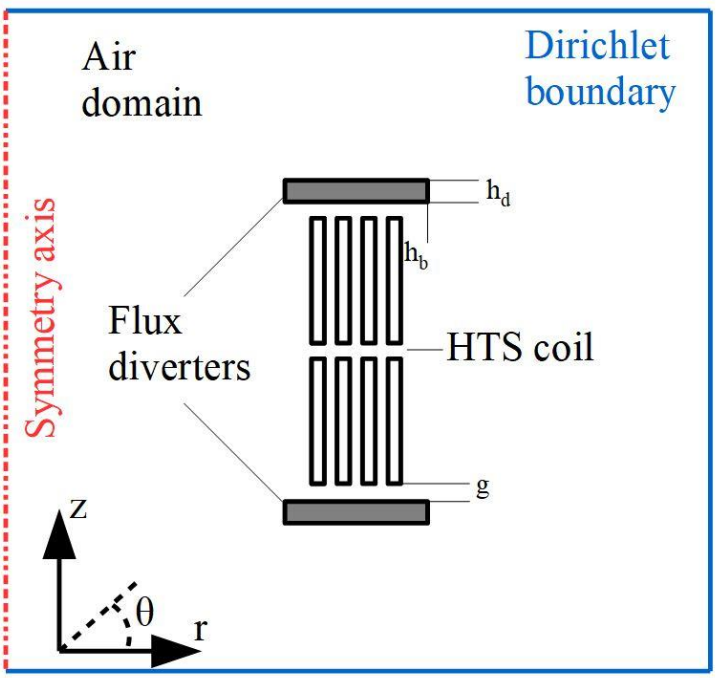

Figure 7-4 2D axisymmetric model layout with flux diverter characterised by the thickness h_d, width h_b and air gap g between coil and diverter

7.3.1 Air gap

Initially, the effect of the air gap between the flux diverter and the coil will be examined. In the cases shown below, the air gap g is varied between 0.5 mm to 2 mm, while the width of the flux diverter and its thickness is kept constant at the length of the winding and 1 mm, respectively. Three different load factors (LF) are investigated, namely LF=0.1, 0.5 and 0.8. The total coil loss, diverter loss and the ratio of total loss Q_{tot_div} and total loss without diverter Q_{tot} for LF=0.1 are shown in Figure 7-5 and Figure 7-6. As shown, the overall coil loss increases with frequency due to the skin effect. This is unchanged for coils using flux diverters, however, through the flux diverter the perpendicular magnetic field component, which is a key factor for the losses generated

by HTS coils, is reduced, resulting in lower overall coil losses. The magnetic field distribution is investigated in more detail in chapter 7.3.4. On the other hand, an additional source of losses is introduced with the magnetic materials used as diverter. Similarly, to the coil losses, the diverter losses increase with frequency too. It is therefore important to consider all losses to evaluate the effectiveness of the diverter. As the *g* decreases, the coil losses decrease. However, the diverter losses increase with smaller air gaps as more magnetic flux is traversed by the diverter. When looking at the ratio of losses with and without a flux diverter it is obvious that the overall losses of the system are reduced e.g. at an air gap of 0.5 mm, the system only has about 60 % of the initial losses at 50 Hz.

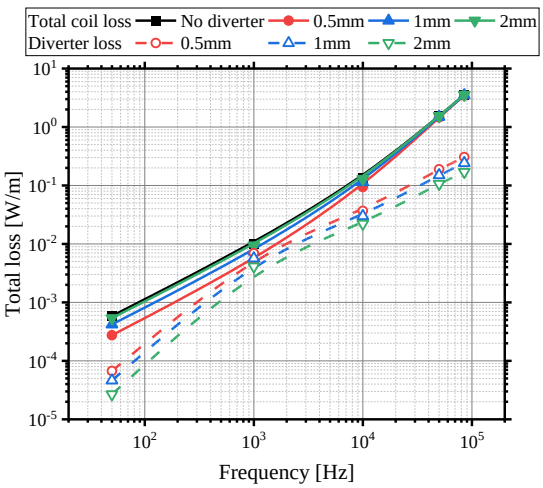

Figure 7-5 Comparison of coil and diverter losses for a double pancake coil with a 1 mm wide flux diverter at LF=0.1 and different gaps

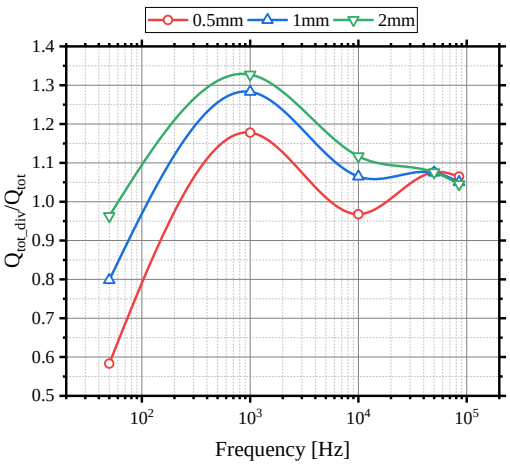

Figure 7-6 Ratio of total losses of a double pancake coil with flux diverter over total coil losses without flux diverter at LF=0.1 and different gaps

If the air gap is increased to 2 mm, the loss reduction vanishes completely and the flux diverter has almost no effect on the system losses as the diverter losses offset the reduction in coil losses. As the frequency increases, the loss reduction decreases. There exists a maximum in loss ratio around 1 kHz as the diverter losses increase faster than the coil losses. Furthermore, at this frequency both loss components have approximately the same magnitude. It is a direct result of the skin effect in the HTS coil, which pushes the current towards the outer edges of the tape. Therefore, the magnetic field in the gap increases. At about 1 kHz, the magnetic field strength reaches a value that results in the maximum μ_r and fully saturates the Ni-alloy. Afterwards the coil losses increase more rapidly with frequency, which reduces the loss ratio to about 1.05 at 85 kHz independent of air gap as the coil losses at different *g* approach each other and drastically

outweigh the diverter losses. Therefore, the flux diverter has an adverse effect on the system performance at elevated frequencies and low LF. It should be noted that this set of results was obtained at a very low load factor, while the loss reduction effect becomes much more substantial towards high load factors as discussed below.

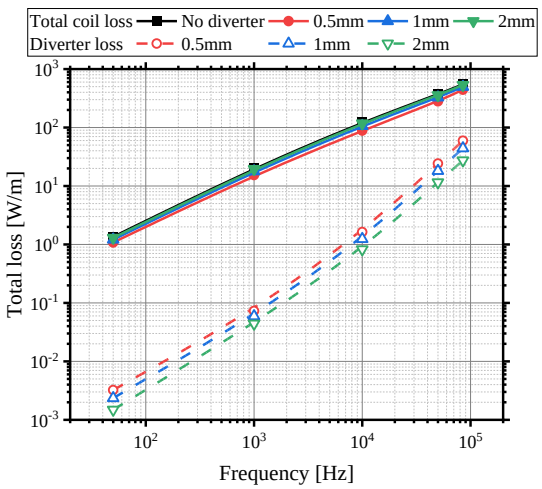

Figure 7-7 Comparison of coil and diverter losses for a double pancake coil with a 1 mm wide flux diverter at LF=0.8 and different gaps

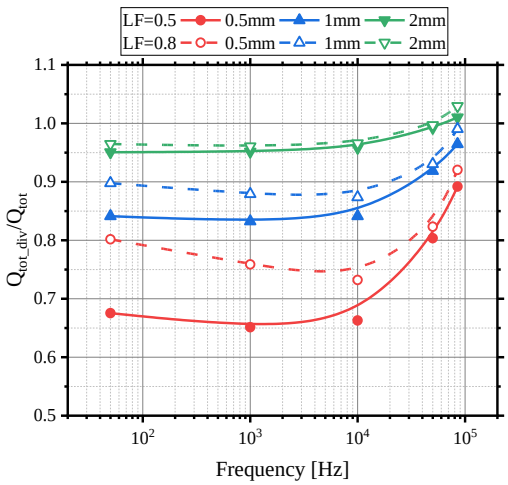

Figure 7-8 Ratio of total losses of a double pancake coil with flux diverter over total coil losses without flux diverter at LF=0.5 and LF=0.8 and different gaps

If the superconducting coil is carrying a larger transport current such as LFs of 0.5 and 0.8, the trend becomes more stable as shown in Figure 7-7 and Figure 7-8. Both loss components increase linearly with frequency up to 10 kHz for LF=0.5 and 1 kHz at LF=0.8. At this frequency, the flux diverter approaches saturation as the magnetic field inside the diverter peaks at approximately 1.6 T. After the diverter saturates the losses increase more rapidly, which negatively affects the loss ratio. For both LFs the loss ratio stays nearly constant up to a frequency of 10 kHz or even decreases in the case of LF=0.8 and g=0.5 mm. At higher frequencies it rises rapidly due to saturation of the flux diverter. However, it remains at around 0.9 for g=0.5 mm and rises above 1 for g=2 mm. On the contrary to LF=0.1, there is a clear distinction between the loss ratios for different air gap lengths. To maximise the loss reduction at low frequencies, the diverter should be as close as possible to the coil. However, the saturation should always be considered. On the other hand, the operating conditions such as the LF must be considered as it has a great impact on whether the flux diverter reduces or increases the overall coil losses.

A comparison for the loss ratios versus load factor is illustrated in Figure 7-9. The loss ratio becomes strongly dependent on LF for a frequency of 50 Hz as the g decreases. But at 85 kHz it

stays approximately constant for LFs of 0.5 and above. One exception is the case of an air gap of 2 mm where the effect of the diverter on the coil losses is very small, while also having a very small loss associated with the diverter.

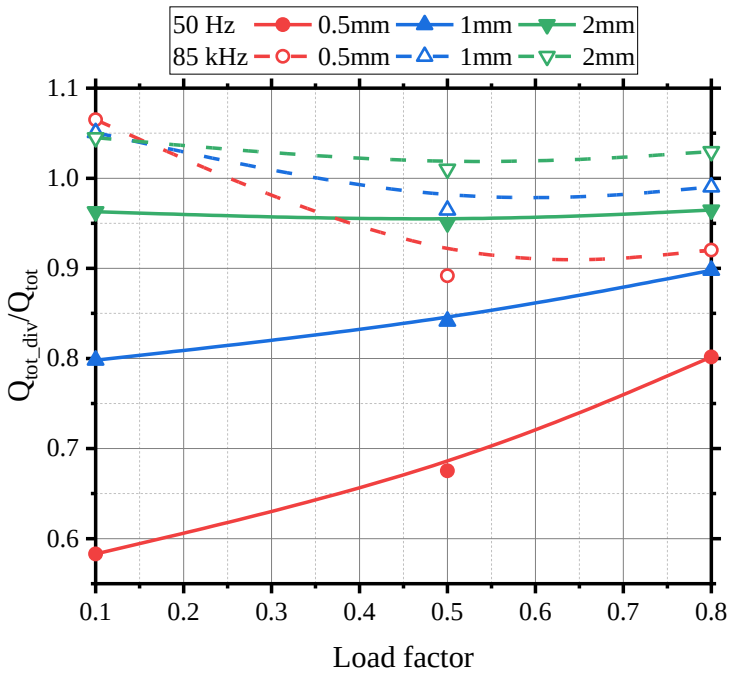

Figure 7-9 Loss ratio for different air gaps *g* versus load factor for 50 Hz and 85 kHz

7.3.2 Thickness

Another parameter determining the effectiveness of the flux diverter is its thickness h_d. In this chapter, h_d varies from 0.5 mm to 5 mm while diverter width and *g* are set to be equal to the width of the winding and 1 mm, respectively.

Total coil losses and diverter losses for a load factor of 0.1 are illustrated in Figure 7-10. As h_d increases, the losses of the coil decrease. In addition, as the frequency increases the coil losses increase too. Similarly, to the different air gap lengths, the coil losses approach each other at frequencies above 10 kHz. However, the losses in the diverter increase with its thickness and frequency. For a thickness of 2 mm, the loss is about one third of the coil losses at 50 Hz. Losses quickly rise with frequency and are larger at 1 kHz. But at higher frequencies the losses in the HTS coil increase more rapidly. If the diverter thickness is increased to 5 mm, the losses are always higher than the coil losses. This is reflected in the loss ratio depicted in Figure 7-11, as a width of

5 mm approximately doubles to quadruples the system losses compared to an HTS coil without a flux diverter. In general, while at low frequencies the overall system losses are reduced by almost 50%, as the frequencies increase wider flux diverters are not viable for a LF=0.1 due to the ferromagnetic losses associated with them.

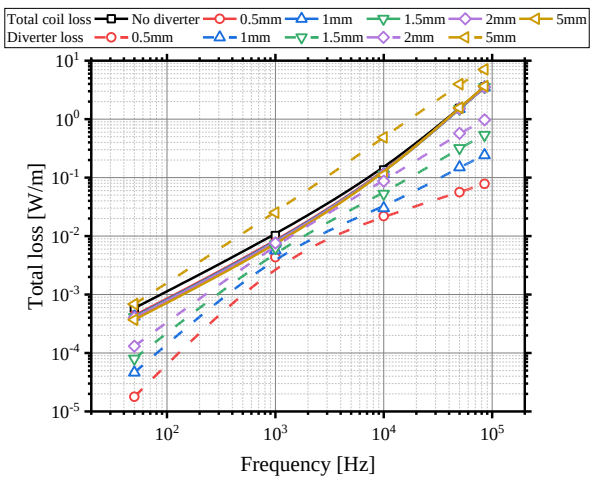

Figure 7-10 Comparison of coil and diverter losses for a double pancake coil with a flux diverter of different thicknesses at LF=0.1 and a 1mm gap

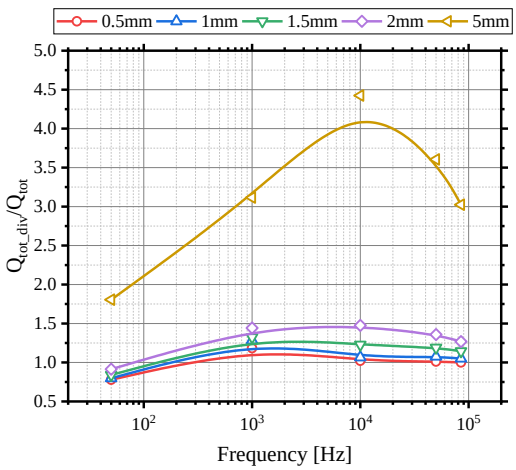

Figure 7-11 Ratio of total losses of a double pancake coil with flux diverter over total coil losses without flux diverter at LF=0.1 for different diverter thicknesses

However, as the load factor is increased to 0.8 (Figure 7-12), the losses in the HTS coil drastically increase, while the diverter losses increase at a lower rate. Therefore, the negative effects are offset. The diverter losses at h_d= 2 mm and less are always below the coil losses, while they approach each other at a frequency of 85 kHz. In the case of h_d= 5 mm, the diverter losses are two orders of magnitude below the coil losses at 50 Hz but exceed them at frequencies above 50 kHz. The thickness of the flux diver has a negligible effect on the AC losses of the HTS coil. At low frequencies this slight improvement outweighs the additional diverter losses.

However, as the frequency increases the losses in the diverter offset the reduced coil losses. When looking at the loss ratio for higher load factors, as seen in Figure 7-13, narrower diverters are advantageous even at more elevated frequencies of 85 kHz with a loss reduction of approximately 7-8%. A 5 mm wide flux diverter can initially reduce the losses by circa 15-20% for high LFs and 50 Hz, however, losses are almost quadrupled for the same LFs and 85 kHz. Figure 7-14 illustrates the effect of different LFs on the loss ratio for frequencies of 50 Hz and 85 kHz. At 50 Hz, systems with 5 mm wide flux diverters have the highest loss ratio for LFs below 0.5 as it is dominated by

the diverter losses. However, as LFs increase above 0.5, narrower diverters have a higher loss ratio as the coil losses decrease more with increasing diverter thickness. This trend does not exist for a frequency of 85 kHz, where the loss ratio is largely unaffected by the LF for h_d up to 2 mm. Nevertheless, thicker diverters have a higher loss ratio compared to narrow diverters.

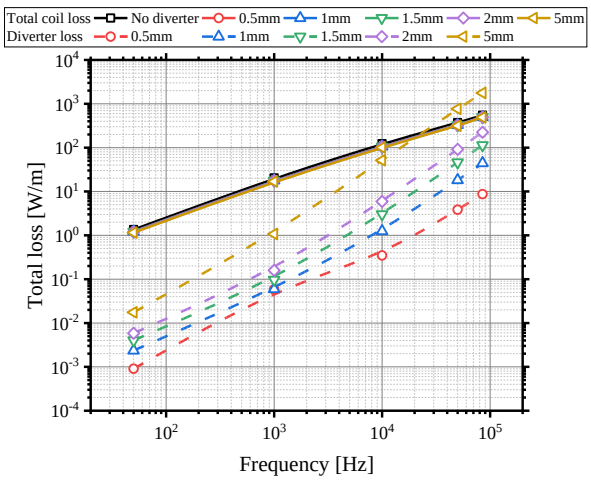

Figure 7-12 Comparison of coil and diverter losses for a double pancake coil with a flux diverter of different thicknesses at LF=0.8 and a 1 mm gap

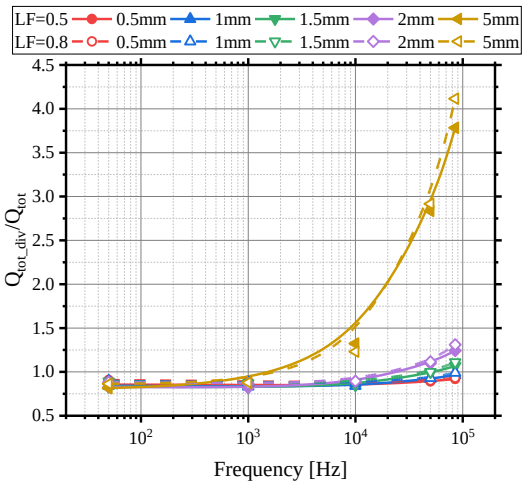

Figure 7-13 Ratio of total losses of a double pancake coil with flux diverter over total coil losses without flux diverter at LF=0.5 and LF=0.8 for different diverter thicknesses

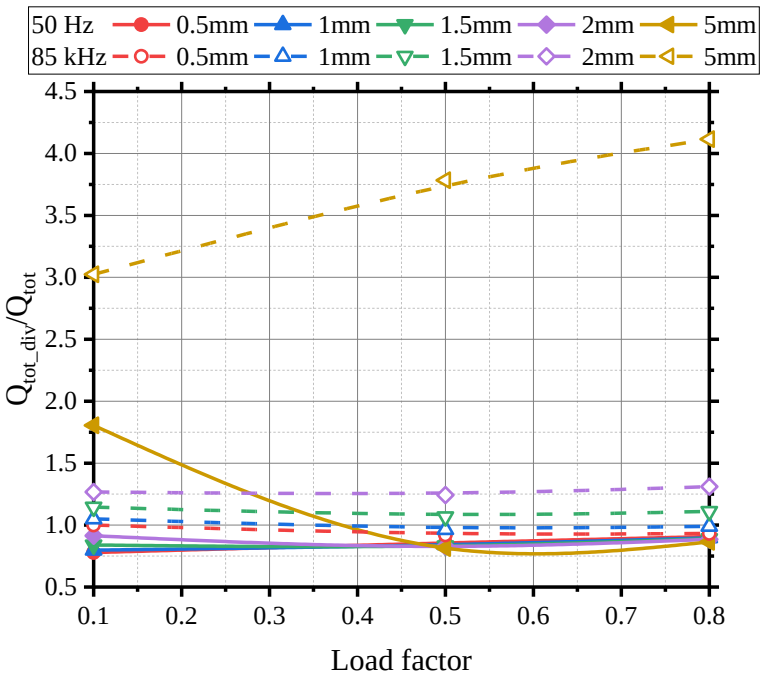

Figure 7-14 Loss ratio for different thicknesses h_d versus load factor for 50 Hz and 85 kHz

7.3.3 Width

The last parameter investigated is the width h_b of the flux diverter over the coil. So far, all flux diverters examined had a width equal to the thickness of the coil windings. In this chapter h_b is varied between 0.25 mm and 2 mm above the coil thickness. Similarly to previous cases, the gap between the flux diverter and the coil is 1 mm and the thickness of the diverter is set to 1 mm.

The diverter losses for low LFs dominate the overall system losses, especially at low frequencies as shown in Figure 7-15. Wider diverters generate higher losses due to their larger volume and the interaction between the stronger magnetic field in the centre of the coil. As the frequency increases, the coil losses surpass the diverter losses. For LF= 0.1, almost no combination of diverter and coil can reduce the overall system loss as shown through the loss ratio in Figure 7-16. On the contrary, the system loss can be up to quadrupled due to the large diverter losses for frequencies below 10 kHz. Furthermore, at frequencies above 50 kHz, the loss ratio is nearly constant and independent of the diverter width due to the marginal decrease in coil losses.

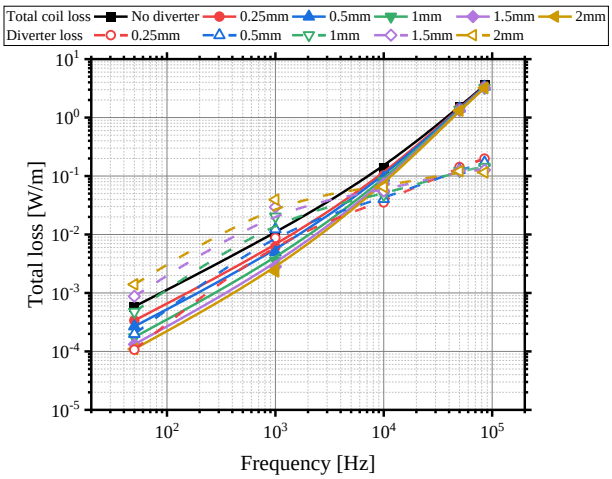

Figure 7-15 Comparison of coil and diverter losses for a double pancake coil with a flux diverter of different widths at LF=0.1 and a 1 mm gap

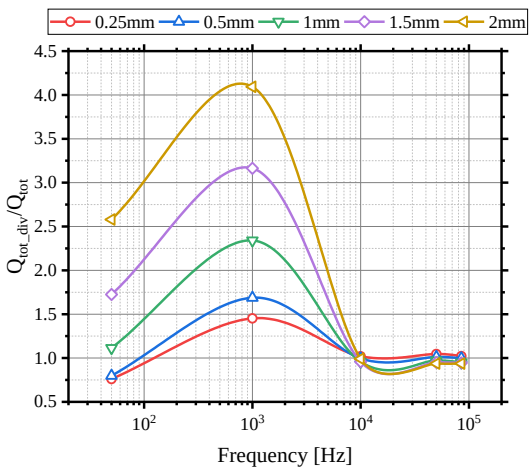

Figure 7-16 Ratio of total losses of a double pancake coil with flux diverter over total coil losses without flux diverter at LF=0.1 for different diverter widths

A higher LF will lead to more losses generated by the HTS coil. Figure 7-17 illustrates that the relative increase of the HTS coil loss is much higher than that of the diverter losses, which increases the effectiveness of the diverter. There exists a crossover point, where the highest losses are generated in the shortest flux diverter at frequencies above 10 kHz. As the frequency increases, the current in the HTS coils is pushed outwards to the edges of the tape, which increases the magnetic field in the surrounding area of the coil. A shorter diverter is subjected to this amplified

magnetic field over its entire width whereas wider diverter can distribute the internal magnetic field more evenly, reducing the chance of magnetic hotspots. In addition, the reduction in coil losses is given even for higher frequencies unlike the case of LF= 0.1. Therefore, the loss reduction is higher for high LFs as depicted in Figure 7-18. The shortest flux diverter has the smallest loss reduction due to the reduction in the perpendicular field component. However, if the width is increased, a higher portion of the surrounding magnetic field can be reduced. With a width of 0.5 mm a reduction between 10-25% for LF= 0.5 can be achieved. Whereas a diverter with a width of 2 mm can reduce the losses by 40-60%. The effect of the diverter is more pronounced for lower frequencies with a sharp decrease in loss reduction for frequencies between 10 and 85 kHz.

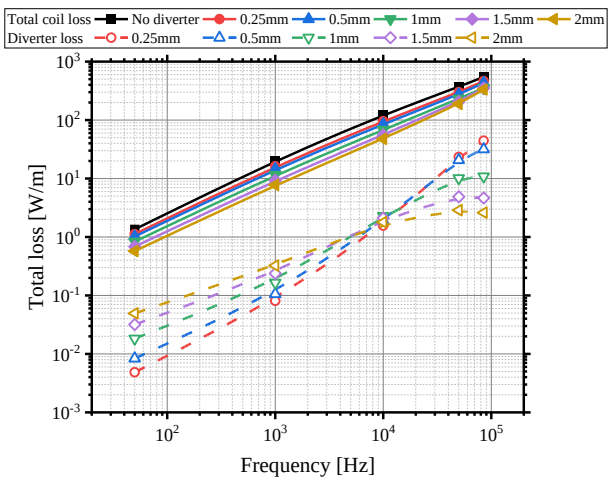

Figure 7-17 Comparison of coil and diverter losses for a double pancake coil with a flux diverter of different widths at LF=0.8 and a 1 mm gap

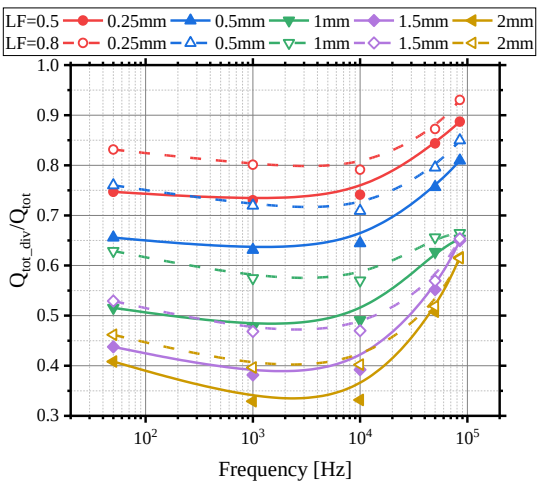

Figure 7-18 Ratio of total losses of a double pancake coil with flux diverter over total coil losses without flux diverter at LF=0.8 for different diverter widths

A comparison of the loss ratio for different load factors operating at 50 Hz and 85 kHz is given in Figure 7-19. Similar to the trend observed for the thickness of the diverter, wider diverters increase losses of the coil-diverter system for low LFs as the diverter losses are higher than the coil losses for 50 Hz. This trend reverses and wider diverters are favourable for a frequency of 85 kHz due to the higher coil losses at this operating frequency. As LF increases and most of the losses shift towards the HTS coil, a flux diverter becomes more important to reduce the perpendicular component of the magnetic field. While the performance of the diverter at 50 Hz is strongly dependent on the LF, the loss ratio is widely unaffected by it. Therefore, it is crucial to design the flux diverter based on the transport current of the application, particularly for low frequencies, while higher operating frequencies allow for more flexibility.

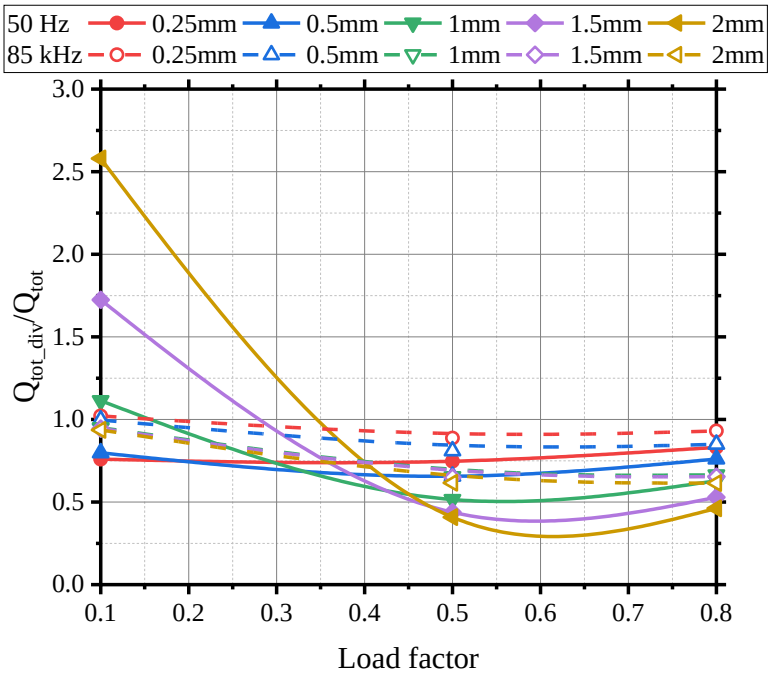

Figure 7-19 Loss ratio for different widths h_b versus load factor for 50 Hz and 85 kHz

7.3.4 Effect of the flux diverter on the coil

Finally, the effect of the flux diverter on key system characteristics of a wireless power transfer system is investigated. An important quantity of such a system is the magnetic field density above the coil that links both charging pads and ultimately is responsible for the power transfer. Figure 7-20 depicts the magnetic field 3 cm above the coil. This is equivalent to approximately 50% of the coil radius. The magnetic field above a coil without flux diverter is compared to a flux diverter with 2 mm width, one with a thickness of 0.5 mm and lastly a diverter located 0.5 mm above the coil. As shown, the magnetic field is not affected by the flux diverters, yet the system losses can be reduced substantially.

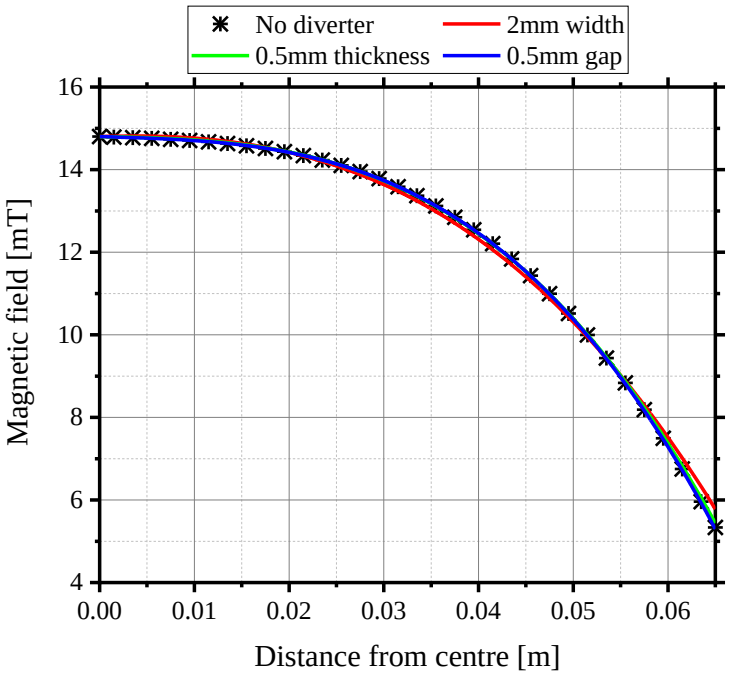

Figure 7-20 Magnetic field density 3 cm above double pancake coil with flux diverters of different sizes: a) 2 mm width, 1 mm thickness at 1 mm gap, b) 1 mm width, 0.5 mm thickness at 1 mm gap, c) 1 mm width, 1 mm thickness at 0.5 mm gap

Furthermore, Figure 7-21 to Figure 7-23 are compared with Figure 6-18 to show the different loss distributions amongst the individual turns of the coil without a flux diverter and with the previously described diverters operating at a load factor of 0.5. Normally, the losses are evenly distributed for a frequency of 50 Hz amongst the turns and as the frequency increases the innermost turns generate the highest losses due to the higher magnetic field in the centre of the coil. In addition, the turns in the middle of the coil are somewhat shielded by the outermost turns. With the introduction of a flux diverter there is no significant change to the loss distribution of the different turns, therefore no change to the cooling system is required to remove the heat generated at different locations and local hotspots can be avoided, while lowering the overall burden on the cooling system through reduced losses.

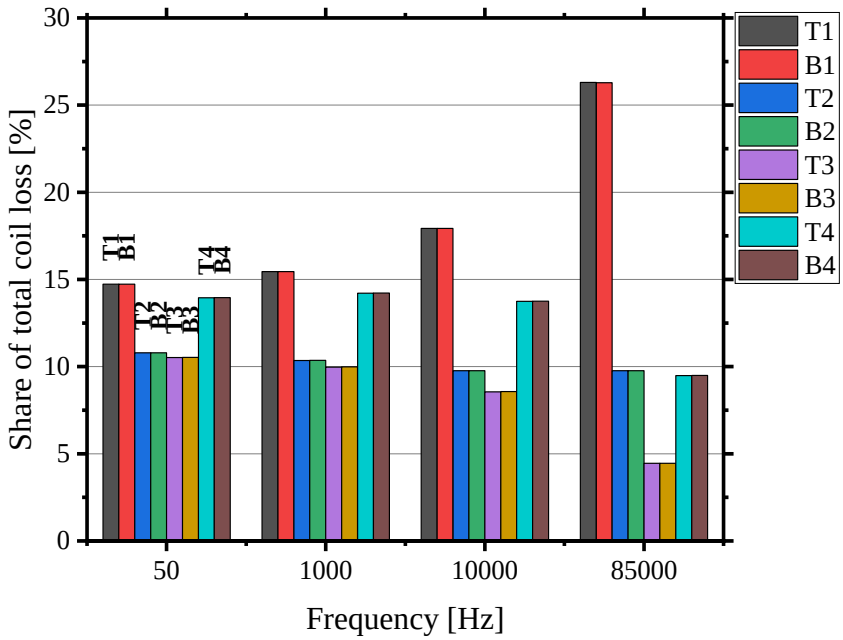

Figure 7-21 Turn loss contribution of an eight-turn double pancake coil at LF=0.5 with a flux diverter at an air gap length g of 0.5 mm, h_d=1 mm and h_b=0 mm

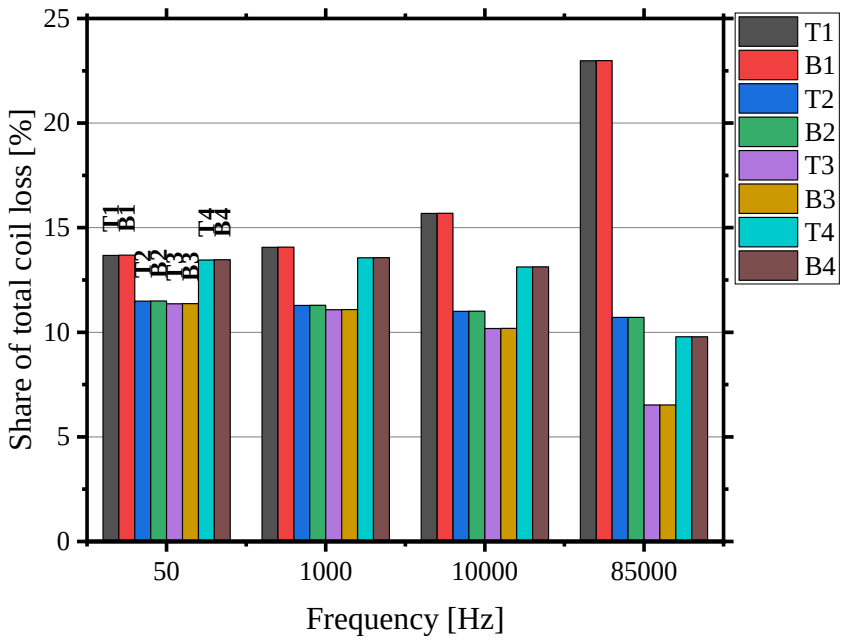

Figure 7-22 Turn loss contribution of an eight-turn double pancake coil at LF=0.5 with a flux diverter (h_d=0.5 mm, g=1 mm and h_b=0 mm)

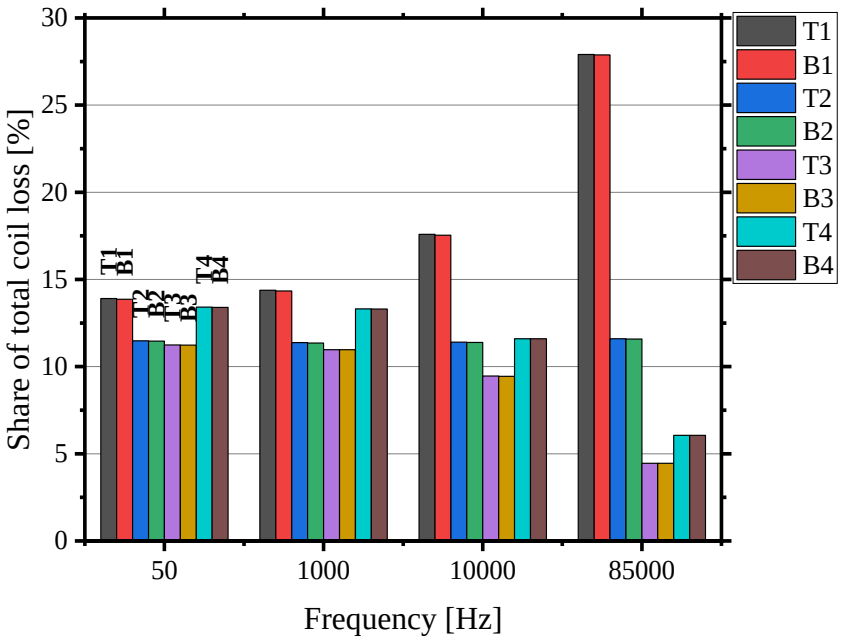

Figure 7-23 Turn loss contribution of an eight-turn double pancake coil at LF=0.5 with a flux diverter (h_d=1 mm, g=1 mm and h_b=2 mm)

In addition, Figure 7-24 depicts the magnetic field distribution of the HTS coil turns in the absence of a flux diverter at 50 Hz (a) and 85 kHz (b) and compares it with the magnetic field distribution when a flux diverter is used with different geometrical features (c)-(h). In all cases the applied LF is 0.5. The magnetic field has the biggest influence on the losses within the HTS coil. As shown, the innermost turns i.e. leftmost turns in the figure experience the highest magnetic field due to the field build-up in the centre of the coil. This is true irrespective of the operating frequency. Additionally, the skin effect at higher frequencies can clearly be seen. The magnetic field density in the HTS turns decreases when a flux diverter is used as indicated by the change in colour distribution and the maximum values for the magnetic field density. This reduction occurs for both frequencies and is the cause for the reduction in AC losses in the HTS coil. Furthermore, as discussed in the previous section, the width of the flux diverter has the highest impact on the magnetic field density, while the thickness and the air gap only have a minor effect on the magnetic field.

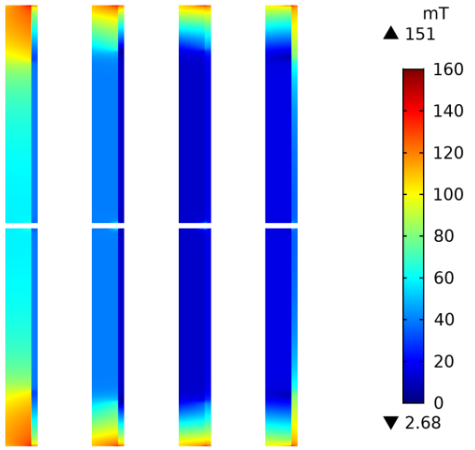
mT
▲ 151
160
140
120
100
80
60
40
20
0
▼ 2.68

a)

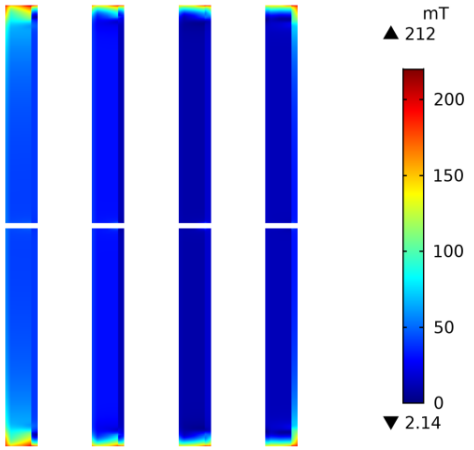
mT
▲ 212
200
150
100
50
0
▼ 2.14

b)

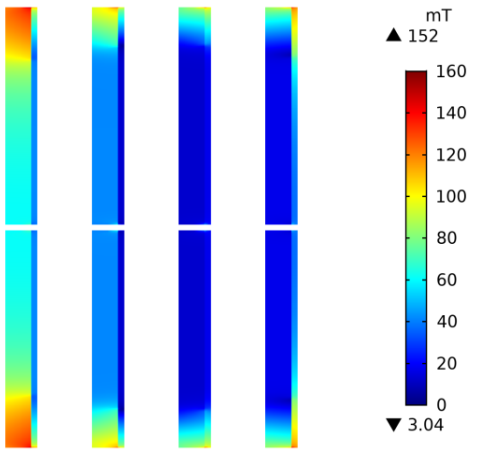
mT
▲ 152
160
140
120
100
80
60
40
20
0
▼ 3.04

c)

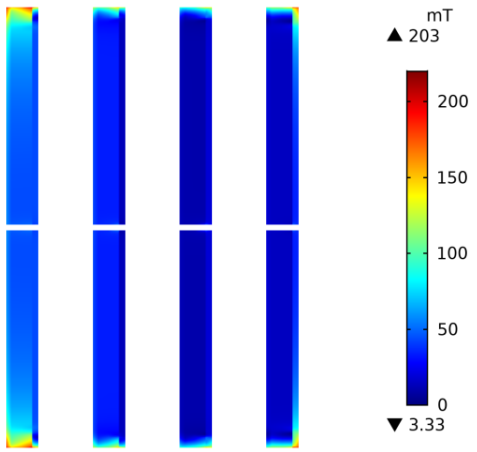
mT
▲ 203
200
150
100
50
0
▼ 3.33

d)

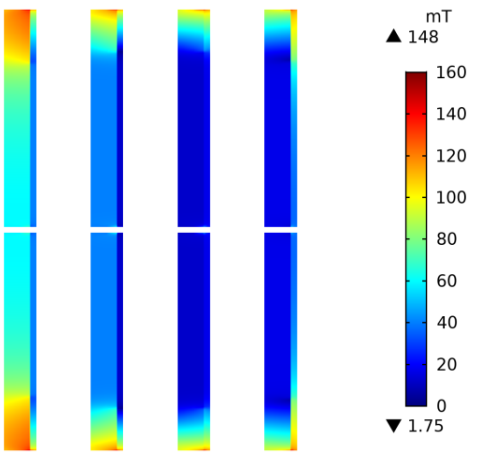
mT
▲ 148
160
140
120
100
80
60
40
20
0
▼ 1.75

e)

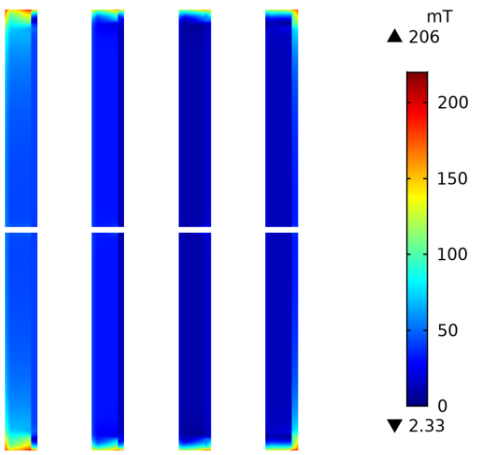
mT
▲ 206
200
150
100
50
0
▼ 2.33

f)

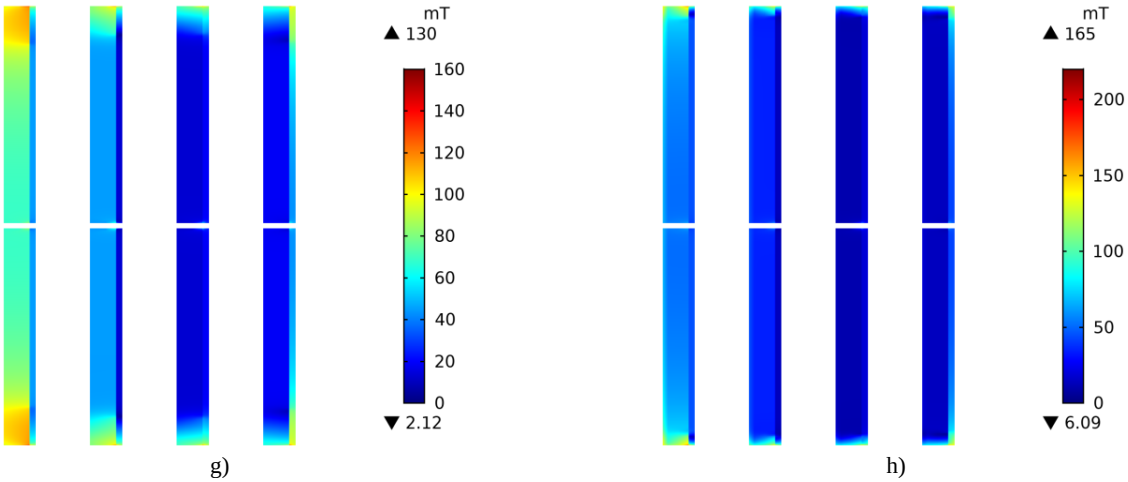

g) h)

Figure 7-24 Magnetic field distribution of an eight-turn double pancake coil at LF= 0.5 for different cases: a) 50 Hz no flux diverter, b) 85 kHz no flux diverter, c) 50 Hz with a flux diverter (g=0.5 mm, h_d=1 mm and h_b=0 mm), d) 85 kHz with a flux diverter (g=0.5 mm, h_d=1 mm and h_b=0 mm), e) 50 Hz with a flux diverter (g=1 mm, h_d=0.5 mm and h_b=0 mm), f) 85 kHz with a flux diverter (g=1 mm, h_d=0.5 mm and h_b=0 mm), g) 50 Hz with a flux diverter (g=1 mm, h_d=1 mm and h_b=2 mm) and h) 85 kHz with a flux diverter (g=1 mm, h_d=1 mm and h_b=2 mm)

7.4 Conclusion

Here, the possibility of using other materials and tape structures was evaluated. MgB_2 is a strong contender to reduce the AC losses of superconducting systems, however, there is no literature or reliable analytical solution for the AC loss characteristics available, which makes it difficult to gauge its effectiveness and applicability for high frequency applications. In addition, stabiliser-free tapes have been investigated, but they are not a reliable method of reducing the losses.

Furthermore, the impact of flux diverters on high frequency HTS applications, particularly wireless power transfer was investigated. Flux diverters have been used to reduce losses via lowering the applied magnetic field at the conductors. However, their applicability has only been demonstrated at low operating frequencies. Therefore, a wide frequency range was covered between conventionally used 50 Hz up to 85 kHz. Furthermore, three different LFs were included in the investigation, namely 0.1, 0.5 and 0.8. With the aid of a 2D axisymmetric numerical multilayer FEA model, the high frequency AC losses occurring in a DP coil were investigated. In addition, the total losses of the Ni-alloy flux diverter were explored at such frequencies. Key geometric features of the flux diverters such as width, thickness and the air gap between diverter and HTS coil were studied.

It was shown that a small air gap between the flux diverter and the HTS coil is favourable as it has the biggest effect on the perpendicular magnetic field component responsible for HTS losses.

However, it is important to note that the LF has a major impact on the effectiveness of the diverter as it shifts the majority of the losses in the diverter at low load factors to the AC loss in the HTS coil at higher LFs. The loss ratio for different air gaps at LFs above 0.5 is mainly constant with frequency up to 10 kHz. If the frequency is increased further, the loss ratio increases rapidly, lowering the effectiveness of the flux diverter.

Similarly, to the air gap, thinner flux diverters have a higher impact on the coil losses and reduce the overall losses of the diverter-coil system. Flux diverters are more advantageous for lower frequencies, but thinner diverters can still achieve a loss reduction of approximately 7-8% at 85 kHz.

The width of the flux diverter has the biggest impact on the losses of the HTS coil and the overall losses can be reduced by up to 60% with a width of 2 mm at LF= 0.5. Additionally, the impact of the flux diverter on the WPT system was demonstrated. As shown, the diverter does not affect the magnetic field above the coil which is responsible for linking both charging pads and its effect on the loss distribution of the coil is small. Therefore, existing cooling system are not required to be modified if a flux diverter is employed to reduce the coil losses.

To summarise, at low LFs and high frequencies, the effect of flux diverters is negligible or has adverse effects on the system performance. On the other hand, even though flux diverters can be applied to reduce the overall losses of the HTS coils at high LFs, the reduction is not sufficient to enable the use of such coils in WPT systems. Therefore, other techniques must be employed in conjunction with diverters to effectively enable high frequency superconducting WPT. Nevertheless, this research can be used as base for future research into flux diverter design for high frequency applications.

8 Conclusion

8.1 WPT case studies

To conclude this research some case studies for HTS WPT-systems are presented, which were partly published in [4]. Current literature generally uses inapplicable equations to assess losses of HTS coils and neglects the impact of the cooling system on the HTS WPT-system. To estimate the impact of the AC losses and cooling power requirements of HTS WPT systems, three case studies have been investigated. Namely, a low-power scenario with a LF of 0.1, a medium-power case operating at a LF of 0.4 and a high-power case with a LF of 0.8. The WPT systems use the double pancake coil introduced in chapter 5 and the FEA model introduced in chapter 6.2, with the same dimensions and operating frequencies between 1 kHz and 85 kHz. All scenarios look at three different transmission distances i.e. 0.01 m, 0.05 m and 0.125 m, which are equivalent to an air gap to coil diameter ratio of 8%, 40% and 100%. The LF in the transmitting coil (Tx) determines the primary current I_p which is used as input of the FEA model to calculate the magnetic field present at the Tx, while the induced current I_s in the receiving coil (Rx) is calculated and used as a base for the magnetic field in the Rx. With the aid of the current in the respective coils and their magnetic field, the AC losses are calculated and converted into an equivalent resistance $R_{eqTx/Rx}$. Parasitic resistances, e.g. from capacitor banks and connectors, are not included in the calculation. Input power P_{in} and output power P_{out} are calculated using Eq. 8.1 and Eq. 8.2 and the cooling power required for each coil is calculated using Eq. 8.3 where k_c is the specific power introduced in chapter 2.4, which is approximately 9.65 for an operating temperature of 77K, ω is the angular frequency, M is the mutual inductance between Tx and Rx and R_L is the optimal load resistance. R_L can be obtained from $\partial\eta/\partial R_L$ where η is the transfer efficiency at resonance frequency (Eq. 3.9). The overall system efficiency can then be calculated using Eq. 8.4.

$$P_{\mathrm{in}} = \left|I_{\mathrm{p}}\right|^2 \left(R_{\mathrm{eqTx}} + \frac{(\omega M)^2 * (R_{\mathrm{eqTx}} + R_{\mathrm{L}})}{(R_{\mathrm{eqRx}} + R_{\mathrm{L}})^2}\right) \tag{8.1}$$

$$P_{\mathrm{out}} = \left|I_{\mathrm{p}}\right|^2 \left(R_{\mathrm{eqTx}} + \frac{(\omega M)^2 * R_{\mathrm{L}}}{(R_{\mathrm{eqRx}} + R_{\mathrm{L}})^2}\right) \tag{8.2}$$

$$P_{\mathrm{cool\ Tx/Rx}} = k_{\mathrm{c}} \left|I_{\mathrm{p/s}}\right|^2 R_{\mathrm{eqTx/Rx}} \tag{8.3}$$

$$\eta_{\mathrm{sys}} = \frac{P_{\mathrm{out}}}{P_{\mathrm{in}} + P_{\mathrm{cool\ Tx}} + P_{\mathrm{cool\ Rx}}} \tag{8.4}$$

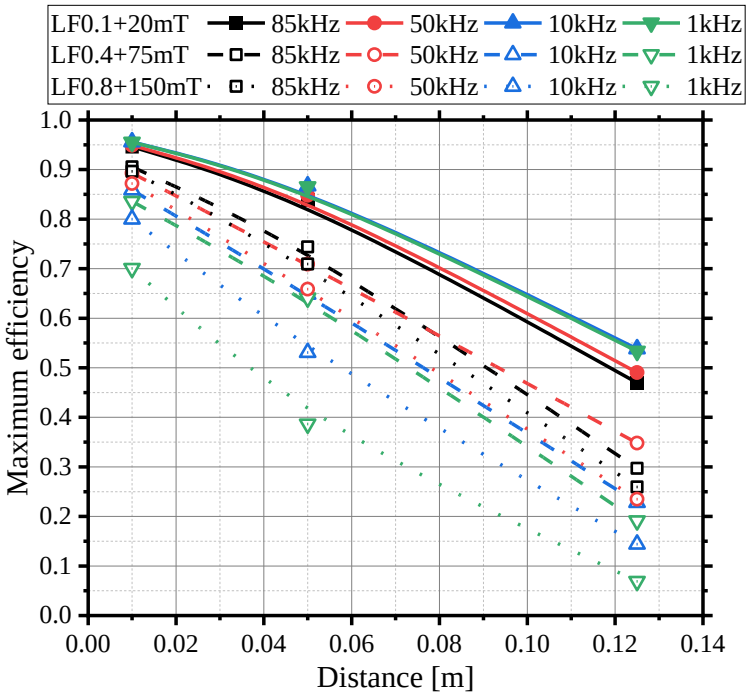

Figure 8-1 Maximum transfer efficiency for a HTS WPT-system with load factors of 0.1, 0.4 and 0.8 at different operating frequencies

As demonstrated in Figure 8-1, the achievable transfer efficiency decreases with increasing air gap lengths as the intercepted magnetic flux, linking transmitting and receiving coil, weakens. Additionally, higher operating frequencies result in higher achievable efficiencies as a higher voltage is induced while also the quality factor $Q_x = \frac{\omega_0 * L_x}{R_x}$ of the resonating coils increases, which are key factors for high efficiency systems. This trend is clearly visible for the medium and high-power cases. However, for low load factors such as 0.1, the trend reverses and the transfer efficiency increases, while the operating frequency decreases. This reversal is explained by the quality factor shown in Figure 8-2. For a load factor of 0.1, the quality factor is inversely proportional to the frequency as the numerator $\omega_0 * L_x$ is approximately constant for each operating frequency, while the denominator R_x decreases rapidly with frequency for the low-power case. Furthermore, the achievable efficiency is the highest for the low-power case as the equivalent resistance of the coils increases rapidly with load factor and external magnetic field density as outlined in chapter 6.5.

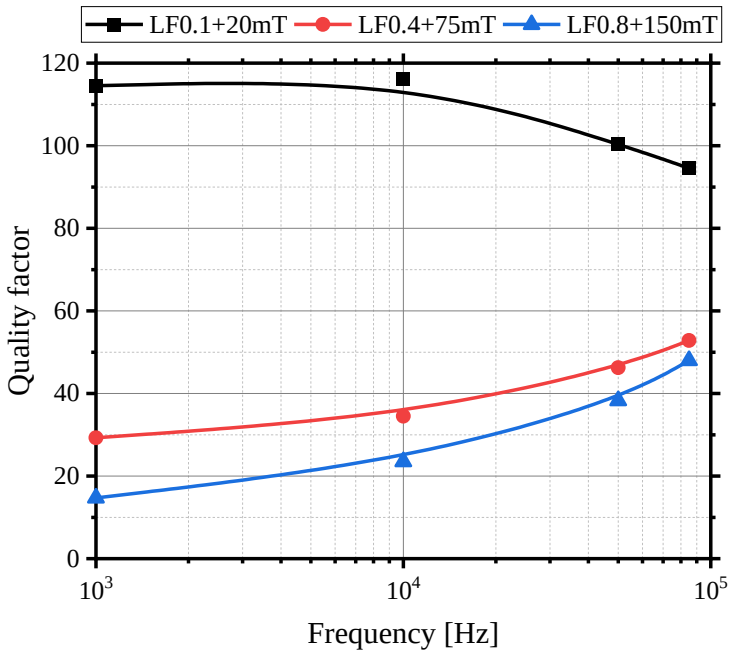

Figure 8-2 Quality factor of HTS coils at different load factors and frequencies for an air gap length of 0.01 m

Table 8-1 summarises the system performance parameters for the different case studies investigated at an operating frequency of 85 kHz. As shown, the transfer efficiency is high for the low power scenario due to the low air gap length, but also due to the low equivalent resistance of the HTS coils used. On the contrary, for the high-power scenario, the transmission efficiency decreases rapidly with distance as the equivalent resistance of the HTS coils has a great impact. Naturally, the transfer efficiency decreases with increasing air gap length. However, if the cooling power is taken into account and an overall system efficiency is derived, the performance of the HTS system is greatly affected. A comparison between the different operating frequencies and the respective system efficiency is illustrated in Figure 8-3. As indicated through the different trend of the quality factor, the system efficiency also increases with decreasing frequency for a load factor of 0.1. This trend is also unaffected by the air gap length. For the medium and high-power cases, the overall tendency of the HTS system is similar to a copper system, where the efficiency increases with frequency. In general, the system efficiency decreases rapidly due to the low operating temperature and the cooling penalty, defined by k_c. Furthermore, the cooling requirement is the highest for high load factors and it decreases with frequency. However, as the frequency decreases, the overall amount of power that can be transferred decreases as well. Therefore, the effectiveness of the WPT system is greatly limited and the maximum achievable

efficiency for an air gap of 0.01 m is approximately 67%. According to SAE J2954 [99], the WPT-efficiency should be at least 85%, which is difficult to achieve as demonstrated, particularly for high-power, high frequency applications such as EV charging. Nevertheless, some advantages of HTS-WPT can be used for low-power applications, which require high efficiencies.

Table 8-1 HTS-WPT case studies at 85 kHz using double pancake coils

Cases	d=0.01 m	d=0.05 m	d=0.125 m
	Input power [W]		
LF 0.1 with B_{ext}=20 mT	2,259	718	174
LF 0.4 with B_{ext}=75 mT	36,175	12,236	3,314
LF 0.8 with B_{ext}=150 mT	144,737	46,876	13,463
	Output power [W]		
LF 0.1 with B_{ext}=20 mT	2,137	602	81.67
LF 0.4 with B_{ext}=75 mT	32,753	9,104	985
LF 0.8 with B_{ext}=150 mT	129,730	33,335	3,495
	Transfer efficiency [%]		
LF 0.1 with B_{ext}=20 mT	94.60	83.92	46.97
LF 0.4 with B_{ext}=75 mT	90.54	74.40	29.71
LF 0.8 with B_{ext}=150 mT	89.63	71.11	25.96
	Cooling power Tx [W]		
LF 0.1 with B_{ext}=20 mT	605.54	605.54	605.54
LF 0.4 with B_{ext}=75 mT	17,338	17,338	17,338
LF 0.8 with B_{ext}=150 mT	76,396	76,396	76,396
	Cooling power Rx [W]		
LF 0.1 with B_{ext}=20 mT	572.82	508.19	357.71
LF 0.4 with B_{ext}=75 mT	15,697	12,900	5,152
LF 0.8 with B_{ext}=150 mT	68,475	54,327	19,833
	System efficiency [%]		
LF 0.1 with B_{ext}=20 mT	62.17	32.89	7.68
LF 0.4 with B_{ext}=75 mT	47.32	21.43	3.82
LF 0.8 with B_{ext}=150 mT	44.80	18.77	3.19

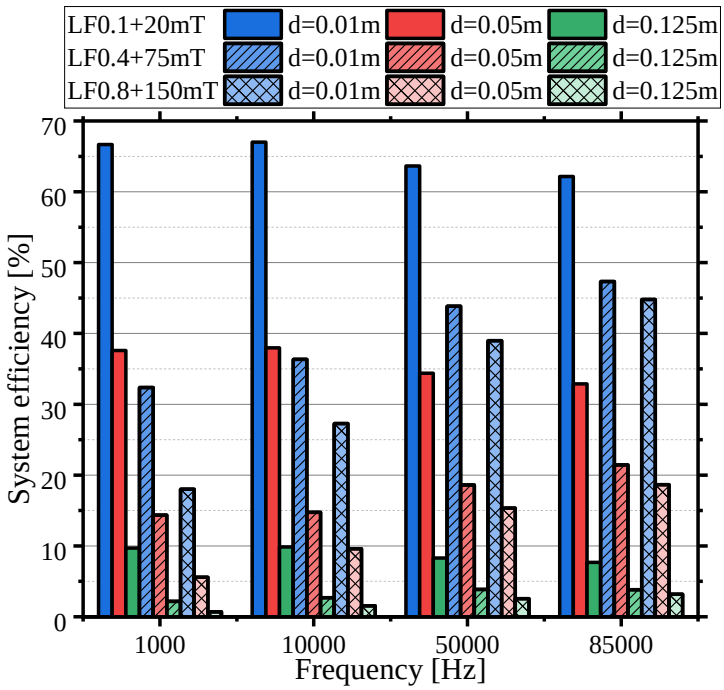

Figure 8-3 Comparison of the system efficiency for different load factors and operating frequencies

HTS WPT-system performance was demonstrated from the perspective of HTS coated conductor properties. Previous research has outlined HTS-WPT for EVs as a promising technology, however, the skin effect at high frequencies and the associated cooling requirements have widely been neglected. Therefore, such conclusions do not show the full picture. For the first time, the AC losses of an HTS WPT-system are quantified based on the multilayer structure of HTS CCs. Results show that the application of HTS CCs in high power WPT is not practical, because the cooling power required is too large, compromising the overall WPT-system efficiency.

8.2 Thesis summary

This thesis presents an innovative investigation of wireless power transfer systems for EVs and the use of HTS coils in these systems. EVs are a key technology to allow renewable energies to penetrate into the transportation sector and substitute fossil fuels on a large scale to enable the transition towards a more sustainable energy system. Currently, large scale deployment of EVs is lacking due to concerns regarding the charging infrastructure and the achievable range compared to conventional internal combustion engine vehicles. Wireless charging is a more flexible and convenient charging method which has attracted broad attention. It uses an inductive link between the charging pad installed in the road pavement and the vehicle pad on the underbody of the EV.

An in-depth review of the key components and respective research as well as topics related to WPT-systems for EV charging was presented.

Initially, the achievable driving range of electric vehicles charged by static, quasi-dynamic, dynamic or combined WPT systems was investigated. To this aim, an extended battery model was coupled with a force-based vehicle model in Matlab to study the impact of wireless charging on the battery system of an EV. Based on different driving cycles, multiple environments were modelled. For the first time, external and internal factors, such as the ambient temperature and the age of the battery system were considered. As shown, a deviation from the rated temperature of the battery has a high impact on the change in SoC due to the reduction in available capacity and change in auxiliary power demand. Lower temperatures have a stronger impact compared to higher temperatures. The viability of wireless charging increases with the age of the battery due to the limited driving range and amplified ratio of added and removed charge. Therefore, WPT technology will alleviate the issue of range anxiety by extending the achievable range significantly. While SWPT is best employed on busy roads, DWPT should be used on highways. However, when combining both systems, the size and power level can be reduced significantly, which lowers EMF emissions. On one hand, the proposed model can be extended and applied to any given routes and driving cycles. On the other hand, it is difficult to get such information from real routes.

After demonstrating the viability of wireless charging, system and performance changes due to the implementation of HTS coils are investigated. HTS can improve transfer performance through higher quality factors Q, compared to copper coils. Through experimental work the efficiency of multiple WPT systems using copper coils, HTS coils and copper coils submerged in LN_2 was investigated. A practical numerical method to estimate the power transfer performance of the wireless charging systems is proposed. Different frequencies relevant for EV wireless charging from 11 kHz up to 85 kHz were used. The measurements show that HTS-HTS systems have superior transfer efficiency over Cu-Cu systems below 50 kHz. As the frequency increases, the difference between the systems becomes negligible. Additionally, hybrid systems which use HTS and copper coils as either transmitting or receiving coils show a similar performance to HTS-HTS systems. However, no clear advantage in terms of efficiency of one hybrid system over the other emerged. The measured efficiency was compared with simulation results obtained from a combination of FEA modelling and circuit modelling.

For the first time, a comprehensive investigation of the transport current loss, magnetisation loss, combined loss and their angular dependence of HTS coils in the frequency relevant to WPT (up to 85 kHz) for EVs has been carried out. Therefore, a 2D axisymmetric multilayer coil model was set up in COMSOL. It was shown that the loss in the copper layer surpasses the loss generated by the HTS layer at higher frequencies. The most common coil configurations were examined, including spiral, solenoid and double pancake. For transport current losses, the skin effect must be considered. In general, the frequency has a great impact on the transport current loss and its effect increases at higher load factors. Solenoid coils have the lowest transport current loss, while spiral coils have the highest. Contrary to the results obtained from the transport current loss calculations, the spiral configuration has the lowest magnetisation loss, while the solenoid layout has the highest. Depending on the frequency, the main contributor towards the magnetisation loss shifts between the copper and the HTS layer. Furthermore, the angular dependency of the coil configurations drastically changes with frequency. When subjecting HTS coils to both transport current and external magnetic field, the impact of the magnetic field changes depending on the load factor, frequency and winding layout. A transition frequency was introduced for the different loss mechanisms, at which copper losses are equal to the losses in the HTS layer. This frequency is strongly affected by the load factor, external magnetic field density and coil structure. The different loss contributions of individual turns within the coil were examined too.

As the losses generated are too high to reliably and feasibly use HTS coils in wireless charging systems, the possibility of reducing them was evaluated. MgB_2 is a strong contender to reduce the AC losses of superconducting systems, however, the lack of suitable literature for high frequency applications i.e. tens of kHz, makes it difficult to gauge its effectiveness and applicability. In addition, stabiliser-free tapes have been investigated, but they are not a reliable method of reducing the losses. Flux diverters seem to be the best option to reduce the AC losses of HTS coils. With the aid of a 2D axisymmetric numerical multilayer FEA model, a broad analysis of different geometric parameters of the flux diverter and related impacts was conducted. With the aid of a 2D axisymmetric numerical multilayer FEA model, the AC losses occurring of in a double pancake coil operated at a wide range of frequencies was investigated. The width of the diverter has the biggest impact on the losses of the HTS coil and the overall losses can be reduced by up to 60% with a width of 2 mm at a load factor of 0.5. In general, flux diverters are more suitable for applications that use high load factors and therefore are not dominated by the ferromagnetic losses

in the flux diverter. In addition, other techniques to reduce the losses within the HTS coils must be combined with flux diverters to enable high frequency superconducting WPT.

8.3 Future research

The research presented in this thesis demonstrates the advantages and disadvantages of the use of HTS in wireless charging systems for EVs. Future research should be conducted to alleviate shortcomings of the results and further improve achieved outcomes in the following areas:

The influence of the magnetic field is only partially covered by the FEA model used in this project due to its axisymmetric nature. A 3D multilayer model would show the true impact of the magnetic field on the losses and would allow for a true representation of the magnetic field between misaligned coils. Furthermore, with a 3D model, different coil geometries, that are not axisymmetric can be achieved, which would lead to improved coil designs to maximise WPT performance. In addition, the FEA simulations can be directly coupled with circuit models to allow for circuit optimisation. However, using such a 3D model is challenging and has a very high computational demand due to the large aspect ratios of the individual layers within the HTS CC and the overall size of the HTS coil.

As shown, AC losses are an important factor for the HTS WPT-system as they directly impact the cooling system. The design of the cooling system was not part of the research conducted here but should not be neglected in future work. The existing model can be combined with a thermal and/or mechanical module to simultaneously solve for local hotspots or mechanical stresses.

An impedance matching circuit should be added to the experimental set-up used in chapter 5 to improve the resonance link between transmitting and receiving side for large air gaps. Ideally such experiments should have the same scale as their copper coil counterpart. Additionally, high frequency AC loss measurements of HTS coils should be conducted. As shown the coil geometry is an important factor for AC losses. Therefore, different layouts should be investigated and experimentally validated. Finally, the proposed flux diverters should be validated for high frequencies and the overall design optimisation is an important area that needs further work. Furthermore, more research into AC loss reduction techniques must be conducted as flux diverters alone are not sufficient to enable HTS wireless power transfer.

Table A-1: Total impedance, power transfer efficiency and primary capacitance of SS, SP, PS, PP topology [128], [130], [131], [132]

Comp. Topology	Total impedance Z_{tot}	Power transfer efficiency at resonance η	Primary Capacitance C_1
SS	$R_1 + j\left(L_1\omega - \frac{1}{C_1\omega}\right) + \frac{(\omega M)^2}{\left(R_2 + R_L + j\left(L_2\omega - \frac{1}{C_2\omega}\right)\right)}$	$\frac{R_L}{R_2 + R_L + R_1\left(\frac{R_2 + R_L}{\omega M}\right)^2}$	$\frac{L_2 C_2}{L_1}$
SP	$R_1 + j\left(L_1\omega + \frac{1}{C_1\omega}\right) + \frac{(\omega M)^2}{\left(R_2 + jL_2\omega + \frac{R_L}{1 + jR_L C_2\omega}\right)}$	$\frac{R_L}{R_2 + R_L + \frac{R_2 {R_L}^2}{(\omega L_2)^2} + \frac{R_1 {R_2}^2}{(\omega M)^2} + \frac{R_1\left(L_2\omega^2 + \frac{R_L R_2}{\omega^2 L_2}\right)^2}{(\omega M)^2}}$	$\frac{{L_2}^2 C_2}{L_1 L_2 - M^2}$
PS	$\frac{1}{R_1 + j\omega(L_1 + C_1) + \frac{(\omega M)^2}{\left(R_2 + R_L + j\left(L_2\omega - \frac{1}{C_2\omega}\right)\right)}}$	$\frac{R_L}{R_2 + R_L + R_1\left(\frac{R_2 + R_L}{\omega M}\right)^2}$	$\frac{L_1 (C_2 L_2 R_L)^2}{M^4 + L_1 L_2 {R_L}^2}$
PP	$\frac{1}{\frac{1}{R_1 + jL_1\omega + \frac{(\omega M)^2 (1 + jR_L C_2\omega)}{\left(R_L + (R_2 + jL_2\omega)(1 + jR_L C_2\omega)\right)}} + jC_1\omega}$	$\frac{R_L}{R_2 + R_L + \frac{R_2 {R_L}^2}{(\omega L_2)^2} + \frac{R_1 {R_2}^2}{(\omega M)^2} + \frac{R_1\left(L_2\omega^2 + \frac{R_L R_2}{\omega^2 L_2}\right)^2}{(\omega M)^2}}$	$\frac{{L_2}^2 (L_1 L_2 - M^2) C_2}{(L_1 L_2 - M^2)^2 + M^4 {R_L}^2 L_2 C_2}$

References

[1] P. Machura and Q. Li, "A critical review on wireless charging for electric vehicles," *Renewable and Sustainable Energy Reviews,* vol. 104, pp. 209-234, 2019.

[2] P. Machura, K. Kails and Q. Li, "Loss analysis of superconducting wireless charging of electric vehicles," *Journal of Physics: Conference Series,* vol. 1559, p. 012095, 2020.

[3] P. Machura, V. De Santis and Q. Li, "Driving Range of Electric Vehicles Charged by Wireless Power Transfer," *IEEE Transactions on Vehicular Technology,* vol. 69, no. 6, pp. 5968-5982, 2020.

[4] P. Machura, H. Zhang, K. Kails and Q. Li, "Loss characteristics of superconducting pancake, solenoid and spiral coils for wireless power transfer," *Superconductor Science and Technology,* vol. 33, no. 7, p. 074008, 2020.

[5] P. Machura and Q. Li, "AC Loss Reduction through Flux Diverters for Superconducting Wireless Charging Coils at High Frequency," *IEEE Transactions on Applied Superconductivity,* 2021.

[6] K. Kails, M. Yao, H. Zhang, P. Machura, M. Mueller and Q. Li, "T-formulation based numerical modelling of dynamic loss with a DC background field," *Journal of Physics: Conference Series,* vol. 1559, p. 012145, 2020.

[7] K. Kails, H. Zhang, P. Machura, M. Mueller and Q. Li, "Dynamic loss of HTS field windings in rotating electric machines," *Superconductor Science and Technology,* vol. 33, no. 4, 2020.

[8] H. Zhang, M. Yao, K. Kails, P. Machura, M. Mueller, Z. Jiang, Y. Xin and Q. Li, "Modelling of electromagnetic loss in HTS coated conductors over a wide frequency band," *Superconductor Science and Technology,* vol. 33, no. 2, 2020.

[9] H. Zhang, P. Machura, K. Kails, H. Chen and M. Mueller, “Dynamic loss and magnetization loss of HTS coated conductors, stacks, and coils for high-speed synchronous machines,” *Superconductor Science and Technology,* vol. 33, no. 8, p. 084008, 2020.

[10] H. Zhang, K. Kails, P. Machura and M. Mueller, “Conceptual Design of Electrodynamic Wheels Based on HTS Halbach Array Magnets,” *IEEE Transactions on Applied Superconductivity,* vol. 31, no. 5, p. 3601306, 2021.

[11] International Energy Agency (IEA), "Global Energy & CO2 Status Report 2017," IEA, 2018.

[12] BP, "BP Energy Outlook 2017," 2017. [Online]. Available: https://www.bp.com/content/dam/bp/pdf/energy-economics/energy-outlook-2017/bp-energy-outlook-2017.pdf. [Accessed 14 March 2018].

[13] International Energy Agency (IEA), “Global EV Outlook 2019,” IEA, Paris, France, 2019.

[14] BloombergNEF, “Electric Vehicle Outlook 2019,” BloombergNEF, 2019.

[15] S. Sachan and N. Adnan, “Stochastic charging of electric vehicles in smart power distribution grids,” *Sustainable Cities and Society,* vol. 40, pp. 91-100, 2018.

[16] N. Adnan, S. M. Nordin and O. M. Althawadi, “Barriers Towards Widespread Adoption of V2G Technology in Smart Grid ENvironment: From Laboratories to Commercialization,” in *Sustainable Interdependent Networks - From Theory to Application*, Cham, Switzerland, Springer International Publishing AG, 2018, pp. 121-134.

[17] S. Li and C. C. Mi, “Wireless Power Transfer for Electric Vehicle Applications,” *Journal of Emerging and Selected Topics in Power Electronics,* vol. 3, no. 1, pp. 4-17, 2015.

[18] N. Tesla, "Apparatus for Transmitting Electrical Energy". New York, USA Patent 1119732, 1914.

[19] A. Kurs, A. Karalis, R. Moffatt, J. Joannopoulos, P. Fisher and M. Soljacic, "Wireless Power Transfer via Strongly Coupled Magnetic Resonances," *Science,* vol. 317, no. 5834, pp. 83-86, 2007.

[20] B. Regensburger, S. sinha, A. Kumar, J. Vance, Z. Popovic and K. K. Afridi, "Kilowatt-Scale Large Air-Gap Multi-Modular Capacitive Wireless Power Transfer System for Electric Vehicle Charging," in *IEEE Applied Power Electronics Conference and Exposition (APEC)*, San Antonio, USA, 2018.

[21] M. Kline, I. Izyumin, B. Boser and S. Sanders, "Capacitive Power Transfer for Contactless Charging," in *Twenty-Sixth Annual IEEE Applied Power Electronics Conference and Exposition (APEC)*, Forth Worth, USA, 2011.

[22] C. T. Rim and C. Mi, "The Future of Wireless Power," in *Wireless Power Transfer for Electric Vehicles and Mobile Devices*, Hoboken, USA, John Wiley & Sons Ltd, 2017, pp. 607-612.

[23] J. Kim, H.-c. Son, D.-h. Kim and Y.-j. Park, "Optimal Design of a Wireless Power Transfer System with Multiple Self-Resonators for an LED TV," *IEEE Transactions on Consumer Electronics*, vol. 58, no. 3, pp. 775-780, 2012.

[24] J. Moon, H. Hwang, B. Jo, C.-K. Kwon, T.-G. Kim and S.-W. Kim, "Design and Implementation of a high-efficiency 6.78MHz resonant wireless power transfer system with a 5W fully integrated power receiver," *IET Power Electronics*, vol. 10, no. 5, pp. 577-578, 2017.

[25] V. Esteve, J. Jordán, E. Sanchis-Kilders, E. J. Dede, E. Maset, J. B. Ejea and A. Ferreres, "Comparative Study of a Single Inverter Bridge for Dual-Frequency Induction Heating Using Si and SiC MOSFETs," *IEEE Transactions on Industrial Electronics*, vol. 62, no. 3, pp. 1440-1450, 2015.

[26] J. Martis and P. Vorel, "Apparatus for Induction Heating 2.5kW Using a Series Resonant Circuit," in *Proceedings of the 16th International Conference on Mechatronics - Mechatronika*, Brno, Czech Republic, 2014.

[27] J. Serrano, J. Acerco, I. Lope, C. Carretero and J. M. Burdio, "A Flexible Cooking Zone Composed of Partially Overlapped Inductors," *IEEE Transactions on Industrial Electronics*, vol. 65, no. 10, pp. 7762-7771, 2018.

[28] K. Agrawal, R. Jegadeesan, Y.-X. Guo and N. V. Thakor, “Wireless Power Transfer Strategies for Implantable Bioelectronics: Methodological Review,” *IEEE Reviews in Biomedical Engineering*, vol. 10, pp. 1-28, 2017.

[29] T. Campi, S. Cruciani, V. De Santis, F. Maradei and M. Feliziani, “Near Field Wireless Power of Deep Medical Implants,” *Energies*, vol. 12, no. 14, pp. 1-18, 2019.

[30] V. B. Gore and D. H. Gawali, "Wireless Power Transfer Technology for Medical Applications," in *Conference on Advances in Signal Processing (CASP)*, Pune, India, 2016.

[31] C. Xiao, D. Cheng and K. Wei, "An LCC-C Compensated Wireless Charging System for Implantable Cardiac Pacemakers: Theory, Experiment, and Safety Evaluation," *IEEE Transactions on Power Electronics*, vol. 33, no. 6, pp. 4894-4905, 2018.

[32] T. Sun, X. Xie and Z. Wang, Wireless Power Transfer for Medical Microsystems, First ed., New York, USA: Springer, 2013.

[33] D.-B. Lin, T.-H. Wang and F.-J. Chen, "Wireless Power Transfer via RFID Technology for Wearable Device Applications," in *International Microwave Workshop Series on RF and Wireless Technologies for Biomedical and Healthcare Applications (IMWS-BIO)*, Taipei, Taiwan, 2015.

[34] K. Finkenzeller, RFID Handbook - Fundamentals and Applications in Contactless Smart Cards, Radio Frequency Identification and Near-Field Communication, Third ed., Chichester, United Kingdom: Wiley, 2010.

[35] R. W. Porto, V. J. Brusamarello, I. Müller, F. L. Cabrera Riaño and F. R. De Sousa, "Wireless Power Transfer for Contactless Instrumentation and Measurement," *IEEE Instrumentation & Measurement Magazine*, vol. 20, no. 4, pp. 49-54, 2017.

[36] R. Trevisan and A. Costanzo, "A UHF Near-Field Link for Passive Sensing in Industrial Wireless Power Transfer Systems," *IEEE Transactions on Microwave Theory and Techniques*, vol. 64, no. 5, pp. 1634-1643, 2016.

[37] M. Sugino and T. Masamura, "The wireless power transfer systems using the Class E push-pull inverter for industrial robots," in *IEEE Wireless Power Transfer Conference (WPTC)*, Taipei, Taiwan, 2017.

[38] R. Narayanamoorthi, A. V. Juliet and C. Bharatiraja, "Frequency Splitting-Based Wireless Power Transfer and Simultaneous Propulsion Generation to Multiple Micro-Robots," *IEEE Sensors Journal*, vol. 18, no. 13, pp. 5566-5575, 2018.

[39] S. Chopra and P. Bauer, "Driving Range Extension of EV With On-Road Contactless Power Transfer-A Case Study," *IEEE Transactions on Industrial Electronics*, vol. 60, no. 1, pp. 329-338, 2013.

[40] R. J. Sedwick, "Long range inductive power transfer with superconducting oscillators," *Annals of Physics*, vol. 325, pp. 287-299, 2010.

[41] H. Kamerlingh Onnes, *Commun. Phys. Lab. Univ. Leiden*, Vols. 119,120,122,124, 1911.

[42] D. van Delft and P. Kes, "The discovery of superconductivity," *Physics Today*, vol. 63, no. 9, pp. 38-42, 2010.

[43] W. Meissner and R. Ochsenfeld, "Ein neuer Effekt bei Eintritt der Supraleitfähigkeit," *Naturwissenschaften*, vol. 21, pp. 787-788, 1933.

[44] F. London and H. London, "The electromagnetic equations of the supraconductor," *Proceedings of the Royal Society of London*, vol. 149, no. 866, pp. 71-88, 1935.

[45] V. Ginzburg and L. Landau, "On the theory of superconductivity," *Zh Eksperim Teor Fiz*, vol. 20, 1950.

[46] J. Bardeen, C. Leon and J. Schrieffer, "Microscopic Theory of Superconductivity," *Physical Review*, vol. 106, no. 1, p. 162, 1957.

[47] J. Bardeen, J. Cooper and J. Schrieffer, "Theory of Superconductivity," *Physical Review*, vol. 108, no. 5, p. 1175, 1957.

[48] A. Abrikosov, “On the Magnetic Properties of Superconductors of the Second Group,” *Journal of Experimental and Theoretical Physics,* vol. 32, no. 6, pp. 1174-1182, 1957.

[49] F. Silsbee, “A note on electrical conduction in metals at low temperatures,” *Journal of the Washongton Acadamy of Sciences,* vol. 6, no. 17, pp. 597-602, 1916.

[50] P. J. Ray, “Structural investigation of La2–xSrxCuO4+y - Following staging as a function of temperature,” Master Thesis University of Copenhagen, Copenhagen, Denmark, 2015.

[51] J. Bednorz and K. Müller, “Possible High Tc Superconductivity in the Ba-La-Cu-O System,” *Zeitschrift für Physik B: Condensed Matter,* vol. 64, p. 189, 1986.

[52] Kirschner, I. et al., “High-Tc Superconductivity in La-Ba-Cu-O and Y-Ba-Cu-O,” *Europhysics Letters,* vol. 3, no. 12, p. 1309, 1987.

[53] S. Martin, A. Fiory, R. Fleming, L. Schneemeyer and J. Waszczak, “Temperature dependence of the resistivity tensor in superconducting Bi2Sr2.2Ca0.8Cu2O8 crystals,” *Physical review letters,* vol. 60, no. 21, p. 2194, 1988.

[54] S. Jin, H. Mavoori, C. Bower and R. Van Dover, “High critical currents in iron-clad superconducting MgB2 wires,” *Nature,* vol. 411, no. 6837, pp. 563-565, 2001.

[55] F. Grilli, E. Pardo, A. Stenvall, D. N. Nguyen, W. Yuan and F. Gömöry, "Computation of Losses in HTS Under the Action of Varying Magnetic Fields and Currents," *IEEE Transactions on Applied Superconductivity,* vol. 24, no. 1, 2014.

[56] C. Bean, “Magnetization of hard superconductors,” *Physical Review Letters,* vol. 8, pp. 250-253, 1962.

[57] C. Bean, “Magnetization of high-field superconductors,” *Reviews of Modern Physics,* vol. 9, pp. 31-38, 1964.

[58] C. P. J. Poole, R. Prozorov, H. A. Farach and R. J. Creswick, Superconductivity, Amsterdam, Netherlands: Elsevier Inc., 2014.

[59] Y. Kim, C. Hempstead and A. Strnad, “Critical Persistent Currets in Hard Superconductors,” *Physical Review Letters,* vol. 9, no. 7, pp. 306-309, 1962.

[60] Y. Kim, C. Hempstead and A. Strnad, “Magnetization and Critical Supercurrents,” *Physical Review Letters,* vol. 129, pp. 528-535, 1963.

[61] P. Anderson, “Theory of flux creep in hard superconductors,” *Physical Review Letters,* vol. 9, no. 7, pp. 309-311, 1963.

[62] Q. Jiang, M. Majoros, Z. Hong, A. Campbell and T. Coombs, “Design and AC loss analysis of a superconducting synchronous motor,” *Superconductor Science and Technology,* vol. 19, pp. 1164-1168, 2006.

[63] F. Gömöry, “Improvement of the self-field critical current of a high-Tc superconducting tape by the edge cover from soft ferromagnetic material,” *Applied Physics Letters 89,* vol. 89, 2006.

[64] J. Rhyner, “Magnetic properties and AC-losses of superconductors with power law Current-voltage characteristics,” *Physica C,* vol. 212, pp. 292-300, 1993.

[65] Fujikura, Interviewee, *personal correspondence.* [Interview]. 2018.

[66] R. Brambilla, F. Grilli and L. Martini, “Development of an edge-element model for AC loss computation of high-temperature superconductors,” *Superconductor Science and Technology,* vol. 20, no. 1, 2006.

[67] M. D. Ainslie, W. Yuan, Z. Hong, R. Pei, T. J. Flack and T. A. Coombs, “Modeling and Electrical Measurement of Transport AC Loss in HTS-Based Superconducting Coils for Electric Machines,” *IEEE Transactions on Applied Superconductivity,* vol. 21, no. 3, pp. 3265-3268, 2010.

[68] F. Grilli, R. Brambilla and L. Martini, “Modeling high-temperature superconducting tapes by means of edge finite elements,” *IEEE Transactions on Applied Superconductivity,* vol. 17, no. 2, pp. 3155-3158, 2007.

[69] K. Kajikawa, T. Hayashi, R. Yoshida, M. Iwakuma and K. Funaki, “Numerical evaluastion of AC losses in HTS wires with 2D FEM formulated by self magnetic field,” *IEEE Transactions on Applied Superconductivity,* vol. 19, no. 12, pp. 1246-1252, 2003.

[70] N. Amemiya, K. Yoda, S. Kasai, Z. Jiang, G. A. Levin, P. N. Barnes and C. E. Oberly, “AC Loss Characteristics of Multifilamentary YBCO Coated Conductors,” *IEEE Transactions on Applied Superconductivity,* vol. 15, no. 2, pp. 1637-1642, 2005.

[71] F. Kimura and N. Amemiya, “Numerical Analysis of AC Losses in Multifilamentary Coated Conductors With Non-Uniform Electric Properties,” *IEEE Transactions on Applied Superconductivity,* vol. 17, no. 2, pp. 2402-2405, 2007.

[72] N. Amemiya, S. Murasawa, N. Banno and K. Miyamoto, “Numerical modelings of superconducting wires for AC loss calculations,” *Physica C,* vol. 310, pp. 16-29, 1998.

[73] A. Stenvall and T. Tarhasaari, “Programming finite element method based hysteresis loss computation software using non-linear superconductor resistivity and T-φ formulation,” *Superconductor Science and Technology,* vol. 23, p. 075010, 2010.

[74] A. Stenvall and T. Tarhasaari, “An eddy current vector potential formulation for estimating hysteresis losses of superconductors with FEM,” *Superconductor Science and Technology,* vol. 23, no. 12, p. 125013, 2010.

[75] A. Campbell, “A direct method for obtaining the critical state in two and three dimensions,” *Superconductor Science and Technology,* vol. 22, p. 034005, 2009.

[76] G. Lousberg, M. Ausloos, C. Geuzaine, P. Dular, P. Vanderbemden and B. Vanderheyden, “Numerical simulation of the magnetization of high-temperature superconductors: a 3d finite element method using a single time-step iteration,” *Superconductor Science and Technology,* vol. 22, p. 055005, 2009.

[77] Y. Liu, Z. Jiang, G. Sidorov, C. Bumby, R. Badcock and J. Fang, "Dynamic resistance measurement in a YBCO wire under perpendicular magnetic field at various operating temperatures," *Journal of Applied Physics,* vol. 126, p. 243904, 2019.

[78] V. Parma, “Cryostat Design,” in *CAS - CERN Accelerator School: Course on Superconductivity for Accelerators*, Erice, Italy, 2013.

[79] M. Ainslie, A. George, R. Shaw, L. Dawson, A. Winfield, M. Steketee and S. Stockley, "Design and market considerations for axial flux superconducting electric machine design," *Journal of Physics: Conference Series*, vol. 507, p. 032022, 2014.

[80] K. Kails , Q. Li and M. Mueller, “Novel model of stator design to reduce the mass of superconducting generators,” *Superconductor Science and Technology*, vol. 31, no. 5, p. 055009, 2018.

[81] M. Saruwatari, K. Yun, M. Iwakuma, K. Tamura, Y. Hase, Y. Sasamori and T. Izumi, “Design Study of 15-MW Fully Superconducting Generators for Offshore Wind Turbine,” *IEEE Transactions on Applied Superconductivity*, vol. 26, no. 4, p. 5206805, 2016.

[82] J. Lee, G. Seo, J. Mun, M. Park and S. Kim, “Thermal and Mechanical Design for Refrigeration System of 10MW Class HTS Wind Power Generator,” *IEEE Transactions on Applied Superconductivity*, vol. 30, no. 4, p. 5201905, 2020.

[83] K. Yang, Y. Yang, M. Junaid, S. Liu, Z. Liu, Y. Geng and J. Wang, “Direct-Current Vacuum Circuit Breaker With Superconducting Fault-Current Limiter,” *IEEE Transactions on Applied Superconductivity*, vol. 28, no. 1, p. 5600108, 2018.

[84] D. Xia, Q. Qiu, Z. Zhang, S. Liu and Z. Xia, “Magnetic Field and Characteristic Analysis of the Superconducting Fault Current Limiter for DC Applications,” *IEEE Transactions on Applied Superconductivity*, vol. 28, no. 3, p. 5601405, 2018.

[85] J. Sun, J. Du, S. Mo, Y. Cai, W. Yuan and T. Ma, “Design and Performance Test of a 20-kV DC Superconducting Fault Current Limiter,” *IEEE Transactions on Applied Superconductivity*, vol. 30, no. 2, p. 5600305, 2020.

[86] J. Lim, H. Yang, S. Sohn, S. Yim, S. Jung, S. Han, H. Kim, Y. Kim and S. Hwang, “Cryogenic System for 80-kV DC HTS Cable in the KEPCO Power Grid,” *IEEE Transactions on Applied Superconductivity*, vol. 25, no. 3, p. 5402804, 2015.

[87] W. Yuan, S. Venuturumilli, Z. Zhang, Y. Mavrocostanti and M. Zhang, "Economic Feasibility Study of Using High-Temperature Superconducting Cables in U.K.'s Electrical Distribution Networks," *IEEE Transactions on Applied Superconductivity,* vol. 28, no. 4, p. 5401505, 2018.

[88] F. Weng, M. Zhang, T. Lan, Y. Wang and W. Yuan, "Fully superconducting machine for electric aircraft propulsion: study of AC loss for HTS stator," *Superconductor Science and Technology,* 2020.

[89] K. Kails, H. Zhang, M. Mueller and Q. Li, "Loss characteristics of HTS coated conductors in field windings of electric aircraft propulsion motors," *Superconductor Science and Technology,* vol. 33, p. 064006, 2020.

[90] M. Oomen, "AC Loss in superconducting Tapes and Cables," PhD Thesis, University of Twente, 2000.

[91] M. Erdogan, S. Tunc, S. Yildiz and F. Inanir, "A Comparative Studz of AC Transport and Eddy Current Losses for Coil Made of HTS Tapes Coated with Copper Stabilizer," *Journal of Superconductivity and Novel Magnetism,* vol. 30, pp. 3277-3283, 2017.

[92] J. Rabbers, B. ten Haken, O. Shevchenko and H. ten Kate, "Total AC loss of BSCCO/Ag tapes in power applications, an engineering approach to describe the AC loss in tapes and coils," *Physica C,* Vols. 372-376, pp. 1781-1783, 2002.

[93] M. Ainslie, V. Rodriguez-Zermeno, Z. Hong, W. Yuan, T. Flack and T. Coombs, "An improved FEM model for computing transport AC loss in coils made of RABiTS YBCO coated conductors for electric machines," *Superconductor Science and Technology,* vol. 24, no. 4, p. 045005, 2011.

[94] M. Ainslie, T. Flack and A. Campbell, "Calculating transport AC losses in stacks of high temperature superconductor coated ocnductors with magnetic substrates using FEM," *Physica C: Superconductivity,* vol. 472, no. 1, pp. 50-56, 2012.

[95] W. Norris, “Calculation of hysteresis losses in hard superconductors carrying ac: isolated conductors and edges of thin sheets,” *Journal of Physics D: Applied Physics*, vol. 3, no. 4, p. 489, 1970.

[96] E. H. Brandt and M. Indenbom, “Type-II-superconductor strip with current in a perpendicular magnetic field,” *Physical review B*, vol. 48, no. 17, p. 12893, 1993.

[97] S. Stavrev and B. Dutoit, “Frequency dependence of AC loss in Bi/2223/Ag-sheathed tapes,” *Physica C*, vol. 310, pp. 86-89, 1998.

[98] F. Gömöry, L. Gherardi, R. Mele, D. Morin and G. Crotti, “Critical state and AC losses in multifilamentary BiSrCaCuO-2223/Ag tapes studied by transport and magnetic measurements,” *Physica C*, vol. 279, pp. 39-46, 1997.

[99] Society of Automotive Engineers (SAE), “J2954 - Wireless Power Transfer for Light-Duty Plug-In/ Electric Vehicles and Alignment Methodology,” SAE international, Warrendale, USA, 2016.

[100] H. L. Li, P. A. Hu and G. Covic, "A High Frequency AC-AC Converter for Inductive Power Transfer (IPT) Applications," in *Wireless Power Transfer - Principles and Engineering Explorations*, K. Y. Kim, Ed., InTech, 2012, pp. 253-272.

[101] M. Petersen and F. W. Fuchs, "Development of a 5 kW Inductive Power Transfer System Including Control Strategy for Electric Vehicles," in *International Exhibition and Conference for Power Electronics, Intelligent Motion, Renewable Energy and Energy Management*, Nuremberg, Germany, 2014.

[102] A. Pevere, R. Petrella, C. C. Mi and S. Zhou, "Design of a high efficiency 22 kW wireless power transfer system for EVs fast contactless charging stations," in *IEEE International Electric Vehicle Conference (IEVC)*, Florence, Italy, 2014.

[103] D. Vilathgamuwa and J. Sampath, “Wireless Power Transfer (WPT) for Electric Vehicles (EVs) - Present and Future Trends,” in *Plug In Electric Vehicles in Smart Grids - Integration Techniques*, S. Rajakaruna, A. Gosh and F. Shahnia, Eds., Singapore, Springer Science+Business Media Singapore, 2015, pp. 33-61.

[104] A. Triviño, J. González-González and J. Aguado, "Evaluation of Losses in a Bidirectional Wireless Power Transfer System for Electric Vehicles," in *IEEE International Conference on Environment and Electrical Engineering and IEEE Industrial and Commercial Power Systems Europe (EEEIC / I&CPS Europe)*, Milan, Italy, 2017.

[105] B. Singh, B. N. Singh, A. Chandra, K. Al-Haddad, A. Pandey and D. P. Kothari, "A Review of Single-Phase Improved Power Quality AC-DC Converter," *IEEE Transactions on Industrial Electronics*, vol. 50, no. 5, pp. 962-981, 2003.

[106] E. Ciprioano dos Santos, C. Brandao Jacobina, E. R. Cabral da Silva and N. Rocha, "Single-Phase to Three-Phase Power Converters: State of the Art," *IEEE Transactions on Power Electronics*, vol. 27, no. 5, pp. 2437-2452, 2012.

[107] B. Singh, B. N. Singh, A. Chandra, K. Al-Haddad, A. Pandey and D. P. Kothari, "A Review of Three-Phase Improved Power QUality AC-DC Converter," *IEEE Transactions on Industrial Electronics*, vol. 51, no. 3, pp. 641-660, 2004.

[108] P. Raval, D. Kacprzak and A. P. Hu, "Technology Overview and Concept of Wireless Charging Systems," in *Wireless Power Transfer*, J. I. Agbinya, A. Jamalipour, M. Ruggeri and H. Nikookar, Eds., Aalborg, Denmark, River Publishers, 2016, pp. 347-384.

[109] P. Ning, J. M. Miller, O. C. Onar and C. P. White, “A Compact Wireless Charging System for Electric Vehicles,” in *IEEE Energy Conversion Congress and Exposition*, Denver, USA, 2013.

[110] S. Rosu, M. Khallian, V. Cirimele and P. Guglielmi, "A Dynamic Wireless Charging System for Electric Vehicles Based on DC/AC Converters with SiC MOSFET-IGBT Switches and Resonant Gate-Drive," in *Annual Conference of the IEEE Industrial Electronics Society (IECON)*, Florence, Italy, 2016.

[111] K. F. Hoffmann and J. P. Kärst, "High Frequency Power Switch - Improved Performance by MOSFETs and IGBTs Connected in Parallel," in *European Conference on Power Electronics and Applications*, Dresden, Germany, 2005.

[112] S. Zhang, U. K. Madawala, D. J. Thrimawithana and B. S. Riar, "A Model for a Three-phase Modular Multi-level Converter based on Inductive Power Transfer Technology (M2LC-IPT)," in *IEEE 2nd International Future Energy Electronics Conference (IFEEC)*, Taipei, Taiwan, 2015.

[113] D. Baros, K. Bampouras, P. Apostolidou, E. Ioannou and N. Papanikolaou, "Multilevel Inverters for Motor Drives and Wireless Power Transfer Applications," in *Panhellenic Conference on Electronics and Telecommunications (PACET)*, Xanthi, Greece, 2017.

[114] E. Asa, K. Colak, M. Bojarski and D. Czarkowski, "A Novel Multi-Level Phase-Controlled Resonant Inverter with Common Mode Capacitor for Wireless EV Chargers," in *IEEE Transportation Electrification Conference and Expo (ITEC)*, Dearborn, USA, 2015.

[115] M. Malinowski, K. Gopakumar, J. Rodriguez and M. A. Perez, "A Survey on Cascaded Multilevel Inverters," *IEEE Transactions on Industrial Electronics*, vol. 57, no. 7, pp. 2197-2206, 2010.

[116] B. X. Nguyen, D. Vilathgamuwa, G. Foo, A. Ong, P. K. Sampath and U. K. Madawala, "Cascaded Multilevel Converter based Bidirectional Inductive Power Transfer (BIPT) System," in *International Power Electronics Conference*, Hiroshima, Japan, 2014.

[117] B. X. Nguyen, D. M. Vilathgamuwa, G. Foo, P. Wang and A. Ong, "A Modified Cascaded Multilevel Converter Topology for High Power Bidirectional Inductive Power Transfer Systems With The Reduction Of Switching Devices and Power Losses," in *IEEE 11th International Conference on Power Electronics and Drive Systems*, Sydney, Australia, 2015.

[118] X. B. Nguyen, D. M. Vilathgamuwa and U. K. Madawala, "A SiC-Based Matrix Converter Topology for Inductive Power Transfer System," *IEEE Transactions on Power Electronics*, vol. 29, no. 8, pp. 4029-4038, 2014.

[119] A. Ecklebe and A. Lindemann, "Bi-directional Switch Commutation for a Resonant Matrix Converter supplying a Contactless Energy Transmission System," in *Power Conversion Conference*, Nagoya, Japan, 2007.

[120] B. S. Riar, U. K. Madawala and D. J. Thrimawithana, "Analysis and Control of a Three-Phase Modular Multi-level Converter based on Inductive Power Transfer Technology (M2LC-IPT)," in *IEEE International Conference on Industrial Technology (ICIT)*, Cape Town, South Africa, 2013.

[121] M. Bland, L. Empringham, J. Clare and P. Wheeler, "A new resonant soft switching topology for direct AC-AC converters," in *2002 IEEE 33rd Annual IEEE Power Electronics Specialists Conference. Proceedings*, Cairns, Australia, 2002.

[122] S. Ruddell, U. K. Madawala, D. J. Thrimawithana and M. Neuburger, "A Novel Wireless Converter Topology for Dynamic EV Charging," in *IEEE Transportation Electrification Conference and Expo (ITEC)*, Dearborn, USA, 2016.

[123] S. M. Lukic, J. Cao, R. C. Bansal, F. Rodriguez and A. Emadi, "Energy Storage Systems for Automotive Applications," *IEEE Transactions on Industrial Electronics*, vol. 55, no. 6, pp. 2258-2267, 2008.

[124] M. Moghaddami and A. I. Sarwat, "Single-Phase Soft-Switched AC-AC Matrix Converter With Power Controller for Bidirectional Inductive Power Transfer Systems," *IEEE Transactions on Industry Applications*, vol. 54, no. 4, pp. 3760-3770, 2018.

[125] H. N. Nguyen, C. Zhang and J. Zhang, "Dynamic Demand Control of Electric Vehicles to Support Power Grid With High Penetration Level of Renewable Energy," *IEEE Transactions on Transportation Electrification*, vol. 2, no. 1, pp. 66-75, 2016.

[126] H. N. Nguyen, C. Zhang and M. A. Mahmud, "Optimal Coordination of G2V and V2G to Support Power Grids With High Penetration of Renewable Energy," *IEEE Transactions on Transportation Electrification*, vol. 1, no. 2, pp. 188-195, 2015.

[127] W. Zhang and C. C. Mi, "Compensation Topologies of High-Power Wireless Power Transfer Systems," *IEEE Transactions on Vehicular Technology*, vol. 65, no. 6, pp. 4768-4778, 2016.

[128] C.-S. Wang, G. A. Covic and O. H. Stielau, "Power Transfer Capability and Bifurcation Phenomena of Loosely Coupled Inductive Power Transfer Systems," *IEEE Transactions on Industrial Electronics*, vol. 51, no. 1, pp. 148-157, 2004.

[129] C.-S. Wang, O. H. Stielau and G. A. Covic, "Design Considerations for a Contactless Electric Vehicle Battery Charger," *IEEE Transactions on Industrial Electronics*, vol. 52, no. 5, pp. 1308-1314, 2005.

[130] S. Chopra and P. Bauer, "Analysis and Design Considerations for a Contactless Power Transfer System," in *IEEE 33rd International Telecommunications Energy Conference (INTELEC)*, Amsterdam, Netherlands, 2011.

[131] J. L. Villa, J. Sallan, J. F. S. Osorio and A. Llombart , "High-Misalignment Tolerant Compensation Topology For ICPT System," *IEEE Transactions on Industrial Electronics*, vol. 59, no. 2, pp. 945-951, 2012.

[132] J. Sallán, J. L. Villa, A. Llombart and J. F. Sanz, "Optimal Design of ICPT Systems Applied to Electric Vehicle Battery Charge," *IEEE Transactions on Industrial Electronics*, vol. 56, no. 6, pp. 2140-2149, 2009.

[133] K. Aditya and S. S. Williamson, "Design Guidelines to Avoid Bifurcation in a Series-Series Compensated Inductive Power Transfer System," *IEEE Transactions on Industrial Electronics*, vol. 66, no. 5, pp. 3973-3982, 2018.

[134] J. Hou, Q. Chen, S.-C. Wong, C. K. Tse and X. Ruan, "Analysis and Control of Series/Series-Parallel Compensated Resonant Converter for Contactless Power Transfer," *IEEE Journal of Emerging and Selected Topics in Power Electronics*, vol. 3, no. 1, pp. 124-136, 2015.

[135] W. Li, H. Zhao, S. Li, J. Deng, T. Kan and C. C. Mi, "Integrated LCC Compensation Topology for Wireless Charger in Electric and Plug-in Electric Vehicles," *IEEE Transactions on Industrial Electronics*, vol. 62, no. 7, pp. 4215-4225, 2015.

[136] S. Samanta and A. K. Rathore, "A New Current-Fed CLC Transmitter and LC Receiver Topology for Inductively Wireless Power Transfer Application: Analysis, Design, and

Experimental Results," *IEEE Transactions on Transportation Electrification*, vol. 1, no. 4, pp. 357-368, 2015.

[137] N. A. Keeling, G. A. Covic and J. T. Boys, "A Unity-Power-Factor IPT Pickup for High-Power Applications," *IEEE Transactions on Industrial Electronics*, vol. 57, no. 2, pp. 744-751, 2010.

[138] C.-Y. Huang, J. T. Boys and G. A. Covic, "LCL Pickup Circulating Current Controller for Inductive Power Transfer Systems," *IEEE Transactions on Power Electronics*, vol. 28, no. 4, pp. 2081-2093, 2013.

[139] U. K. Madalawa and D. J. Thrimawithana, "A Bidirectional Inductive Power Interface for Electric Vehicles in V2G Systems," *IEEE Transactions on Industrial Electronics*, vol. 58, no. 10, pp. 4789-4796, 2011.

[140] D. J. Thrimawithana, U. K. Madawala and M. Neath, "A Synchronization Technique for Bidirectional IPT Systems," *IEEE Transactions on Industrial Electronics*, vol. 60, no. 1, pp. 301-309, 2013.

[141] T. Campi, S. Cruciani, F. Maradei and M. Feliziani, "Near-Field Reduction in a Wireless Power Transfer System Using LCC Compensation," *IEEE Transactions on Electromagnetic Compatibility*, vol. 59, no. 2, pp. 686-694, 2017.

[142] S. Li, W. Li, J. Deng, T. D. Nguyen and C. C. Mi, "A Double-Sided LCC Compensation Network and Its Tuning Method for Wireless Power Transfer," *IEEE Transactions on Vehicular Technology*, vol. 64, no. 6, pp. 2261-2273, 2015.

[143] T. Kan, T.-D. Nguyen, J. C. White, R. K. Malhan and C. C. Mi, "A New Integration Method for an Electric Vehicle Wireless Charging System Using LCC Compensation Topology: Analysis and Design," *IEEE Transactions on Power Electronics*, vol. 32, no. 2, pp. 1638-1650, 2017.

[144] Y. Zhang, L. Wang, Y. Guo and C. Tao, "Null-Coupled Magnetic Integration for EV Wireless Power Transfer System," *IEEE Transactions on Transportation Electrification*, vol. 5, no. 4, pp. 968-976, 2019.

[145] T. Kan, F. Lu, T.-D. Nguyen, P. P. Mercier and C. C. Mi, "Integrated Coil Design for EV Wireless Charging Systems Using LCC Compensation Topology," *IEEE Transactions on Power Electronics*, vol. 33, no. 11, pp. 9231-9241, 2018.

[146] J. Deng, B. Pang, W. Shi and Z. Wang, "A new integration method with minized extra coupling effects using inductor and capacitor series-parallel compensation for wireless EV charger," *Applied Energy*, vol. 207, pp. 405-416, 2017.

[147] H. Feng, T. Cai, S. Duan, J. Zhao, X. Zhang and C. Chen, "An LCC-Compensated Resonant Converter Optimized for Robust Reaction to Large Coupling Variation in Dynamic Wireless Power Transfer," *IEEE Transactions on Industrial Electronics*, vol. 63, no. 10, pp. 6591-6601, 2016.

[148] W. Li, H. Zhao, J. Deng, S. Li and C. C. Mi, "Comparison Study on SS and Double-Sided LCC Compensation Topologies for EV/PHEV Wireless Chargers," *IEEE Transactions on Vehicular Technology*, vol. 65, no. 6, pp. 4429-4439, 2016.

[149] G. Zhu, D. Gao, S. Wang and S. Chen, "Misalignment Tolerance Improvement in Wireless Power Transfer Using LCC Compensation Topology," in *IEEE PELS Workshop on Emerging Technologies: Wireless Power Transfer (WoW)*, Chongqing, China, 2017.

[150] C. Xia, R. Chen, Y. Liu, G. Chen and X. Wu, "LCL/LCC resonant topology of WPT system for constant current, stable frequency and high-quality power transmission," in *IEEE PELS Workshop on Emerging Technologies: Wireless Power Transfer (WoW)*, Knoxville, USA, 2016.

[151] B. R. Long, J. M. Miller, A. Daga, P. C. Schrafel and J. Wolgemuth, "Which Way for Wireless Power: High Q or High K," in *IEEE PELS Workshop on Emerging Technologies: Wireless Power Transfer (WoW)*, Knoxville, USA, 2016.

[152] J. M. Miller, P. C. Schrafel, B. R. Long and A. Daga, "The WPT dilemma - High k or high Q?," in *IEEE PELS Workshop on Emerging Technologies: Wireless Power Transfer (WoW)*, Knoxville, USA, 2016.

[153] R. Bosshard, J. Muehlethaler, J. Kolar and I. Stevanovic, “Optimized Magnetic Design for Inductive Power Transfer Coils,” in *Twenty-Eighth Annual IEEE Applied Power Electronics Conference and Exposition (APEC)*, Long Beach, USA, 2013.

[154] R. Laouamer, M. Brunello, J. P. Ferieux, O. Normand and N. Buchheit, “A Multi-Resonant Converter for Non-Contact Charging with Electromagnetic Coupling,” in *23rd International Conference on Industrial Electronics, Control and Instrumentation (IECON)*, New Orleans, USA, 1997.

[155] A. J. Moradewicz and M. P. Kazmierkowski, "Contactless Energy Transfer System With FPGA-Controlled Resonant Converter," *IEEE Transactions on Industrial Electronics*, vol. 57, no. 9, pp. 3181-3190, 2010.

[156] J. Hirai, T.-W. Kim and A. Kawamura, "Study on Intelligent Battery Charging Using Inductive Transmission of Power and Information," *IEEE Transactions on Power Electronics*, vol. 15, no. 2, pp. 335-345, 2000.

[157] F. Nakao, Y. Matsuo, M. Kitaoka and H. Sakamoto, “Ferrite Core Couplers for Inductive Chargers,” in *Proceedings of the Power Conversion Conference-Osaka 2002* , Osaka, Japan, 2002.

[158] M. Budhia, G. A. Covic and J. T. Boys, “Design and Optimization of Circular Magnetic Structures for Lumped Inductive Power Transfer Systems,” *IEEE Transactions on Power Electronics*, vol. 26, no. 11, pp. 3096-3108, 2011.

[159] R. Bosshard, J. W. Kolar, J. Mühlethaler, I. Stevanovic, B. Wunsch and F. Canales, "Modeling and η-α-Pareto Optimization of Inductive Power Transfer Coils for Electric Vehicles," *IEEE Journal of Emerging and Selected Topics in Power Electronics*, vol. 3, no. 1, pp. 50-64, 2015.

[160] J. Han, Y. D. Kim and N.-H. Myung, "Efficient performance optimisation of wireless power transmission using genetic algorithm," *Electronics Letters*, vol. 50, no. 6, pp. 462-464, 2014.

[161] T. Yilmaz, N. Hasan, R. Zane and Z. Pantic, "Multi-Objective Optimization of Circular Magnetic Couplers for Wireless Power Transfer Applications," *IEEE Transactions on Magnetics*, vol. 53, no. 8, 2017.

[162] R. Bosshard and J. W. Kolar, “Multi-Objective Optimization of 50 kW/85 kHz IPT System for Public Transport,” *IEEE Journal of Emerging and Selected Topics in Power Electronics*, vol. 4, no. 4, pp. 1370-1382, 2016.

[163] Z. Luo and X. Wei, "Analysis of Square and Circular Planar Spiral Coils in Wireless Power Transfer System for Electrical Vehicles," *IEEE Transactions on Industrial Electronics*, vol. 65, no. 1, pp. 331-341, 2018.

[164] W. Chen, C. Liu, C. H. Lee and Z. Shan, "Cost-Effectiveness Comparison of Coupler Designs of Wireless Power Transfer for Electric Vehicle Dynamic Charging," *Energies*, vol. 9, no. 906, 2016.

[165] M. Budhia, G. Covic and J. Boys, "A New IPT Magnetic Coupler for Electric Vehicle Charging Systems," in *36th Annual Conference on IEEE Industrial Electronics Society*, Glendale, USA, 2010.

[166] Y. Nagatsuka, N. Ehara, Y. Kaneko, S. Abe and T. Yasuda, “Compact Contactless Power Transfer System for Electric Vehicles,” in *International Power Electronics Conference - ECCE ASIA -*, Hokkaido, Japan, 2010.

[167] M. Chigira, Y. Nagatsuka, Y. Kaneko, S. Abe, T. Yasuda and A. Suzuki, “Small-Size Light-Weight Transformer with New Core Structure for Contactless Electric Vehicle Power Transfer System,” in *IEEE Energy Conversion Congress and Exposition*, Phoenix, USA, 2011.

[168] G. A. J. Elliott, S. Raabe, G. A. Covic and J. T. Boys, “Multiphase Pickups for Large Lateral Tolerance Contactless Power-Transfer Systems,” *IEEE Transactions on Industrial Electronics*, vol. 57, no. 5, pp. 1590-1598, 2010.

[169] S. Raabe and G. A. Covic, "Practical Design Considerations for Contactless Power Transfer Quadrature Pick-Ups," *IEEE Transactions on Industrial Electronics*, vol. 60, no. 1, pp. 400-409, 2013.

[170] M. Budhia, G. A. Covic, J. T. Boys and C.-Y. Huang, "Development and evaluation of single sided flux couplers for contactless electric vehicle charging," in *IEEE Energy Conversion Congress and Exposition*, Phoenix, USA, 2011.

[171] M. Budhia, J. T. Boys, G. A. Covic and C.-Y. Huang, "Development of a Single-Sided Flux Magnetic Coupler for Electric Vehicle IPT Charging Systems," *IEEE Transactions on Industrial Electronics*, vol. 60, no. 1, pp. 318-328, 2013.

[172] G. A. Covic, M. L. G. Kissin, D. Kacprzak, N. Clausen and H. Hao, "A Bipolar Primary Pad Topology for EV Stationary Charging and Highway Power by Inductive Coupling," in *IEEE Energy Conversion Congress and Exposition*, Phoenix, USA, 2011.

[173] A. Zaheer, D. Kacprzak and G. A. Covic, "A Bipolar Receiver Pad in a Lumped IPT System for Electric Vehicle Charging Applications," in *IEEE Energy Conversion Congress and Exposition (ECCE)*, Raleigh, USA, 2012.

[174] S. Kim, G. A. Covic and J. T. Boys, "Analysis on Tripolar Pad for Inductive Power Transfer Systems," in *IEEE PELS Workshop on Emerging Technologies: Wireless Power Transfer (WoW)*, Knoxville, USA, 2016.

[175] S. Kim, G. A. Covic and J. T. Boys, "Tripolar Pad for Inductive Power Transfer Systems for EV Charging," *IEEE Transactions on Power Electronics*, vol. 32, no. 7, pp. 5045-5057, 2017.

[176] M. M. Alam, S. Mekhilef, M. Seyedmahmoudian and B. Horan, "Dynamic Charging of Electric Vehicle with Negligible Power Transfer Fluctuation," *Energies*, vol. 10, no. 701, 2017.

[177] R. Bosshard, U. Iruretagoyena and J. W. Kolar, "Comprehensive Evaluation of Rectangular and Double-D Coil Geometry for 50 kW/85kHz IPT System," *IEEE Journal of Emerging and Selected Topics in Power Electronics*, vol. 4, no. 4, pp. 1406-1415, 2016.

[178] Y. Liu, R. Mai, D. Liu, Y. Li and Z. He, "Efficiency Optimization for Wireless Dynamic Charging System With Overlapped DD Coil Arrays," *IEEE Transactions on Power Electronics*, vol. 33, no. 4, pp. 2832-2846, 2018.

[179] L. Xiang, X. Li, J. Tian and Y. Tian, "A Crossed DD Geometry and Its Double-Coil Excitation Method for Electric Vehicle Dynamic Wireless Charging Systems," *IEEE Access*, vol. 6, pp. 45120-45128, 2018.

[180] A. Zaheer, H. Hao, G. A. Covic and D. Kacprzak, "Investigation of Multiple Decoupled Coil Primary Pad Topologies in Lumped IPT Systems for Interoperable Electric Vehicle Charging," *IEEE Transactions on Power Electronics*, vol. 30, no. 4, pp. 1937-1955, 2015.

[181] S. Kim, A. Zaheer, G. Covic and J. Boys, "Tripolar Pad for Inductive Power Transfer System," in *40th Annual Conference of the IEEE Industrial Electronics Society*, Dallas, USA, 2014.

[182] S. Kim, G. A. Covic and J. T. Boys , "Comparison of Tripolar and Circular Pads for IPT Charging Systems," *IEEE Transactions on Power Electronics*, vol. 33, no. 7, pp. 6093-6103, 2018.

[183] I. Castillo-Zamora, P. S. Huynh, D. Vincent, F. J. Perez-Pinal, M. A. Rodriguez-Licea and S. Williamson, “Hexagonal Geometry Coil for a WPT High-Power Fast Charging Application,” *IEEE Transaction on Transportation Electrification*, vol. 5, no. 4, pp. 946-956, 2019.

[184] D. H. Tran, V. B. Vu and W. Choi, "Design of a High-Efficiency Wireless Power Transfer System WIth Intermediate Coils for the On-Board Chargers of Electric Vehicles," *IEEE Transactions on Power Electronics*, vol. 33, no. 1, pp. 175-187, 2018.

[185] R. Narayanamoorthi and A. V. Juliet, “Capacitor-Less High-Strength Resonant Wireless Power Transfer Using Open Bifilar Spiral Coils,” *IEEE Transactions on Applied Superconductivity*, vol. 29, no. 1, p. 5500108, 2019.

[186] A. Abrahamsen, N. Mijatovaic, E. Seiler, T. Zirngibl, C. Træholt, P. Nørgard, N. Pedersen, N. Andersen and J. Østergard, "Superconducting wind turbine generators," *Superconductor Science and Technology,* vol. 23, 2010.

[187] T.-K. Hoang, L. Queval, C. Berriaud and L. Vido, "Design of a 20MW Fully Superconducting Wind Turbine Generator to Minimize the Levelized Cost of Energy," *IEEE Transactions on Applied Superconductivity,* vol. 28, no. 4, p. 5206705, 2018.

[188] D. Lee, H.-C. Jo and S.-K. Joo, "Economic Evaluation Method for Fault Current Limiting Superconducting Cables Considering Network Congestion in a Power System," *IEEE Transactions on Applied Superconductivity,* vol. 26, no. 4, 2016.

[189] Y. He, Y. Wang, X. Nie, W. Chen and Z. Yan, "High-Temperature Superconducting Capacitor and Its Application to a Superconducting Wireless Power Transfer System," *IEEE Transactions on Applied Superconductivity,* vol. 29, no. 1, 2019.

[190] I.-S. Jeong, H.-S. Choi and M.-S. Kang, "Application of the Superconductor Coil for the Improvement of Wireless Power Transmission Using Magnetic Resonance," *Journal of Superconductivity and Novel Magnetism,* vol. 28, pp. 639-644, 2015.

[191] B. Yoo, J.-B. Song, J. C. Kim, Y.-G. Kim, J. Kim, K. Sim, I. Shin, D. Y. Hwang and H. Lee, "Superconducting Properties of Reacted Mono- and Multifilament MgB2 Wires With Respect to Bending Diameters Using a Custom-Made Bending Test Probe," *IEEE Transactions on Applied Superconductivity,* vol. 28, no. 3, 2018.

[192] Q. Li, M. Yao, Z. Jiang, C. Bumby and N. Amemiya, "Numerical modelling of dynamic loss in HTS coated conductors under perpendicular magnetic field," *IEEE Transactions on Applied Superconductivity,* vol. 28, no. 2, 2018.

[193] Q. Li, N. Amemiya, K. Takeuchi, T. Nakamura and N. Fujiwara, "Effects of Unevenly Distributed Critical Currents and Damaged Coated Conductors to AC losses of Superconducting Power Transmission Cables," *IEEE Transactions on Applied Superconductivity,* vol. 21, no. 3, pp. 953-956, 2011.

[194] Q. Li, Y. Xin and S. Wang, “Dependance of AC Loss on Structural Compactness of Superconducting Power Cables with Narrow Coated Conductors,” *IEEE Transactions on Applied Superconductivity,* vol. 26, no. 7, 2016.

[195] G. Zhang, H. Yu, L. Jing, J. Li, Q. Liu and X. Feng, “Wireless Power Transfer Using High Temperature Superconducting Pancake Coils,” *IEEE Transactions on Applied Superconductivity,* vol. 24, no. 3, 2014.

[196] Y. D. Chung, C. Y. Lee, H. K. Kang and Y. G. Park, "Desing Consideration and Efficiency Comparison of Wireless Power Transfer With HTS and Cooled Copper Antennas for Electric Vehicle," *IEEE Transactions on Applied Superconductivity*, vol. 25, no. 3, 2015.

[197] D. W. Kim, Y. D. Chung, H. K. Kang, Y. S. Yoon and T. K. Ko, “Characteristics of Contactless Power Transfer for HTS Coil Based on Electromagnetic Resonance Coupling,” *IEEE Transactions on Applied Superconductivity*, vol. 22, no. 3, 2012.

[198] H. Yu, G. Zhang, G. Liu, L. Jing and Q. Liu, "Asymmetry in Wireless Power Transfer Between a Superconducting Coil and a Copper Coil," *IEEE Transactions on Applied Superconductivity,* vol. 28, no. 3, 2018.

[199] D. W. Kim, Y. D. Chung, K. Khang, C. Y. Lee, H. M. Kim, H. C. Jo, Y. J. Hwang, J. Y. Jang and Y. S. Yoon, “Effects and Properties of Contactless Power Transfer for HTS Receivers With Four-Separate Resonance Coils,” *IEEE Transactions on Applied Superconductivity,* vol. 23, no. 3, 2013.

[200] Y. D. Chung, C. Y. Lee, H. Kang and Y. G. Park, “Design Considerations of Superconducting Wireless Power Transfer for Electric Vehicle at Different Inserted Resonators,” *IEEE Transactions on Applied Superconductivity*, vol. 26, no. 4, 2016.

[201] X. Wang, X. Nie, Y. Liang, F. Lu, Z. Yan and Y. Wang, “Analysis and experimental study of wireless power transfer with HTS coil and copper coil as the intermediate resonators system,” *Physica C: Superconductivity and its applications,* vol. 532, pp. 6-12, 2017.

[202] R. Inoue, D. Miyagi, M. Tsuda and H. Matsuki, “High-Efficiency Transmission of a Wireless Power Transmission System for Low-Frequency Using REBCO Double-Pancake Coils,” *IEEE Transactions on Applied Superconductivity,* vol. 27, no. 1, 2017.

[203] F. Chen, N. Taylor, R. Balieu and N. Kringos, "Dynamic application of the Inductive Power Transfer (IPT) systems in an electrified road: Dielectric power loss due to pavement materials," *Construction and Building Materials,* vol. 147, pp. 9-16, 2017.

[204] I.-S. Jeong, Y.-K. Lee and H.-S. Choi, “Characteristics analysis on a superconductor resonance coil WPT system according to cooling vessel materials in different distances,” *Physica C: Superconductivity and its applications,* vol. 530, pp. 123-132, 2016.

[205] U. Berardi and N. Dembsey, "Thermal and Fire Characteristics of FRP Composites for Architectural Applications," *Polymers,* vol. 7, pp. 2276-2289, 2015.

[206] H. K. Kang, Y. D. Chung and S. W. Yim, “Conceptual design of contactless power transfer into HTS receiver coil using normal conducting resonance antenna,” *Cryogenics,* vol. 63, pp. 209-214, 2014.

[207] Y. D. Chung, E. Y. Park, W. S. Lee and J. Y. Lee, “Impact Investigations and Characteristics by Strong Electromagentic Field of Wireless Power Charging System for Electric Vehicle Under Air and Water Exposure Indexes,” *IEEE Transactions on Applied Superconductivity,* vol. 28, no. 3, 2018.

[208] Y. D. Chung, C. Y. Lee, H. C. Jo, Y. G. Park and S. W. Yim, “Operating characteristics of contactless power transfer for electric vehicle from HTS antenna to normal conducting receiver,” *Physica C* , vol. 504, pp. 115-119, 2014.

[209] M. Yilmaz, V. T. Buyukdegirmenci and P. T. Krein, "General Design Requirements and Analysis of Roadbed Inductive Power Transfer System for Dynamic Electric Vehicle Charging," in *IEEE Transportation Electrification Conference and Expo (ITEC)*, Dearborn, USA, 2012.

[210] M. L. Kissin, J. T. Boys and G. A. Covic, "Interphase Mutual Inductance in Polyphase Inductive Power Transfer Systems," *IEEE Transactions on Industrial Electronics*, vol. 56, no. 7, pp. 2393-2400, 2009.

[211] Y. D. Chung, C. Y. Lee and H. R. Jeon, "Operating characteristics and cooling cost evaluation for HTS receiver arrays of wireless power charging system in superconducting MAGLEV train," *Cryogenics*, vol. 94, pp. 79-83, 2018.

[212] G. R. Nagendra, G. A. Covic and J. T. Boys, "Sizing of Inductive Power Pads for Dynamic Charging of EVs on IPT Highways," *IEEE Transactions on Transportation Electrification*, vol. 3, no. 2, pp. 405-417, 2017.

[213] T. Fujita, T. Yasuda and H. Akagi, "A Dynamic Wireless Power Transfer System Applicable to a Stationary System," *IEEE Transactions on Industry Applications*, vol. 53, no. 4, pp. 3748-3757, 2017.

[214] L. Chen, G. R. Nagendra, J. T. Boys and G. A. Covic, "Double-Coupled Systems for IPT Roadway Applications," *IEEE Journal of Emerging and Selected Topics in Power Electronics*, vol. 3, no. 1, pp. 37-49, 2015.

[215] W. Zhang, S.-C. Wong, C. K. Tse and Q. Chen, "An Optimized Track Length in Roadway Inductive Power Transfer Systems," *IEEE Journal of Emerging and Selected Topics in Power Electronics*, vol. 2, no. 3, pp. 598-608, 2014.

[216] G. Buja, M. Bertoluzza and H. K. Dashora, "Lumped Track Layout Design for Dynamic Wireless Charging of Electric Vehicles," *IEEE Transactions on Industrial Electronics*, vol. 63, no. 10, pp. 6631-6640, 2016.

[217] H. L. Li, A. P. Hu, G. A. Covic and C. Tang, "A New Primary Power Regulation Method for Contactless Power Transfer," in *IEEE International Conference on Industrial Technology*, Churchill, Australia, 2009.

[218] J. M. Miller, O. C. Onar and M. Chinthavali, “Primary-Side Power Flow Control of Wireless Power Transfer for Electric Vehicle Charging,” *IEEE Journal of Emerging and Selected Topics in Power Electronics*, vol. 3, no. 1, pp. 147-162, 2015.

[219] K. Hata, T. Imura and Y. Hori, "Dynamic Wireless Power Transfer System for Electric Vehicles to Simplifiy Ground Facilities - Power Control and Efficiency Maximization on the Secondary Side," in *IEEE Applied Power Electronics Conference and Exposition (APEC)*, Long Beach, USA, 2016.

[220] F. Gürbüz, T. Sürgevil and M. Boztepe, "Analysis and Design of a Secondary-Side Controlled Active Rectifier for Wireless Battery Charging Application," in *10th International Conference on Electrical and Electronics Engineering (ELECO)*, Bursa, Turkey, 2017.

[221] R. Tavakoli and Z. Pantic, "Analysis, Design, and Demonstration of a 25-kW Dynamic Wireless Charging System for Roadway Electric Vehicles," *IEEE Journal of Emerging and Selected Topics in Power Electronics*, vol. 6, no. 3, pp. 1378-1393, 2018.

[222] U. K. Madawala, M. Neath and D. J. Thrimawithana, "A Power-Frequency Controller for Bidirectional Inductive Power Transfer Systems," *IEEE Transactions on Industrial Electronics*, vol. 60, no. 1, pp. 310-317, 2013.

[223] A. Babaki, S. Vaez-Zadeh and A. Zakerian, "Performance Optimization of Dynamic Wireless EV Charger Under Varying Driving Conditions Without Resonant Information," *IEEE Transactions on Vehicular Technology*, vol. 68, no. 11, pp. 10429-10438, 2019.

[224] Y.-H. Chao, J.-J. Shieh, C.-T. Pan, W.-C. Shen and M.-P. Chen, "A Primary-Side Control Strategy for Series Parallel Loosely Coupled Inductive Power Transfer Systems," in *IEEE Conference on Industrial Electronics and Applications*, Harbin, China, 2007.

[225] G. A. Covic and J. T. Boys, "Modern Trends in Inductive Power Transfer for Transportation Applications," *IEEE Journal of Emerging and Selected Topics in Power Electronics*, vol. 1, no. 1, pp. 28-41, 2013.

[226] R. Bosshard, U. Badstübner, J. Kolar and I. Stevanovic, "Comparative Evaluation of Control Methods for Inductive Power Transfer," in *International Conference on Renewable Energy Research and Applications (ICRERA)*, Nagasaki, Japan, 2012.

[227] W. Choi, W. Ho, X. Liu and S. Hui, "Comparative Study on Power Conversion Methods for Wireless Battery Charging Platform," in *14th International Power Electronics and Motion Control Conference*, Ohrid, Macedonia, 2010.

[228] R. Bosshard, J. Kolar and B. Wunsch, “Control Method for Inductive Power Transfer with High Partial-Load Efficiency and Resonance Tracking,” in *International Power Electronics Conference*, Hiroshima, Japan, 2014.

[229] J. T. Boys, G. A. Covic and A. W. Green, “Stability and control of inductively coupled power transfer systems,” *IEE Proceedings - Electric Power Applications,* vol. 147, no. 1, pp. 37-43, 2000.

[230] H. H. Wu, A. Gilchrist, K. D. Sealy and D. Bronson, “A High Efficiency 5 kW Inductive Charger for EVs Using Dual Side Control,” *IEEE Transaction on Industrial Informatics,* vol. 8, no. 3, pp. 585-595, 2012.

[231] T. Diekhans and R. W. De Doncker, "A Dual-Side Controlled Inductive Power Trnasfer System Optimized for Large Coupling Factor Variations and Partial Load," *IEEE Transactions on Power Electronics,* vol. 30, no. 11, pp. 6320-6328, 2015.

[232] Y. Tang, Y. Chen, U. K. Madawala, D. J. Thrimawithana and H. Ma, “A New Controller for Bi-directional Wireless Power Transfer Systems,” *IEEE Transactions on Power Electronics,* vol. 33, no. 10, pp. 9076-9087, 2018.

[233] A. Esser, "Contactless Charging and Communication for Electric Vehicles," *IEEE Industry Applications Magazine,* pp. 4-11, 1995.

[234] Z. Yuan, H. Xu, H. Han and Y. Zhao, "Research of Smart Charging Management System for Electric Vehicles Based on Wireless Communication Networks," in *IEEE 6th International Conference on Information and Automation for Sustainability*, Beijing, China, 2012.

[235] Y. Zhao, H. Xu, Y. Shen, H. Han and Z. Yuan, "Research of Orderly Charging Control System for Electrical Vehicles Based on Zigbee and GPRS Networks," in *IEEE Conference*

and Expo Transportation Electrification Asia-Pacific (ITEC Asia-Pacific), Beijing, China, 2014.

[236] UNPLUGGED, "Deliverable 2.4.Data analysis and conclusions," UNPLUGGED, 2015.

[237] B. R. Long, "A Near Field Communication System for Wireless Charging," in *IEEE PELS Workshop on Emerging Technologies: Wireless Power Transfer (WoW)*, Knoxville, USA, 2016.

[238] A. Gil, Sauras-Perez and J. Taiber, "Communication Requirements for Dynamic Wireless Power Transfer for Battery Electric Vehicles," in *IEEE International Electric Vehicle Conference (IEVC)*, Florence, Italy, 2014.

[239] J. Baillieul and P. Antsaklis, "Control and Communication Challenges in Networked Real-Time Systems," *Proceedings of the IEEE,* vol. 95, no. 1, pp. 9-28, 2007.

[240] G. R. Nagendra, L. Chen, G. A. Covic and J. T. Boys , "Detection of EVs on IPT Highways," *IEEE Journal of Emerging and Selected Topics in Power Electronics,* vol. 2, no. 3, pp. 584-597, 2014.

[241] F. Bai and H. Krishnan, "Reliability Analysis of DSRC Wireless Communication for Vehicle Safety Applications," in *IEEE Intelligent Transportation Systems Conference*, Toronto, Canada, 2006.

[242] A. Echols, S. Mukherjee, M. Mickelsen and Z. Pantic, "Communication Infrastructure for Dynamic Wireless Charging of Electric Vehicles," in *IEEE Wireless Communications and Networking Conference (WCNC)*, San Francisco, USA, 2017.

[243] A. Gil Batres, A. Moghe and J. Taiber, "A Communication Architecture for Wireless Power Transfer Services based on DSRC Technology," in *IEEE Transportation Electrification Conference and Expo (ITEC)*, Dearborn, USA, 2016.

[244] M. Sinaie, P.-H. Lin, A. Zappone, P. Azmi and E. A. Jorswieck, "Delay-Aware Resource Allocation for 5G Wireless Networks With Wireless Power Transfer," *IEEE Transactions on Vehicular Technology*, vol. 67, no. 7, pp. 5841-5855, 2018.

[245] GSMA Intelligence, "Understanding 5G: Perspectives on future technological advancements in mobile," GSMA Intelligence, 2014.

[246] R. I. Ansari, C. Chrysostomos, S. A. Hassan, M. Guizani, S. Mumtaz, J. Rodriguez and J. J. Rodrigues, "5G D2D Networks: Techniques, Challenges, and Future Prospects," *IEEE Systems Journal*, vol. 12, no. 4, pp. 3970-3984, 2018.

[247] C. T. Rim and C. Mi, "Foreign Object Detection," in *Wireless Power Transfer for Electric Vehicles and Mobile Devices*, Hoboken, USA, John Wiley & Sons Ltd, 2017, pp. 457-469.

[248] N. Kuyvenhoven, C. Dean, J. Melton, J. Schwannecke and A. E. Umenei, "Development of a Foreign Object Detection and Analysis Method for Wireless Power Systems," in *IEEE Symposium on Product Compliance Engineering Proceedings*, San Diego, USA, 2011.

[249] S. Fukuda, H. Nakano, Y. Murayama, T. Murakami, O. Kozakai and K. Fujimaki, "A Novel Metal Detector using the Quality Factor of the Secondary Coil for Wireless Power Transfer Systems," in *IEEE MTT-S International Microwave Workshop Series on Innovative Wireless Power Transmission: Technologies, Systems, and Applications*, Kyoto, Japan, 2012.

[250] G. C. Jang, S. Y. Jeong, H. G. Kwak and C. T. Rim, "Metal Object Detection Circuit with Non-overlapped Coils for Wireless EV Chargers," in *IEEE 2nd Annual Southern Power Electronics Conference (SPEC)*, Auckland, New Zealand, 2016.

[251] S. Y. Jeong, H. G. Kwak, G. C. Jang and C. T. Rim, "Living Object Detection System Based on Comb Pattern Capacitive Sensor for Wireless EV Chargers," in *IEEE 2nd Annual Southern Power Electronics Conference (SPEC)*, Auckland, New Zealand, 2016.

[252] S. Y. Jeong, H. G. Kwak, G. C. Jang, S. Y. Choi and C. T. Rim, "Dual-Purpose Nonoverlapping Coil Sets as Metal Object and Vehicle Position Detections for Wireless Stationary EV Chargers," *IEEE Transactions on Power Electronics*, vol. 33, no. 9, pp. 7387-7397, 2018.

[253] A. N. Azad, A. Echols, V. A. Kulyukin, R. Zane and Z. Pantic, “Analysis, Optimization, and Demonstration of a Vehicular Detection System Intended for Dynamic Wireless

Charging Applications," *IEEE Transactions on Transportation Electrification,* vol. 5, no. 1, pp. 147-161, 2019.

[254] A. Kamineni, M. J. Neath, A. Zaheer, G. A. Covic and J. T. Boys, "Interoperable EV Detection for Dynamic Wireless Charging With Existing Hardware and Free Resonance," *IEEE Transactions on Transportation Electrification*, vol. 3, no. 2, pp. 370-379, 2017.

[255] Q. Deng, J. Liu, D. Czarkowski, M. Bojarski, J. Chen, W. Hu and H. Zhou, "Edge Position Detection of On-line Charged Vehicles With Segmental Wireless Power Supply," *IEEE Transactions on Vehicular Technology,* vol. 66, no. 5, pp. 3610-3621, 2017.

[256] L. Lisboa Cardoso, J. Afonso, M. Comesaña Martinez and A. Nogueiras Meléndez, "RFID-Triggered Power Activation for Smart Dynamic Inductive Wireless Power Transfer," in *IECON 2017 - 43rd Annual Conference of the IEEE Industrial Electronics Society*, Beijing, China, 2017.

[257] K. Hwang, J. Cho, J. Park, D. Har and S. Ahn, "Ferrite position identification system operating with wireless power transfer for intelligent train position detection," *IEEE Transactions on Intelligent Transportation Systems,* vol. 20, no. 1, pp. 374-382, 2019.

[258] Y. Shin, K. Hwang, J. Park, D. Kim and S. Ahn, "Precise Vehicle Locations Detection Method Using a Wireless Power Transfer (WPT) System," *IEEE Transactions on Vehicular Technology*, vol. 68, no. 2, pp. 1167-1177, 2019.

[259] N. Khan, H. Matsumoto and O. Trescases, "Wireless Electric Vehicles Charger With Electromagnetic Coil-Based Position Correction Using Impedance and Resonant Frequency Detection," *IEEE Transactions on Power Electronics,* vol. 35, no. 8, pp. 7873-7883, 2020.

[260] H. Jiang, P. Brazis, M. Tabaddor and J. Bablo, "Safety Considerations of Wireless Charger For Electric Vehicles - A Review Paper," in *IEEE Symposium on Product Compliance Engineering Proceedings*, Portland, USA, 2012.

[261] P. C. Schrafel, B. R. Long, J. M. Miller and A. Daga, "The Reality of Safety Concerns Relative to WPT Systems for Automotive Applications," in *IEEE PELS Workshop on Emerging Technologies: Wireless Power Transfer (WoW)*, Knoxville, USA, 2016.

[262] International Commission on Non-Ionizing Radiation Protection (ICNIRP), "ICNIRP Guidlines - For Limiting Exposure to Time-varying Electric and Magnetic Fields (1Hz-100kHz)," *Health Physics,* vol. 99, no. 6, pp. 818-836, 2010.

[263] International Commission on Non-Ionizing Radiation Protection (ICNIRP), "ICNIRP Guidlines - For Limiting Exposure to Time-varying Electric, Magnetic Fields and Electromagnetic Fields (up to 300GHz)," *Health Physics*, vol. 74, no. 4, pp. 494-522, 1998.

[264] World Health Organization (WHO), "Extremely Low Frequency Fields. Environmental Health Criteria No.238," WHO Press, Geneva, Switzerland, 2007.

[265] K. Wada, K. Matsubara, H. Yoshino, Y. Suzuki, A. Ushiyama, S. Ohtani, K. Hattori and K. Ishii, "Development of an Exposure System for 85 kHz Magnetic Field for the Evaluation Biological Effects," in *IEEE PELS Workshop on Emerging Technologies: Wireless Power Transfer (WoW)*, Knoxville, USA, 2016.

[266] I. Nishimura, A. Oshima, K. Shibuya, T. Mitani and T. Negishi, "Absence of reproductive and developmental toxicity in rats following exposure to a 20-kHz or 60-kHz magnetic field," *Regulatory Toxicology and Pharmacology*, vol. 64, pp. 394-401, 2012.

[267] J. Chakarothai, K. Wake, T. Arima, S. Watanabe and T. Uno, "Exposure Evaluation of an Actual Wireless Power Transfer System for an Electric Vehicle With Near-Field Measurement," *IEEE Transactions on Microwave Theory and Techniques,* vol. 66, no. 3, pp. 1543-1552, 2018.

[268] A. Christ, M. G. Douglas, J. M. Roman, E. B. Cooper, A. P. Sample, B. H. Waters, J. R. Smith and N. Kuster, "Evaluation of Wireless Resonant Power Transfer Systems With Human Electromagnetic Exposure Limits," *IEEE Transactions on Electromagnetic Compatibility*, vol. 55, no. 2, pp. 265-274, 2013.

[269] S. W. Park, K. Wake and S. Watanabe, "Incident Electric Field Effect and Numerical Dosimetry for a Wireless Power Transfer System Using Magnetically Coupled Resonances," *IEEE Transactions on Microwave Theory and Techniques*, vol. 61, no. 9, pp. 3461-3469, 2013.

[270] I. Laakso and A. Hirata, "Evaluation of the induced electric field and compliance procedure for a wireless power transfer system in an electrical vehicle," *Physics in Medicine & Biology*, vol. 58, no. 21, pp. 7583-7593, 2013.

[271] T. Campi, S. Cruciani, V. De Santis, F. Maradei and M. Feliziani, "EMC and EMF Safety Issues in Wireless Charging System for an Electric Vehicle (EV)," in *International Conference of Electrical and Electronic Technologies for Automotive*, Turin, Italy, 2017.

[272] T. Shimamoto, I. Laakso and A. Hirata, "In-situ electric field in human body model in different postures for wireless power transfer system in an electrical vehicle," *Physics in Medicine & Biology*, vol. 60, no. 1, pp. 163-173, 2015.

[273] S. W. Park, "Evaluation of Electromagnetic Exposure during 85kHz Wireless Power Transfer for Electric Vehicles," *IEEE Transactions on Magnetics*, vol. 54, no. 1, p. 5100208, 2018.

[274] M. Kim, S. Park and H.-K. Jung, "Numerical Method for Exposure Assessment of Wireless Power Transmission under Low-Frequency Band," *Journal of Magnetics*, vol. 21, no. 3, pp. 442-449, 2016.

[275] T. Campi, S. Cruciani, M. Feliziani and F. Maradei, “Magnetic Field Generated by a 22 kW-85 kHz Wireless Power Transfer System for an EV,” in *AEIT International Annual Conference*, Cagliaria, Italy, 2017.

[276] T. Campi, S. Cruciani, F. Maradei and M. Feliziani, “Pacemaker Lead Coupling With an Automotive Wireless Power Transfer System,” *IEEE Transactions on Electromagnetic Compatibility*, vol. 61, no. 6, pp. 1935-1943, 2019.

[277] K. Miwa, T. Takenaka and A. Hirata, “Electromagnetic Dosimetry and Compliance for Wireless Power Transfer Systems in Vehicles,” *IEEE Transactions on Electromagnetic Compatibility*, vol. 61, no. 6, pp. 2024-2030, 2019.

[278] Z. Chen, W. Liu and Y. Yin, "Deployment of stationary and dynamic charging infrastructure for electric vehicles along traffic corridors," *Transportation Research Part C*, vol. 77, pp. 185-206, 2017.

[279] Transport Research Laboratory, “Feasibility study: Power electric vehicles on England's major roads,” Highways England, 2015.

[280] R. Tell, R. Kavet, J. Bailey and J. Halliwell, “Very-low-frequency and low-frequency electric and magnetic fields associated with electric shuttle bus wireless charging,” *Radiation Proctection Dosimetry*, vol. 158, no. 2, pp. 123-134, 2014.

[281] A. Kyriakou, A. Christ, E. Neufeld and N. Kuster, "Local Tissue Temperature Increase of a Generic Implant Compared to the Basic Restrictions Defined in Safety Guidlines," *Bioelectromagnetics*, vol. 33, pp. 366-374, 2012.

[282] T. Campi, S. Cruciani, V. De Santis and M. Feliziani, “EMF Safety and Thermal Aspects in a Pacemaker Equipped With a Wireless Power Transfer System Working at Low Frequency,” *IEEE Transactions on Microwave Theory and Techniques*, vol. 64, no. 2, pp. 375-382, 2016.

[283] International Organization for Standardization (ISO), "ISO 14117:2012 Active implantable medical devices -- Electromagnetic compatibility -- EMC test protocols for implantable cardiac pacemakers, implantable cardioverter defibrillators and cardiac resynchronization devices," ISO, Geneva, Switzerland, 2012.

[284] Y. Gao, K. B. Farley, A. Ginart and Z. T. H. Tse, "Safety and efficiency of the wireless charging of electric vehicles," *Proceedings of the Institution of Mechanical Engineers, Part D: Journal of Automobile Engineering*, vol. 230, no. 9, pp. 1196-1207, 2015.

[285] S. Ahn and J. Kim, "Magnetic Field Design for High Efficient and Low EMF Wireless Power Transfer in On-Line Electric Vehicle," in *Proceedings of the 5th European Conference on Antennas and Propagation (EUCAP)*, Rome, Italy, 2011.

[286] M. Feliziani, S. Cruciani, T. Campi and F. Maradei, "Near Field Shielding of a Wireless Power Transfer (WPT) Current Coil," *Progress In Electromagnetics Research C*, vol. 77, pp. 39-48, 2017.

[287] J. Kim, J. Kim, S. Kong, H. Kim, I.-S. Suh, N. P. Suh, D.-H. Cho, J. Kim and S. Ahn, "Coil Design and Shielding Methods for a Magnetic Resonant Wireless Power Transfer System," *Proceedings of the IEEE*, vol. 101, no. 6, pp. 1332-1342, 2013.

[288] P. R. Bannister, "New Theoretical Expressions for Predicting Shielding Effectiveness for the Plane Shield Case," *IEEE Transactions on Electromagnetic Compatibility*, vol. 10, no. 1, pp. 2-7, 1968.

[289] P. Moreno and R. G. Olsen, "A Simple Theory for Optimizing Finite Width ELF Magnetic Field Shields for Minimum Dependence on Source Orientation," *IEEE Transactions on Electromagnetic Compatibility*, vol. 39, no. 4, pp. 340-348, 1997.

[290] S. Lee, W. Lee, J. Huh, H.-J. Kim, C. Park, G.-H. Cho and C.-T. Rim, "Active EMF cancellation method for I-type pickup of On-Line Electric Vehicles," in *Twenty-Sixth Annual IEEE Applied Power Electronics Conference and Exposition (APEC)*, Fort Worth, USA, 2011.

[291] S. Kim, H.-H. Park, J. Kim, J. Kim and S. Ahn, "Design and Analysis of a Resonant Reactive Shield for a Wireless Power Electric Vehicle," *IEEE Transactions on Microwave Theory and Techniques*, vol. 62, no. 4, pp. 1057-1066, 2014.

[292] H. Moon, S. Kim, H. H. Park and S. Ahn, "Design of a Resonant Reactive Shield With Double Coils and a Phase Shifter for Wireless Charging of Electric Vehicles," *IEEE Transactions on Magnetics*, vol. 51, no. 3, 2015.

[293] C. T. Rim and C. Mi, "Electromagnetic Field (EMF) Cancel," in *Wireless Power Transfer for Electric Vehicles and Mobile Devices*, Hoboken, USA, John Wiley & Sons Ltd, 2017, pp. 313-335.

[294] Q. Zhu, Y. Zhang, Y. Guo, C. Liao, L. Wang and L. Wang, "Null-Coupled Electromagnetic Field Canceling Coil for Wireless Power Transfer System," *IEEE Transactions on Transportation Electrification*, vol. 3, no. 2, pp. 464-473, 2017.

[295] C. Song, H. Kim, D. H. Jung, J. J. Kim, S. Kong, J. Kim, S. Ahn, J. Kim and J. Kim, "Low EMF and EMI Design of a Tightly Coupled Handheld Resonant Magnetic Field (HH-RMF) Charger for Automotive Battery Charging," *IEEE Transactions on Electromagnetic Compatibility*, vol. 58, no. 4, pp. 1194-1206, 2016.

[296] Wireless Power Consortium (WPC), "The QI Wireless Power Transfer System Power Class 0 Specification Parts 1 and 2: Interface Definitions Version 1.2.2," WPC, 2016.

[297] Alliance for Wireless Power (A4WP), "A4WP Wireless Power Transfer System Baseline System Specification (BSS)," A4WP, Fremont, USA, 2014.

[298] Society of Automotive Engineers (SAE), "J2954 - Wireless Power Transfer for Light-Duty Plug-In/ Electric Vehicles and Alignment Methodology," SAE International, Warrendale, USA, 2019.

[299] International Organization for Standardization (ISO), "ISO/PAS 19363:2017 - Electrically propelled road vehicles -- Magnetic field wireless Power transfer -- Safety and interoperability requirements," ISO, Geneva, Switzerland, 2017.

[300] Society of Automotive Engineers (SAE), "J2894/1 - Power Quality Requirements for Plug-In Electric Vehicle Chargers," SAE International, Warrendale, USA, 2011.

[301] Society of Automotive Engineers (SAE), "J2847/6 - Communication between Wireless Charged Vehicles and Wireless EV Chargers," SAE International, Warrendale, USA, 2015.

[302] Society of Automotive Engineers (SAE), "J2931/6 - Signaling Communication for Wirelessly Charged Electric Vehicles," SAE International, Warrendale, USA, 2015.

[303] International Organization for Standardization (ISO), "15118:2013 Road vehicles -- Vehicle to grid communication interface," ISO, Geneva, Switzerland, 2013.

[304] International Electrotechnical Commission (IEC), "IEC 61980:2015 Electric vehicle wireless power transfer (WPT) systems - Part 1: General requirements," IEC, Geneva, Switzerland, 2015.

[305] Y. Ma, B. Zhang and X. Zhou, "An Overview on Impacts of Electric Vehicles Integration into Distribution Network," in *IEEE International Conference on Mechatronics and Automation (ICMA)*, Beijing, China, 2015.

[306] R. C. Green II, L. Wang and M. Alam, "The impact of plug-in hybrid electric vehicles on distribution networks: A review and outlook," *Renewable and Sustainable Energy Reviews,* vol. 15, pp. 544-553, 2011.

[307] M. Kintner-Meyer, K. Schneider and R. Pratt, "Impacts assessment of plug-in hybrid electric vehicles on electric utilities and regional U.S. power grids - part 1: technical assessment," 2007.

[308] P. Olivella-Rosell, R. Villafafila-Robles and A. Sumper, "Impact Evaluation of Plug-in Elecetric Vehicles on Power Systems," in *Plug In Electric Vehicles in Smart Grids*, S. Rajakaruna, A. Ghosh and F. Shahnia, Eds., Singapore, Republic of Singapore, Springer Science+Business Media Singapore 2015, 2015, pp. 149-179.

[309] S. Zhang, X. Ai, W. Liang and R. Dong, "The influence of the electric vehicle charging on the distribution network and the solution," in *IEEE Conference and Expo Transportation Electrification Asia-Pacific (ITEC Asia-Pacific)*, Beijing, China, 2014.

[310] T. Ma and O. Mohammed, "Real-Time Plug-In Electric Vehicles Charging Control for V2G Frequency Regulation," in *39th Annual Conference of the IEEE Industrial Electronics Society (IECON)*, Vienna, Austria, 2013.

[311] T. Theodoropoulos, A. Amditis, J. Sallán, H. Bludszuweit, B. Berseneff, P. Guglielmi and F. Deflorio, "Impact of dynamic EV wireless charging on the grid," in *IEEE International Electric Vehicle Conference (IEVC)*, Florence, Italy, 2014.

[312] F. Deflorio, L. Castello, I. Pinna and P. Guglielmi, ""Charge while driving" for electric vehicles: road traffic modeling and energy assessment," *Journal of Mdern Power Systems and Clean Energy,* vol. 3, no. 2, pp. 277-288, 2015.

[313] F. Deflorio and L. Castello, "Dynamic charging-while-driving systems for freight delivery services with electric vehicles: Traffic and energy modelling," *Transportation Research Part C,* vol. 81, pp. 342-362, 2017.

[314] S. D. Manshadi, M. E. Khodayar, K. Abdelghany and H. Uster, "Wireless Charging of Electric Vehicles in Electricity and Transportation Networks," *IEEE Transaction on Smart Grid,* vol. 9, no. 5, pp. 4503-4512, 2017.

[315] I. Karakitsios, E. Karfopoulos and N. Hatziargyriou, “Impact of dynamic and static fast inductive charging of electric vehicles on the distribution network,” *Electric Power Systems Research,* vol. 140, pp. 107-115, 2016.

[316] C. A. Garcia-Vazquez, F. LLoren-Iborra, L. M. Fernandez-Ramirez, H. Sanchez-Sainz and F. Jurado, "Comparative study of dynamic wireless charging of electric vehicles in motorway, highway and urban stretches," *Energy*, vol. 137, pp. 42-57, 2017.

[317] J. H. Park and Y. H. Jeong, "The Economics of Wireless Charging on the Road," in *The On-line Electric Vehicle - Wireless Electric Ground Transportation Systems*, Cham, Switzerland, Springer International Publishing, 2017, pp. 329-347.

[318] M. Yilmaz and P. T. Krein, "Review of Battery Charger Topologies, Charging Power Levels, and Infrastructure for Plug-In Electric and Hybrid Vehicles," *IEEE Transactions on Power Electronics,* vol. 28, no. 5, pp. 2151-2169, 2013.

[319] S. Lukic and Z. Pantic , "Cutting the Cord - Static and dynamic inductive wireless charging of electric vehicles," *IEEE Electrification Magazine,* vol. September, pp. 57-64, 2013.

[320] S. Jeong, Y. J. Jang, D. Kum and M. S. Lee, "Charging Automation for Electric Vehicles: Is a Smaller Battery Good for the Wireless Charging Electric Vehicles?," *IEEE Transactions on Automation Science and Engineering*, pp. 1-12, 2018.

[321] Department for Transport, "Road Traffic Estimates Great Britain 2017," Department of Transport, Great Britain, 2018.

[322] Y. J. Jang, S. Jeong and M. S. Lee, "Initial Energy Logistics Cost Analysis for Stationary, Quasi-Dynamic, and Dynamic Wirless Charging Public Transportation Systems," *Energies*, vol. 9, no. 483, 2016.

[323] C. T. Rim and C. Mi, "History of RPEVs," in *Wireless Power Transfer for Electric Vehicles and Mobile Devices*, First ed., Chichester, United Kingdom, John Wiley & Sons Ltd, 2017, pp. 161-208.

[324] J. Shin, S. Shin, Y. Kim, S. Ahn, S. Lee, G. Jung, S.-J. Jeon and D.-H. Cho, "Design and Implementation of Shaped Magnetic-Resonance-Based Wireless Power Transfer System for Roadway-Powered Moving Electric Vehicles," *IEEE Transactions on Industrial Electronics*, vol. 61, no. 3, pp. 1179-1192, 2014.

[325] A. Shekhar, V. Prasanth, P. Bauer and M. Bolech, "Economic Viability Study of an On-Road Wireless Charging System with a Generic Driving Range Estimation Method," *Energies*, vol. 9, no. 76, 2016.

[326] S. Jeong, Y. J. Jang and D. Kum, "Economic Analysis of the Dynamic Charging Electric Vehicle," *IEEE Transactions on Power Electronics*, vol. 30, no. 11, pp. 6368-6377, 2015.

[327] N. Omar, M. A. Monem, Y. Firouz, J. Salminen, J. Smekens, O. Hegazy, H. Gaulous, G. Mulder, P. Van den Bossche, T. Cossemans and J. Van Mierlo, "Lithium iron phosphate based battery - Assessment of the aging parameters and development of cycle life model," *Applied Energy*, vol. 113, pp. 175-1585, 2014.

[328] Z. Bi, R. De Kleine and G. A. Keoleian, "Integrated Life Cycle Assessment and Life Cycle Cost Model for Comparin Plug-in Versus Wireless Charging for an Electric Bus System," *Journal of Industrial Ecology*, vol. 21, no. 2, pp. 344-355, 2017.

[329] Y. Wang, W. Ding, L. Huang, Z. Wei, H. Liu and J. A. Stankovic, "Toward Urban Electric Taxi Systems in Smart Cities: The Battery Swapping Challenge," *IEEE Transactions on Vehicular Technology*, vol. 67, no. 3, pp. 1946-1960, 2018.

[330] Z. Chen, Y. Yin and Z. Song, "A cost-competitiveness analysis of charging infrastructure for electric bus operations," *Transportation Research Part C*, vol. 93, pp. 351-366, 2018.

[331] B. J. Limb, T. H. Bradley, B. Crabb, R. Zane, C. McGinty and J. C. Quinn, "Economic and Environmental Feasibility, Architecture Optimization, and Grid Impact of Dynamic Charging of Electric Vehicles using Wireless Power Transfer," in *6th Hybrid and Electric Vehicles Conference (HEVC 2016)*, London, United Kingdom, 2016.

[332] B. J. Limb, R. Zane and J. C. Quinn, "Infrastructure Optimization and Economic Feasibility of In-Motion Wireless Power Transfer," in *IEEE Transportation Electrification Conference and Expo (ITEC)*, Metro Deroit, USA, 2016.

[333] J. C. Quinn, B. J. Limb, Z. Pantic, P. Barr, R. Zane and T. H. Bradley, "Feasibility of Wireless Power Transfer for Electrification of Transportation: Techno-economics and Life Cycle Assessment," in *IEEE Conference on Technologies for Sustainability (SusTech)*, Ogden, USA, 2015.

[334] M. Fuller, "Wireless charging in California: Range, recharge, and vehicle electrification," *Transportation Research Part C*, vol. 67, pp. 343-356, 2016.

[335] Y. D. Chung, C. Y. Lee, H. K. Kang and Y. G. Park, "Design Consideration and Efficiency Comparison of Wireless Power Transfer With HTS and Cooled Copper Antennas for Electric Vehicle," *IEEE Transactions on Applied Superconductivity*, vol. 25, no. 3, 2015.

[336] J. Deng, W. Li, T. D. Nguyen, S. Li and C. C. Mi, "Compact and Efficient Bipolar Coupler for Wireless Power Chargers: Design and Analysis," *IEEE Transaction on Power Electronics*, vol. 30, no. 11, pp. 6130-6140, 2015.

[337] J. M. Miller and A. Daga, "Elements of Wireless Power Transfer Essential to High Power Charging of Heavy Duty Vehicles," *IEEE Transactions on Transportation Electrification*, vol. 1, no. 1, pp. 26-39, 2015.

[338] F. Y. Lin, G. A. Covic and J. T. Boys, "Evaluation of Magnetic Pad Sizes and Topologies for Electric Vehicle Charging," *IEEE Transactions on Power Electronics,* vol. 30, no. 11, pp. 6391-6407, 2015.

[339] IEEE, IEEE Standard for Safety Levels with Respect to Human Exposure to Radio Frequency Electromagnetic Fields, 3kHz to 300GHz, IEEE Std C95.1-2005 ed., New York, USA: IEEE, 2005.

[340] C. Mi and M. Abdul, Hybrid Electrical Vehicles, Hoboken, USA: John Wiley & Sons Ltd, 2018.

[341] M. Allen, "Range Ramifications of Heating and AC for Electric Vehicles," 2014. [Online]. Available: https://www.fleetcarma.com/electric-vehicle-heating-chevrolet-volt-nissan-leaf/. [Accessed 22 October 2018].

[342] J. Larminie and J. Lowry, Electric Vehicle Technology Explained, United Kingdom: John Wiley & Sons Ltd, 2003.

[343] Nissan, "Nissan Leaf," [Online]. Available: https://www.nissanusa.com/content/dam/Nissan/us/vehicle-brochures/2018/2018-leaf-brochure-en.pdf. [Accessed 03 September 2018].

[344] R. Gu, P. Malysz, H. Yang and A. Emadi, "On the Suitability of Electrochemical-Based Modeling for Lithium-Ion Batteries," *IEEE Transactions on Transportation Electrification,* vol. 2, no. 4, pp. 417-431, 2016.

[345] N. Lotfi, R. G. Landers, J. Li and J. Park, "Reduced-Order Electrochemical Model-Based SOC Observer With Output Model Uncertainty Estimation," *IEEE Transactions on Control Systems Technology,* vol. 25, no. 4, pp. 1217-1230, 2017.

[346] L. Zheng, J. Zhu, G. Wang, D. D.-C. Lu and T. He, "Lithium-ion Battery Instantaneous Available Power Prediction Using Surface Lithium Concentration of Solid Particles in a Simplified Electrochemical Model," *IEEE Transactions on Power Electronics,* vol. 33, no. 11, pp. 9551-9560, 2018.

[347] K. S. Hariharan, P. Tagade and S. Ramachandran, Mathematical Modeling of Lithium Batteries - From Electrochemical Models to State Estimator Algorithms, Cham, Switzerland: Springer International Publishing AG, 2018.

[348] P. Rong and M. Pedram, "An Analytical Model for Predicting the Remaining Battery Capacity of Lithium-Ion Batteries," *IEEE Transactions on Very Large Scale Integration (VLSI) Systems,* vol. 14, no. 5, pp. 441-451, 2006.

[349] D. Wang, F. Yang, K.-L. Tsui, Q. Zhou and S. J. Bae, "Remaining Useful Life Prediction of Lithium-Ion Batteries Based on Spherical Cubature Particle Filter," *IEEE Transactions on Instrumentation and Measurement,* vol. 65, no. 6, pp. 1282-1291, 2016.

[350] M. Chen and G. A. Rincon-Mora, "Accurate Electrical Battery Model Capable of Predicting Runtime and I-V Performance," *IEEE Transactions on Energy Conversion,* vol. 21, no. 2, pp. 504-511, 2006.

[351] O. Tremblay and L.-A. Dessaint, "Experimental Validation of a Battery Dynamic Model for EV Applications," *World Electric Vehicle Journal,* vol. 3, pp. 0289-0298, 2009.

[352] T. B. Reddy, Linden's Handbook of Batteries, Fourth Edition, New York, USA: McGraw-Hill Education, 2011.

[353] C. Zhou, Y. Guo, W. Huang, H. Jiang and L. Wu, "Research on Heat Dissipation of Electric Vehicle Based on Safety Architecture Optimization," *Journal of Physics: Conference Series,* vol. 916, no. 012036, 2017.

[354] M. Schimpe, M. von Kuepach, M. Naumann, H. Hesse, K. Smith and A. Jossen, "Comprehensive Modeling of Temperature-Dependent Degradation Mechanisms in Lithium Iron Phosphate Batteries," *Journal of The Electrochemical Society,* vol. 165, no. 2, pp. A181-A193, 2018.

[355] F. Leng, C. M. Tan and M. Pecht, "Effect of Temperature on the Aging rate of Li Ion Battery Operating above Room Temperature," *Scientific Reports,* vol. 5, no. 12967, 2015.

[356] Department for Transport UK, "Official Statistics," 8 September 2016. [Online]. Available:

https://assets.publishing.service.gov.uk/government/uploads/system/uploads/attachment_data/file/551446/electric-vehicles-survey-2016.pdf. [Accessed 19 April 2018].

[357] T. Imura, T. Uchida and Y. Hori, "Flexibility of Contactless Power Transfer using Magnetic Resonance Coupling to Air Gap and Misalignment for EV," *World Electric Vehicle Journal,* vol. 3, pp. 332-341, 2009.

[358] X. Zhang, X. Kong, G. Li and J. Li, "Thermodynamic assessment of active cooling/heating methods for lithium-ion batteries of electric vehicles in extreme conditions," *Energy,* vol. 64, pp. 1092-1101, 2014.

[359] T. Campi, S. Cruciani, V. De Santis, F. Maradei and M. Feliziani, "Wireless Power Transfer (WPT) system for an Electric Vehicle (EV): How to shield the car from the magnetic field generated by two planar coils," *Wireless Power Transfer,* vol. 5, no. 1, pp. 1-8, 2018.

[360] V. De Santis, T. Campi, S. Cruciani, I. Laakso and M. Feliziani, "Assessment of the induced electric fields in a Carbon-Fiber Electrical Vehicle equipped with a Wireless Power Transfer system," *Energies,* vol. 11, no. 3, pp. 684-692, 2018.

[361] W. Zuo, S. Wang, Y. Liao and Y. Xu, "Investigation of Efficiency and Load Characterisitcs of Superconducting Wireless Power Transfer System," *IEEE Transactions on Applied Superconductivity,* vol. 25, no. 3, 2015.

[362] D. W. Kim, Y. D. Chung, H. K. Kang, C. Y. Lee, H. M. Kim, H. C. Jo, Y. J. Hwang, J. Y. Jang and Y. S. Yoon, "Effects and Properties of Contactless Power Transfer for HTS Receivers With Four-Separate Resonance Coils," *IEEE Transactions on Applied Superconductivity,* vol. 23, no. 3, 2013.

[363] I.-S. Jeong, H.-S. Choi and M.-S. Kang, "Application of the Superconductor Coil for the Improvement of Wireless Power Transmission Using Magnetic Resonance," *Journal of Superconductivity and Novel Magnetism,* vol. 28, pp. 639-644, 2015.

[364] G. Zhang, H. Yu, L. Jing, J. Li, Q. Liu and X. Feng, “Wireless Power Transfer Using High Temperature Superconducting Pancake Coils,” *IEEE Transactions on Applied Superconductivity,* vol. 24, no. 3, 2014.

[365] Y. D. Chung, C. Y. Lee, H. K. Kang and Y. G. Park, “Design Consideration and Efficiency Comparison of Wireless Power Transfer With HTS and Cooled Copper Antennas for Electric Vehicle,” *IEEE Transactions on Applied Superconductivity,* vol. 25, no. 3, 2015.

[366] D. W. Kim, Y. D. Chung, H. K. Kang, Y. S. Yoon and T. K. Ko, “Characteristics of Contactless Power Transfer for HTS Coil Based on Electromagnetic Resonance Coupling,” *IEEE Transactions on Applied Superconductivity,* vol. 22, no. 3, 2012.

[367] R. Sedwick, "Long range inductive power transfer with superconducting oscillators," *Annals of Physics,* vol. 325, no. 2, pp. 287-299, 2010.

[368] P. Zhou, G. Ma and L. Quéval, “Transition frequency of transport ac losses in high temperature superconducting coated conductors,” *Journal of Applied Physics,* vol. 126, p. 063901, 2019.

[369] F. Grilli and P. Ashworth, "Measuring transport AC losses in YBCO-coated conductor coils," *Superconductor Science and Technology,* vol. 20, pp. 794-799, 2007.

[370] R. Inoue, D. Miyagi, M. Tsuda and H. Matsuki, "AC Loss Characteristics in Kilohertz Frequency Band of a High-Temperature Superconducting Coil for a Wireless Power Transmission System," *IEEE Transactions on Applied Superconductivity,* vol. 27, no. 4, 2017.

[371] H. Zhang, M. Zhang, J. Zhu, Z. Zhang and W. Yuan, "Influence of Anisotropy in Low Magnetic Field on 2G HTS Pancake Coils Under Liquid Nitrogen," *IEEE Transactions on Applied Superconductivity,* vol. 26, no. 4, 2016.

[372] R. Inoue, D. Miyagi, M. Tsuda and H. Matsuki, "Magnetization Loss Characteristics of a GdBCO Tape in kHz Frequency Band," *IEEE Transactions on Applied Superconductivity,* vol. 28, no. 4, 2018.

[373] M. Ainslie, Y. Jiang, W. Xian, Z. Hong, W. Yuan, R. Pei, T. Flack and T. Coombs, “Numerical analysis and finite element modelling of an HTS synchronous motor,” *Physica C*, vol. 470, pp. 1752-1755, 2010.

[374] V. M. Zermeno, A. B. Abrahamsen, N. Mijatovic, B. B. Jensen and M. P. Sørensen, "Calculation of alternating current losses in stacks and coils made of second generation high temperature superconducting tapes for large scale applications," *Journal of Physics*, vol. 114, no. 173901, pp. 1-9, 2013.

[375] Fujikura, “Data sheet FYSC,” Toyko, Japan, 2019.

[376] V. M. Zermeño, A. B. Abrahamsen, N. Mijatovic, B. B. Jensen and M. P. Sørensen, “Calculation of alternating current losses in stacks and coils made of second generation high temperature superconducting tapes for large scale applications,” *Journal of Applied Physics*, vol. 114, 2013.

[377] F. Grilli, V. M. R. Zermeño, E. Pardo, M. Vojenciak, J. Brand, A. Kario and W. Goldacker, "Self-Field Effects and AC Losses in Pancake Coils Assembled From Coated Conductor Roebel Cables," *IEEE Transactions on Applied Superconductivity*, vol. 24, no. 3, 2014.

[378] B. Shen, C. Li, J. Geng, X. Zhang, J. Gawith, J. Ma, Y. Liu, F. Grilli and T. A. Coombs, “Power disspation in HTS coated conductor coil under the simultaneous action of AC and DC currents and fields,” *Superconductor Science and Technology*, vol. 31, 2018.

[379] V. Zermeño, F. Sirois, M. Takayasu, M. Vojenciak, A. Kario and F. Grilli, "A self-consistent model for estimating the critical current of superconducting devices," *Superconductor Science and Technology*, vol. 28, no. 085004, 2015.

[380] Y. Terao, W. Kong, H. Ohsaki, H. Oyori and N. Morioka, “Electromagnetic Design of Superconducting Synchronous Motors for Electric Aircraft Propulsion,” *IEEE Transactions on Applied Superconducitivity*, vol. 28, no. 4, 2018.

[381] M. Feddersen, K. S. Haran and F. Berg, “AC Loss Analysis of MgB2-Based Fully Superconducting Machiens,” in *IOP Conference Series: Materials Science and Engineering*, 2017.

[382] N. Magnusson, A. Abrahamsen, D. Liu, M. Runde and H. Polinder, “Hysteresis losses in MgB2 superconductors exposed to combinations of low AC and high DC magnetic fields and transport currents,” *Physica C,* vol. 506, pp. 133-137, 2014.

[383] C. D. Manolopoulos, M. F. Iacchetti, A. C. Smith, K. Berger, M. Husband and P. Miller, “Stator Design and Performance of Superconducting Motors for Aerospace Electric Propulsion Systems,” *IEEE Transactions on Applied Superconductivity,* vol. 28, no. 4, 2018.

[384] P. Kovac, I. Husek, J. Kovac, T. Melisek, M. Kulich and L. Kopera, “Filamentary MgB2 Wires With Low Magnetization AC Loss,” *IEEE Transactions on Applied Superconductivity,* vol. 26, no. 6, p. 6200705, 2016.

[385] W. Carr, AC loss and macroscopic theory of superconductors, London: CRC Press, 2001.

[386] F. Fiorillo, Characterization and Measurement of Magnetic Materials, Amsterdam, The Netherlands: Elsevier, 2004.

[387] M. Oomen, J. Rieger, M. Leghissa and H. ten Kate, “Field-angle dependence of alternating current loss in multifilamentary high-Tc superconducting tapes,” *Applied Physics Letters,* vol. 70, no. 22, pp. 3038-3040, 1997.

[388] C. P. Steinmetz, “On the law of hysteresis,” *Proceedings of the IEEE,* vol. 72, no. 2, pp. 197-221, 1984.

[389] G. Escamez, F. Sirois, V. Lahtinen, A. Stenvall, A. Badel, P. Tixador, B. Ramdane, G. Meunier, R. Perrin-Bit and C.-E. Bruzek, “§-D Numerical Modeling of AC Losses in Multifilamentary MgB2 Wires,” *IEEE Transactions on Applied Superconducitivity,* vol. 26, no. 3, p. 4701907, 2016.

[390] B. Shen, J. Li, J. Geng, L. Fu, X. Zhang, C. Li, H. Zhang, Q. Dong, J. Ma and T. Coombs, “Investigation and comparison of AC losses on stabilizer-free and copper stabilizer HTS tapes,” *Physica C: Superconductivity and its applications,* vol. 541, pp. 40-44, 2017.

[391] G. Liu, G. Zhang, L. Jing, L. Ai, H. Yu, W. Li and Q. Liu, “Study on the AC Loss Reduction of REBCO Double Pancake Coil,” *IEEE Transactions on Applied Superconductivity,* vol. 28, no. 8, p. 8201606, 2019.

[392] M. K. Al-Mosawi, C. Beduz, Y. Yang, M. Webb and A. Power , “The Effect of FLux Diverters on AC Losses of a 10kVA High Temperature Superconducting Demonstrator Transformer,” *IEEE Transactions on Applied Superconductivity,* vol. 11, no. 1, pp. 2800-2803, 2001.

[393] S. Wu, J. Fang, L. Fang, A. Zhang, Y. Wang and Y. Wu, “The Influence of Flux Diverter Structures on the AC Loss of HTS Transformer Windings,” *IEEE Transactions on Applied Superconductivity,* vol. 29, no. 2, p. 5501105, 2019.

[394] M. D. Ainlie, W. Yuan and T. J. Flack, “Numerical Analysis of AC Loss Reduction in HTS Superconducting Coils Using Magnetic Materials to Divert Flux,” *IEEE Transactions on Applied Superconductivity,* vol. 23, no. 3, p. 4700104, 2013.

[395] G. Liu, G. Zhang, L. Jing and H. Yu, “Numerical study on AC loss reduction of stacked HTS tapes by optimal design of flux diverter,” *Superconductor Science and Technology,* vol. 30, p. 125014, 2017.

[396] D. Miyagi, Y. Yunoki, M. Umabuchi, N. Takahashi and O. Tsukamoto, "Measurement of magnetic properties of Ni-alloy substrate of HTS coated conductor in LN2," *Physica C,* vol. 468, pp. 1743-1746, 2008.